The Application of Osmotically Assisted Reverse Osmosis (OARO) Processes for Low-Cost and Sustainable Zero-Liquid Discharge (ZLD) Desalination



By: Christian Dietrich Peters

Supervisor: Professor Nicholas P. Hankins

October 4, 2021

Abstract

Freshwater scarcity is a globally increasing threat that is aggravated by population growth, economic development, the concomitant increase in consumption, and global climate change. Potable water is mostly extracted from natural fresh water sources, such as rivers, lakes, and aquifers, as these facilitate the cheapest and least energy intensive means of extraction. However, unsustainable extraction rates, which exceed the natural refill rate, inevitably lead to their depletion. Global warming further amplifies freshwater scarcity in arid regions, as these regions face higher evaporation rates and a growing reduction in the annual rainfall.

Desalination may potentially offer a long-term solution to our freshwater shortages, but it is expensive in terms of the resources required for its operation and this factor limits its accessibility, especially in low- and medium-income countries. Another concern is the environmental impact of desalination due to its high energy demand and the discharge of untreated brine, which may contain a wide range of pollutants. To combat both of these issues, the principal focus of this thesis is therefore on developing energy efficient brine volume minimisation (BVM) and zero-liquid discharge (ZLD) desalination processes.

Osmotically assisted reverse osmosis (OARO) is chosen as the sole focus of this study for its potential as a high-recovery, low-cost, energy efficient, and sustainable BVM and ZLD technology. The ability of OARO to draw water from concentrated brine (> 75 g/L) can be attributed to the combined effect of reducing the transmembrane osmotic pressure difference via the use of a draw solution and operating at high hydraulic feed pressures.

To first of all determine the technology's potential for BVM, OARO has been incorporated into a standard ultrafiltration and reverse osmosis desalination plant to increase the process

recovery. In total, six different OARO integrated flow processes, of which two are novel, are modelled numerically to determine their technical and economic feasibility in maximising the process recovery. At lower feed salinities, split feed OARO (SF-OARO) is the optimal OARO integrated flow process. Recoveries of up to 72% from a 35 g/L saline feed are possible when operating at the membrane burst pressure of 48.3 bar. Furthermore, the energy consumption of SF-OARO is approximately 4.00 kWh/m3, which is significantly lower than that in currently employed high recovery thermal processes, such as mechanical vapour compression ($7-25\ \mathrm{kWh/m^3}$). C-2, a cascading OARO (C-OARO) process, is a proposed novel OARO integrated flow process and is the most attractive at a higher feed salinity of 70 g/L. The maximum recovery of 44% is achieved at an average energy consumption of 6.37 kWh/m3. The presented numerical results demonstrate that the OARO integrated processes can competitively concentrate brine streams to concentrations of up to 125 g/L, whereas the maximum achievable brine salinity of a conventional single-stage RO process is generally limited to 75 g/L or less.

In order to improve the recovery of the standard OARO process, which utilises a non-responsive draw solute (i.e., NaCl), the incorporation of a thermo-responsive draw solute is investigated to see whether this novel combination can outperform 1) a forward osmosis (FO) process utilising the same draw solution, 2) the standard OARO process with non-responsive draw solutes, and 3) other high-recovery membrane processes. The findings from this parametric and technoeconomic analysis indicate that OARO mitigates several shortcomings of FO when utilising the same thermo-responsive draw solute, making it more energy efficient (energy savings of ≈10.8%), less susceptible to internal concentration polarisation, and more economical (cost savings of ≈15.5%). Furthermore, a key advantage of OARO is that it operates with lower draw solute concentrations, allowing for the draw solute to be regenerated at temperatures 12 °C lower than with FO operation. This means that low-grade waste heat

(LGWH) is more easily utilised as an energy source. In comparison to other hydraulic pressure-driven ZLD technologies, such as low-salt-rejection RO (LSRRO), the electrical energy consumption of OARO can be significantly offset when powered by LGWH and using a thermo-responsive draw solute. The specific electrical energy consumption can be as low as 3.47 kWh/m3 when concentrating a saline stream from 0.6 M to 4 M using 4 membrane stages. At the same time, a 4-stage LSRRO system would consume approximately 48% more electricity to achieve the same concentration factor. Furthermore, OARO processes operating with a thermo-responsive draw solution can outperform those using non-responsive draw solutes. Brine concentrations of up to 245 g/kg can be achieved using technically feasible operating pressures and draw solute concentrations, while the number of required membrane stages is almost halved from 6 to 4.

The previously presented numerical results highlight the potential of OARO for low-cost and energy-efficient brine management. However, its performance can be significantly limited by membrane fouling. Hence, a comprehensive experimental study on OARO membrane fouling is also performed to explore the associated fouling mechanisms, and to evaluate the fouling reversibility in OARO via simple physical cleaning strategies. Firstly, the experimental results show that internal membrane fouling at the draw (permeate) side is insignificant. Flux behaviour in short-term operation is correlated to both the evolution of fouling and the change of internal concentration polarization. In long-term operation, membrane fouling constrains the OARO water flux to a singular, common upper limit, in terms of limiting flux, which is demonstrated to be independent of operating pressures and membrane properties. Generally, once the limiting flux is exceeded, the OARO process performance cannot be improved by higher pressure operation or by utilising more permeable and selective membranes. Instead, different cyclic cleaning strategies are shown to be more promising alternatives for improving performance. While both surface flushing and osmotic backwashing (OB) are found to be

highly effective when using pure water, a full flux recovery cannot be achieved when a non-pure solution is used during OB; this is due to severe internal clogging during OB.

The presented numerical and experimental findings offer valuable insights into the technical and economic feasibility of OARO as a brine management technology during desalination. The presented findings also generate significant implications for OARO operation and fouling control.

Publications

2021 - C. D. Peters, T. Rantissi, V. Gitis, N. P. Hankins. Retention of natural organic matter by ultrafiltration and the mitigation of membrane fouling through pre-treatment, membrane enhancement and cleaning-A review. Journal of Water Process Engineering, 2021, 44.

- C. D. Peters, D. Y. F. Ng, N. P. Hankins, and Q. She, A novel method for the accurate characterization of transport and structural parameters of deformable membranes utilized in pressure- and osmotically driven membrane processes. Journal of Membrane Science, 2021, 638.

- C.D. Peters and N.P. Hankins, Making zero-liquid discharge desalination greener: Utilising low-grade heat and vacuum membrane distillation for the regeneration of volatile draw solutes. Desalination, 2021, 507.

2020 - C.D. Peters and N.P. Hankins, The synergy between osmotically assisted reverse osmosis (OARO) and the use of thermo-responsive draw solutions for energy efficient, zero-liquid discharge desalination. Desalination, 2020, 493.

- B. Al-Najar*, C.D. Peters*, H. Al Buflasa and N.P. Hankins, Pressure and osmotically driven membrane processes: A review of the benefits and production of nano-enhanced membranes for desalination. Desalination, 2020, 479. (*: First co-authorship)

2019 - C.D. Peters and N.P. Hankins, Osmotically assisted reverse osmosis (OARO): Five approaches to dewatering saline brines using pressure-driven membrane processes. Desalination, 2019, 458, 1-13.

Under Review

2021 - C. D. Peters, D. Li, Z. Mo, N. P. Hankins, Q She. Exploring the limitations of osmotically assisted reverse osmosis (OARO) processes: Membrane fouling and the limiting flux. Journal of Environmental Science & Technology. (Under Review)

- C. D. Peters, Z. Mo, N. P. Hankins, Q She. Dynamic operation of OARO: How OARO can outperform conventional RO processes with varying electricity tariffs. Desalination. (Under Review)

Conferences

2021 - C.D. Peters, D. Li, Q. She and N.P. Hankins: “Exploring the limitations of osmotically assisted reverse osmosis (OARO) processes: Membrane fouling and the limiting flux”, will be presented at the 5th International Conference on Desalination using Membrane Technology: Virtual conference, 14th-17th November 2021.

2020 - C.D. Peters and Q. She: "Accurate characterisation of deformable membranes utilised in pressure and osmotically driven membrane processes", presented at the International Congress on Membranes & Membrane Processes 2020: Virtual conference, 6th-11th December 2020.

2019 - C.D. Peters and N.P. Hankins: "Multi-stage vacuum membrane distillation (MS-VMD) for the recovery of volatile draw solutes using low-grade waste heat", presented at the 4th International Conference on Desalination using Membrane Technology: Perth, Australia, 1st-4th December 2019.

- N.P. Hankins and C.D. Peters: "Osmotically Assisted Reverse Osmosis (OARO): Some New Approaches to Dewatering High Salinity Brines to High Recovery using Membrane Processes", presented at the 4th International Conference on Desalination using Membrane Technology: Perth, Australia, 1st-4th December 2019.

- C.D. Peters and N.P. Hankins: "The role of osmotically assisted reverse osmosis (OARO) in zero liquid discharge desalination processes", presented at the Royal Society conference: “Ensuring water safety in a changing climate by enhanced water and wastewater treatment”: Chicheley Hall, Buckinghamshire, UK, 25th-26th March 2019.

2018 - C.D. Peters and N.P. Hankins: "Exploring the synergy between membrane desalination and thermal power generation via co-location", presented at the WESII (Water and Energy Sustainable Innovation and Industry) conference: Manama, Kingdom of Bahrain, 24th-28th April 2018.

Acknowledgements

First and foremost, I am extremely grateful to my supervisor, Prof. Nick Hankins for his invaluable advice, continuous support, and patience during my D.Phil study. Nick has given me the liberty to explore the world of water and has offered me the support that I needed to achieve my goals. I am especially grateful for the opportunities that he has offered me by organising my scholarship, setting up the extensive collaboration with Professor Qianhong She at SMTC, and for involving me in other collaborations and projects that expand beyond my D.Phil. I hope that we can continue our work to find solutions to some of the great issues surrounding water.

I would like to offer my special thanks to Professor Qianhong She and his research group at SMTC who have warmheartedly welcomed me in Singapore. I was greeted with so much kindness and I am very grateful for his/their help and support throughout my stay. A special thanks also to my collaborators Dan Li and Zijing Mo who have kindly helped me to complete my experimental work. Our continued collaboration means a lot to me, and I hope that we can continue with other fruitful projects and grand ideas.

I am also grateful for the scholarship offered to me during my D.Phil from the University of Bahrain.

Finally, I would like to express my gratitude to my parents and Ailish, the people closest to my heart. Without their tremendous understanding and encouragement in the past few years, it would have been impossible for me to complete my D.Phil. Thank you for your unwavering support and belief in me.

Contents

Abstract 1
Publications 5
Under Review 6
Conferences 7
Acknowledgements 9
Contents 10
List of Figures 14
List of Tables 19
Nomenclature 20
Chapter 1 1
Introduction 1
1.1. Project background 1
1.1.1. Freshwater scarcity, and brine - the unwanted by-product of desalination 1
1.1.2. Membrane technologies used for BVM and ZLD 5
1.2. Status of OARO research 10
1.2.1. Numerical OARO research 10
1.2.2. Gaps in numerical OARO research 16
1.2.3. Experimental OARO research 17
1.2.4. Gaps in experimental OARO research 18
1.3. Research objectives 19
1.4. Thesis layout 21
Chapter 2 23
Background Theory 23
2.1. OARO governing equations 23
2.2. Optimal OARO membrane properties 27
2.2.1. Membrane water permeability 27
2.2.2. Membrane selectivity and ICP 29
2.3. Membrane deformation and fouling phenomena in OARO 32
2.4. The critical and limiting flux theorems 37
Chapter 3 41

Six approaches for brine volume minimisation using OARO with non-responsive draw solutes 41
3.1. Analysis of the stand-alone OARO process 44
3.1.1. Optimal OARO membrane properties 44
3.1.2. Optimal OARO feed flowrate 47
3.1.3. Optimal flowrate ratio between OARO streams 48
3.1.4. Optimal OARO feed pressure 50
3.2. The standard UF-RO process 51
3.3. The OARO integrated processes 54
3.3.1. MP-OARO 55
3.3.2. C-OARO 58
3.3.3. SF-OARO 59
3.4. Analysis of the OARO configurations 61
3.4.1. Scenario 1 ($CF = 35 g/L$ and $YS = 72\%$) 63
3.4.2. Scenario 2 ($CF = 70 g/L$ and $YS = 44\%$) 64
3.5. OARO vs. MSRO 66
3.6. Prospect of OARO using non-responsive draw solutes 69
3.7. Chapter conclusions 71
Chapter 4 73
Achieving zero-liquid discharge with OARO and thermo-responsive draw solutes 73
4.1. ZLD process layout 75
4.2. Simulation set-up 78
4.2.1. The draw solution 81
4.2.2. The membrane processes 84
4.2.3. The draw solute regeneration (DSR) system 86
4.3. Analysis of the DSR distillation columns 90
4.4. Parametric optimisation of the FO and OARO integrated ZLD flow processes 93
4.4.1. Effect of N/C ratio 94
4.4.2. Effect of the FO/OARO feed flowrate 96
4.4.3. Effect of RR 100
4.4.4. Effect of the inlet salinity 100
4.5. Techno-economic comparison of the OARO and FO integrated ZLD processes 102
4.5.1. UWC of the steam-powered FO and OARO base cases 102
4.5.2. UWC of the LGWH powered FO and OARO base cases 104

4.6. Comparing the FO and OARO MBC with the LSRRO and the standard OARO processes 106
4.7. Chapter conclusions 111
Chapter 5 113
Exploring the technical limitations of OARO: Membrane fouling and the limiting flux 113
5.1. Materials and methods 116
5.1.1. Experimental setup, membranes and spacer backing 116
5.1.2. Chemicals and solutions 118
5.1.3. OARO fouling experiments 121
5.1.4. OARO cleaning experiments 121
5.2. Effect of feed and draw solution composition on OARO fouling 122
5.3. Pressure independent limiting flux in OARO 126
5.4. Membrane independent limiting flux in OARO 130
5.5. OARO membrane fouling reversibility 135
5.6. Chapter conclusions 138
Chapter 6 140
Conclusions and future work 140
6.1. Chapter summaries 142
6.2. Future work 146
Appendix A 1
A.1. Practical SEC and PMax of the single-stage SF-OARO process 1
A.2. Practical SEC and PMax of the two-stage SF-OARO process 3
Appendix B 7
B.1. Model validation using ROSA 7
B.1.2. Validation of NF modelling capability 9
B.2. Model validation using experimental data for PAFO module testing 12
Appendix C 15
C.1. The equivalent work principle and the unit water cost calculation 15
C.1.1. Equivalent work principle 15
C.1.2. Unit water cost calculation 17
Appendix D 19
D.1. OARO cleaning strategies 19
D.2. Plugged OARO draw spacer 21
D.3. The ICP self-compensation effect at different water fluxes 22

D.4. Ideal OB of the AQP and BW30LE membrane 24
Appendix E 26
E.1. Chapter 3 Matlab source code 26
E.1.1. Main Function 26
E.1.2. FD (Flow-diagram) function 32
E.2. Chapter 4 source code 51
E.2.1. Main function 51
E.2.2. DSR (Aspen) Interface 55
E.2.3. MBC stages 57
E.3. General functions 59
E.3.1. SM (Shooting method) function 59
E.3.2. Q_M_It (Mass flowrate) function 60
References 1

List of Figures

Figure 1: Brine and feed volume with respect to the freshwater recovery of the desalination plant with a constant permeate production rate of 1. 3

Figure 2:Water flux JW with respect to the operating pressure ΔP for FO, PAO, OARO and RO. 8

Figure 3: MSRO and the three main OARO configurations. High-pressure pumps and energy recovery devices (ERD) are displayed to indicate which streams are pressurised for OARO/RO operation. The water flux direction is indicated by the orange arrow. 10

Figure 4: The practical specific electrical energy consumption (SEC) and the maximum operating pressure (PMax) of MSRO, MP-OARO, C-OARO and SF-OARO. The over-pressurisation factor k is set as 1.15, the system recovery YS is set as 70% and the inlet feed salinity is set as 35 g/L NaCl. The results for MSRO, MP-OARO and C-OARO were obtained from Chen & Yip [18]. The practical SEC and PMax for the SF-OARO system are derived in Appendix A. 11

Figure 5: Schematics of a 4-stage low-salt-rejection RO process. 14

Figure 6: Concentration profile for typical membrane orientations for HPRO and OARO membrane processes. In HPRO and OARO the effective osmotic pressure $\Delta\pi Eff$ is positive, as the permeate (draw) is less concentrated than the feed. 24

Figure 7: The practical SEC of SSRO, MSRO and the three main OARO configurations with respect to the system recovery. The total energy consumption associated with over-pressurisation is represented by the hatched area. The grey shaded SSRO region highlights the energy that can be saved by employing MSRO or one of the OARO configurations instead of SSRO. The SEC diagrams for MSRO, MP-OARO and C-OARO have been adopted from Chen et al. [69]. 29

Figure 8: Internal concentration polarisation factor of the draw solution with respect to the water flux for three different structural parameters. 32

Figure 9: OARO performance affecting phenomena that can arise due to membrane deformation and fouling. 35

Figure 10: Specific energy consumption and diluted draw concentration for three different membranes with respect to OARO process recovery. ($QF = 8\ m3 / h,\ RR = 0.5$). 46

Figure 11: Specific energy consumption and diluted draw concentration for three different feed flowrates with respect to OARO process recovery. (TFC-FO membrane with $RR = 0.5$). 48

Figure 12: Specific energy consumption and diluted draw concentration for three flowrate ratios RR with respect to OARO process recovery. (TFC-FO membrane with $QF = 8\ m3\ /\ h$). 49

Figure 13: The UF-RO reference model. 51

Figure 14: MP-OARO, the first two OARO integrated flow process that are being investigated. 56

Figure 15: The other four OARO integrated flow processes that are being investigated. 57

Figure 16: Pressure profile in an osmotically assisted reverse osmosis process with 3 stages in series. 58

Figure 17: Simulation results for the OARO integrated flow processes for scenario 1 ($CF = 35g/L$ and $YS = 72\%$) in the left column, and scenario 2 ($CF = 70g/L$ and $YS = 44\%$) in the right column. The shaded regions indicate infeasible operating regions. In the SEC plots, the thermodynamic minimum energy for both scenarios is indicated by the dashed lines above the shaded regions. 62

Figure 18: The FO zero-liquid discharge process installed at the Changxing coal-fired power plant, China. Adapted from Pendergast et al.[147]. 77

Figure 19: The simulation algorithm of the FO/OARO MBC and the two-pass RO system. The orange box indicates the commands run in Matlab whereas the grey box indicates the command run in ASPEN Plus. Communication and sharing of stream data between the two programs is initiated using the 'actxserver' function in Matlab. 80

Figure 20: The osmotic pressure of the $NH3 - CO2$ thermo-responsive DS for various ammonia and carbon dioxide ratios (N/C) and draw solute concentrations on a carbon basis. The horizontal red line indicates the osmotic pressure of the final NaCl brine stream with a concentration of 220 g/L. The osmotic pressures are determined using ASPEN Plus with the DSR set-up given in Section 4.2.3. 82

Figure 21: The draw solute regeneration system with heat integration. Adapted from Pendergast et al. [147]. 87

Figure 22: Parametric analysis of a single distillation column for various NaCl feed concentrations. Figures (a) and (b) depict the effect of the column operating pressure on the reboiler temperature and its heat duty per kilogram of feed solution containing a 1 mol/kg thermo-responsive draw solution on a carbon basis and a N/C ratio of 2.4. Figures (c) and (d) depict the effect of the draw solute on the reboiler temperature and its heat duty per kilogram of feed at a constant column pressure of 1 bar. The N/C ratio of the feed solution is also kept constant at 2.4. 90

Figure 23: The equivalent work WEq of the FO (left column) and OARO (right column) integrated ZLD processes with respect to various operational parameters. The standard operational parameters are as follows: N/C is 2.4, $QMBC$ is $5\ m3/h$, RR is 0.33, $TCond$ is

40°C, feed inlet salinity CF is 45 g/L and 5 bar saturated steam is used as heat supply to the DSR system. The FO/OARO base case is always given by the central column in each figure. 95

Figure 24: The osmotic pressure of the $NH3-CO2$ thermo-responsive draw solution for two N/C ratios with respect to the ammonia concentration. 96

Figure 25: Total ammonia concentration in the brine stream exiting the final FO/OARO stage at various QMBC. 98

Figure 26: The saturation pressure and the DC1 and DC2 reboiler temperature for the FO and OARO DSR system at various QMBC and at a constant condenser temperature of 40°C. ...100

Figure 27: Sensitivity analysis of the unit water cost for the FO and OARO base cases with respect to the electricity cost. 103

Figure 28: The required concentration of the thermo-responsive DS in the CDS stream CDSTh with respect to the target brine concentration. The initial feed concentration is 3 g/kg NaCl. 109

Figure 29: Schematic of the experimental setup (modified from She et al.[97]). 116

Figure 29: Schematic of the experimental setup (modified from She et al.[97]). 118

Figure 30: Effect of feed and draw solution composition on OARO permeate flux evolution. All fouling experiments were carried out using the AQP membrane at 50 bar with cross-flow velocity of 10 cm/s. RC: Reference case, and solution compositions for F1-F5 are listed in Table 7. 122

Figure 31: (a) Effect of the applied hydraulic pressure on OARO permeate flux evolution. All fouling experiments were carried out using the AQP membrane using the solutions specified for test case F5 in Table 7. (b) Relationship between the initial and final, pseudo-stable water flux. 128

Figure 32: Effect of the membrane properties on OARO permeate flux evolution. All fouling experiments were carried out using the solutions specified for test case F5 in Table 1. The AQP and BW30LE membrane were operated at 50 bar and 40 bar, respectively. 131

Figure 33: (a) Visualisation of the ICP self-compensation effect for the AQP and BW30LE membrane using the change of $fDCP$ as indicator, (b) the change of the effective driving force with fouling progression, and (c) the calculated foulant resistance of both membranes during the F5 fouling scenario. 133

Figure 34: The effectiveness of the three cleaning scenarios. Ideal OB: Osmotic backwash using 2.4M NaCl feed and DI water as draw. Real OB: Osmotic backwash using OARO brine as feed and draw according to test case F5 (Table 7). Flush: surface flushing using DI water as feed and draw solution. The different cleaning conditions are specified in Section 5.1.4. and Appendix D. All fouling experiments were carried out using the solutions specified for test case F5 in Table 1. The AQP membrane was operated at 50 bar with a CFV of 10 cm/s

during the fouling cycles. Each of the three fouling cycles lasted 80 min, to give a total fouling duration of 4 hours whereas each cleaning cycle lasted 10 minutes. The negative flux in the figure indicates that the flux is reversed during cleaning. 136

Figure 35: Single stage SF-OARO process layout 1

Figure 36: Two stage SF-OARO process layout 4

Figure 37: The SEC and the maximum operating pressure for the SF-OARO system as a function of the flowrate ratio RR 6

Figure 38: Water flux with respect to the RO feed pressure for two different inlet flowrates. .7

Figure 39: Permeate salinity with respect to the RO feed pressure for two different inlet flowrates.....8

Figure 40: Water flux with respect to the feed inlet salinity for two different RO operating pressures.....9

Figure 41: Permeate salinity with respect to the feed inlet salinity for two different RO operating pressures.....9

Figure 42: Water flux with respect to the NF feed pressure for two different inlet flowrates. 10

Figure 43: Permeate salinity with respect to the NF feed pressure for two different inlet flowrates.....11

Figure 44: Water flux with respect to the NF feed pressure and inlet salinity. 11

Figure 45: Permeate salinity with respect to the NF feed pressure and inlet salinity. 12

Figure 46: Water flux with respect to the concentration difference between the feed and draw stream. Experimental data is obtained from Jeon et al. [136]. 13

Figure 47: The experimental and modelled water flux for two different FO membrane modules under PAFO operation. Experimental data is obtained from (Kim, Blandin, & Phuntsho, 2017) 14

Figure 48: The ratio of the salt to water flux with respect to the PAFO feed pressure. Experimental data is obtained from (Kim, Blandin, & Phuntsho, 2017).....14

Figure 49: The three different cleaning scenarios investigated. 20

Figure 50: Plugged OARO draw spacer. 21

Figure 51: (a) The dilutive concentration polarisation factor $fDCP$ and (b) it's derivative with respect to the water flux. The S-value of the AQP and BW30LE membrane are 810 μm and 2100 μm, respectively.....23

Figure 52: Comparing the effectiveness of the ideal OB cleaning strategy on the AQP and BW30LE membrane. The AQP membrane and BW30LE membrane are operated at 50 bar and 40 bar with a CFV of 10 cm/s during the fouling cycles. Each of the three fouling cycles lasted 80 min, to give a total fouling duration of 4 hours whereas each cleaning cycle lasted 10 minutes. 25

List of Tables

Table 1: Membrane properties of the three simulated membranes.....45

Table 2: System recovery YS, specific energy consumption (SEC), permeate salinity CP and number of UF modules NUF and RO modules NRO required for the UF-RO process at two varying inlet salinities CF.....52

Table 3: Comparison of OARO vs MSRO for the two scenarios. For this comparison, the OARO integrated flow processes are modelled with a total of three OARO stages and the terminal RO stage. Similarly, MSRO has an equivalent number of stages (4), including the terminal RO stage. 67

Table 4: Prospective improvements in OARO membrane and module development for SF-1 with $SOA = 3$ and $CF = 35\ g/L$: for each membrane, the effect of increasing the burst pressure to 70 bar is shown. 69

Table 5: Membrane properties of the simulated RO and FO/OARO membranes.....85

Table 6: Comparison of the LSRRO, the standard OARO and the FO and OARO MBC with a thermo-responsive DS to concentrate a 35 g/kg saline stream to 205 g/kg (0.6 M to 4 M). The FO and OARO MBC are operated using a single RO pass and with the following parameters: N/C = 2.4, $QMBC = 5\ m3/h$, RR = 0.33, $PRO1 = 80\ bar$, $QRO = 12\ m3/h$.....107

Table 7: Composition of the synthetic feed and draw solutions used for the OARO fouling experiments. 120

Table 8: Financial parameters for the calculation of the unit water cost.....18

Nomenclature

Abbreviations

AL-DS	Active layer - draw side
AL-FS	Active layer - feed side
AQP	Aquaporin
BVM	Brine volume minimisation
BWRO	Brackish water reverse osmosis
CapEx	Capital expenditures
CECP	Cake-enhanced concentration polarization
CCP	Concentrative concentration polarisation
CDS	Concentrated draw solution
CF	Capitalisation factor
CFV	Crossflow velocity
CTA	Cellulose acetate
C-OARO	Cascading OARO
DC	Distillation column
DCP	Dilutive concentration polarisation
DDS	Diluted draw solution
DF	Driving force
DI	Deionised
DS	Draw solution
DSR	Draw solute regeneration
ECP	External concentration polarisation
ERD	Energy recovery device
FO	Forward osmosis
FS	Feed solution
FSD	Forward solute diffusion
GOR	Gained output ratio
HEX	Heat exchanger
HPP	High pressure pump
HPRO	High-pressure reverse osmosis
ICP	Internal concentration polarisation
LGWH	Low-grade waste heat
LMH	Water flux, $L/(m^2h)$
LSRRO	Low salt rejection reverse osmosis
MBC	Membrane brine concentrator
MCr	Membrane crystallisation
MD	Membrane distillation
MED	Multiple effect distillation
MP-OARO	Multi-pass OARO
MSRO	Multi-stage reverse osmosis
MVC	Mechanical vapour compression
N/C	Ammonia to carbon dioxide ratio
NF	Nanofiltration

OARO	Osmotically assisted reverse osmosis
OB	Osmotic backwash
OpEx	Operational expenditures
ORF	Osmotic resistance filtration
PAO	Pressure assisted osmosis
PRO	Pressure retarded osmosis
RC	Reference case
RO	Reverse osmosis
ROSA	RO system analysis software
RSD	Reverse solute diffusion
RSF	Reverse solute flux
SCL	Specific cooling load
SEC	Specific energy consumption
SEEC	Specific electrical energy consumption
SF-OARO	Split feed OARO
STEC	Specific thermal energy consumption
SDI	Silt density index
SI	Saturation index
SSRO	Single-stage RO
SWRO	Seawater reverse osmosis
TAC	Total annual cost
TDS	Total dissolved solids
TFC	Thin-film composite
TMP	Transmembrane pressure
UF	Ultrafiltration
UWC	Unit water cost
WHO	World Health Organisation
WW	Wastewater
ZLD	Zero liquid discharge

Symbols

A	Water permeability coefficient, $\mathrm{L/(m^2 h\ bar)}$
B	Salt permeability coefficient, $\mathrm{L/(m^2 h)}$
C_{BP}	Booster pump cost, \$
C_{CO2}	Carbon dioxide concentration, $\mathrm{mol/kg}$
C_{Cond}	Condenser cost, \$
C_D	Draw concentration, $\mathrm{g/L}$
C_{DC}	Distillation column cost, \$
C_{DS}	Draw solute purchasing cost, \$
C_{ERD}	ERD cost, \$
C_F	Feed concentration, $\mathrm{g/L}$
C_{HEX}	HEX cost, \$
C_{HPP}	High-pressure pump cost, \$
C_{Mem}	Membrane unit cost, \$
C_{NaCl}	NaCl concentration, $\mathrm{mol/kg}$
C_{NH3}	Ammonia concentration, $\mathrm{mol/kg}$
C_P	Permeate concentration, $\mathrm{g/L}$

C_{PV}	Pressure vessel unit cost, \$
C_{Reb}	Reboiler unit cost, \$
$CapEx_{DSR}$	CapEx of the DSR system, \$
$CapEx_{Mem}$	CapEx of the membrane systems, \$
D	Diffusivity coefficient, m^2/s
DF_{Eff}	Effective driving force, bar
E_{Min}	Thermodynamic minimum energy of separation, kWh/m^3
F	Practical investment factor
F_{App}	Apparent driving force, bar
$F_{Barrier}$	Barrier force, N
F_{CCP}	Loss of driving force due to CCP, bar
F_{DCP}	Loss of driving force due to DCP, bar
F_{Drag}	Drag force, N
f_{CCP}	CCP factor
f_{DCP}	DCP factor
$h_{fg,Steam}$	Enthalpy of vaporization, kJ/kg
$h_{g,Cond}$	Steam enthalpy in the condenser,kJ/kg
$h_{g,Steam}$	Enthalpy of the extracted steam, kJ/kg
J_C	Critical flux, $L/(m^2h)$
J_L	Limiting flux, $L/(m^2h)$
J_S	Salt flux, $mol/(m^2h)$
J_0	Initial water flux, $L/(m^2h)$
J_W	Water flux, $L/(m^2h)$
k	Over-pressurization factor
k_D	Mass transfer coefficient in draw stream, $L/(m^2h)$
k_F	Mass transfer coefficient in feed stream, $L/(m^2h)$
k_M	Mass transfer coefficient in the membrane, $L/(m^2h)$
N_{OA}	Number of OARO pressure vessels
N_{RO}	Number of RO pressure vessels
N_{UF}	Number of UF pressure vessels
n_{OA}	Number of OARO modules in series
O_{Chem}	Chemical consumption cost, \$/year
O_{CW}	Cooling water cost, \$/kWh
O_{DS}	Draw solute replenishment cost, \$/year
O_{Elec}	Electricity cost, \$/kWh
O_{Mem}	Membrane replacement cost, \$/year
O_{ML}	Maintenance and labour cost, \$/year
$OpEx_{DSR}$	OpEx of the DSR system, \$/year
$OpEx_{Mem}$	OpEx of the membrane systems, \$/year
P_D	Pressure of the draw solution, bar
P_F	Pressure of the feed solution, bar
P_{Max}	Maximum operating pressure, bar
P_{OA}	OARO feed pressure, bar
P_{RO}	Maximum RO feed pressure, bar
P_{Sat}	Saturation pressure, bar
Q_D	Draw flowrate, m^3/h
Q_F	Feed flowrate, m^3/h
Q_{MBC}	Feed flowrate of the MBC membrane modules, m^3/h

Q_P	Permeate flowrate, $\frac{\mathrm{m}^3}{\mathrm{h}}$
R_F	Foulant resistance, m^{-1}
R_G	Universal gas constant, $\mathrm{J/(mol\ K)}$
R_h	Characteristic hydrodynamic radius, m
R_M	Membrane resistance, m^{-1}
RR	Ratio between draw and total flowrate
RSF_{MBC}	Reverse solute flux in the MBC membrane modules, $\mathrm{g_{NH3}/kg}$
S	Structural parameter, m
S_1 to S_4	Number of membrane stage
S_{In}	Inlet salinity, $\mathrm{g/L}$
S_{OA}	Number of OARO membrane stages
T	Temperature, °C
T_{Reb}	Reboiler temperature, °C
W_{Eq}	Equivalent work, $\mathrm{kWh/m^3}$
Y_S	System recovery
β	Van't Hoff factor
ΔP	Transmembrane pressure difference, bar
ΔP_L	Pressure loss, bar
$\Delta\pi$	Osmotic pressure difference, bar
$\Delta\pi_{Eff}$	Effective osmotic pressure difference, bar
η_{II}	Second law efficiency
η_{Tur}	Turbine efficiency
ϕ	Osmotic coefficient
μ	Fluid viscosity, Pa s
π_D	Osmotic pressure of draw solution, bar
π_F	Osmotic pressure of feed solution, bar

Chapter 1

Introduction

1.1. Project background

1.1.1. Freshwater scarcity, and brine - the unwanted by-product of desalination

According to the United Nations, more than 844 million people currently lack access to clean drinking water [1]. Within the coming years, the global water crisis is expected to worsen as population growth, increasing consumption, economic development and global warming are set to create new, and further aggravate existing, freshwater shortages. It is estimated that by 2050, up to 3.9 billion people may be living in areas with severe water stress [2].

Working along the lines of reduce and reuse, saving freshwater by (1) reducing agricultural, urban, and industrial water consumption and wastage, by (2) preventing leakage from water infrastructure, and by (3) improving wastewater reuse, are the most sustainable options to curb the rapid depletion of freshwater sources. Implementing freshwater saving measures alone, however, may not be sufficient to meet the growing demand and hence, alternative freshwater sources are sought. As only 2.5% of the global water inventory can be qualified as freshwater [3], with the remaining vast majority as saline (and principally seawater), desalination is deemed a viable alternative source of freshwater that could potentially help humanity to overcome the anticipated future water crises.

Desalination, however, faces several hurdles to becoming truly sustainable and affordable in low- and medium-income countries. Of the currently available desalination technologies,

reverse osmosis (RO) is the most energy efficient choice. Being a pressure driven process, those irreversible losses associated with a phase transition of the product water, as required for achieving separation in thermal desalination processes, can be avoided [4]. This allows RO to operate closer to the thermodynamic minimum energy of separation. However, the maximum operating pressure, which is that required to overcome the maximum feed osmotic pressure, is limited by the membrane burst pressure [5]. This limits the maximum water recovery of RO, especially at the higher feed concentrations (> 75 g/L) [6].

Unfortunately, lower process recoveries have adverse economic and environmental implications, as larger volumes of feedwater must be extracted and pre-treated to produce the same amount of freshwater. Furthermore, larger volumes of brine, the rejected concentrate from the process, must be disposed of. On a worldwide level, desalination technologies produce more than 140 million m3/day of brine. This is almost 50% greater than the amount of freshwater they produce (95 million m3/day) [7]. Brine is an unwanted desalination by-product that is most economically disposed of by discharging it back into the environment in its untreated state [8]. However, untreated brine is often severely polluted and can contain contaminants, such as anti-fouling and anti-scaling additives, antifoaming additives, oxygen scavengers and corrosion products [9,10]. Furthermore, brine is also highly saline and can be discharged at elevated temperatures from thermal desalination processes. Thus, brine in its untreated state can cause severe damage to ocean life and marine ecosystems [11–13].

These negative ecological effects can be circumvented by developing more economically viable and environmentally sound brine management solutions. According to Morillo et al. [14], brine management solutions can be utilised for (1) brine volume minimisation (BVM), (2) salt and metal recovery, and (3) brine adaptations for industry. Salt and metal recovery processes utilise the brine to produce valuable by-products. As stated by Loganathan et al. [15], the potential exists to extract minerals, such as sodium, magnesium, calcium and bromide, from seawater in

an economically favourable manner. Another possibility is to valorise the brine stream by concentrating and adapting it for the chlor-alkali industry and acid-base production [16,17]. The ability to withdraw water from saline brines (50–350 g/L TDS) in a more energy efficient manner would also be beneficial for many industries, such as the oil, gas, and energy sectors [10,18]. For example, it would facilitate the reuse of high salinity wastewaters, and allow other processes, such as inland desalination, to circumvent regulatory, economical, and environmental restrictions due to brine volume minimisation [19]. Furthermore, zero-liquid discharge processes could increase profit margins, as valuable by-products, such as minerals, are then produced at reduced electricity costs.

Although BVM may not appear to offer any direct economic value, as no additional by-products are produced, higher process recoveries do lead to an exponential decrease in the final brine volume and the required seawater extraction rate (feed) for a constant freshwater production rate. This trend is depicted in Figure 1. Lower brine volumes simplify brine disposal and minimise the associated costs, and lower feed volumes can reduce pre-treatment costs [7].

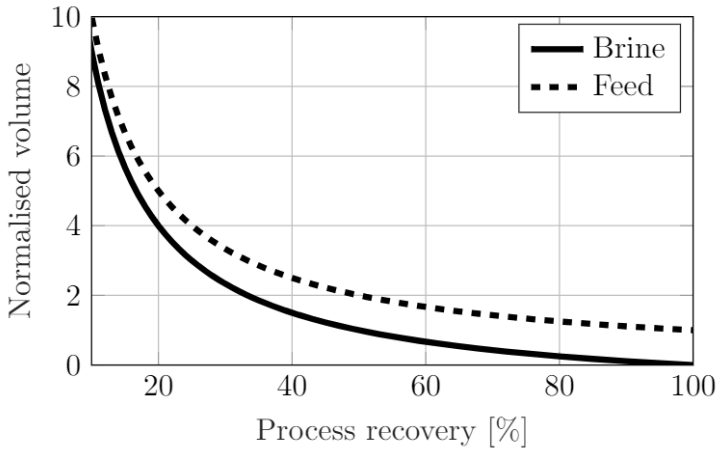


Figure 1: Brine and feed volume with respect to the freshwater recovery of the desalination plant with a constant permeate production rate of 1.

According to Morillo et al. [14], brine disposal costs account for between 5% and 33% of the total cost of desalination. A reduction in brine volume can lower the costs associated with its

disposal and treatment, where the latter may be required to meet local regulations and to reduce the environmental impact of disposal. Thus, more environmentally friendly brine management solutions may become economically feasible with lower brine volumes and higher process recoveries. However, BVM and ultimately zero-liquid discharge (ZLD) processes are not widespread, due to the availability of other more economically viable brine disposal options [4]. In addition, the dewatering of such highly saline brines (> 75 g/L) poses considerable technical challenges.

Currently, thermal processes, such as mechanical vapor compression (MVC), are the prevailing techniques of choice to dewater brines with a TDS content exceeding 70 g/L up to final brine salinities of approximately 250 g/L [19]. MVC comprises of a volumetric flow compressor that acts as a 'heat pump', which continuously recycles and keeps the latent heat exchanged in the evaporation and condensation steps within the system. The compressed vapour is condensed by rejecting heat to evaporate part of the processed feed via a heat transfer surface. This cycle of evaporation and condensation operates continuously. Brine concentrators and crystallisers work on a similar basis and also utilise a compressor to supply the required heat for brine concentration.

High capital costs and energy consumption are associated with these thermal processes (e.g., MVC: 7 kWh/m^3 to 25 kWh/m^3; brine concentrator: 18 kWh/m^3 to 26 kWh/m^3 [4]), which limits their widespread application. Furthermore, concentrating the brine stream above its solubility limit and crystallising it using thermal-based technologies (if not performed using solar evaporation), proves to be even more capital and energy intensive (e.g., brine crystalliser: 52 kWh/m^3 to 66 kWh/m^3). Solar evaporation has its own deficiencies, such as being limited to dry and warm regions and requiring large amounts of land [20].

1.1.2. Membrane technologies used for BVM and ZLD

Membrane processes that can achieve higher brine concentrations than the conventional, single-stage RO process include membrane distillation (MD) and crystallisation (MCr) [21–23], multi-stage reverse osmosis (MSRO), high pressure reverse osmosis (HPRO) [19], low-salt-rejection RO (LSRRO) [24], osmotically assisted reverse osmosis (OARO) [18,25], pressure assisted osmosis (PAO) [26,27], and forward osmosis (FO) [28]. Electrodialysis and capacitive deionization can also be utilised in BVM processes [6], although they are mainly applied for low salinity feeds. This is due to their relatively high capital and operating expenses and their lower water/salt selectivity in comparison to RO [29,30].

Desalination by membrane-based distillation consumes relatively large amounts of energy, especially when it is compared to other well-established desalination technologies [31]. The low thermal efficiency of MD systems is related to the relatively high sensible heat losses associated with their operation, and the difficulties associated with efficient heat integration in these systems. Mistry et al. [32] modelled the entropy generated by different desalination technologies and estimated that the second law efficiency η_{II} of direct contact MD can be as low as 1%. In comparison, the second law efficiencies of other thermal desalination technologies, such as that of MVC and multiple effect distillation (MED), were estimated to be several times higher (MVC: $\eta_{II} = 8.5\%$ and MED $\eta_{II} = 5.9\%$). Thermal desalination processes are plagued by severe irreversible losses incurred by phase change during the separation process. As previously mentioned, these irreversible losses can be circumvented by RO, as the mechanism of separation for RO does not involve thermodynamic phase change but instead is based on the relative kinetics of sorption and diffusion. Hence, the second law efficiency of RO was estimated by Mistry et al. [32] to be substantially higher ($\eta_{II} = 32\%$).

Pressure driven membrane processes have the potential to operate closer to the thermodynamic minimum energy of separation, which is equivalent to the Gibbs free energy of separation [18,33]. This makes them attractive alternatives to thermal based BVM/ZLD technologies. Similarly, osmotically driven membrane processes, such as FO, PAO or OARO, can also outperform thermal based BVM/ZLD technologies [34–36]. A generic FO brine concentration system consists of an (1) FO membrane system, in which the feed is concentrated by osmosis while the draw is diluted across a semi-permeable membrane, and a (2) draw solute regeneration (DSR) system that reconcentrates the draw solution by extracting the final product water. Although almost no energy is consumed in the FO membrane system (except in the form of low-pressure pump work), the DSR system is energetically costly. For brine dewatering to occur in the FO membrane system, the draw solution must have a higher osmotic potential than the feed solution. As described by Elimelech & Phillip [33], the minimum energy of separation increases with an increase in the osmotic potential of the draw solution and hence, the theoretical and actual energy requirements for draw regeneration are increased above those of direct desalination [34,37]. In other words, osmotically driven membrane processes in which the draw solution (1) is more concentrated than the feed solution (i.e., FO and PAO) and (2) is regenerated for reuse, will be more energy intensive than their purely pressure driven counterparts (Assuming that draw solute regeneration is done by single-stage RO), at least when considered in terms of thermodynamic minimum energies of separation. In practice, the choice of process will have an influence on reversibility and second law efficiency, and any required pre-treatment may also have a significant effect on energy consumption. For example, if FO is regarded as a feed pre-treatment for sea or brackish water RO, gains in the energy budget can potentially be made.

In exceptional cases, however, the draw solution is not regenerated for reuse in the FO/PAO process. In these instances, the FO/PAO integrated system can certainly be more energy

efficient than stand-alone RO. Examples of this are (1) FO-RO systems in which low salinity waste streams are concentrated to dilute the saline draw solution (e.g., seawater) prior to being processed in the RO system [38–40] or (2) FO systems where the diluted draw solution forms the end product, such as in 'fertigation' in which fertilizer-drawn forward osmosis processes can be used for irrigation [41,42]. FO-RO systems can also be more energy efficient when compared to two-pass RO. Shaffer et al. [43] found that the FO-RO process consumed less energy than two-pass RO while still achieving the stringent boron and chloride standards for agricultural irrigation water when using seawater as freshwater source. However, the FO-RO process has a higher membrane area requirement than two-pass RO, due to the lower water flux in the FO process. Hence, Ban et al. [44] found that the FO-RO process is overall the more expensive process, due to the increased capital expenditure.

Of the osmotically driven membrane processes, OARO is the most energy efficient choice. The conceptual dependency of the water flux J_W on the transmembrane hydraulic pressure difference ΔP for the four main pressure and/or osmotically driven membrane processes is depicted in Figure 2. While RO and FO are respectively pressure and osmotically driven, both working principles are incorporated by PAO and OARO to ensure water transport across the membrane. Compared to FO and PAO, the OARO draw solution is less concentrated than the feed solution ($\pi_D < \pi_F$) and is only utilised to lower the trans-membrane osmotic pressure $\Delta\pi$. For comparative purposes, in order for all processes to achieve the same water flux, the low hydraulic pressure processes ($\Delta P_{FO} < \Delta P_{PAO} < \Delta P_{OARO} < \Delta P_{RO}$) must utilise a correspondingly stronger osmotic draw solution ($\pi_{D,FO} > \pi_{D,PAO} > \pi_{D,OARO} > \pi_{D,RO}$) in order to provide an increasing fraction of the overall driving force. As previously described, however, utilising stronger draw solutions can result in an overall lower energy efficiency, as the DSR process becomes more energy intensive. Hence, when comparing reversible processes, one expects that $\eta_{II,OARO} > \eta_{II,PAO} > \eta_{II,FO}$ [45].

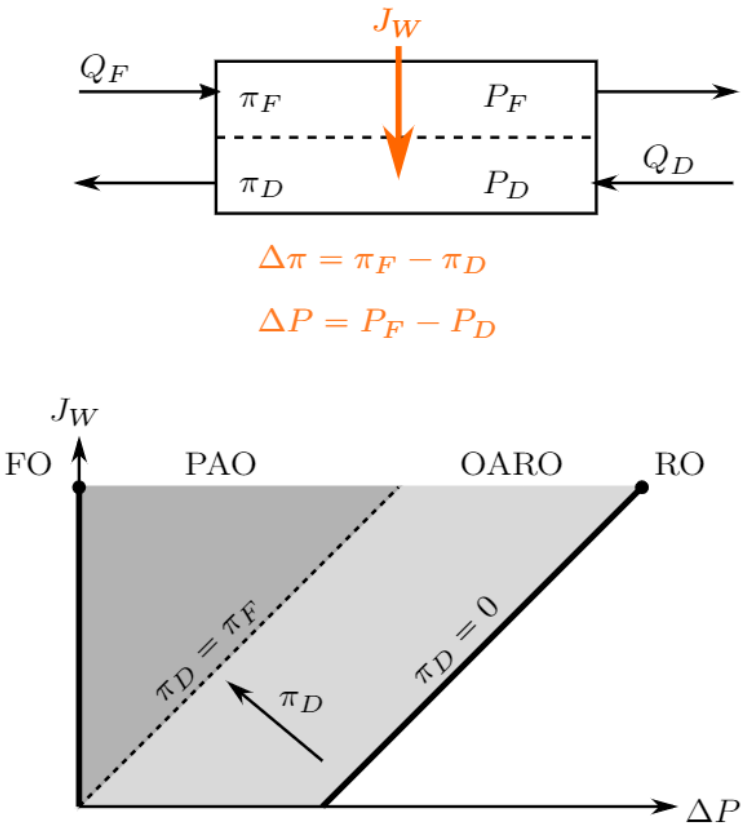


Figure 2:Water flux J_W with respect to the operating pressure ΔP for FO, PAO, OARO and RO.

Two of the main advantages of OARO are its energy efficiency and its capability to circumvent the maximum recovery constraints of RO and its related processes (e.g., MSRO, HPRO). The use of an additional draw solution in OARO reduces the required hydraulic pressure to achieve an RO equivalent water flux. This permits dewatering of more saline feed streams using OARO without exceeding the maximum allowable hydraulic pressure rating of the membrane module. In other words, OARO configurations are possible in which the process recovery is not limited by the membrane burst pressure. Any limitations on recovery will originate rather from other factors, such as fouling and scaling, cost constraints, or the inability of materials to handle high salinity conditions [25]. Additional benefits of OARO are its multi-barrier protection against feedwater contaminants for in-series membrane processes [46], and the possibility of regenerating responsive draw solutes (DS) using forms of low-grade thermal energy which are cheaper and more renewable than grid-sourced electricity [47–49]. All of these benefits make

OARO a promising BVM and ZLD technology and hence, OARO will form the main focus of this thesis.

1.2. Status of OARO research

1.2.1. Numerical OARO research

While there are numerous research publications on RO and FO, the published research work on OARO is more limited. In terms of numerical studies, there are three main OARO process layouts that have been investigated. These are displayed in combination with MSRO in Figure 3.

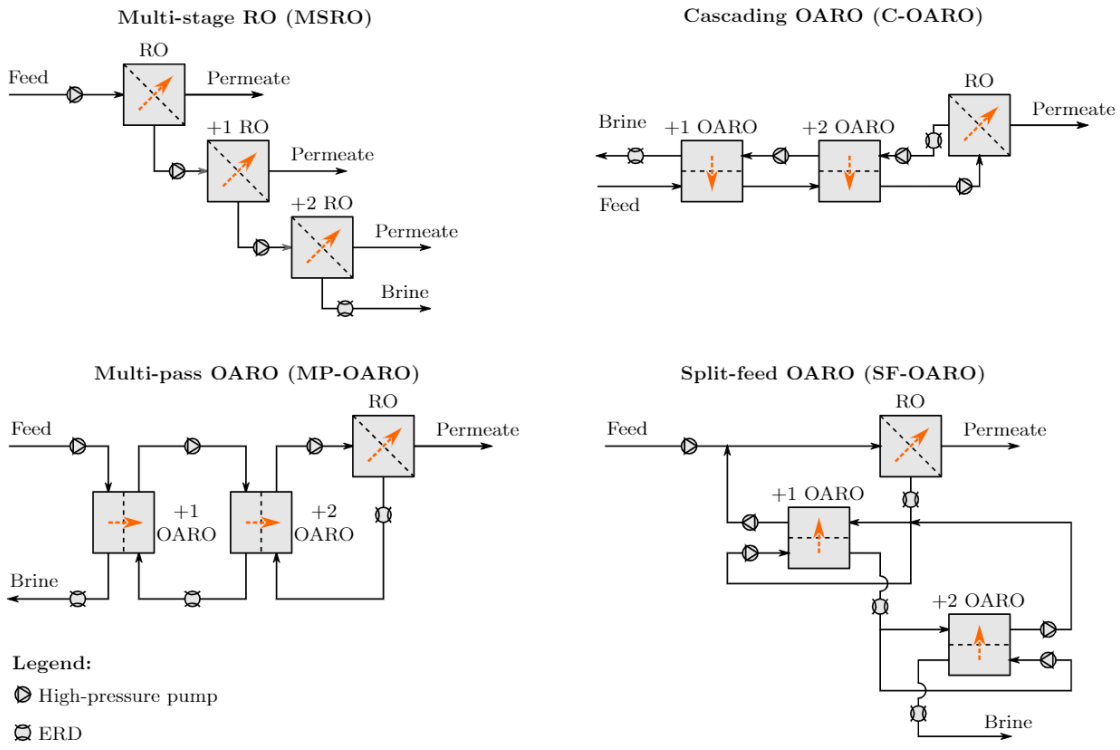


Figure 3: MSRO and the three main OARO configurations. High-pressure pumps and energy recovery devices (ERD) are displayed to indicate which streams are pressurised for OARO/RO operation. The water flux direction is indicated by the orange arrow.

The practical specific energy consumption (SEC) and the maximum operating pressure P_{Max} of all OARO and MSRO configurations are compared in Figure 4 to highlight the advantages and disadvantages of each OARO configuration. The objective of the investigated scenario is to achieve an overall system recovery Y_S of 70% for a 35g/L saline feed (i.e., the global average seawater salinity), using either one of the OARO and MSRO configurations. In Figure 4, E_{Min}

constitutes the thermodynamic minimum energy of separation (i.e., the Gibbs free energy of separation) for this scenario and is calculated using [18]:

$$\mathrm{E_{Min}} \approx \frac{\pi_F}{Y_S}\, ln\left(\frac{1}{1-Y_S}\right) \tag{1}$$

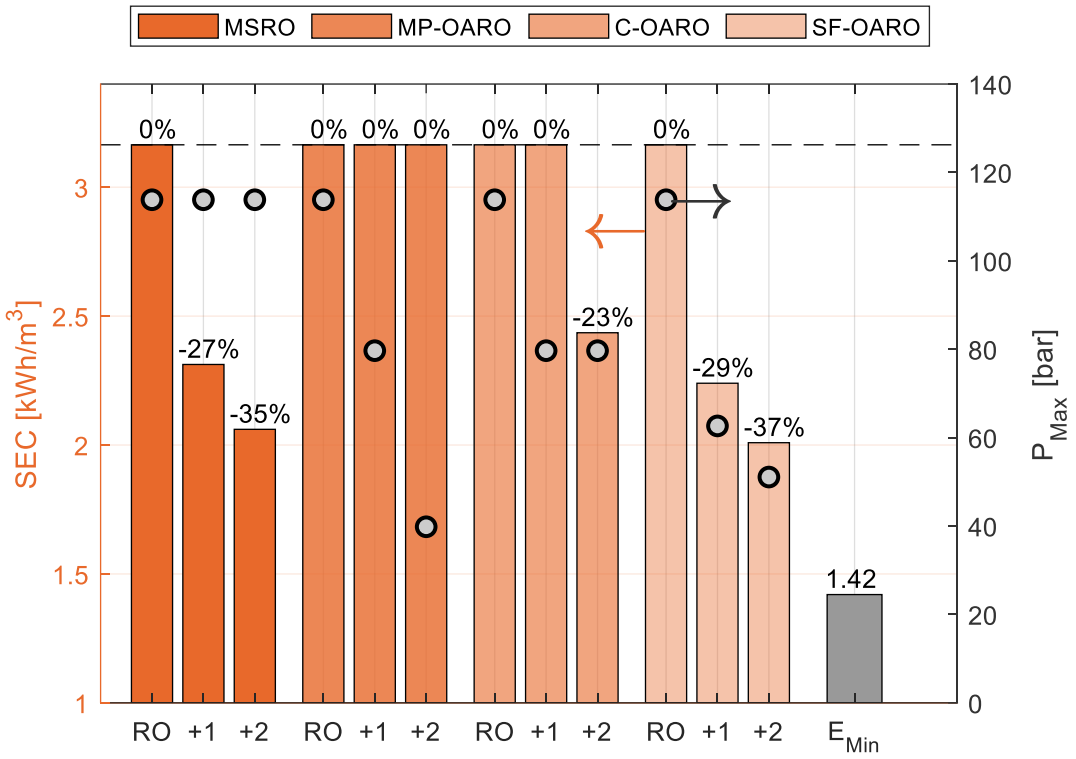


Figure 4: The practical specific electrical energy consumption (SEC) and the maximum operating pressure (P_{Max}) of MSRO, MP-OARO, C-OARO and SF-OARO. The over-pressurisation factor k is set as 1.15, the system recovery Y_S is set as 70% and the inlet feed salinity is set as 35 g/L NaCl. The results for MSRO, MP-OARO and C-OARO were obtained from Chen & Yip [18]. The practical SEC and P_{Max} for the SF-OARO system are derived in Appendix A.

The practical SEC and P_{Max} values displayed in Figure 4 for the MSRO, the multi-pass OARO (MP-OARO) and the cascading OARO (C-OARO) configurations were obtained from Chen & Yip [18]. The split-feed OARO (SF-OARO) process was not discussed by Chen & Yip [18] and hence, its practical SEC and P_{Max} values were calculated in this thesis. The derivation is detailed in Appendix A. It is assumed that all pumps and energy recovery devices (ERDs) have

a 100% efficiency and that all membranes have a 100% solute rejection. Furthermore, an over-pressurization of 15% is assumed ($k = 1.15$) in each membrane stage to maintain an adequate water flux for practical operation. It is important to note that no entropic mixing losses are assumed in the OARO membrane stages. Entropic mixing losses arise in all osmotic processes as the low salinity water permeating through the membrane uncontrollably mixes with the more saline draw solution, which inevitably generates entropy that requires extra energy to reduce in the following separation process [50,51].

In the MP-OARO process, the salinity in each subsequent loop is lowered until RO processable levels are reached [5,52]. The RO process is not in direct contact with the feed stream but is instead supplied by the diluted draw solution of the previous OARO pass. The diluted draw solution of each OARO process is reconcentrated in the subsequent OARO/RO process and then reused as draw solution. As shown in Figure 4, the MP-OARO process cannot lower the practical energy consumption of the single-stage RO (SSRO) process, but the maximum operating pressure can be significantly reduced with each additional OARO stage.

Bartholomew et al. [5] investigated the MP-OARO process layout in detail and found that a water recovery of 35–50% is possible at an energy consumption of 6–19 kWh per cubic meter of product water, when the feed salinity lies between 100–140 g/L. In terms of cost, the unit water cost (UWC) was estimated by Bartholomew et al. [52] to be below $6 per cubic meter of product water when treating feed streams with salinities of 50−125 g/L. These results suggest that OARO can achieve higher recoveries than stand-alone RO while operating at lower energy consumptions than MVC. In terms of cost, the MP-OARO UWC is stated to be competitive with that of MVC. Depending on the MVC process configuration, the UWC can exceed $10 per cubic meter when concentrating brine streams to salinity levels near to salt saturation (i.e., 300 g/kg) [53]. The UWC of MP-OARO is, however, significantly higher than that of large-scale seawater RO plants that operate at lower recoveries (<$1 per cubic meter [54,55]).

Chen & Yip [18] have suggested the C-OARO configuration, which uses several OARO stages in series to concentrate the RO brine stream in an energy efficient manner while diluting its feed. In terms of energy efficiency, the C-OARO process cannot compete with MSRO as MSRO is more energy efficient at an equivalent number of stages. However, the two-stage C-OARO configuration can still save up to 23% more energy than the SSRO process while operating at a technically more feasible pressure ($P_{Max} < 80$ bar). Although C-OARO is shown to be more energy efficient than MP-OARO for low inlet salinities, a recent techno-economic study by Atia et al. [56] has shown that MP-OARO outperforms C-OARO (and LSRRO) when concentrating a high salinity feed (70 g/L) to nearly 250 g/L ($Y_S = 70\%$). The LSRRO, C-OARO and MP-OARO respective UWC was estimated to be 6.63, 7.90 and 5.14 $ per cubic meter of product water, while the corresponding SEC values were 28.9, 12.8, and 10.3 kWh/m^3.

For clarity, the LSRRO process is depicted in Figure 5. In the LSRRO process, the brine stream exiting the initial RO process is further concentrated in subsequent low salt rejection NF or RO membrane stages. While the brine exiting each membrane stage is further concentrated in the subsequent membrane stage, the permeate stream is repressurised and recycled to the inlet of the previous membrane stage. In this way the seawater feed can be highly concentrated while the produced freshwater from the first RO stage remains at a relatively low salinity.

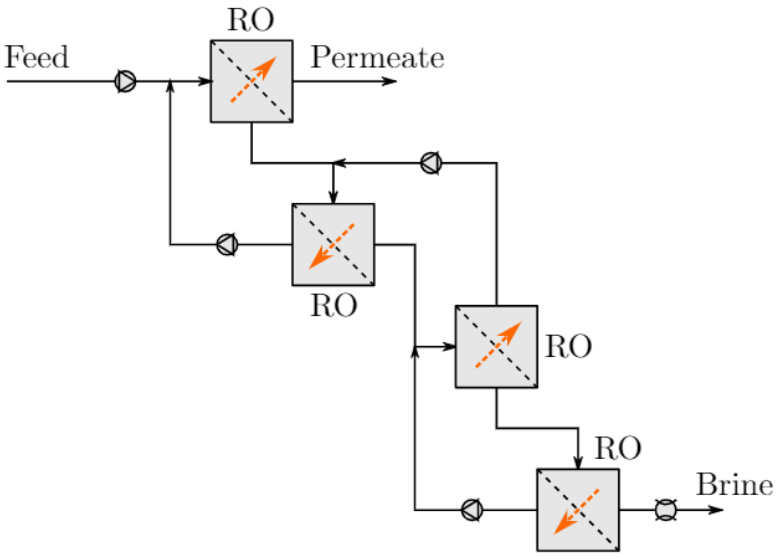


Figure 5: Schematics of a 4-stage low-salt-rejection RO process.

SF-OARO is another OARO configuration (Figure 3) and was firstly investigated by Bouma & Lienhard [25]. For a single-stage SF-OARO process, an OARO stage is incorporated into a semi-batch RO system where the RO brine stream is split into both the OARO feed and draw. Similarly, the brine of the previous membrane stage (RO or OARO) is split into the feed and draw of the subsequent OARO stage in the multistage SF-OARO configuration. The OARO diluted brine stream is then recirculated and mixed with the feed stream of the previous membrane stage. Ideally, both the recirculated brine and feed streams have the same salinity to minimise the entropy generation caused by mixing of streams with different concentrations [57]. In terms of the OARO process itself, the advantage is that both streams enter at the same concentration. Thus, the average transmembrane osmotic pressure difference is lower than for any of the other OARO configurations. Under these ideal operating conditions, SF-OARO is even more energy efficient than MSRO and can operate at pressures lower than MSRO and C-OARO (Figure 4). However, entropic mixing losses in the OARO membrane stages would lower the energy efficiencies of the proposed OARO processes.

The possibility of operating at similar energy efficiencies and lower pressures than MSRO highlight the potential of OARO as a suitable BVM and ZLD technology. Furthermore, it should also be mentioned that all OARO configurations offer multi-barrier protection to the permeate against feed contaminants, which is not the case for MSRO. This can lead to improved permeate qualities when using real membranes with selectivities below 100%.

In addition to the numerical analyses of continuous OARO processes, a batch OARO system was also investigated by Das & Warsinger [58]. The investigated batch SF-OARO process was found to be 30% more energy efficient than its continuous counterpart. The overall SEC of the batch SF-OARO process was estimated to be as low as $1.95\ \mathrm{kWh/m^3}$ at an overall recovery of 62%.

In spite of the advantages of OARO, recent studies (such as that by Wang et al. [24]) have highlighted the disadvantages of osmotically driven membrane processes, especially those of OARO. One such disadvantage of OARO (and also of FO, for that matter) is that the design of the membrane module and its operation is more complex in comparison to that of purely pressure-driven processes. In addition, internal concentration polarisation (ICP), which is discussed in greater detail in Section 2.1., can have deleterious effects on the performance of all osmotically driven processes, and hence membranes with a porous, non-tortuous and thin support layer (i.e., a small structural parameter) are required to minimise this phenomenon. Membranes with such substrate specifications suffer from a lower mechanical strength; thus, high pressure operation, as required in OARO, may inevitably lead to their failure. While these technical issues remain to be solved, FO and specifically OARO have the potential to significantly reduce the overall energy consumption and/or increase the maximum recovery of BVM and ZLD processes. For example, Bouma & Lienhard [25] could concentrate a feed stream using SF-OARO from 0.6 M to 4 M using only $3.9\ \mathrm{kWh/m^3}$, whereas a 3-stage and 4-stage

LSRRO system with similar operating conditions consumed 9.11 kWh/m^3 and 5.14 kWh/m^3, respectively [24].

1.2.2. Gaps in numerical OARO research

The OARO configurations discussed in Section 1.1. were presented in different studies with often widely varying assumptions and operating conditions. Therefore, a single, economically-based comparison of all OARO configurations with non-idealities included in the modelling would be needed to fully showcase the potential of OARO as a BVM/ZLD technology.

Process non-idealities can significantly affect the energy efficiency, maximum recovery and permeate quality of the OARO system. These non-idealities include (1) ICP, (2) pump and ERD efficiencies, (3) module pressure losses, (4) the use of real, non-ideal membranes (i.e., membrane selectivity < 100%, limited membrane burst pressure), and (5) the use of finite membrane areas.

Furthermore, all of the presented studies focus on the sole use of non-responsive draw solutes (i.e., NaCl) in OARO, although the inclusion of other responsive draw solutes may offer additional benefits to OARO integrated systems. Non-responsive draw solutes refer here to draw solutes that do not have significant changes in their water affinity in response to stimuli such as changes in temperature, pH or electro-magnetic field. On the other hand, when responsive draw solutes are exposed to stimuli, they experience a substantial change in their water affinity, which is often accompanied by phase transitions between two states with different water affinities. This allows ease of regeneration in one state (i.e., when the draw solutes have a low water affinity) while maintaining sufficiently high drawing ability in the other (i.e., when the draw solutes have a high water affinity) [48]. For example, low-grade waste heat (LGWH) can be used as an alternative energy source for the DSR process with the use of thermo-responsive draw solutes in OARO. This could potentially lower the cost and electricity

consumption of the OARO system, something which is not possible with conventional, purely hydraulic pressure-based desalination systems.

1.2.3. Experimental OARO research

Several studies have focused on experimentally validating numerical OARO models using pure NaCl solutions [59–63]. In all cases, the OARO models were based on the solution-diffusion model for membrane transport [64]. The results presented by the different studies show a good correlation between the experimentally and numerically determined water and solute fluxes, suggesting that the modelling assumptions were sound. A wide variety of membranes and modules were tested at salinities and transmembrane pressures that ranged up to 2.4 M NaCl [62] and 40 bar [60], respectively. Although most of the OARO studies focused on the application of OARO for desalination, OARO was also previously used for the concentration of sugar solutions in the food processing industry [65] and for membrane assisted crystallisation of ammonium sulphate and adipic acid solutions [66].

As previously mentioned, the ideal OARO membrane can withstand high operating pressures while having only a thin and porous substrate, which is necessary to minimise ICP. Askari et al. [67] have focused on the development of such high mechanical strength, thin-film composite (TFC), hollow fibre membranes for OARO processes. By controlling the dope to bore flow ratio, fibre dimension and the morphology of the TFC hollow fibre membrane, an OARO membrane could be synthesised with an unprecedented burst pressure of 95 bar, even though the membrane substrate remained thin and porous ($S = 795\mu m$).

At such high operating pressures, membrane compaction and the associated change of the membrane's transport and structural properties is a serious concern for OARO operation [68]. Chen et al. [69] have investigated the effects of hydraulic pressure and salinity on the transport and structural properties of TFC osmotic membranes. Membrane compaction was shown to

reduce the membrane's water permeability, while the membrane selectivity significantly improved. Furthermore, the study showed that ICP is less detrimental for OARO than for FO operation, as solute transport for OARO is in the same direction as water permeation. Because of the latter, the OARO operational water flux can be enhanced by utilising membranes with a lower selectivity to minimise ICP (and a similar observation would hold for RO).

1.2.4. Gaps in experimental OARO research

Despite the many numerical and experimental research studies already made on OARO, membrane fouling in OARO processes has not been investigated to date. Membrane fouling will undoubtedly cause an increase in energy demand, and lead to operational challenges. Thus, understanding how membrane fouling can affect OARO operation and how it can be mitigated will offer valuable insights into the technical feasibility of OARO and its limitations for the dewatering of highly concentrated streams.

1.3. Research objectives

As the title of this thesis suggests, the main research objective is to determine whether OARO can be used to lower the environmental impact of desalination and improve its sustainability in a cost-effective way. This would be feasible, at least on a techno-economic level, if the use of OARO can simultaneously lower the capital and/or operating cost of BVM and ZLD processes, improve their water recovery and reduce discharges. This would tend to accelerate their broader application, especially in low- and medium-income countries.

Already speaking in favour of the economic and technical viability of OARO is the fact that this technology is commercially deployed for BVM and ZLD processes by several companies, such as Hyrec, Fluid Technology Solutions, Osmotic Engineering and Gradiant. However, as highlighted in the previous section, several important questions remain unanswered as to whether OARO can outperform other high-recovery membrane processes in terms of energy efficiency, cost, sustainability, and technical viability. To address these questions, the two main research objectives of this thesis are then as follows:

Numerically quantify the economic potential and the environmental impact of OARO

In Chapter 3, a numerical comparison of different OARO process layouts for BVM is conducted. In addition to the OARO configurations presented in Section 1.1., novel OARO configurations are developed and modelled. The objective is to maximise the process recovery while lowering the energy consumption and cost. The recovery of the OARO process is then further enhanced by the incorporation of a thermo-responsive draw solute (DS) in Chapter 4. This DS can be potentially regenerated at low temperatures, enabling the incorporation of LGWH as a potentially cheaper energy source to electricity. The objective in Chapter 4 is then to further decarbonise ZLD

desalination by lowering the electricity consumption and minimizing the brine volume in a cost-effective manner using OARO. In both chapters, OARO is compared to other high-recovery membrane systems, such as MSRO/HPRO, LSRRO and FO.

Experimentally investigate the technical limitations of OARO

OARO processes are generally operated under extreme operating conditions (i.e., high-pressure operation and the treatment of highly concentrated and polluted feed streams) and hence, membrane deformation and fouling can severely affect the OARO process performance. In Chapter 5, a principal fouling investigation is carried out to determine the effects of organic and inorganic membrane fouling on the OARO process performance. Furthermore, fouling mitigation techniques, such as membrane flushing and osmotic backwashing, are investigated in terms of their efficacy at restoring the initial water flux. The insights gathered from the experimental analysis in Chapter 5 will highlight how OARO is affected by fouling and how its performance under fouling conditions then compares to the modelled performance in Chapter 3 and 4 under ideal, non-fouling conditions.

1.4. Thesis layout

This thesis is structured as follows:

Chapter 2: Methodology

The osmotic resistance filtration (ORF) model is used to derive the OARO governing equations. Furthermore, general concepts are discussed with respect to the ideal OARO membrane properties, likely phenomena caused by membrane deformation and fouling, and the limiting and critical flux theorems.

Chapter 3: Six OARO approaches for BVM using non-responsive draw solutes

In Chapter 3, six different OARO process layouts are proposed, two of which are novel, and numerically analysed to determine the best layout for two different operating scenarios. The focus is on optimising the overall process energy efficiency, the capital cost and the permeate quality while operating the OARO process below its membrane burst pressure. The optimal OARO integrated processes are then compared to MSRO/HPRO systems operating under similar conditions to demonstrate their potential superiority in terms of environmental, technical, and economic sustainability.

Chapter 4: Achieving zero-liquid discharge with OARO and thermo-responsive draw solutes

In Chapter 4, the feasibility of integrating thermo-responsive draw solutes into OARO systems is numerically investigated. A thermolytic $NH_3 - CO_2$ salt is chosen as a representative draw solution, as its use in FO has been widely investigated and it has been commercially tested in an FO ZLD process. A techno-economic comparison between FO and OARO is used to determine the preferred process for ZLD. Furthermore, to showcase the advantages of the proposed integration of OARO with

thermo-responsive draw solutes, a techno-economic comparison is made with LSRRO and OARO using non-responsive draw solutes.

Chapter 5: Exploring the technical limitations of OARO: Membrane fouling, cleaning, and the limiting flux

In Chapter 5, organic and inorganic fouling of OARO membranes is investigated under representative operating conditions. Furthermore, fouling mitigation techniques are discussed, as well as the limiting flux theorem and how it applies to OARO processes. The conclusions drawn from this Chapter will highlight the technical feasibility of OARO for the use of dewatering concentrated and polluted water streams, and the extent to which system performance is worsened as compared to ideal, non-fouling operation.

Chapter 6: Conclusions and future work

In Chapter 6, the main numerical and experimental findings and conclusions are summarised. Based on the conclusions drawn, suggestions for future work are given.

Chapter 2

Background Theory

2.1. OARO governing equations

Figure 6 shows the concentration profiles with the internal concentration polarisation (ICP) and external concentration polarisation (ECP) in asymmetric membranes. The typical membrane orientations for RO and OARO are shown. These are widely used to prevent the intrusion of the spacer backing into the membrane's active layer under high applied pressures, which can lead to membrane damage [70,71]. Therefore, the active layer preferentially faces the pressurised solution, i.e., with the active layer facing feed side (AL-FS) for RO and OARO.

The ORF model is used to describe the water and solute transport in RO and OARO based on the membrane's intrinsic properties, namely its water permeability A, solute permeability B, water/solute selectivity B/A and its structural parameter S. The ideal OARO membrane properties are discussed in greater detail in Section 2.2.

According to She et al. [72], the ORF model separates the driving forces across the membrane into different components, i.e., the apparent driving force F_{App}, the driving force loss due to concentrative concentration polarisation (CCP) F_{CCP}, and the driving force loss due to dilutive concentration polarisation (DCP) F_{DCP}. The effective driving force is then taken as the difference between the apparent driving force and the sum of the driving force losses:

$$J_W = A\,(F_{APP} - F_{CCP} - F_{DCP}) \quad (2)$$

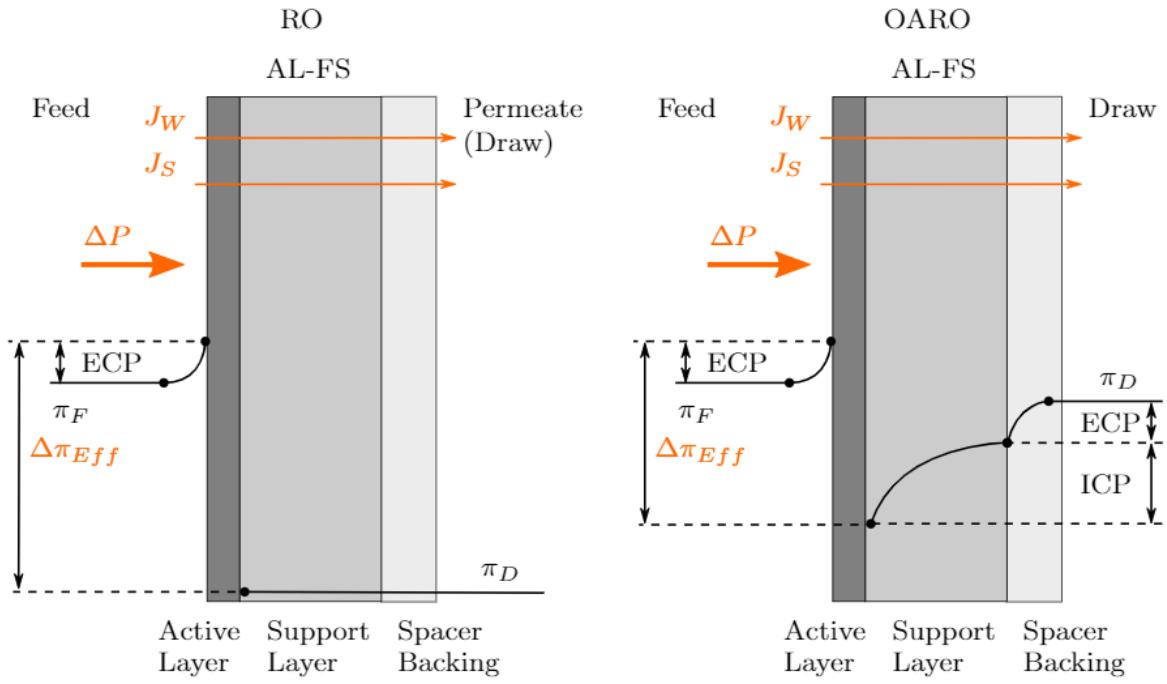


Figure 6: Concentration profile for typical membrane orientations for HPRO and OARO membrane processes. In HPRO and OARO the effective osmotic pressure $\Delta\pi_{Eff}$ is positive, as the permeate (draw) is less concentrated than the feed.

For the indicated directions of the water flux J_W, solute flux J_S and the transmembrane pressure ΔP in Figure 6, Equation (2) can be mathematically expressed as:

$$J_W = A\left[(\Delta P - \Delta\pi) - f_{CCP}\left(\pi_F - \frac{J_S}{J_W}\beta R_G T\right) - f_{DCP}\left(\pi_D - \frac{J_S}{J_W}\beta R_G T\right)\right] \quad (3)$$

Equation (3) indicates that the concentration polarisation terms are not only affected by the convective conditions in the feed and draw solutions but also by the solute diffusion across the membrane (i.e., in terms of J_S/J_W) [73]. In PAO and PRO, the reverse solute diffusion (from the draw to the feed solution) exacerbates both CCP and DCP, and thus leads to the decrease of the water flux. On the other hand, forward solute diffusion (from the feed to the draw) solution reduces both CCP and DCP and hence compensates driving force losses in HPRO and OARO operation. However, an increase in forward solute diffusion reduces the useful work done by

the system, resulting in a reduced 2nd law efficiency [25], and is indicative of a lower membrane selectivity. Specifically, J_S/J_W in Equation (3) can be described by the following equation [72]:

$$\frac{J_S}{J_W} = \frac{B}{A\beta R_G T}\left(A\frac{\Delta P}{J_W} - 1\right) \quad (4)$$

Equation (3) and Equation (4) have been derived on the assumption that the bulk osmotic pressure of the feed (π_F) and draw (π_D) solution can be related to their concentrations (C_F and C_D) using the Morse equation:

$$\pi = \beta R_G T C \quad (5)$$

where β, R_G, T and C are the van't Hoff factor, the universal gas constant, the fluid temperature, and the solution concentration, respectively. The CCP factor f_{CCP} and the DCP factor f_{DCP} can be expressed by the following equations:

$$f_{CCP} = \exp\left(\frac{J_W}{k_{CCP}}\right) - 1 \quad (6)$$

and

$$f_{DCP} = 1 - \exp\left(-\frac{J_W}{k_{DCP}}\right) \quad (7)$$

where $1/k_{CCP}$ and $1/k_{DCP}$ represent the induced mass transfer resistances due to concentrative and dilutive concentration polarisation, respectively. For the AL-FS membrane orientation, $1/k_{CCP}$ and $1/k_{DCP}$ are given by:

$$\frac{1}{k_{CCP}} = \frac{1}{k_F} \quad (8)$$

and

$$\frac{1}{k_{DCP}} = \frac{1}{k_M} + \frac{1}{k_D} \quad (9)$$

where k_F and k_D are the mass transfer coefficients in the fluid boundary layers that form on the membrane's feed and draw side, respectively [74]. For membranes with a thick and less porous

support layer, the solute resistance to diffusion in the support layer $1/k_M$ is dominant, and is given by [75]:

$$\frac{1}{k_M} = \frac{S}{D} \tag{10}$$

where D is the diffusivity of the solute.

In cases where membrane fouling affects the OARO water flux, the foulant resistance R_F can be calculated [76]. The effective driving force (DF_{Eff}) of OARO is given by:

$$DF_{Eff} = (\Delta P - \Delta\pi) - \left(e^{\frac{J_W}{k_F}} - 1\right)\left(\pi_F - \frac{J_S}{J_W}\beta R_G T\right) - (1 - e^{-\frac{J_W S}{D}})\left(\pi_D - \frac{J_S}{J_W}\beta R_G T\right) \tag{11}$$

The water flux can then be described as:

$$J_W = \frac{DF}{\mu(R_M + R_F)} \tag{12}$$

where μ is the fluid viscosity and $1/\mu R_M$ is the same as the water permeability A of the pristine membrane.

2.2. Optimal OARO membrane properties

The ideal membrane is generally described as (1) highly water permeable (High A-value), (2) selective (Low B-value), (3) not significantly affected by ICP (Low S-value), (4) fouling resistant, (5) mechanically and chemically stable, (6) easily manufacturable, (7) produced from cheap and abundant materials, and (8) recyclable [77].

The focus of this section is on Points (1) to (3), as the OARO governing equations are directly dependent on the membrane's intrinsic properties (A, B and S). Regarding Points (4) and (5), common membrane deformation and fouling phenomena and their effects on the OARO process performance are discussed in Section 2.3. Furthermore, the critical and limiting flux theorems are discussed in Section 2.4., and highlight when and how fouling is dependent on the OARO membrane properties. Points (6) to (8) are not directly addressed, as membrane manufacture is beyond the scope of this thesis.

2.2.1. Membrane water permeability

The numerous developments of ultra-permeable membranes foresee membranes with permeabilities exceeding those of current TFC membranes. However, enhancing the water permeability of membranes beyond that achieved by current TFC polyamide membranes will not lead to significant improvements in pressure and osmotically driven membrane processes (e.g., lower SEC and/or lower capital and operational costs). Convincing arguments supporting this statement are offered by Werber et al. [78] and are shortly summarised here.

Firstly, membrane permeability would solely affect the energy consumption in the desalination step. Intake, pre-treatment, post-treatment and brine discharge would remain unaffected and can in total contribute to more than $1 kWh/m^3$ of the total desalination energy consumption [33].

Secondly, energy savings achieved by employing ultra-permeable membranes are limited to reducing the over-pressurisation required to (1) achieve an acceptable water flux and to (2)

overcome any pressure losses in the membrane desalination process. Figure 7 shows the total energy consumption of SSRO, MSRO and the three main OARO configurations with two OARO stages. The total energy consumed by over-pressurisation is indicated by the hatched region. As shown, the energy savings attainable by reducing over-pressurisation are insignificant in comparison to those achievable by utilising alternative process configurations (e.g., MSRO, C-OARO and SF-OARO) that aim at minimising the irreversible losses associated with SSRO operation.

Thirdly, Cohen-Tanugi et al. [79] show that ultra-permeable membranes require less pressure vessels to produce the same total permeate output under non-fouling conditions. However, concentration polarisation is directly dependent on the water flux and hinders the increase of the water flux for membranes with higher A values. Although external concentration polarisation can be minimised using better feed spacer designs or higher cross-flow velocities, the increase in turbulence leads to higher channel pressure losses and increases the SEC. Furthermore, for real feedwaters containing contaminants, fouling is more severe at higher water fluxes, which also hinders the increase of J_W. Due to increased concentration polarisation and fouling, only minor savings in terms of RO membrane area can be achieved at higher water permeabilities. This also applies to osmotically driven membrane processes that are typically operated at lower water fluxes than RO [78]. The main water flux resistance in osmotically driven membrane processes is caused by membrane substrates with a high structural parameter S (i.e., due to ICP) and not due to the active layer permeability. The FO/OARO water flux can be significantly improved if S is minimised, while the water flux plateaus at water permeabilities exceeding those of current TFC membranes [78]. To conclude, utilising OARO membranes with water permeabilities of current TFC membranes is an acceptable paradigm. The focus should rather be on utilising and developing OARO membranes with minimal ICP.

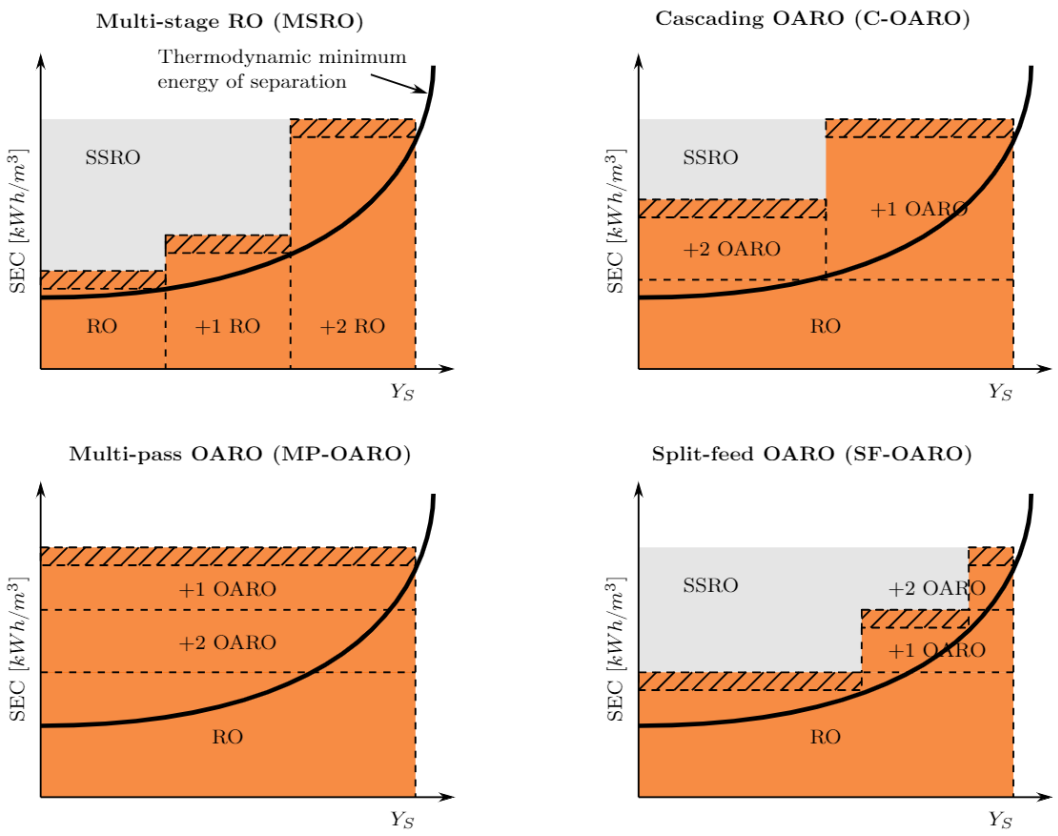


Figure 7: The practical SEC of SSRO, MSRO and the three main OARO configurations with respect to the system recovery. The total energy consumption associated with over-pressurisation is represented by the hatched area. The grey shaded SSRO region highlights the energy that can be saved by employing MSRO or one of the OARO configurations instead of SSRO. The SEC diagrams for MSRO, MP-OARO and C-OARO have been adopted from Chen et al. [69].

2.2.2. Membrane selectivity and ICP

For dense polymeric membranes, the water permeability coefficient A and its salt permeability coefficient B are not independent and indeed demonstrate a permeability-selectivity trade-off [78]. According to Yip & Elimelech [80], the relationship is given by $B \propto A^3$ for TFC membranes. Therefore, tweaking the polyamide structure of the membrane's active layer to be more water permeable results in a simultaneous and significant increase in solute permeability. It can thus be suggested that more permeable membranes offer negligible improvements to the

desalination process. Thus, Werber et al. [78] argue that current membrane research should focus on developing more selective rather than more permeable membranes.

The development of more selective membranes will offer several advantages in terms of improving the water purification process. Firstly, better retention of feed impurities offers a more efficient process and a higher purity permeate. Improved process efficiency originates from a higher second law efficiency, as a higher selectivity results in more useful work being done in the desalination process [25]. Furthermore, if a draw solution is employed that differs from the feed solution, a better rejection of solutes by the membrane results in a lower cross-contamination of the two streams. This lowers the loss of draw solutes in the purification process (e.g., FO, PAO), for which the draw solutes can be valuable and must be continuously replenished, and thus reduces the operational costs of the process. Secondly, a higher solute removal in the desalination step eliminates pre-treatment and post-treatment steps that are otherwise required to ensure an adequate permeate quality. This could lead to significant chemical, energy, and cost efficiency gains [78].

Bouma & Lienhard [25] state that although the OARO system efficiency decreases with an increase of the membrane's B-value, the water flux increases due to the reduced internal concentration polarization effect. In the conventional OARO process, forward salt diffusion (FSD) helps mitigate ICP and thus Chen et al. [69] points out that the membrane's active layer properties (A and B) are important parameters that need to be considered for OARO optimisation. Hence, purposefully developing "leaky" membranes may seem counterintuitive, but the reductions in ICP that result from FSD can significantly increase the water flux and allow for a system to operate with reduced membrane area (i.e., reduced capital costs) [25]. The reduction of ICP by FSD also suggests that the membrane's S-value plays a less crucial role in OARO than in FO. This finding has important implications in the design of OARO membranes and means that less dense membranes with thicker support layers may be ideal and allow for

higher pressure operation to achieve high brine concentrations with conventional OARO processes.

Nonetheless, OARO membranes with a lower structural parameter are preferred to minimise the loss in driving force caused by dilutive concentration polarisation. Seawater RO (SWRO) desalination plants are generally designed to operate at an average water flux of approximately $10 - 15\ \mathrm{L/(m^2h)}$ [19]. Optimally, the OARO process is operated at similar water fluxes to reduce capital expenditure, but this could be problematic as concentration polarisation is more severe at higher water fluxes. As shown by Equation (7), the exponential term representing dilutive ICP rapidly approaches zero for thicker membranes at higher water fluxes. The f_{DCP} term is plotted in Figure 8 for three different S values with respect to the water flux. ECP is assumed negligible compared to ICP (by ensuring high cross-flow velocities) and hence, Equation (9) is reduced to $1/k_{DCP} = 1/k_M$. If f_{DCP} reaches one, the draw solution concentration (and hence the 'osmotic asistance') is effectively nullified and does not affect J_W. Therefore, S must be less than 5 mm for the draw solution to be effective in OARO at similar water fluxes to SWRO.

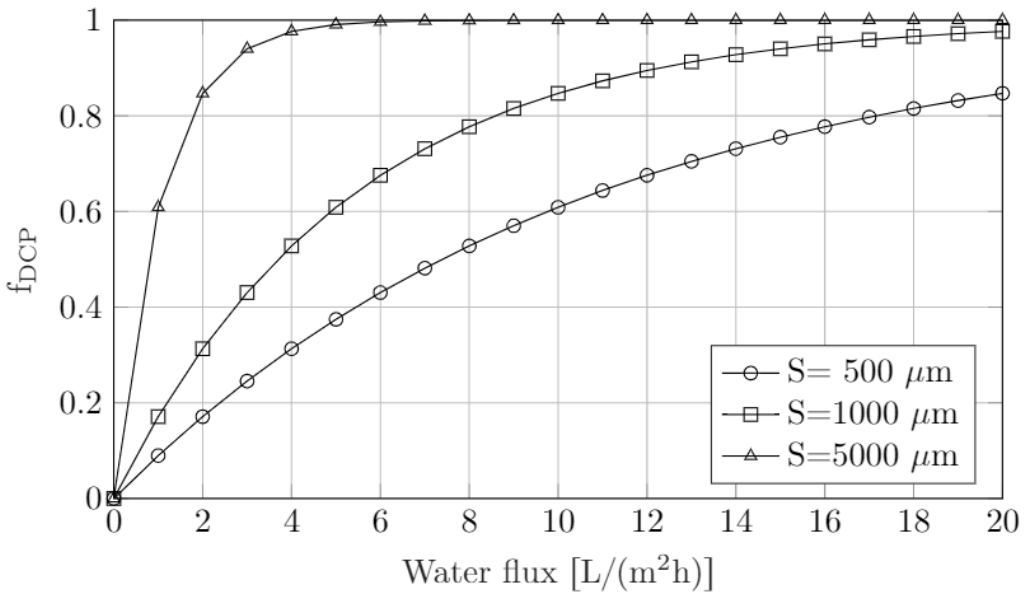


Figure 8: Internal concentration polarisation factor of the draw solution with respect to the water flux for three different structural parameters.

2.3. Membrane deformation and fouling phenomena in OARO

OARO, like many other membrane processes [19,26,27,70,71,81–85] that are operated at high transmembrane pressures and/or utilise thin membranes, is plagued by membrane deformation. It has been recognised that severe membrane deformation can drastically deteriorate membrane performance by altering the membrane intrinsic properties.

Recently, Davenport et al. [84] recorded a 35% reduction in the water permeability of commercially available RO membranes as the operating pressure was increased from 70 bar to 150 bar. The main cause for this decline in water permeability was identified to be due to membrane compaction, which led to a 95% reduction in the surface porosity of the membrane's support layer. Similar findings were reported by Aghajani et al. [86], who found that the support layer porosity decreased as it yielded at high operating pressures, which in turn increased the overall permeation resistance of the utilised TFC membranes. Furthermore, de Roever et al. [87] found that compaction and spacer intrusions in the membrane are a common phenomenon in spiral-wound RO membrane modules after year-long operation, and that deeper spacer intrusions are more likely to be found in membrane modules operated at high temperatures and pressures.

While membrane compression and the associated loss in permeability is common in a well-supported membrane with a thicker and less porous substrate and a less open spacer backing, an increase in the water and solute permeability is also possible for a membrane with a thinner and more porous substrate and a more open spacer backing, as shown by Idarraga-Mora et al. [88], Madsen et al. [81], She et al. [89] and She et al. [90]. A thinner membrane with an open spacer backing is prone to membrane deformation by coupled tensile stretching and hydraulic

compression [89], which can lead to 1) the displacement and elongation of polymer chains in the membrane's active and support layers, 2) an increase in active membrane area, and 3) even to the breakage of chain covalent bonds within the polymer crystallites. All of these effects can further lead to the change of the membrane's intrinsic properties [91,92].

As showcased in Figure 9, several non-idealities can be caused by membrane deformation and fouling, which can severely affect the OARO process performance. From the findings presented in our study [68], it is evident that membrane deformation, especially at high operating pressures, leads to changes in the membrane's intrinsic properties and its morphology. For example, membrane compaction was found to improve the selectivity (B/A) of both an Aquaporin and BW30LE membrane, while the water permeability A of the membranes reduced. Several other studies have presented similar findings for all ranges of membrane processes [81,84,86,93,94].

The loss in water permeability is not only caused by changes in the membrane's morphology but also by a phenomenon called the 'shadow effect' that occurs in flat-sheet or spiral-wound membrane modules. At higher operating pressures, the membrane surface is compressed against the spacer support, which increases the contact area between the spacer and the membrane and thus, reduces the available membrane area for water permeation [70,95,96]. As mentioned by Oh et al. [70], the membrane orientation plays a vital role with regards to the 'shadow effect'. For a pressurised feed, the active membrane area is not significantly reduced in AL-FS mode, because the membrane's support layer acts as an additional buffer to prevent the full blockage of the membrane's active surface area. Therefore, to minimise the 'shadow effect' and the possibility of premature membrane rupture [70,96], the AL-FS mode is generally the preferred membrane orientation for RO, OARO and PAO.

High pressure operation can also lead to changes of the hydrodynamic conditions within the membrane module. For example, She et al. [97] investigated organic fouling in PRO and found that at high operating pressures the membrane supporting feed spacer was compacted. This not only caused an increase in the feed side channel pressure loss [96] but also led to plugging of the feed spacer by organic material. Hence, changes brought about by membrane deformation are also expected to affect the fouling propensity of the OARO process. As another example, forward and reverse solute diffusion (RSD) across the membrane can be inhibited when the membrane is compacted, as its selectivity improves [68]. This can alleviate membrane fouling, as the interaction between feed and draw side contaminants is prevented by hindering the diffusion of (1) fouling promoters (e.g., Ca^{2+} and Mg^{2+}) that can exacerbate organic/colloidal fouling [97–99], (2) scale precursor ions (e.g. Ca^{2+}, Mg^{2+} and SO_4^{2-}) that can accelerate scale formation [100,101], and (3) nutrients that can aid biofilm formation [102].

In general, the structure (thickness and compactness) and evolution of the fouling layer is affected by the foulant characteristics, feed and draw solution chemistry (temperature, pH, concentration and variety of solutes present), hydrodynamic conditions (turbulence intensity, water flux) and the membrane properties (roughness, surface charge, hydrophilicity) [102,103]. As shown in Figure 9, fouling can either evolve externally or internally. External fouling is likely to occur on the membrane's feed side as foulants are deposited onto the surface of the active layer and agglomerate to form a cake layer. The formation of a fouling/cake layer induces another type of concentration polarisation, namely cake-enhanced concentration polarisation (CECP). This phenomenon arises as the cake layer prevents cross/tangential flow in its 'porous' structure, thus hindering solute back diffusion [104]. The solute concentration and the osmotic pressure are enhanced on the membrane's feed side due to CECP, ultimately lowering the effective driving force for J_W [105]. The higher feed side concentration also leads to an increased FSD, which lowers the membrane's selectivity. It was also shown by Lee et al. [106] that CECP

causes a greater flux decline in FO than in RO due to the additional contribution of RSD to CECP. Therefore, CECP can be minimised in FO by combatting RSD; i.e. when using membranes with a very low solute permeability [107]. On the other hand, CECP is actually enhanced in purely pressure driven membrane processes (e.g., nanofiltration (NF) and RO) when using highly selective membranes, as more feed solutes are rejected by the membrane and retained in the cake layer [104,108]. This raises the question as to whether more selective membranes are preferred to minimise CECP in pressure and osmotically driven membrane processes, such as OARO.

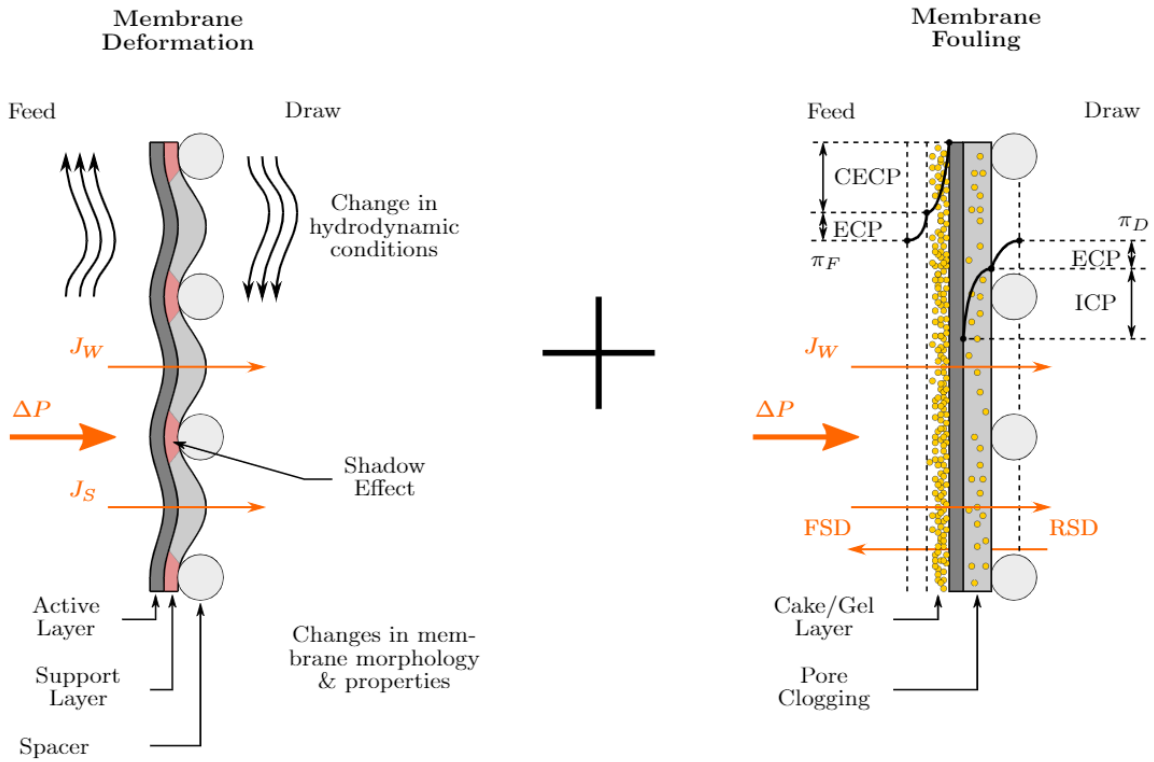


Figure 9: OARO performance affecting phenomena that can arise due to membrane deformation and fouling.

Internal fouling can also occur on the membrane's draw side, as the draw solution in OARO is generally not free of foulants (it may in fact be self-fouling) and may range from concentrated saline solutions, such as wastewater [62], seawater or brine [5,18,25,35,52], to specially designed draw solutions, such as $NH_3 - CO_2$ solutions [36]. If relatively small foulants enter the membrane's

porous substrate they can be adsorbed onto the pore walls. Subsequently, other foulants can then be further adsorbed onto the deposited foulants, which may eventually lead to pore clogging [102]. Zohrabian et al. [109] found that when the foulant's adsorptive and diffusive forces exceeded the counteracting convective forces (i.e., the permeate water flux), internal membrane fouling in FO in AL-FS mode was possible and hence, internal membrane fouling may also be possible in OARO. In this case, fouling enhanced ICP would substantially lower the OARO water flux.

As OARO is partially an osmotically driven membrane process, the so-called ICP self-compensation effect may also affect the membrane's flux behaviour. In several studies, it has been observed that the FO flux remained relatively stable during membrane fouling in AL-FS mode [110–112]. Tang et al. [113] related this observation to the fact that any minute reduction in the membrane's water flux due to fouling will immediately be counterbalanced by a reduction in ICP and hence, will result in a more gradual reduction of the membrane's water flux. While this phenomenon will also occur in OARO, its effect on the water flux may be less significant, as a weaker draw solution is utilised in OARO processes than in FO to achieve the same water flux and process recovery [36].

2.4. The critical and limiting flux theorems

Operation at higher water fluxes induces a greater hydrodynamic drag force F_{Drag} on the foulants contained within the feed towards the membrane surface; hence, foulant transportation, deposition and cake layer formation are accelerated at higher J_W [114,115]. For small particles ($\ll 100$ nm), the lifting force and lateral migration by cross-flow can be ignored [116,117] so that particle motion is solely described by Stokes law [115]:

$$F_{Drag} = 6\pi\mu R_h J_W \quad (13)$$

where μ and R_h are the fluid viscosity and the characteristic hydrodynamic radius of the foulant [115]. Foulant deposition and flux reduction continue as long as the drag force overpowers the barrier force $F_{Barrier}$, which opposes foulant accumulation on the membrane surface (i.e., the repulsion forces between membrane-foulant and deposited foulant-foulant) [117,118]. The membrane fouling rate and its reversibility greatly depend on the various foulant-membrane and foulant-foulant interactions, and may include van der Waals forces, electrostatic interactions, hydration interactions and hydrogen bonds [119]. The water flux stabilises once the hydrodynamic drag force reduces to levels approaching those of the barrier force [115]:

$$F_{Drag} = F_{Barrier} \quad (14)$$

Reversible and irreversible fouling are differentiated by the degree of foulant attachment to the membrane surface. More precisely, reversible fouling is defined as a loosely attached fouling layer that is removable via physical cleaning methods, which is not the case for irreversible fouling [46]. Significant and irreversible foulant accumulation on a pristine membrane, and the associated flux reduction, are defined to occur once the water flux exceeds the so-called critical flux J_C [46,108,114]. In other words, the hydrodynamic drag force must exceed the barrier force offered by the membrane-foulant interactions $F_{Barrier}^{f-m}$ for fouling to occur. The critical flux is reached once:

$$F_{Drag} = F_{Barrier}^{f-m} \quad (15)$$

and is given by rearranging Equation (13) and Equation (15):

$$J_C = \frac{F_{Barrier}^{f-m}}{6\pi\mu R_h} \quad (16)$$

Higher water flux operation requires less initial membrane area (lower capital expenditures) for a certain total permeate output, but irreversible membrane fouling will increase downtime due to membrane cleaning and replacement. Thus, operation below the critical flux is favoured to ensure economical operation of the membrane process [114]. The exact value of the critical flux varies for every single operation, and depends on membrane properties (surface charge, membrane orientation, roughness, hydrophilicity), concentration of foulants present, feedwater characteristics (pH, temperature, crossflow velocity), and operational time [114].

As stated by Tang et al. [115] and Bacchin [120], pristine membranes are generally less repulsive towards foulants than their fouled counterparts, due to the stronger repulsion forces acting between the already deposited foulants and the approaching foulants:

$$F_{Barrier}^{f-m} < F_{Barrier}^{f-f} \quad (17)$$

In the case of severe membrane fouling, when the entire membrane surface is covered by a foulant cake layer, the barrier force depends solely on the interaction forces between the already deposited foulant and the approaching foulants. As defined by Tang et al. [115], the so-called limiting flux is reached once:

$$F_{Drag} = F_{Barrier}^{f-f} \quad (18)$$

and is given by rearranging Equation (13) and Equation (18):

$$J_L = \frac{F_{Barrier}^{f-f}}{6\pi\mu R_h} \quad (19)$$

The electrostatic repulsion forces between the deposited foulants and the approaching foulants are strongly dependent on the feed solution chemistry (e.g. pH, ionic strength, and calcium concentration) and are at their minimum for neutral foulants [121]. This means that $F_{Barrier}^{f-f}$ and hence the limiting flux are greatly reduced by enhanced humic acid and/or alginate fouling at lower pH operation or in the presence of higher divalent cation concentrations, due to the associated charge neutralisation of the organic foulants [97,115,122,123].

As stated by Tang et al. [115,121], the limiting flux was found to be independent of the membrane properties in pressure driven membrane processes. Similarly, Morrow et al. [124] also found that the limiting flux obtained in FO operation is membrane independent in AL-FS mode. This is, however, not the case when the membrane is operated in AL-DS mode, as commonly done in PRO operation. During PRO operation in AL-DS mode, She et al. [125] found that the limiting flux is inversely proportional to the membrane's structural parameter S, as inorganic fouling occurred on the membrane's feed side (i.e. within the membrane's substrate). This inverse dependence of J_L on S in AL-DS operation is related to the fact that foulants are concentrated within the membrane's substrate, due to concentrative internal concentration polarisation. Hence, She et al. [125] derived the following relationship:

$$J_L = \frac{D_i}{S} \ln\left(\frac{C_{F,M,i}^L}{C_{F,i}}\right) \quad (20)$$

where D_i is the diffusivity of specific solute i (i.e., divalent ions in the case of membrane scaling). $C_{F,i}$ is the bulk feed concentration of solute i and $C_{F,M,i}^L$ is the final stable solute concentration at the membrane's active layer surface (i.e., at the active layer – support layer interface when used in AL-DS mode) at which no further foulant precipitation and/or gelation will occur.

A similar relationship can be derived for pressure and/or osmotically driven membrane processes that are operated in AL-FS mode. With fouling on the membrane's feed side being

the main cause for flux decline, the stable concentration of foulant i on the membrane's active layer surface on the feed side is given by either [102]:

$$\text{FSD:} \quad C_{F,M,i}^{L} = C_{F,i} e^{\left(\frac{J_L}{k_F}\right)} - \frac{J_{S,i}}{J_L}\left(e^{\left(\frac{J_L}{k_F}\right)} - 1\right) \tag{21}$$

or by:

$$\text{RSD:} \quad C_{F,M,i}^{L} = C_{F,i} e^{\left(\frac{J_L}{k_F}\right)} + \frac{J_{S,i}}{J_W}\left(e^{\left(\frac{J_L}{k_F}\right)} - 1\right) \tag{22}$$

depending on the direction of $J_{S,i}$. By rearranging Equation (21) and Equation (22), the FSD and RSD respective limiting flux is given by:

$$\text{FSD:} \quad J_L = k_F \ln\left(\frac{C_{F,M,i}^{L} - \frac{J_{S,i}}{J_L}}{C_{F,i} - \frac{J_{S,i}}{J_L}}\right) \tag{23}$$

and:

$$\text{RSD:} \quad J_L = k_F \ln\left(\frac{C_{F,M,i}^{L} + \frac{J_{S,i}}{J_L}}{C_{F,i} + \frac{J_{S,i}}{J_L}}\right) \tag{24}$$

Equation (23) and Equation (24) show that the limiting flux in AL-FS mode, is mainly dependent on the feed side mass transfer coefficient k_F and not on the membrane properties. Although the $J_{S,i}/J_L$ terms are dependent on the membrane selectivity (B/A), these terms can be generally neglected, as $J_{S,i}/J_L$ is negligible for the main fouling contributors (e.g., divalent cations and alginate) when using highly selective membranes. Hence, with the $J_{S,i}/J_L$ terms excluded, Equation (23) and Equation (24) are in agreement with the findings of Tang et al. [115,121] and Morrow et al. [124], namely that the limiting flux is independent of the membrane properties. Another important finding stated by Tang et al. [115,121] is that the limiting flux has no apparent dependence on the organic foulant concentration in the feed solution. This can also be seen by Equation (23) and Equation (24), in which the ratio of $C_{F,M,i}^{L}/C_{F,i}$ is used and thus, J_L is not strongly dependent on the absolute feed solution concentration.

Chapter 3

Six approaches for brine volume minimisation using OARO with non-responsive draw solutes

In this chapter, the technical and economic viability of six OARO integrated flow processes for BVM are determined. The overall objective of this Chapter is to benchmark the various OARO processes against each other and against MSRO at equivalent operating conditions. All processes are modelled using the ORF governing equations presented in Section 2.1. Only non-responsive draw solutes (i.e., NaCl) are utilised in the six OARO integrated flow processes to minimise the process complexity and the cost associated with the regeneration of responsive draw solutes.

A numerical model was developed to simulate the counter-current flow arrangement in all OARO membrane modules. The numerical findings presented by Xiao et al. [41] show that a counter-current flow arrangement has several advantages over a co-current flow arrangement, such as a more uniformly distributed water flux along the FO module. The governing equations in Equation (3) and (4) are solved explicitly on a finite set of iteration segments along the membrane module. The draw solution salinity and mass flowrate at the module outlet are obtained with the shooting method [41]. The OARO and RO numerical model was validated using ROSA, which is an RO system analysis (ROSA) software developed by the membrane manufacturer DOW Filmtec [126]. The validation process is detailed in Appendix B.

Non-idealities, such as ICP, finite membrane areas, pressure losses and the efficiencies of pump and ERDs, are considered in this numerical simulation to offer a realistic evaluation of the OARO integrated flow processes. The objective of these processes is to recover 72% and 44% of the freshwater from feed solutions with a respective salinity of 35 g/L and 70 g/L. Both scenarios result in the same final brine concentration of 125 g/L. This brine concentration target is 50 g/L above the generally achievable RO brine concentration and would result in a 40% reduction in brine volume. A similar brine concentration target has been set in Chen & Yip [18].

The optimal OARO integrated flow process is chosen, based on the following four considerations:

Energy consumption:

As suggested by Semiat [127], energy consumption is the main contributor, with a share of 44% of the overall operational expenditures of a typical SWRO desalination plant. The energy consumption is therefore assumed to be representative of the overall process operational costs. In this Chapter, the energy consumption of the entire desalination process is modelled. This includes the energy consumed by the seawater intake, pre-treatment, brine discharge and post-treatment.

Capital cost:

Henthorne & Boysen [128] and Moser et al. [129] both state that the intake, pre-treatment and brine discharge contribute somewhere between 23% and 33% to the total capital expenditures of a SWRO plant. These costs can be excluded from the comparison, as all the OARO integrated flow processes operate with the same feed and recovery and thus have similar intake, pre-treatment, and brine discharge costs. However, the cost contribution of the desalination system itself, which is mainly comprised of the cost incurred by the pressure vessels, is approximately 35% of the total capital expenditures

of a standard SWRO plant. As the required number of pressure vessels varies for each process, the capital cost of each OARO integrated flow process will be linked to this number. The required number of pressure vessels is determined for a permeate production of 1000 m^3/h at the desired recoveries. Capital costs associated with the high-pressure pumps (HPP) and the ERD are also included.

Permeate salinity:

The maximum allowable permeate salinity is 500 mg/L TDS, as stated in the World Health Organisation (WHO) standards for drinking water [130].

Operating pressure:

The maximum OARO operating pressure P_{OA} is restricted by practical pressure limits of the OARO membrane and module. Straub et al. [131] achieved a maximum burst pressure of 48.3 bar in PRO operation for a commercially available TFC FO membrane backed by two layers of dense tricot woven fabric. Even higher burst pressures, of up to 70 bar, were achieved by Madsen et al. [81] for three cellulose acetate (CTA) FO membranes. However, a porous steel plate was used as feed spacer in the experimental PRO set-up. Implementing porous steel plates as spacers in spiral wound membrane modules is not practical or economically feasible. On the other hand, the tricot woven fabric is commonly utilised in commercial SWRO membrane modules. Therefore, the maximum practical burst pressure is assumed to be 48.3 bar and not 70 bar. The membrane burst pressure is defined as the maximum allowable transmembrane pressure (TMP) under which the selectivity of the membrane's active layer is not compromised.

3.1. Analysis of the stand-alone OARO process

Before the OARO integrated flow processes are analysed, it is important to understand the effect of varying the operating parameters of the stand-alone OARO process. Here, 'stand-alone' refers to a process not yet integrated with the RO unit. All comparisons of the stand-alone OARO process are performed at a constant seawater (draw) and brine (pressurised saline feed) inlet salinity of 35 g/L and 70 g/L, respectively. Further assumptions are that NaCl is the only solute and that the density ($1025\ \mathrm{kg/m^3}$) and temperature ($25°C$) of the feed and draw streams are constant. For energy calculations, the mechanical efficiency of the pump and the energy recovery device are assumed to be 80% and 96%, respectively [132]. The number of membrane modules in series n_{OA} is kept constant at 7; and each module has an active membrane area of $37\ \mathrm{m^2}$, which corresponds to the membrane area of conventional 8-inch Filmtec spiral wound modules [133].

Generally, the feed inlet flowrate Q_F is set as $8\ \mathrm{m^3/h}$ and the flowrate ratio RR is set as 0.5. RR is defined as the ratio between the draw Q_D and the total flowrate (Figure 2):

$$RR = \frac{Q_D}{Q_D + Q_F} \tag{25}$$

Finally, the pressure loss P_L in the feed and draw channels is modelled by:

$$\Delta P_L = 68.95\ n_{OA}(15.85\ Q_F)^{1.7} \tag{26}$$

where ΔP_L is given in bar and Q_F in $\mathrm{m^3/s}$. This equation is adapted from DOW [133] for spiral wound modules.

3.1.1. Optimal OARO membrane properties

A detailed discussion on the optimal membrane properties in Section 2.2. has shown that the ideal OARO membrane is highly water permeable (large A-value), has a thin and porous substrate (small S-value) and has a solute permeability B that minimises the overall cost of

operation (i.e., reduces ICP while also ensuring a high process efficiency). In Figure 10, three different types of membranes are compared in terms of their SEC and diluted seawater salinity with respect to the OARO process recovery. The presented OARO recoveries are achieved by varying P_{OA} between 40-80 bar.

In addition to the TFC-FO membrane, which was used by Straub et al. [131], a nanofiltration (NF90) and reverse osmosis (SW30-HRLE) membrane are also modelled. The NF90 nanofiltration membrane is chosen for this comparison, as it shows high rejection ratios for both monovalent and bivalent ions when compared to other nanofiltration membranes, such as the NF270 or NF200 membrane [134]. According to the manufacturer, the SW30-HRLE seawater reverse osmosis membrane element combines high rejection and low energy requirements and is therefore chosen for this comparison [135]. Each membrane's properties are given in Table 1. For this simulation, it is assumed that it is possible to manufacture all three membranes with the same thin and porous support layer ($S = 0.57$ mm).

Table 1: Membrane properties of the three simulated membranes

Name	Manufacturer	A $[LMH/bar]$	B $[LMH]$
NF90	DOW Filmtec	6.25	1.68
TFC-FO	HTI	2.49	0.39
SW30HRLE	DOW Filmtec	1.13	0.08

The shaded areas in Figure 10 represent infeasible operating conditions, as the feed pressure P_{OA} exceeds the burst pressure of 48.3 bar. At equivalent feed pressures, the more permeable membranes achieve a higher process recovery, as the water flux J_W increases proportionally with A. Almost 23% of the brine stream can be recovered when utilising the NF90 membrane at the burst pressure. On the other hand, the recovery only reaches 15.2% and 12.3% when using the TFC-FO and the SW30-HRLE reverse osmosis membrane, respectively.

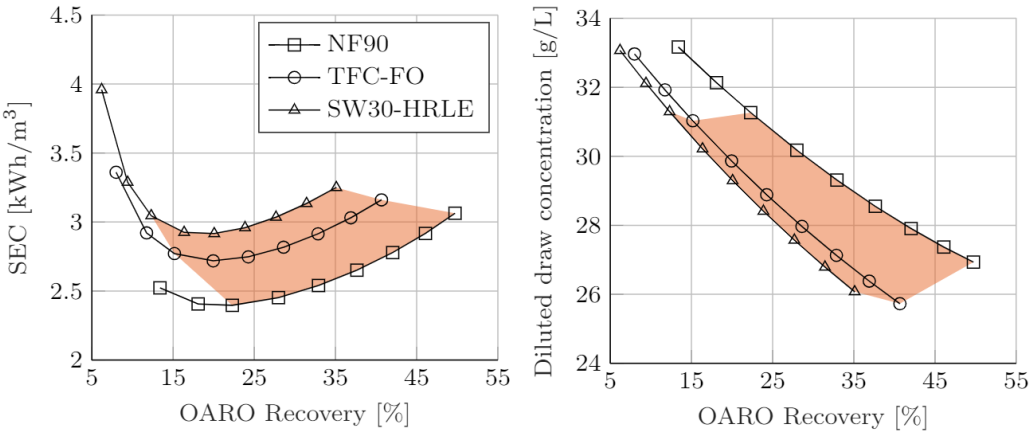


Figure 10: Specific energy consumption and diluted draw concentration for three different membranes with respect to OARO process recovery. ($Q_F = 8\ m^3\ /\ h,\ RR = 0.5$).

Figure 10 also displays the diluted seawater salinity for all three membranes. In general, a higher dilution of the OARO draw solution is preferred, as a secondary purification process is utilised to further desalinate this stream. As shown in the figure, a similar diluted seawater salinity is observed when utilising any membrane and when operating at the membrane burst pressure. This is true even though the membrane properties A and B vary significantly between the chosen membranes. As previously mentioned, dense polymeric membranes with a higher permeability have a lower selectivity due to the permeability-selectivity trade-off phenomenon. Thus, choosing a more permeable membrane, such as the NF90 membrane, leads to a simultaneous increase in the water and solute flux. This results in the observed similarity in draw dilution for all three membranes under the defined OARO operating conditions.

The specific energy consumption of the OARO process, operated at the membrane burst pressure, reduces from $3.05\ kWh/m^3$ (SW30-HRLE) and $2.77\ kWh/m^3$ (TFC-FO) to $2.4\ kWh/m^3$ when using the NF90 membrane instead of the more selective membranes. To conclude, OARO processes seem to benefit more from water permeability than from selectivity in the membrane, as a similar dilution of the draw stream is achieved at a lower specific energy consumption. These results suggest that tight nanofiltration membranes with a thin and porous

support layer should be further developed for these types of applications. However, these membranes are not commercially available with such thin support layers. Since the TFC-FO membrane is commercially available, it is chosen for the subsequent simulations.

3.1.2. Optimal OARO feed flowrate

The process recovery Y_S is inversely dependent to the feed flowrate Q_F:

$$Y_S = Q_P/Q_F \tag{27}$$

where Q_P is the flowrate of the permeate that moves from the feed to the draw solution. Q_P is also dependent on Q_F, as J_W and J_S are indirectly affected by changes in the feed flowrate. The pressure drop ΔP_L in the OARO feed channel increases with Q_F, as shown by Equation (37). An increase in ΔP_L over the length of the membrane module reduces the transmembrane pressure difference, which results in a reduction in Q_P. On the other hand, at higher flowrates, external concentration polarisation is less pronounced, as enhanced mass transfer occurs due to higher turbulence in the feed channels.

The net effect of Q_F on the OARO process recovery is depicted in Figure 11. As shown, the process recovery increases from 10.6% to 23% if operating at the membrane burst pressure and the flowrate is reduced from 12 m^3/h to 4 m^3/h. This suggests that the reduction in ΔP_L and the smaller denominator in Equation (27) affect the process recovery more than the increase in ECP due to the lower flowrates.

The higher OARO process recovery at lower Q_F and equivalent feed pressures result in a lower and more diluted seawater salinity, as shown in Figure 11. Furthermore, the specific energy consumption reduces with a reduction in Q_F when operating at the bursting pressure. This can be attributed to the higher recovery and lower pressure drop in the OARO feed channels.

The higher system recovery, better dilution of the draw stream and lower energy consumption favour operation of the OARO process at lower feed flowrates. Nevertheless, lower feed flowrates result in higher capital expenditures, because more OARO pressure vessels are required in parallel to process the same overall feed rate. Another problem arising from low feed flowrates is enhanced scaling and fouling. In the DOW technical manual [133], a general guideline is given for the concentrate flowrate, which should not be less than 3 m^3/h if the feed silt density index (SDI) is approximately 3. Lower SDI values represent a better feedwater quality and can be achieved by more rigorous pre-treatment.

The trade-off between recovery, energy consumption, capital cost and fouling suggest that an intermediate flowrate is the best choice for the OARO process. Q_F is chosen to be 6 m^3/h for the simulations in Section 3.4., where it is important to show that the OARO process can be operated below its burst pressure while achieving the set recoveries.

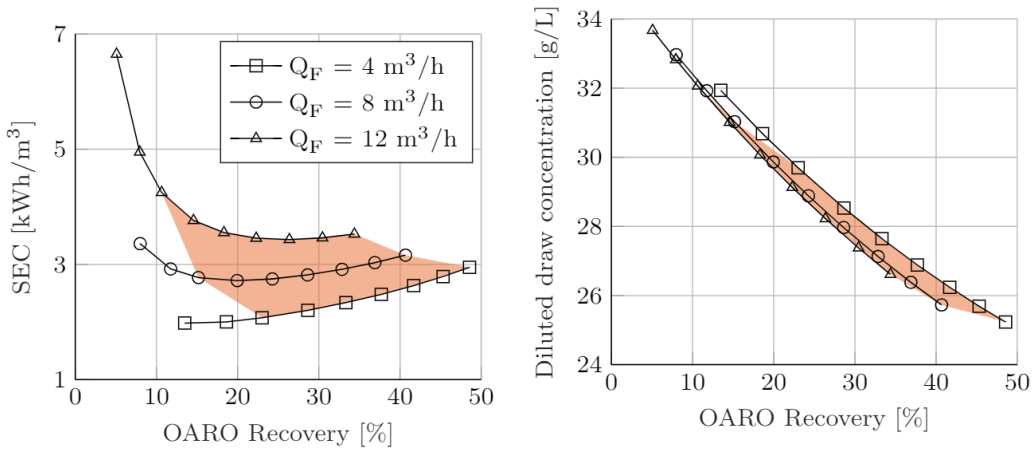


Figure 11: Specific energy consumption and diluted draw concentration for three different feed flowrates with respect to OARO process recovery. (TFC-FO membrane with RR = 0.5).

3.1.3. Optimal flowrate ratio between OARO streams

Figure 12 displays the diluted seawater salinity and the specific energy consumption for three different RR values. Q_F is kept constant at 8 m^3/h while Q_D is adjusted to achieve the desired

RR-value. The figures indicate that the diluted draw concentration is reduced as RR decreases. Smaller RR values indicate a less voluminous draw stream, which is thus easier to dilute. This would suggest that the recovery at the same operating pressure should be less at lower RR values due to the lower osmotic potential of the more diluted draw solution. However, as shown in Figure 12, the RR-value has a negligible effect on the OARO recovery when operated at the same P_{OA}. This is explainable by the higher forward salt diffusion occurring at lower RR values due to the larger transmembrane concentration difference throughout the OARO module, which helps reduce ICP.

If RR is greater, the pressure loss in the draw stream is more severe for no additional increase in recovery. Furthermore, Figure 12 shows that the specific energy consumption is significantly higher at the burst pressure if RR=0.6. In practice, RR will be less than 0.5, as the spacer in the OARO draw channel must be denser than the feed spacer to prevent membrane deformation under high feed pressures. For example, in Jeon et al. [136] the maximum tested RR value never exceeded 0.375 for an FO spiral wound module. To conserve energy and for practical reasons, RR is chosen from here onwards to be 0.5.

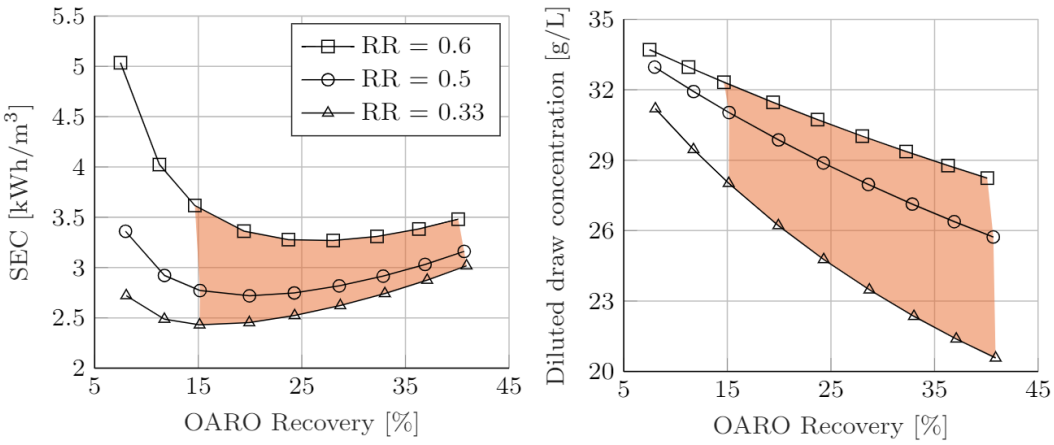


Figure 12: Specific energy consumption and diluted draw concentration for three flowrate ratios RR with respect to OARO process recovery. (TFC-FO membrane with $Q_F = 8\ m^3\ /\ h$).

3.1.4. Optimal OARO feed pressure

Assuming that membranes and modules can be designed to achieve higher burst pressures, the shaded areas in Figure 10 to Figure 12 become feasible operating regions. Each plot marker represents an increase in pressure by 5 bar up to a maximum pressure of 80 bar. As shown in these figures, the specific energy consumption remains relatively constant when increasing P_{OA} above the current burst pressure. This can be attributed to the simultaneous increase in energy consumption and recovery at higher P_{OA}.

From Equation (3) and Equation (4), it can be seen that the transmembrane pressure difference directly affects the water flux J_W, but not the solute flux J_S. The water flux changes proportionally with the feed pressure, which in turn changes the concentration polarisation factors that affect both J_W and J_S. Therefore, an increase in P_{OA} results in a higher process recovery due to the higher water flux. On the other hand, the change in solute flux is less severe when altering P_{OA}. An increase in feed pressure thus leads to an improvement of the OARO draw stream dilution.

Madsen et al. [81] show that current FO membranes are capable of withstanding high feed pressures of up to 70 bar if they are sufficiently supported by the membrane module and spacer. Thus, the development of highly permeable but rigid permeate spacers and of membrane modules with high packing densities is essential to improve the OARO process.

3.2. The standard UF-RO process

In the following section, the OARO process is incorporated into the standard UF-RO process, depicted in Figure 13, to achieve the specified recoveries. Although a single UF and RO process are depicted, each process consists of a number of membrane modules in parallel (N_{UF} and N_{RO}) to process the overall feed rate. The operating conditions of this UF-RO process will remain constant for all simulations. A single stage RO process is chosen, where each pressure vessel contains 7 8-inch spiral wound membrane modules [132]. The RO operating pressure and feed flowrate are set at 80 bar and $12\ m^3/h$, respectively. These process parameters are representative of a general RO process for large operations [133].

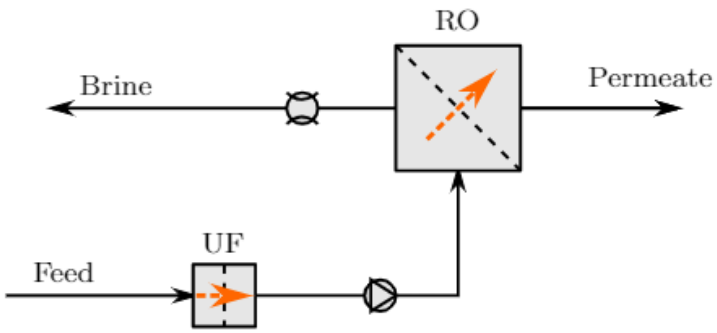


Figure 13: The UF-RO reference model.

Table 2 presents the recoveries achieved by the UF-RO process for the two specified feed concentrations. Relatively high recoveries are achieved for the UF-RO process when operating at 80 bar, which is the typical maximum operating pressure of RO [19]. The DOW technical manual [133] suggests that an additional flow factor FF is incorporated into Equation (3) to adjust the modelled water flux for reversible/irreversible fouling and scaling. Generally, FF is 0.7 if the seawater feed is treated by ultrafiltration (UF) and SDI is below 3. However, empirical data regarding water flux reduction due to reversible/irreversible fouling or scaling is not available; thus, $FF = 1$ is assumed here. In other words, a pure NaCl feed with constant D ($1.33e^{-9}\ m^2/s$ [70]) is considered in the simulations. With a real seawater feed, fouling and scaling phenomena

cannot be neglected, and the achievable recoveries will reduce with operational time. The extent is, however, unknown.

Table 2: System recovery Y_S, specific energy consumption (SEC), permeate salinity C_P and number of UF modules N_{UF} and RO modules N_{RO} required for the UF-RO process at two varying inlet salinities C_F.

$C_F\,[g/L]$	$P_{RO}\,[bar]$	$Y_S\,[\%]$	$SEC\,[kWh/m_P^3]$	$C_P\,[g/L]$	N_{UF}	N_{RO}
35	80	59.21	3.60	0.204	71	141
70	80	23.27	5.14	0.640	180	359

Table 2 also presents the modelled energy consumption of the UF-RO process. Fane [137] mentions that the overall energy consumption of modern SWRO desalination plants lies in the range of $3.0 - 3.5\,\mathrm{kWh/m^3}$. The energy consumption of the UF-RO process lies slightly above this range for a seawater salinity C_F of 35 g/L. The efficiency of the high-pressure pump and energy recovery device are equivalent to those for the OARO process presented in Section 3.1. The energy breakdown for a typical SWRO desalination plant, given by Voutchkov [132], is assumed to be at a 50% system recovery, and is used to determine the additional energy expenditures associated with the intake, pre-treatment, brine discharge and post-treatment. At the same recovery, the UF-RO plant presented in Figure 13 consumes $0.19\,\mathrm{kWh/m^3}$, $0.12\,\mathrm{kWh/m^3}$ and $0.18\,\mathrm{kWh/m^3}$ for the intake, brine discharge and post-treatment, respectively. Ultrafiltration is chosen as a general pre-treatment process and consumes approximately $0.3\,\mathrm{kWh/m^3}$ [137].

Insufficient pre-treatment is the most common cause of RO system failure [138]. Compared to conventional pre-treatment methods, membrane filtration processes such as ultrafiltration offer consistent and high-quality product water. Additionally, a smaller process footprint, less chemical dosage and fully automatic operation is possible when using UF [139]. Suarez et al. [140] offers one-year operational data for an UF-RO plant. According to their findings, the consistently high quality UF filtrate and reduced SDI in comparison to the previously installed

multimedia filters improved reliability and operability of the desalination plant. However, biological growth within the system still remained an issue, as dissolved organics are not effectively reduced by UF. In Ma et al. [141], the issue of RO membrane biofouling is addressed by an additional enhanced coagulation process installed prior to the UF process. This combined pre-treatment effectively reduced silica, iron, and microbial contamination of the RO feed water to minimise biofilm formation on the RO membrane. As mentioned by Jamaly et al. [142], low pressure membrane pre-filtration improves the reverse osmosis membrane lifespan by 20-30% and thus, lowers the operational costs involved in frequent membrane replacement.

The recovery of the UF process is assumed to be 100%, although it can optimally reach only 95% due to frequent backwashing for fouling prevention [142]. The number of UF and RO pressure vessels is based on a permeate production of $1000\ \mathrm{m^3/h}$. N_{UF} is determined by assuming that 4 X-Flow Aquaflex UF modules, each having an active membrane area of $60\ \mathrm{m^2}$, are placed in series in each pressure vessel [143]. An average UF water flux of $100\ \mathrm{L/(m^2 h)}$ is assumed [139].

As shown in Figure 13, it is assumed that a single pumping and energy recovery centre supplies all parallel RO trains. This principle is also chosen for the OARO process, as larger high efficiency pumps can be utilised to increase the pumping efficiency up to 85% [132]. Indeed, this is done at the Ashkelon seawater desalination plant in Israel, where 4 high-pressure pumps supply seawater to 16 RO trains to produce 50 million cubic meters of water a year [144].

3.3. The OARO integrated processes

Six different OARO incorporated processes are displayed in Figure 14 and Figure 15, of which C-OARO 2 and C-OARO 3 are novel processes that were not investigated before. For clarity, the water flux direction is indicated for each membrane process in the figures. As mentioned, the objective in this Chapter is to achieve a final system water recovery of 72% and 44% for a feedwater inlet salinity of 35 g/L and 70 g/L, respectively. These recoveries are obtained for each OARO integrated flow process, with various feed pressures P_{OA} and total number of OARO stages S_{OA}. In this work, the maximum number of OARO stages is limited to 3 ($S_{OA} \leq 3$). Labels S_1 to S_4, that are displayed in Figure 14 and Figure 15, are used to indicate the position of each OARO stage in the process.

An iterative approach is chosen to determine the steady state operation of each OARO integrated flow process. Every iteration commences by modelling each OARO and RO process independently, with its respective feed/draw flowrates and salinities. The iteration is then terminated by passing updated information between the processes before continuing with the following iteration. Steady state operation is reached once all flow streams converge and the salt and water conservation errors are below 1% of the inlet salt and water flowrate.

Each OARO integrated flow process contains a maximum of 3 stages, with each stage containing several pressure vessels in parallel, where the feed flowrate per vessel is given by Q_F. Moser et al. [129] mention that the cost of the membrane module is negligible compared to the cost of the pressure vessel. Therefore, it is financially beneficial to fit the maximum number of membrane modules into each pressure vessel. In Section 3.4., 7 modules per pressure vessel are assumed for the RO process, as this is typical for large scale RO operations. An equivalent number of modules per pressure vessel is assumed for each OARO stage.

FO spiral wound membrane modules generally have a lower active membrane area (between 9 m^2 and 15 m^2 [145]) than their RO counterparts due to their more complex configuration to accommodate the draw solution . However, it is assumed that OARO modules can be designed with an RO equivalent active membrane area. An OARO membrane module with a high packing density should be plausible; Straub et al. [131]employed a tightly woven permeate spacer from a commercial RO membrane to achieve a burst pressure of 48.3 bar. OARO pressure vessels are assumed to be in a similar price range to that of their RO counterparts, as both processes are operated at higher pressures.

Figure 16 shows the hydraulic and osmotic pressure profiles for three subsequent stages (S_1 to S_3) in a single OARO process. Each stage is operated at the same inlet feed and draw pressure by employing booster pumps between each stage. These pumps are also modelled at a mechanical efficiency of 80%. As shown in the figure, π_F and π_D vary in each stage and depend on the process recovery and salt diffusion. Furthermore, no fouling or scaling of membrane surfaces are considered when determining J_W and J_S.

3.3.1. MP-OARO

Two variations of the MP-OARO configuration are modelled. As shown in Figure 14, MP-OARO 1 (MP-1) contains a single OARO loop with up to 3 stages in series ($S_{OA} \geq 1$). The RO process is not in direct contact with the seawater stream but is instead supplied by the diluted draw stream of OARO 1. The RO brine is then recirculated and reused in the OARO 1 process as draw solution. On the other hand, MP-OARO 2 (MP-2) consists of one additional OARO loop with up to 3 stages split between OARO 1 and OARO 2, as depicted in Figure 14. MP-OARO 2 requires a minimum of two stages ($S_{OA} \geq 2$) situated at S_1 and S_2. If a third OARO stage is employed, then it is either situated at S_3 or at S_4. The diluted draw streams of OARO 1 and OARO 2 are further purified in the OARO 2 and RO process, respectively. Furthermore,

the brine streams of the OARO 2 and RO process are reused as draw solutions in the previous membrane process, namely OARO 1 and OARO 2, respectively.

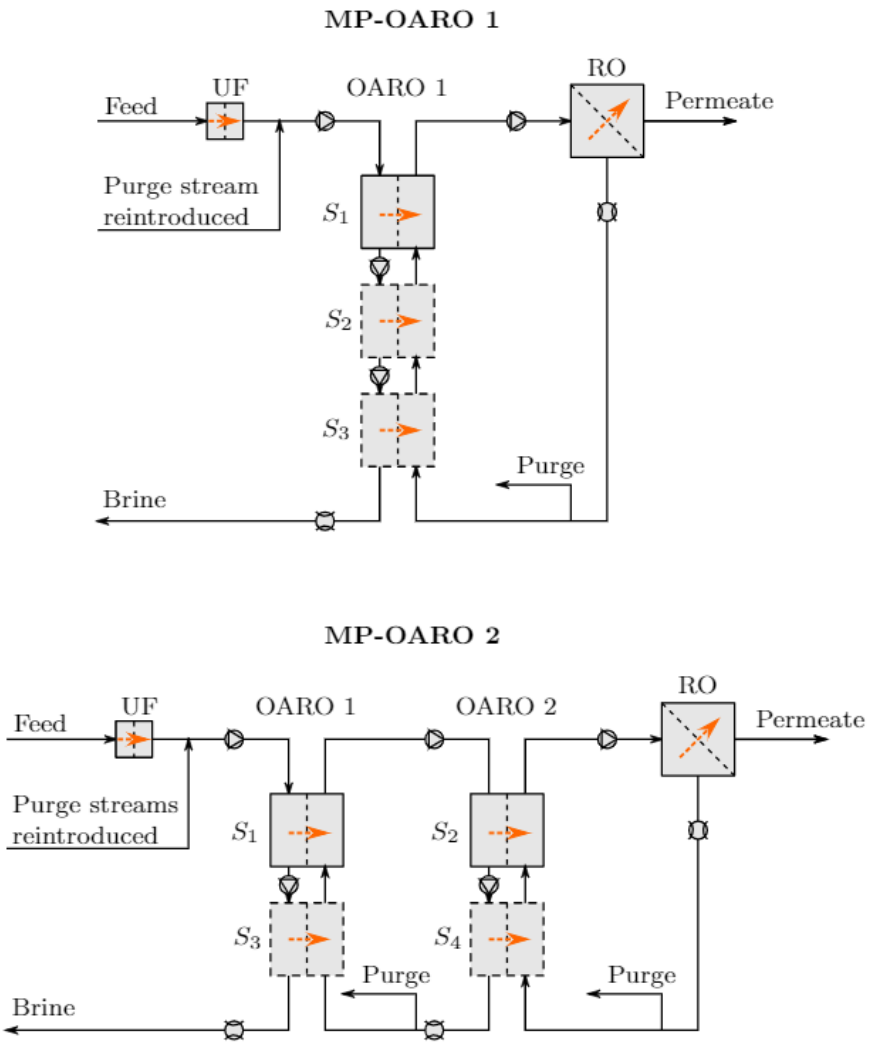


Figure 14: MP-OARO, the first two OARO integrated flow process that are being investigated.

Due to the process layout, solute build-up or depletion in the individual loops occurs because of solute flux if no purge or replenishment streams are introduced [5]. The solute flux J_S varies for each subsequent membrane process as process parameters, such as membrane selectivity, feed pressure, and stream salinities, may differ. As shown in Figure 14, solute concentration is controlled in each loop by incorporating purge streams. These purge streams are reintroduced

on the feed side of OARO 1, with the benefit of introducing water streams with a lower salinity than the concentrated brine stream being discharged.

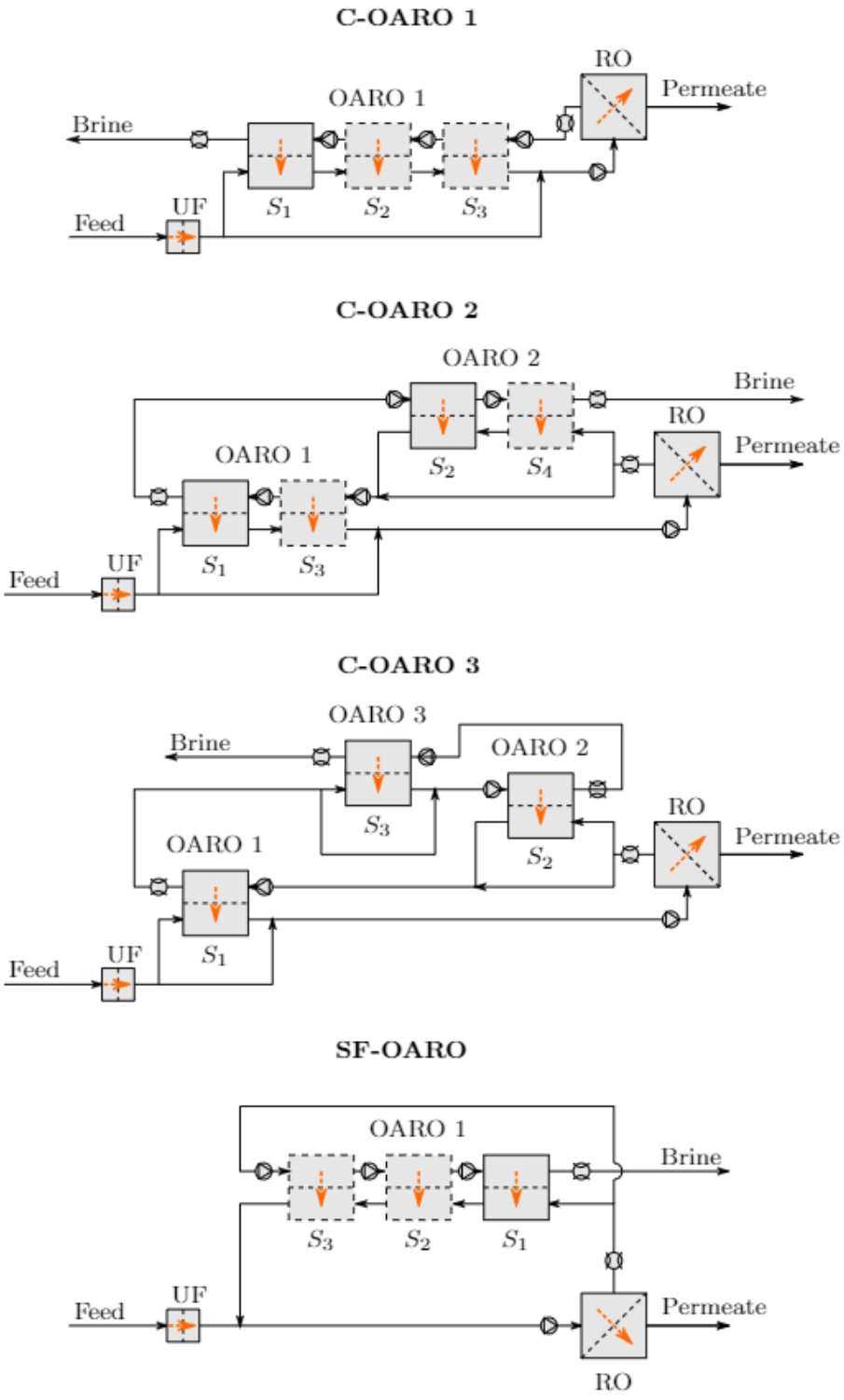


Figure 15: The other four OARO integrated flow processes that are being investigated.

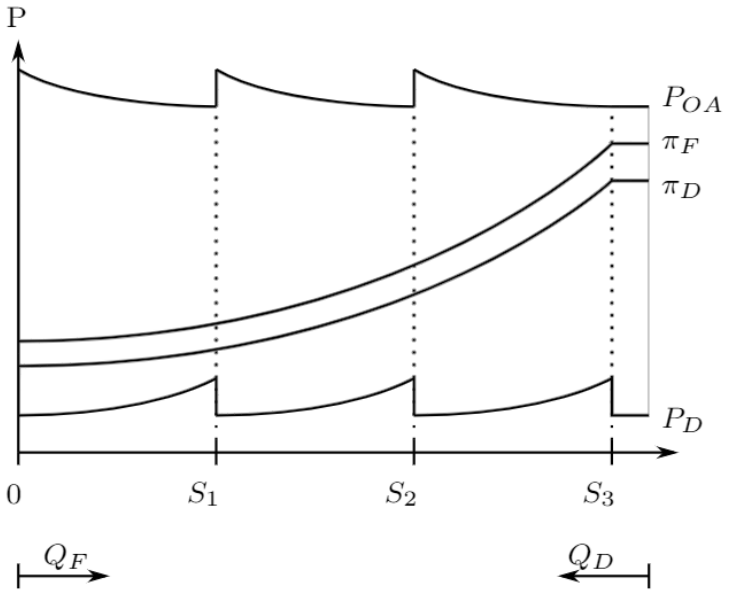


Figure 16: Pressure profile in an osmotically assisted reverse osmosis process with 3 stages in series.

3.3.2. C-OARO

Three different variations of the C-OARO configuration are investigated in this study and are depicted in Figure 15. The cascading OARO process is responsible for simultaneously concentrating the RO brine stream and diluting the RO feed stream, with up to 3 stages in series ($S_{OA} \geq 1$). Only a fraction of the RO feed stream is utilised as draw solution in OARO 1, because RR is set as 0.5 and the volumetric flowrate of the RO brine stream is lower than that of the OARO 1 feed stream.

One set of high-pressure pumps and energy recovery devices is utilised for each of the two high pressure membrane processes. Thus, RO can be operated at its optimal pressure while varying the feed pressure in OARO 1 to achieve the set recoveries for each inlet salinity. In practice, two sets of HPPs and ERDs will be required because the OARO membrane modules have a lower burst pressure, as discussed in Section 3.1.

In C-OARO 2 (C-2), a secondary cascading OARO 2 process is introduced. The advantage is that OARO 2 dilutes the RO brine stream before it enters the first OARO 1 process. Diluting

the RO brine reduces the osmotic pressure difference between the two OARO 1 inlet streams and allows for lower pressure operation. Furthermore, the irreversible losses associated with the process are reduced [62]. The minimum number of stages is 2 ($S_{OA} \geq 2$), because at least one stage is required for each OARO process (S_1 and S_2). If a third OARO stage is incorporated, then it is either situated at S_3 or S_4.

C-OARO 2 is modelled with two additional sets of high-pressure pumps and energy recovery devices, as shown in Figure 15. However, both OARO processes are placed in series and in principle a single set of high-pressure pumps and energy recovery devices could be utilised for both OARO processes. Therefore, no increase in capital cost is expected when choosing C-OARO 2 over C-OARO 1.

The aim of C-OARO 3 (C-3) is similar to that of C-OARO 2, namely, to dilute each feed stream before it enters the following OARO module. This OARO integrated flow process incorporates a third cascading OARO 3 process and is depicted in Figure 15. In this case, it is not possible to operate all three OARO processes using a single set of HPPs and ERDs, as the brine stream is reused in OARO 3 as draw solution and must be de-pressurised for the OARO 3 process to function. C-OARO 3 requires a minimum of 3 sets of high-pressure pumps but is modelled as depicted in Figure 15 with 4. Furthermore, each OARO process requires at least one stage, and therefore is only modelled with S_{OA} being 3.

3.3.3. SF-OARO

In the SF-OARO (SF-1) configuration, an OARO process is integrated into a semi-batch RO process. As displayed in Figure 15, a fraction of the RO brine is used as draw solution to OARO 1 and the other as feed solution to OARO 1. The diluted brine stream is then recirculated and mixed with the original RO feed stream. The advantage of SF-OARO compared to a standalone semi-batch RO process is that a lower concentrated brine is mixed with the initial feed. This

reduces energy losses generated by mixing the two streams of different salinities [57]. In terms of the OARO process itself, the advantage is that both streams enter the OARO 1 process at the same concentration. Thus, the osmotic pressure difference is expected to be lower than for any of the previously presented OARO integrated flow processes. Furthermore, only a fraction of the RO brine stream must be pressurised for OARO 1 operation, which should reduce energy consumption.

3.4. Analysis of the OARO configurations

In this section, the six OARO integrated flow processes using non-responsive draw solutes are evaluated for both recovery scenarios. Figure 17 shows the simulation results obtained for scenario 1 ($C_F = 35 g/L$ and $Y_S = 72\%$) and scenario 2 ($C_F = 70 g/L$ and $Y_S = 44\%$) on the left-hand and right-hand columns, respectively. Although the final brine concentration is equivalent for both processes 125 g/L), major differences in P_{OA}, specific energy consumption, required number of RO and OARO pressure vessels, and permeate salinity can be observed.

The shaded regions in Figure 17 represent infeasible operating conditions. For P_{OA}, any transmembrane pressure exceeding the membrane burst pressure of 48.3 bar is not practical. The thermodynamic minimum energy of separation E_{Min} is determined using Equation (1) and is indicated for both scenarios on the SEC plots by the shaded area. Furthermore, the maximum acceptable permeate salinity is assumed to be 0.5 g/L and is also indicated by the shaded areas on the permeate salinity plots.

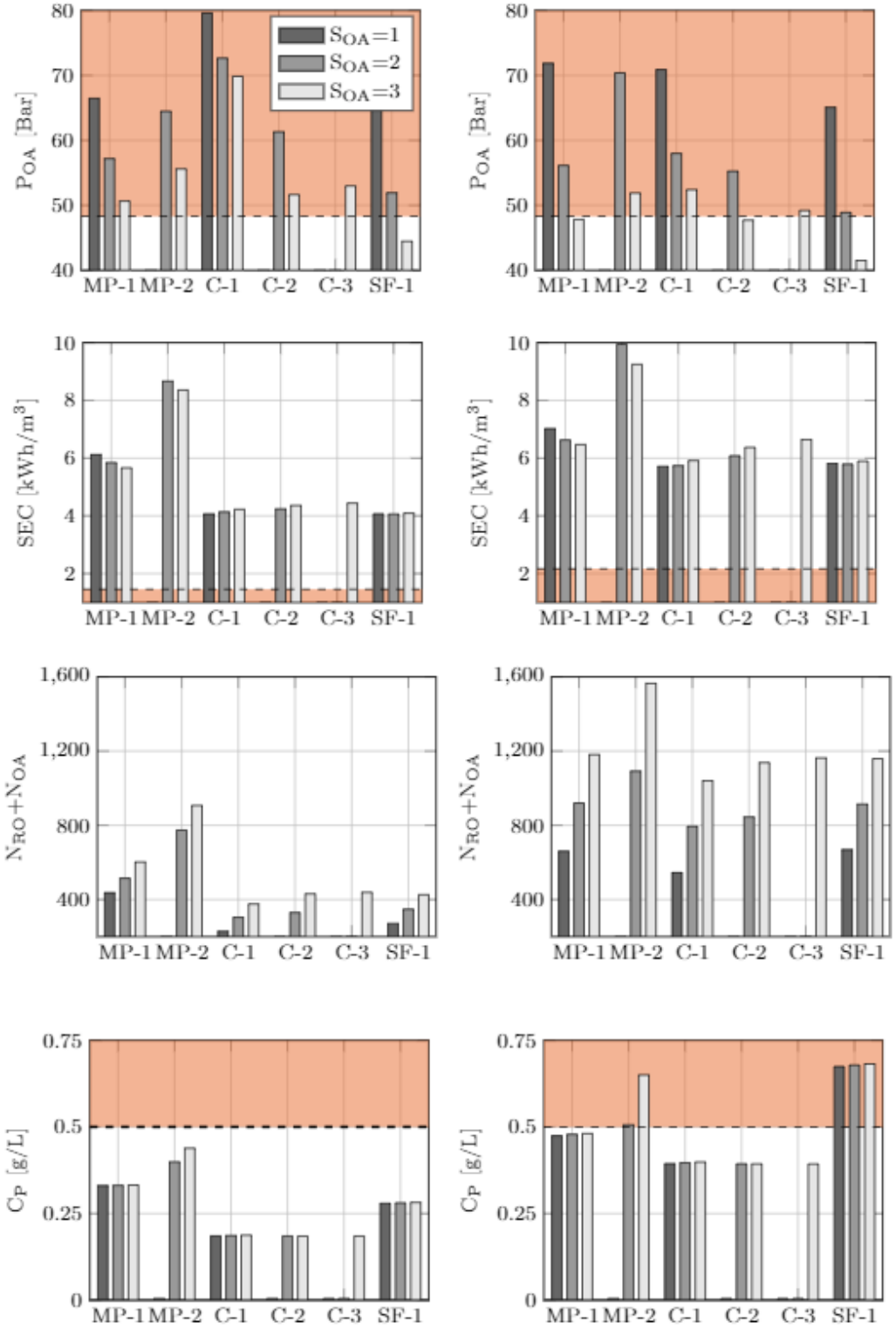


Figure 17: Simulation results for the OARO integrated flow processes for scenario 1 ($C_F = 35 g/L$ and $Y_S = 72\%$) in the left column, and scenario 2 ($C_F = 70 g/L$ and $Y_S = 44\%$) in the right column. The shaded regions indicate infeasible operating regions. In the SEC plots, the thermodynamic minimum energy for both scenarios is indicated by the dashed lines above the shaded regions.

3.4.1. Scenario 1 ($C_F = 35 g/L$ and $Y_S = 72\%$)

Of the six processes presented and according to the simulation results in Figure 17, only SF-1 with three OARO stages ($S_{OA} = 3$) can achieve the desired recovery while operating below the membrane burst pressure of 48.3 bar. Of the three cascading OARO integrated flow processes, C-2 and C3 can be operated at significantly lower P_{OA} than C-1, as the transmembrane osmotic pressure in each OARO process is reduced. For example, in C-2 the dilution of the RO brine stream by OARO 2 reduces the osmotic pressure difference in OARO 1. Furthermore, OARO 2 utilises the RO brine stream as draw solution, which is more saline than the original seawater feed. Therefore, the osmotic pressure difference in OARO 2 is also lower, as a stronger draw solution is utilised.

For the same total number of OARO stages, the permeate salinity, required number of pressure vessels and energy consumption are almost equivalent for all three processes. However, C-2 is the most feasible cascading OARO integrated flow process, as it achieves the same recovery at the lowest P_{OA}. Furthermore, in principle C-2 requires only a single set of high-pressure pumps to supply both OARO processes, which is not possible for C-3.

In MP-1 and MP-2, the OARO process assumes the role of an additional pre-treatment process. All water must pass through OARO 1 (and OARO 2 for MP-2) before reaching the RO process. While this can be beneficial for high salinity and/or high fouling/scaling streams, it comes at a significantly higher operational and capital cost. Each additional loop requires its own set of HPPs and ERDs and the process footprint increases significantly, as more piping is required. Comparing MP-1 with the other OARO integrated flow processes, at least 28% more energy is consumed, and 37% more pressure vessels are required when using a total of three OARO stages ($S_{OA} = 3$).

The results in Figure 17 indicate that the additional OARO loop in MP-2 further increases the operational and capital expenditures and is not advised, as MP-1 is capable of operating at lower P_{OA} and producing a permeate of sufficient quality. Furthermore, each additional loop requires its own set of HPPs and ERDs and the process footprint increases significantly as more piping is required.

SF-1 requires three stages and a minimum feed pressure of 43.5 bar to operate scenario 1. Further advantages of SF-1 include lower operational and capital costs, as it is the most energy efficient process requiring the least amount of pressure vessels (when excluding C-1, as it is infeasible). The only disadvantage of SF-1 is the reduced permeate quality, which is, however, still acceptable according to the drinking water standards of the World Health Organisation.

To conclude, SF-1 shows the best performance and is technically feasible for recovering 72% freshwater from a feed stream with an inlet concentration of 35 g/L.

3.4.2. Scenario 2 ($C_F = 70 g/L$ and $Y_S = 44\%$)

Recovering 44% freshwater from a 70g/L saline brine is more complicated than for the first scenario, although both concentrated brine streams reach the same outlet salinity of 125g/L. This is evidenced by the generally larger number of required pressure vessels, higher energy consumption and lower permeate quality for Scenario 2 than for Scenario 1.

Due to the lower process recovery of 44%, higher flowrates are observed in the entire OARO integrated flow process at fixed permeate volume. Thus, more pressure vessels are required to produce the same amount of permeate for higher salinity brine streams. Dewatering more saline brines also comes at the cost of a lower permeate quality. While it is still at acceptable levels for most of the OARO integrated processes, MP-2 and SF-1 would require a secondary RO pass to reduce the permeate salinity to acceptable limits. Furthermore, dewatering more saline brines is inherently more energy intensive. This is demonstrated by an increase in the

theoretical minimum energy of separation from $1.46\ \mathrm{kWh/m^3}$ to $2.17\ \mathrm{kWh/m^3}$ for Scenario 1 and 2, respectively.

However, one advantage in Scenario 2 is that higher feed concentrations lower the required OARO feed pressure, as the transmembrane osmotic pressure difference is reduced. For example, in C-1 the RO brine salinity is relatively constant for both scenarios, but the higher feed salinity results in a stronger draw solution in the OARO process. Therefore, three of the five proposed OARO integrated flow processes (MP-1, C-2, and SF-1) are capable of recovering 44% of freshwater from a 70g/L saline feed, while operating below the OARO membrane burst pressure.

Similar to the first scenario, C-1 is the least feasible process, as its minimum operating pressure is approximately 4 bar greater than the OARO membrane burst pressure. The best performing OARO integrated flow process at the higher feed concentration is C-2, as it can be operated at the lowest P_{OA} while achieving an acceptable permeate quality (unlike SF-1).

The increase in energy consumption between Scenario 1 and Scenario 2 is more significant for C-1 to SF-1 than for MP-1 and MP-2. This is explainable by the direct relationship between the inlet and RO feed salinity for C-1 to SF-1. In contrast, the RO feed salinity of MP-1 and MP-2 is more constant between Scenarios 1 and 2. At even higher inlet feed salinities, the only viable process will be MP-OARO with one or more loops, as the RO feed salinity is better regulated by separating the RO process from the feed stream. For scenario 1, the difference in the required number of pressure vessels between MP-1 and the other OARO integrated flow process is more pronounced. This is not the case for scenario 2, in which MP-1 becomes more competitive.

3.5. OARO vs. MSRO

From the previous discussion, it becomes evident that SF-1 and C-2 are the optimal OARO integrated flow processes for Scenario 1 and 2, respectively. However, the question still remains: how do these OARO integrated flow processes compare to other conventional high recovery processes?

Of the available high recovery processes, thermal processes are the most widely used, but are inherently inefficient [19]. MVC consumes between $20\ \mathrm{kWh/m^3}$ and $39\ \mathrm{kWh/m^3}$ of electrical energy [4], whereas SF-1 consumes at least 79% less energy when operating at the burst pressure. However, mechanical vapour compression can operate at salinities up to 250 g/L, recover up to 98% of the water and achieve a very pure distillate [4]. At the current stage, this is not possible using OARO integrated flow processes using non-responsive draw solutes.

FO and PAO are membrane processes employing a draw solution, which is similar to OARO, but are plagued by more severe ICP. Besides, the recovery of the osmotic draw solution is more energy intensive for FO/PAO, due to the comparatively higher draw solute concentration required to achieve the same system recovery Y_S. OARO can potentially be operated at similar water fluxes as SWRO and no expensive, purpose-made draw solute is lost by reverse solute flux, which further makes OARO more economically viable than FO/PAO.

Only MSRO is directly comparable to OARO, as it is a pressure-driven membrane process and currently the most energy efficient continuous process. Therefore, MSRO is modelled for Scenario 1 and 2, with the results presented in Table 3. All presented processes in Table 3 have 4 stages, including the terminal RO stage. All MSRO stages are operated at the same recovery by increasing the hydraulic pressure in each subsequent stage. This requires the use of interstage booster pumps but is beneficial for energy cost reduction and balancing the water flux in each stage. In practice, this operation reduces the fouling potential in the initial

membrane modules [57]. For the MSRO process, the feed flowrate in each RO stage is kept constant at 12 m^3/h. As mentioned in Section 3.2., large scale RO plants are generally operated at similar feed flowrates. A reduction in feed flowrate causes the permeate quality to worsen, increases the required number of pressure vessels and the RO operating pressure is not significantly reduced. In Table 3, P_{RO} represents the maximum required operating pressure in the final stage of the MSRO process.

Table 3: Comparison of OARO vs MSRO for the two scenarios. For this comparison, the OARO integrated flow processes are modelled with a total of three OARO stages and the terminal RO stage. Similarly, MSRO has an equivalent number of stages (4), including the terminal RO stage.

Scenario	Process	$P_{OA}/P_{RO}\,[bar]$	$SEC\,[kWh/m_P^3]$	$C_P\,[g/L]$	N_{OA}	N_{RO}
1	SF-1	45.5	4.09	0.282	247	179
1	MSRO	103.5	3.32	0.429	0	308
2	C-2	47.7	6.37	0.393	901	237
2	MSRO	102.5	5.16	1.220	0	619

The MSRO process is more energy efficient, because dilution and mixing of streams at different salinities in the OARO process increases entropy and thus diminishes the net energy efficiency [18,50]. Additionally, less pressure vessels are required in the MSRO process, as permeate is directly produced and no additional dilution steps are required. The latter increases the volume flowrates in the OARO integrated processes (i.e., more pressure vessels are required).

However, the last MSRO stage must be operated at pressures above the typical maximum RO operating pressure of 80 bar. As mentioned in Davenport et al. [19], DOW offers spiral wound RO membrane modules that can be operated at high pressures of up to 120 bar, due to special membrane and module designs [146]. These, however, have a significantly lower membrane area of 6.2 m^2 than the standard RO modules assumed here with an active membrane area of 37 m^2.

Thus, higher operating pressures, lower flowrates or more MSRO stages would be required to achieve the desired recoveries using MSRO.

Indeed, adding more MSRO stages or reducing the flowrate would further worsen the permeate quality and increase the capital expenditure. A secondary RO pass is required for MSRO in scenario 2 to achieve the required permeate quality. In contrast, C-2 achieves an acceptable permeate quality and no secondary RO pass is required.

To conclude, the high MSRO operating pressures required make the process impractical for high recovery processes. On the other hand, OARO integrated flow processes operate at viable pressures and offer a superior permeate quality compared to their MSRO counterparts. The difference in capital cost between the two processes is negligible, as MSRO either requires more stages to achieve the same recovery as OARO or needs a secondary RO pass to ensure an adequate permeate quality.

3.6. Prospect of OARO using non-responsive draw solutes

The main objective of an OARO integrated flow process is to achieve higher process recoveries to minimise the brine volume. Increasing the number of OARO stages would achieve this but would raise the capital cost. In addition, adding more stages becomes less effective, as more stages result in the process operating closer to the equilibrium state and at a lessened driving force. Another option would be to reduce the process flowrate, as discussed in Section 3.1.2. This would, however, also result in higher capital expenditures and increase the membrane fouling/scaling propensity. Optimally, OARO membrane modules should be developed that have a high packing density and are operable at higher feed pressures.

Table 4 shows the potential improvements of SF-1 if more permeable membranes (NF90) with thin support layers can be developed, or if the burst pressure can be raised to 70 bar. The major advantage of higher operating pressures is the reduction in capital cost while increasing the system recovery. The more permeable NF90 membrane allows for even higher recoveries, but at the expense of a higher capital cost incurred by more OARO and RO pressure vessels. As shown in Table 4, the NF90 membrane is more permeable than the TFC-FO membrane, but also less selective. The higher membrane permeability and lower selectivity increase the OARO draw solution volume and its salinity, respectively. This increases the overall volume flowrates in the OARO integrated processes, and thus more pressure vessels are required.

Table 4: Prospective improvements in OARO membrane and module development for SF-1 with $S_{OA} = 3$ and $C_F = 35$ g/L: for each membrane, the effect of increasing the burst pressure to 70 bar is shown.

Membrane	$P_{OA}\,[bar]$	$Y_S\,[\%]$	$SEC\,[kWh/m_P^3]$	$C_P\,[g/L]$	N_{UF}	N_{OA}	N_{RO}
TFC-FO	48.3	72.2	4.00	0.235	58	249	156
TFC-FO	70.0	77.4	4.25	0.226	54	210	152
NF90	48.3	73.5	4.13	0.247	57	254	162
NF90	70.0	78.8	4.47	0.242	53	214	159

Davenport et al. [19] mentions that the development of new permeate spacers is important for the further development of high pressure reverse osmosis. This development would also benefit the OARO process, as both permeate spacers should have the same characteristics. Both spacers should minimise membrane deformation into spacer voids, while not increasing the frictional pressure losses.

3.7. Chapter conclusions

In this chapter, six OARO integrated flow processes are presented. These are compared according to their technical and economic feasibility, at 72% and 44% freshwater recoveries from water sources with respective salinities of 35 g/L and 70 g/L. Prior to modelling the entire process, the stand-alone OARO process was investigated, and the optimal OARO process parameters were determined. The influence of each OARO parameter can be summarised as follows:

Membrane properties:

Higher recoveries at lower energy consumption are achieved for more permeable membranes, but the consequently higher draw dilution is less significant.

Feed flowrate:

A moderate flowrate balances the capital cost and increased fouling/scaling propensity against higher energy costs and lower recoveries.

Flowrate ratio:

Lower RR values are more practical to prevent excessive pressure losses in the draw channel.

Feed pressure:

An increase in P_OA is beneficial, as the energy consumption is relatively constant while a higher draw dilution and recovery is achieved. However, P_OA is limited by the membrane burst pressure.

Of the six OARO integrated flow processes, SF-1 shows the best performance at lower feed concentrations. It is the only technically feasible process to achieve the desired process recovery with a maximum of three OARO stages. SF-1 also has the second lowest energy

consumption and capital expenditure after C-1, which is however the least feasible OARO integrated flow process. Furthermore, the permeate salinity for SF-1 is of acceptable quality according to the WHO drinking water guidelines. At the higher inlet salinity, C-2 shows the greatest promise, as it achieves a reasonable permeate quality while achieving the desired recovery at feasible OARO feed pressures.

OARO integrated processes are economically viable alternatives to current brine dewatering techniques, as they offer the possibility to achieve high system recoveries at comparatively lower energy costs and operating pressures. Pressure driven membrane processes are already proven to be significantly more energy efficient than their thermal counterparts. Furthermore, the lower specific energy consumption of OARO in comparison to other osmotically (chemically) driven membrane processes, such as FO, make it an economically viable process addition for brine volume minimisation. In comparison to MSRO, OARO is a technically feasible process to achieve the desired brine concentration. High pressure RO, MSRO, FO/PAO and OARO are not mutually exclusive processes and can be combined to eventually achieve brine concentrations of up to 250 g/L in a more cost efficient and sustainable manner to compete with or replace thermal processes.

Chapter 4

Achieving zero-liquid discharge with OARO and thermo-responsive draw solutes

In this chapter, the standard OARO process, which utilises a non-responsive draw solute (i.e., NaCl), is expanded to incorporate thermo-responsive draw solutes in order to investigate whether this novel combination can outperform 1) a forward osmosis process utilising the same draw solution, 2) the standard OARO process using non-responsive draw solutes, and 3) the LSRRO process.

Although both FO and OARO are promising BVM technologies, there is currently no literature available on a direct comparison (experimental or numerical) of these two technologies. Thus, the first research objective addressed in this chapter is to investigate whether OARO or FO is the preferable BVM technology. To address this question, a direct parametric and techno-economic comparison is performed. A single test case is chosen here that is based on the membrane brine concentrator (MBC), which forms part of the world's first-ever commercial FO ZLD process [147]. In the chosen test case, the MBC forms part of a ZLD process that is used to treat a combined saline waste stream, including the flue gas desulfurization blowdown wastewater and cooling tower blowdown. Both waste streams originate from an ultra-supercritical coal fired power plant at the Changxing Power Plant in Zhejiang Province, China. To meet water intake and discharge limits, a full ZLD system is designed with recycle of the recovered freshwater to the boiler feed [147]. This test scenario is chosen, due to its industrial applicability and due to the possibility of directly comparing the FO and OARO processes

while using the same feed conditions, the same draw solution (to exclude any variability caused by the choice of the draw solution (DS) on the results), the same process layout and the same target brine concentration. Therefore, the feed hydraulic pressure is the only variable for which its inclusion in OARO can alleviate several of the FO shortcomings. Following this detailed comparison, both the FO and OARO MBC are compared with the LSRRO and the standard OARO process to draw attention to the advantages and possibilities arising when combining OARO with responsive draw solutions. Details of the LSRRO process are provided in Section 1.2.

4.1. ZLD process layout

Figure 18 depicts the entire ZLD system including the membrane brine concentrator. The FO and OARO MBC and the two-pass RO unit are numerically modelled to determine which technology is the superior brine volume minimisation solution. The pre-treatment and brine crystalliser steps are excluded from the comparison. The entire ZLD process comprises of [147]:

Pre-treatment processes:

The waste stream is expected to have a total dissolved solid (TDS) content ranging between 25 g/L and 45 g/L. Due to this variability of the wastewater quality and the high concentration factor of the ZLD system, several pre-treatment processes are required to ensure an uninterrupted operation of the ZLD system. Scaling in the ZLD system is prevented by firstly softening the wastewater stream using chemical precipitation. This treatment step is followed by a multimedia filtration step and a weak acid cation exchange softening process.

Two-pass RO unit:

The two-pass RO unit has two purposes, namely to pre-concentrate the softened feed stream for the MBC system and to polish the permeate to the product water (i.e., in this case boiler make-up water) specification of TDS ≤ 100 mg/L. Concentrating the MBC feed stream reduces its size and takes advantage of the low energy demand of RO in the lower TDS range.

Membrane brine concentrator:

The concentrate from the first RO pass is directed to the counter-flow FO (or OARO) membrane module. The high-pressure pumps and energy recovery devices that are indicated in Figure 18 are only utilised when the MBC is operated in the OARO configuration. However, both the FO and OARO MBC achieve the desired brine

concentration using three stages and employing a thermo-responsive DS comprising of an ammonia and carbon dioxide mixture [147]. The diluted draw solution (DDS) exiting the first stage S_1 of the membrane module is sent to the draw recovery distillation column (DC2) where the draw solutes are volatilised as NH_3 and CO_2 gas. The gases are condensed and mixed with a fraction of the DDS stream to give the CDS to be reused in the membrane process. The intermediate product water from DC2 is mixed with the softened feed stream and the concentrate from the secondary RO pass. This mixed stream is then directed to the RO system for polishing.

Reverse diffusion of the draw solutes into the FO/OARO feed stream will result in the loss of the draw solute if it is not recaptured. This is prevented by recovering the draw solutes in the concentrated brine stream using another distillation column, termed the brine stripper (DC1). The vapor stream from DC1 is sent to DC2 to be further concentrated while the heated brine stream exiting DC1 is pumped to the brine crystalliser at a TDS of 220 g/L. By utilising two distillation columns, the energy consumption of the MBC system increases, but it means that more than 99.75% of the DS is retained in the system, which minimises its replenishment costs [148].

In the FO MBC process, the concentrated draw solution (CDS) has a composition ranging between 4-6 M on a carbon basis. The DS is thermally regenerated using plant steam (5 bar, saturated) as the energy source.

Brine crystalliser:

The brine crystalliser is the most energy intensive process and removes the remaining liquid to crystallise the slurry. The distillate is recovered and mixed with the RO permeate and used as boiler make-up water.

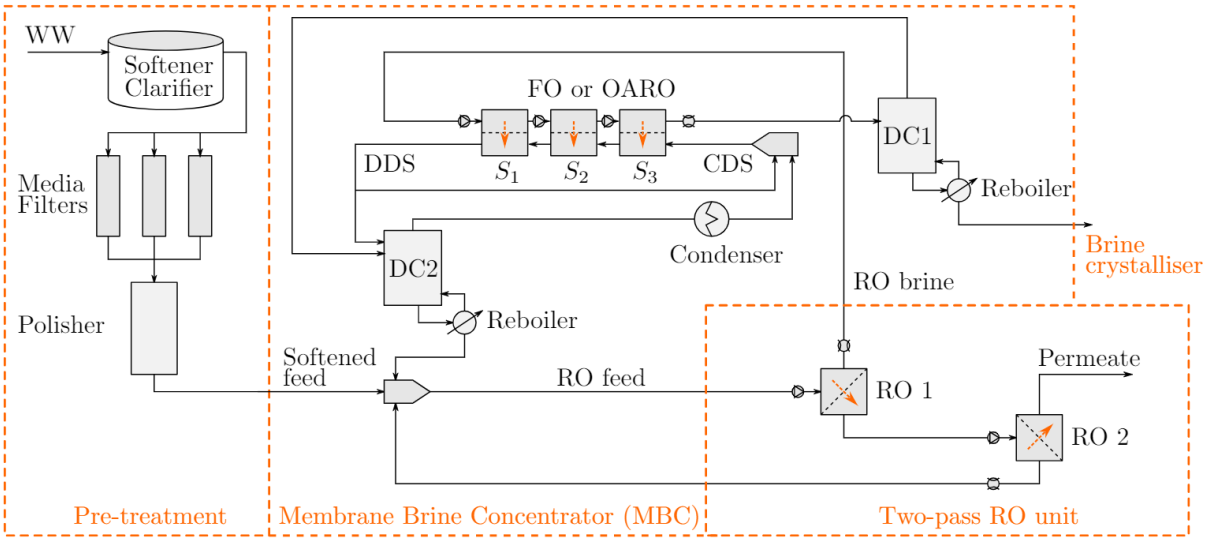


Figure 18: The FO zero-liquid discharge process installed at the Changxing coal-fired power plant, China.

Adapted from Pendergast et al.[147].

4.2. Simulation set-up

As stated in the previous section, only the FO/OARO MBC and the two-pass RO system are numerically modelled. The design specifications and modelling assumptions are summarised in this section.

Firstly, it is assumed that the only solutes present in the system are NaCl and the thermo-responsive draw solute due to the extensive pre-treatment. Thus, the fouling effect on the membrane and thermal process efficiency is not modelled. Additionally, the maximum draw solute concentration in the MBC system is limited to a value below its saturation point to prevent issues associated with precipitation.

Secondly, an iterative approach is chosen to determine the steady state operation of the modelled process. The membrane-based processes are simulated in Matlab using the same model that was previously used in Chapter 3. Meanwhile, the DSR process with the two distillation columns is simulated with the help of ASPEN Plus. The function 'actxserver' is utilised in Matlab to communicate back and forth with ASPEN Plus. This direct link between Matlab and ASPEN Plus is a novel approach, as previously Excel had to be incorporated as an intermediate communicator, which significantly increased the simulation time [149,150]. The algorithm is depicted in Figure 19, and works as follows:

Step 0: Due to the intertwined process layout, the FO/OARO feed and draw stream, as well as the RO2 concentrate stream, must be assumed in the first iteration, as they are unknown and are required to solve the steady state simulation.

Step 1: As the starting point of each iteration, the 3-stage counter-current FO/OARO membrane model is solved. Each stage contains several pressure vessels in parallel so that the feed flowrate per vessel is given by Q_{MBC}. The numerical findings presented by Xiao et al. [74] show that a counter-current flow arrangement has several advantages over a co-current flow

arrangement, such as a more uniformly distributed water flux along the FO/OARO module. Therefore, in this work, all FO/OARO membrane modules are operated in a counter-current flow arrangement. The water flux and solute flux governing equations are solved explicitly on a finite set of iteration segments along the membrane module. The concentration of the draw solution and the mass flowrate at the module outlet are obtained with the shooting method [74]. More information regarding the FO/OARO membrane system is given in Section 4.2.2.

Step 2: The newly determined DDS, CDS and FO/OARO brine stream information are communicated from Matlab to ASPEN Plus to solve the DSR system. The draw solution and the DSR set-up remain unchanged for all simulations and are described in more detail in Section 4.2.1. and Section 4.2.3., respectively.

Step 3: With the MBC modelled using steps 1 and 2, the next step is to model the two-pass RO unit. The softened feed is firstly mixed with the RO 2 concentrate and the intermediate product water from the MBC system. The two-pass RO unit is solved using the same solution procedure and governing equations as stated in Step 1. More information regarding the RO system is given in Section 4.2.2.

Step 4: In each iteration, the only variable adjusted to achieve the desired brine concentration of 220 g/L (3.76 M) NaCl is the CDS concentration. Thus, a new estimate of the required CDS concentration is interpolated using the concentration of the brine stream exiting DC1 and the current estimate of the CDS concentration. The new estimate of the required CDS concentration is then achieved by adjusting the recirculation rate of the DDS stream based on the concentration and volume of the condensed vapour stream from DC2.

Step 5: Steady state operation is reached once all flow streams converge and the overall mass conservation error is below 0.1% of the inlet salt and water flowrate. Additionally, a test is made of whether the desired brine concentration is reached using the given input parameters

and the new interpolated CDS concentration. The iterative process is repeated at Step 1 until convergence is achieved.

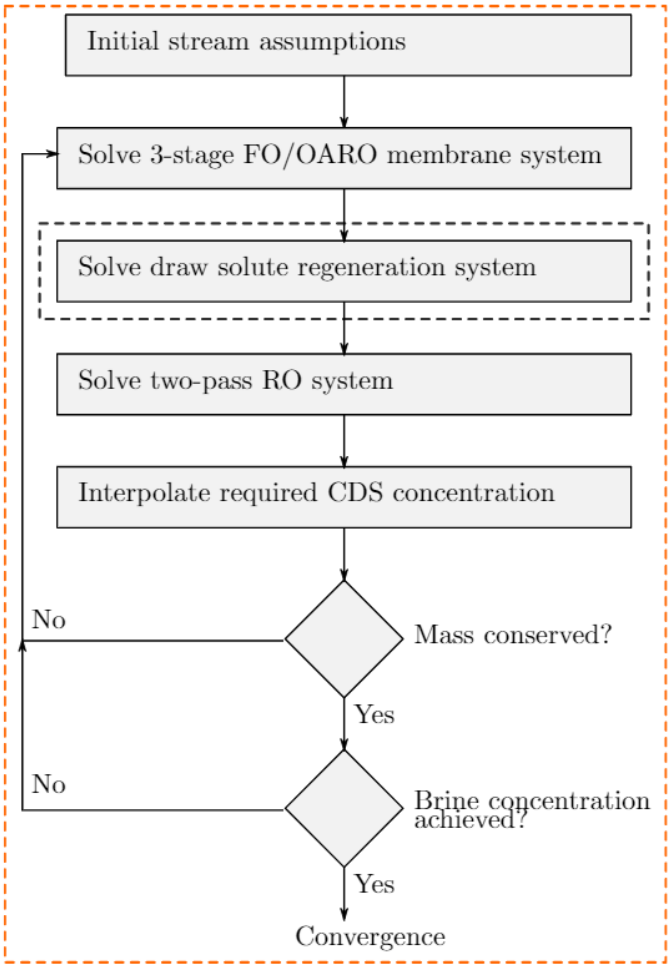


Figure 19: The simulation algorithm of the FO/OARO MBC and the two-pass RO system. The orange box indicates the commands run in Matlab whereas the grey box indicates the command run in ASPEN Plus. Communication and sharing of stream data between the two programs is initiated using the 'actxserver' function in Matlab.

4.2.1. The draw solution

While theoretically any draw solution can be employed in FO and OARO operation, the $NH_3 - CO_2$ thermo-responsive DS is chosen and evaluated here, according to the following characteristics of an ideal draw solution [151]:

High solubility and low molecular weight:

These properties allow the draw solute to produce a high osmotic pressure. As shown in Figure 20, the achievable osmotic pressure of the $NH_3 - CO_2$ thermo-responsive draw solution mainly depends on the ammonia to carbon dioxide ratio (N/C) and the draw solute concentration (displayed on a carbon basis). As indicated in the figure, higher N/C ratios result in a stronger draw solution, because a higher ammonium content increases the number of charged groups per CO_2 molecule. A highly concentrated DS with a high N/C ratio is required to overcome the osmotic pressure of the final brine stream (indicated by the horizontal red line). It is important to note that the figure indicates the osmotic pressure of the bulk streams. Actually, a significantly higher concentrated DS is required, due to internal and external concentration polarisation (explained in Section 2.1.). Therefore, a high N/C ratio of 2.4 is chosen for the numerical simulations. This N/C ratio was also chosen by Zeng et al. [152].

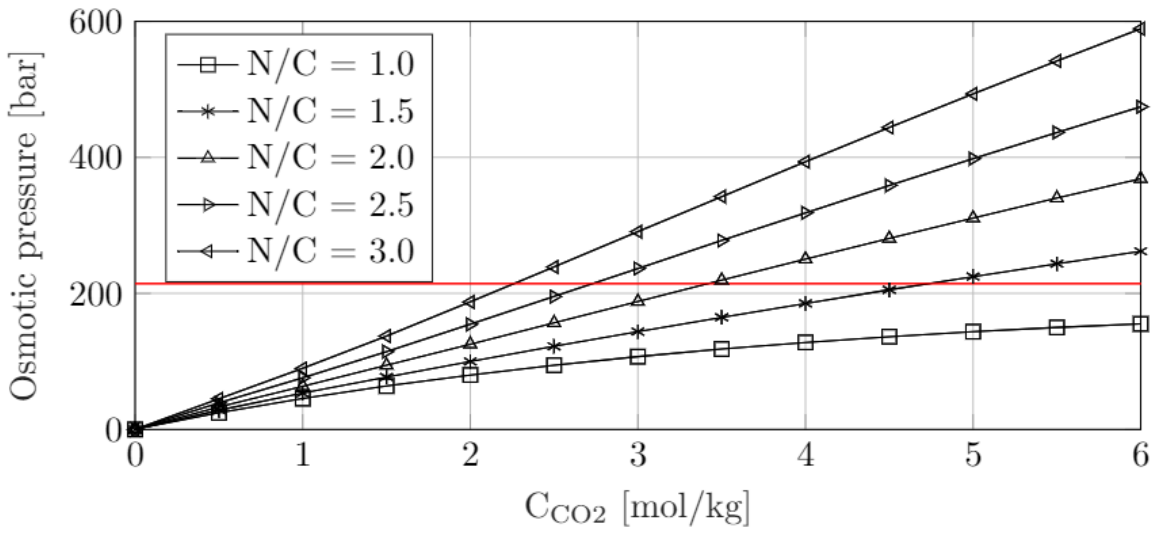


Figure 20: The osmotic pressure of the $NH_3 - CO_2$ thermo-responsive DS for various ammonia and carbon dioxide ratios (N/C) and draw solute concentrations on a carbon basis. The horizontal red line indicates the osmotic pressure of the final NaCl brine stream with a concentration of 220 g/L. The osmotic pressures are determined using ASPEN Plus with the DSR set-up given in Section 4.2.3.

Low viscosity:

A lower viscosity of the DS reduces the internal concentration polarisation, which seriously hinders the water flux, and its pumping costs. ICP occurs in the porous support layer of the asymmetric TFC membrane and is more severe for viscous substances. ICP cannot be eliminated by enhancing turbulence or increasing the cross-flow velocity [153]. In terms of the $NH_3 - CO_2$ draw solution, no issues regarding its viscosity have been mentioned in pilot and industrial scale testing [147,154]. Furthermore, the $NH_3 - CO_2$ draw solutes are fast diffusing, which is further ideal to minimise ICP [154].

Low reverse solute flux:

Due to the composition of the draw solution, ammonia and carbon dioxide do not fully disassociate and their uncharged species are not effectively rejected by the membrane, causing a high reverse solute flux. As stated by McGinnis et al. [154] and by Hancock &

Cath [155], the reverse solute flux of the $NH_3 - CO_2$ thermo-responsive draw solutes is nearly an order of magnitude higher through asymmetric CTA membranes and three times higher through TFC-FO membranes in comparison to sodium chloride. This high reverse solute flux is problematic and is counteracted by including a secondary brine stripper (DC1) in the MBC system to maximise draw solute regeneration.

Ease of regeneration:

The draw solute should be easily separable from the freshwater in the regeneration step. Increasing the draw concentration inevitably increases the required energy of regeneration and hence desalination. However, the vapour pressure of the thermo-responsive DS considerably exceeds that of water, which is desirable as the draw solute can be easily vaporised in a distillation process operating at relatively low temperatures [156]. Although the draw solute decomposes at low temperatures (60°C at 1 atm [157]), the distillation column still has to be operated at significantly higher temperatures to completely remove any ammonia trace (<1 ppm) from the brine and product stream [134].

Economical:

An inexpensive draw solute is preferred to minimize initial purchase and replenishment costs. As ammonia and carbon dioxide are abundant, the draw solute is relatively cheap. For example, NH_4HCO_3 one of the thermolytic salts present in the draw solution is relatively cheap compared to other specialised draw solutes and only costs approximately $8.75/kg [47].

Reusable:

The draw solute should not lose its ability to generate its initial osmotic pressure after its regeneration. Otherwise, it must be purged and replaced at an additional cost. Liquid-gas separation requires complex distillation and re-condensation equipment to

regenerate the draw solute [158]. The thermolytic salt is not thermally stable (i.e. volatile) and thus complicates the gas containment in the system [159].

Non-toxic:

Toxic solutes in the brine stream or in the final freshwater product can have detrimental effects. Ammonia is toxic above a certain threshold, hence the final water quality needs to present less than 1 ppm of ammonia (including related species such as ammonium and carbamate) in the permeate and brine stream to adhere to the limits specified in the Guidelines for Drinking Water Quality (WHO) [134,160].

Compatibility with the FO membrane:

It is important to choose a draw solute that does not degrade the chosen membranes and the other equipment employed [161]. For the chosen N/C ratio of 2.4, the pH ranges between 9 and 9.5 at high concentrations. Under such basic conditions, TFC membranes are required as the basic draw solution can initiate the hydrolysation and degradation of cellulose acetate forward osmosis membranes. Additionally, ammonia back diffusion can serve as a nutrient source and thus can promote increased biofouling on the feed side of the membrane [102].

4.2.2. The membrane processes

The same SW30HRLE membrane is used for the RO process in the numerical analysis of Chapter 3 and Chapter 4. However, a slightly different TFC-FO membrane is used in this Chapter, as it was used in previous work for a similar draw solution (trimethylamine–carbon dioxide thermolytic draw solution [162]). The A, B and S values of the utilised RO and FO/OARO membranes are given in Table 5.

Table 5: Membrane properties of the simulated RO and FO/OARO membranes

Name	A [LMH/bar]	B [LMH]	S [mm]
SW30-HRLE [a]	1.13	0.08 (NaCl) 0.12 (DS) [b]	12.5
HTI-TFC [c]	3.16	0.55 (NaCl) 1.21 (DS) [d]	0.553

[a] DOW [133]
[b] Assumed from Zhou et al. [134]
[c] Boo et al. [162]
[d] Zhou et al. [134]

In the two-pass RO system, RO 1 and RO 2 are operated at 80 bar and 40 bar, respectively. Furthermore, the feed flowrate for each RO pressure vessel is kept constant at 12 m^3/h. Each RO pressure vessel is chosen to have a common number of 7 membrane modules, with each having a membrane area of 37 m^2 [133].

As shown in Chapter 3, OARO can achieve the same recovery as MSRO and HPRO, but at operating pressures below the membrane burst pressure, ensuring it is technically feasible. In addition, OARO offers a better permeate quality than the MSRO process. Low hydraulic operating pressures in OARO are possible, as a draw solution is utilised to lower the osmotic pressure difference ($\pi_D < \pi_F$) across the membrane [62].

In the MBC system, the FO/OARO membrane section consists of 3 stages [147] with each pressure vessel containing 7 membrane modules. In comparison to Chapter 3, a more conservative estimate of the FO/OARO active membrane area per membrane module is made and estimated at 15 m^2 [145]. As mentioned in Section 4.2., the feed flowrate per pressure vessel Q_{MBC}, the operating pressure P_{MBC} and the flowrate ratio RR are varied to determine the optimal FO and OARO MBC operation. Kim & Park [163] tested a single 4040 spiral-wound FO

membrane module with a maximum feed flowrate of $1.08\ m^3/h$. Thus, the upper limit of Q_{MBC} for each pressure vessel containing 7 membrane modules is set at $7\ m^3/h$.

As was done in Chapter 3, the tested P_{MBC} range is limited to 1-48.3 bar, as a minimum transmembrane pressure of 1 bar is required in FO to overcome the feed channel pressure losses [163]. According to Straub et al. [131], the maximum achievable membrane burst pressure for a commercially available thin-film composite (TFC) FO membrane is 48.3 bar, which is chosen here as the upper limit of the membrane burst pressure of FO membranes. The RR range is chosen more arbitrarily and is varied between 0.23 and 0.41. As argued in Chapter 3, the RR value is below 0.5 in practice, as the draw spacer in the membrane module must be denser than the feed spacer to prevent membrane deformation under hydraulic feed pressures.

4.2.3. The draw solute regeneration (DSR) system

In this study, the chosen thermolytic draw solution is regenerated using distillation as is done in the commercially operating MBC unit at the Changxing coal-fired power plant. However, there are numerous other responsive draw solutes that require other forms of regeneration, which may be potentially more energy efficient, less costly, or achievable at lower temperatures [49,164–166]. The inclusion of these responsive draw solutes into the FO and OARO MBC is promising but beyond the scope of this thesis.

Both the FO and OARO MBC are operated with the equivalent heat integrated DSR system, which is depicted in Figure 21. Thus, the ASPEN set-up described here remains unchanged, and applies for all the FO and OARO MBC simulations.

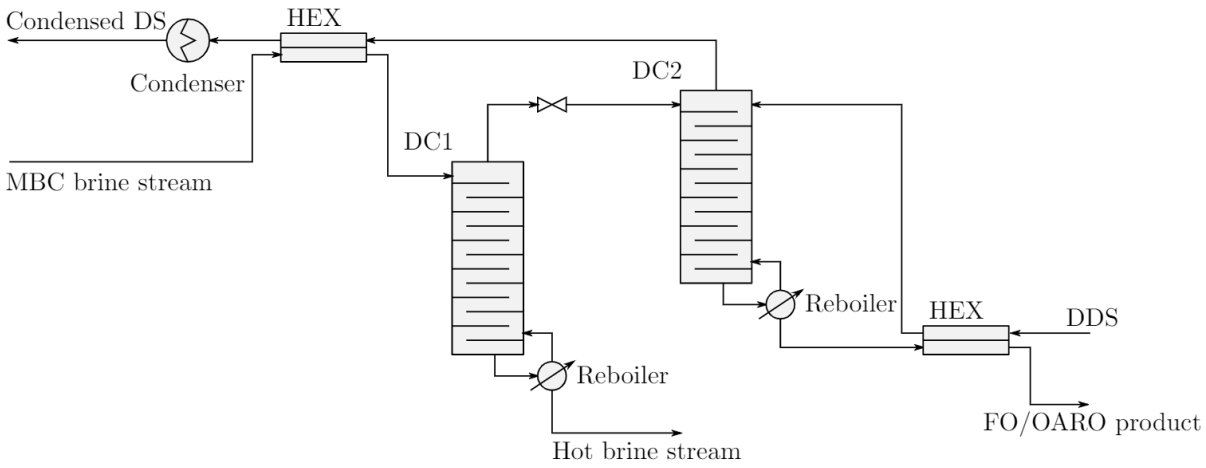


Figure 21: The draw solute regeneration system with heat integration. Adapted from Pendergast et al. [147].

As mentioned in Section 4.2.1., two distillation columns are required to completely recover the volatile draw solutes so that less than 1 ppm of ammonia (including related species such as ammonium and carbamate) remains in the intermediate product and brine stream. DC1 is used to recover the draw solutes that diffused into the MBC brine stream during the FO or OARO process. The draw solute is recovered from the brine stream as vapour, which is passed to DC2 to further concentrate it. DC2 is used to concentrate the draw solution by separating it from the freshwater (FO/OARO product). The volatile draw solutes exiting DC2 are condensed so that the concentrated DS can be reused in the FO/OARO membrane process.

The set-up of the distillation columns in ASPEN Plus is similar to that presented by Zhou et al. [134]. An instantaneous chemical equilibrium-stage model is used with the ENRTL-RK thermodynamic method to simulate the following complex reversible reactions occurring in the distillation process [167]:

$$2H_2O \leftrightarrow H_3O^+ + OH^- \quad (28)$$

$$CO_2 + OH^- \leftrightarrow HCO_3^- \quad (29)$$

$$HCO_3^- + H_2O \leftrightarrow CO_3^{2-} + H_3O^+ \quad (30)$$

$$NH_3 + H_2O \leftrightarrow NH_4^+ + OH^- \quad (31)$$

$$2NH_3 + CO_2 \leftrightarrow NH_2COO^- + NH_4^+ \quad (32)$$

$$NH_4HCO_{3\,(s)} \leftrightarrow NH_4^+ + HCO_3^- \quad (33)$$

The last equation is not included in the simulation, as the maximum concentration of the draw solution is kept below its solubility limit. Furthermore, Equation (29) and (32) are the rate-determining reactions but are here assumed to be instantaneous and thus at equilibrium. As shown by Zhou et al. [134], model inaccuracies arising from neglecting reaction kinetics occur chiefly at low sub-atmospheric pressures. Low sub-atmospheric operating pressures are, however, not considered, as an additional compressor will be required under such conditions to achieve complete condensation of the draw solution. This increases the capital cost and the electrical energy consumption.

Pendergast et al. [147] considers that the distillation columns are operated at atmospheric pressure (i.e., 1 atm) and driven by 5 bar saturated steam. However, running the distillation columns at pressures closer to the saturation vapour pressure of the draw solution allows for the use of lower temperature heat sources. Therefore, the possibility exists to integrate low-grade waste heat as an energy source for the DSR system, which is discussed in greater detail in Section 4.5.2.

As shown by Petchers [168], typical steam condensing temperatures range from 40-60°C, depending on the type of condenser utilised. Here, it is assumed that a water-cooled condenser can achieve a constant condensation temperature of 40°C. It is further assumed that the DC1 and DC2 column pressure vary according to the associated condenser pressure. Due to pressure losses in the system, DC1 and DC2 operate at column pressures that are 0.05 bar and 0.025 bar above the achievable condenser pressures, respectively.

Each distillation column contains Amistco (Goodloe equivalent) structured packing with a height of approximately 2.53m (equivalent to 25 theoretical stages) [134]. The pressure drop across the packing is kept constant and estimated at 0.04 bar.

As shown, heat exchange (HEX) occurs between the DC2 vapor stream and the brine stream entering at the top of DC1. This is advantageous, as the DC2 vapor stream is cooled prior to complete condensation of the draw solution, which lowers the required amount of cooling water, and the brine stream is pre-heated to lower the required reboiler duty of DC1. Additionally, the DDS stream entering at the top of DC2 is firstly heated by cooling the intermediate FO/OARO product water, which lowers the DC2 reboiler duty. From DSR simulations, it is found that the DC2 reboiler duty can be further minimised by feeding the DC1 vapour stream into the fifth stage of DC2.

The minimum approach temperature and the heat transfer coefficient in both HEX units is set to 2.5°C and $850\ \mathrm{W/m^2K}$, respectively [169]. The same heat transfer coefficient is used for the condenser, whereas the reboiler heat transfer coefficient is set at $570\ \mathrm{W/m^2K}$. This is due to the fact that reboilers tend to foul faster because of the higher operating temperature and because non-volatile pollutants with higher fouling potential in the feed drop to the bottom of the column [170]. Note that heat is not extracted from the hot brine stream exiting DC1, as operational issues can arise from cooling a highly concentrated waste stream. Also, energy is saved in the brine crystalliser if the feed remains warm [147].

4.3. Analysis of the DSR distillation columns

In this section, a parametric analysis of a single distillation column with heat integration is performed. Figure 22 (a) and (b) depict the reboiler temperature and heat duty per kilogram of feed. The draw solute concentration and the N/C ratio of the column feed solution are kept constant, at 1 mol/kg on a carbon basis and 2.4, respectively. The achieved temperature profile in Figure 22 (a) at 0 mol/kg NaCl is equivalent to that obtained in Zhou et al. [134], which validates the set-up of the ASPEN simulation.

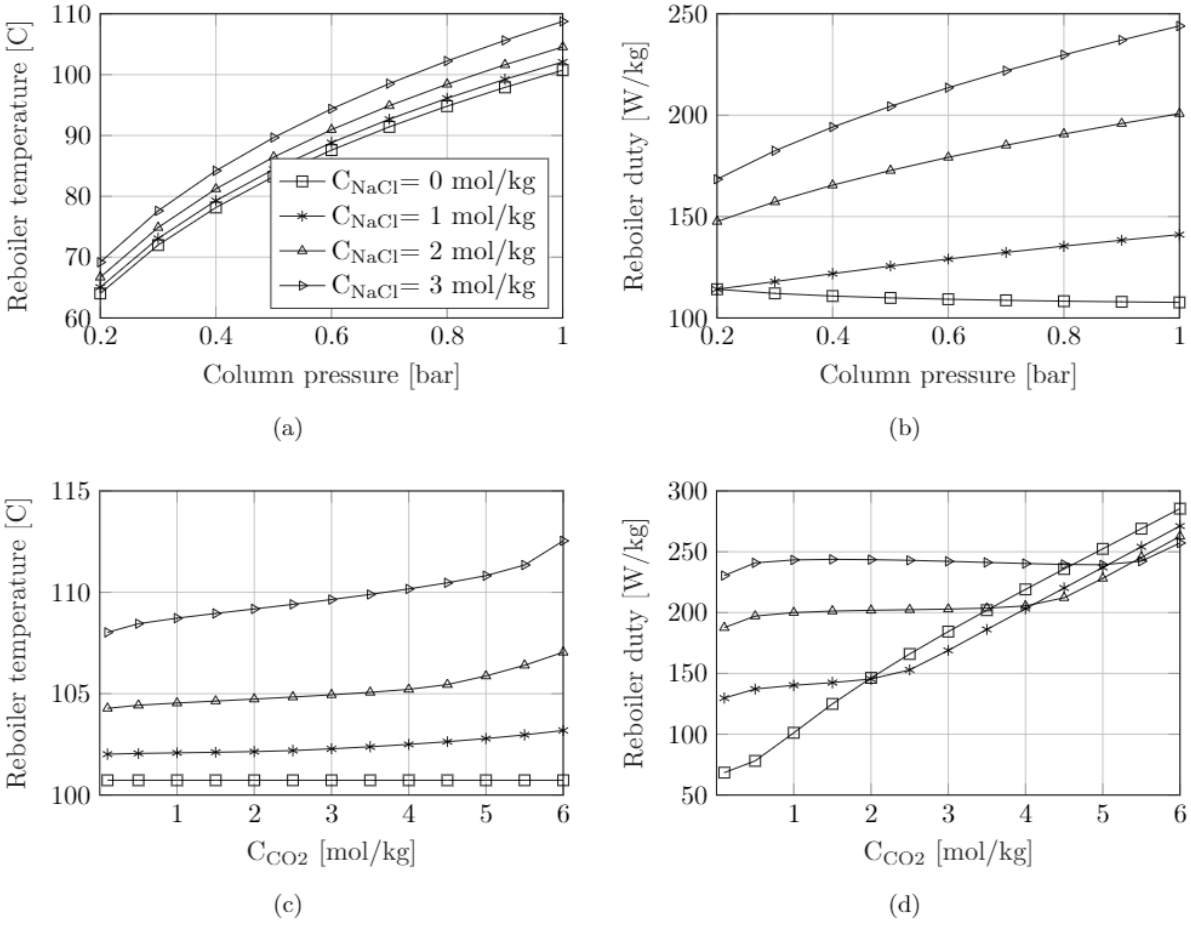


Figure 22: Parametric analysis of a single distillation column for various NaCl feed concentrations. Figures (a) and (b) depict the effect of the column operating pressure on the reboiler temperature and its heat duty per kilogram of feed solution containing a 1 mol/kg thermo-responsive draw solution on a carbon basis and a N/C ratio of 2.4. Figures (c) and (d) depict the effect of the draw solute on the reboiler temperature and its heat duty per kilogram of feed at a constant column pressure of 1 bar. The N/C ratio of the feed solution is also kept constant at 2.4.

Solute diffusion across the FO/OARO membranes results in the cross contamination of the membrane draw and feed streams. Thus, traces of the DS are present in the brine stream and NaCl in the diluted draw solution. Higher NaCl concentrations in the column feed stream thus reduce the chemical potential of the volatile draw solutes. Hence, the temperature and the energy input of the reboiler must be raised to achieve the same target water purity of 1 ppm NH_3, as shown in Figure 22 (a) and (b). Therefore, a high NaCl concentration in the brine stream implies that operation of the brine stripper (DC1) is more energy intensive than that of DC2 per kilogram of feed. Traces of NaCl are, however, also present in the diluted draw solution, as solute diffusion across the FO/OARO membranes results in the cross contamination of the membrane draw and feed streams. Therefore, the reboiler temperature and heat duty of DC2 are also affected by NaCl present in the DDS stream.

Lower column pressures result in a lower reboiler temperature, which is beneficial for the utilisation of cheaper heat sources in the draw solute regeneration step. However, the minimum achievable column pressure without vapour compression is limited by the saturation pressure of the concentrated draw solution. As shown in Figure 22 (b), the reboiler duty also reduces with the column pressure when NaCl is present in the feed solution. This is owing to the fact that less water needs to be evaporated at lower column pressures to achieve the same residual ammonia concentration in the product.

Figure 22 (c) and (d) depict the effect of the draw solute and NaCl concentration on the reboiler temperature and its heat duty per kilogram of feed at a constant column pressure of 1 bar. Figure 22 (c) shows that the reboiler temperature is relatively independent of the draw solute concentration at a constant column pressure. Thus, operation at a constant column pressure is not advised; it is suggested instead to operate at a constant condenser temperature. At lower draw solute concentrations, less ammonia and carbon dioxide are present in the vapour stream, which significantly reduces the saturation pressure of the vapour stream. Therefore, the column

pressure and hence the reboiler temperature can be minimised at a constant condenser temperature.

The findings depicted in Figure 22 (d) indicate that the reboiler duty is less affected by the draw solute concentration at higher NaCl concentrations. This means that the energy cost of DC1, which has a highly concentrated NaCl feed, is not significantly reduced if lower reverse draw solute fluxes are achieved in the FO/OARO membrane section. However, the energy consumption of DC2, which is fed by the low salinity DDS stream, is more affected by lower draw solute concentrations.

Reasonable conclusions on the operation of DC1 and DC2 can be drawn from this analysis, as the interdependence of DC1 and DC2 is minimal. The operational conditions of DC2 are only slightly affected by those of DC1, because the vapour passed from DC1 to DC2 is less voluminous than the DDS stream entering DC2. For that reason, it is less pivotal.

4.4. Parametric optimisation of the FO and OARO integrated ZLD flow processes

In this section, a parametric analysis of the FO and OARO integrated ZLD processes is performed to ensure that the conclusions drawn apply to a wide range of operational conditions. Nevertheless, global optimal performance cannot be guaranteed by this model, as the process configurations, and thus the cost and performance data, are here subject to the unique case specifications and the process parameters that are established by the current modelling work. However, this comparison still offers valuable insights into whether OARO operation can in fact be more energy efficient than FO. The base case parameters are set as N/C = 2.4, $Q_{MBC} = 5 m^3/h$, RR = 0.33 and the inlet salinity $C_F = 45\ g/L$. Furthermore, the OARO process is operated at a transmembrane pressure of 48.3 bar, which corresponds to the maximum membrane burst pressure. Comparatively, the FO process is only operated at a 1 bar transmembrane pressure.

Figure 23 depicts the equivalent electrical energy consumption W_{Eq} for the two-pass RO unit (black), the DC1 (dark grey), the DC2 (light grey) and the three-stage FO/OARO membrane unit (orange), respectively, under various operational conditions. The calculation details of W_{Eq} and the UWC are given in Appendix C. The results for the FO and OARO integrated ZLD processes are represented in the left-hand and right-hand columns, respectively.

Pendergast et al. [147] state that the actual steam-driven MBC with a two-pass RO system consumes roughly 4 kWh of electrical energy per cubic meter of product water. The thermal and cooling demand is estimated to vary between $20 - 200\ kWh/m^3$. These estimates seem to agree well with the results obtained here for the base case, the FO integrated ZLD process. In the FO base case, the electrical, thermal, and cooling demand are $4.54\ kWh/m^3$, $141.58\ kWh/m^3$ ($W_{Eq} = 9.94\ kWh/m^3$) and $114.58\ kWh/m^3$, respectively. Furthermore, the maximum concentration of the concentrated draw solution is 6.18 mol/kg, which is just

above the range of draw solution concentrations (4-6 mol/kg) mentioned by Pendergast et al. [147].

The W_{Eq} of the FO and OARO base case are $14.5\ kWh/m^3$ and $12.93\ kWh/m^3$, respectively. Under these conditions, the total energy savings amount to 10.83% when using the OARO integrated ZLD process. This is achieved due to a lower thermal energy demand ($109.24\ kWh/m^3$), although the electrical energy demand is slightly higher ($5.24\ kWh/m^3$) due to the high-pressure operation of the OARO MBC. Additional savings are incurred by a lower cooling load ($87.93\ kWh/m^3$), with the maximum concentration of the concentrated draw solution being only 3.75 mol/kg.

In the following subsections, a single operational parameter is altered while the remaining parameters are kept constant:

4.4.1. Effect of N/C ratio

Increasing the N/C ratio of the thermo-responsive draw solution leads to an overall reduction in the energy consumption of the FO integrated ZLD process. The main energy savings are achieved in DC2, because the DDS feed stream is less voluminous and contains lower ammonia concentrations. This is due to the fact that higher N/C ratios enhance the osmotic potential of the draw solution at equivalent ammonia concentrations, as shown in Figure 24. However, the energy consumption of DC1 increases with the N/C ratio, as additional energy is required to strip the more soluble, excess ammonia from the saline brine. Another drawback of larger N/C ratios is that the condenser pressure is raised, which leads to higher DC1 and DC2 reboiler temperatures. Darde et al. [171] have shown that this occurs because the partial pressure of ammonia rises when N/C>2, while the partial pressure of carbon dioxide remains relatively constant. Due to this existing trade-off between reboiler temperature and energy consumption, an intermediate N/C ratio of 2.4 is chosen.

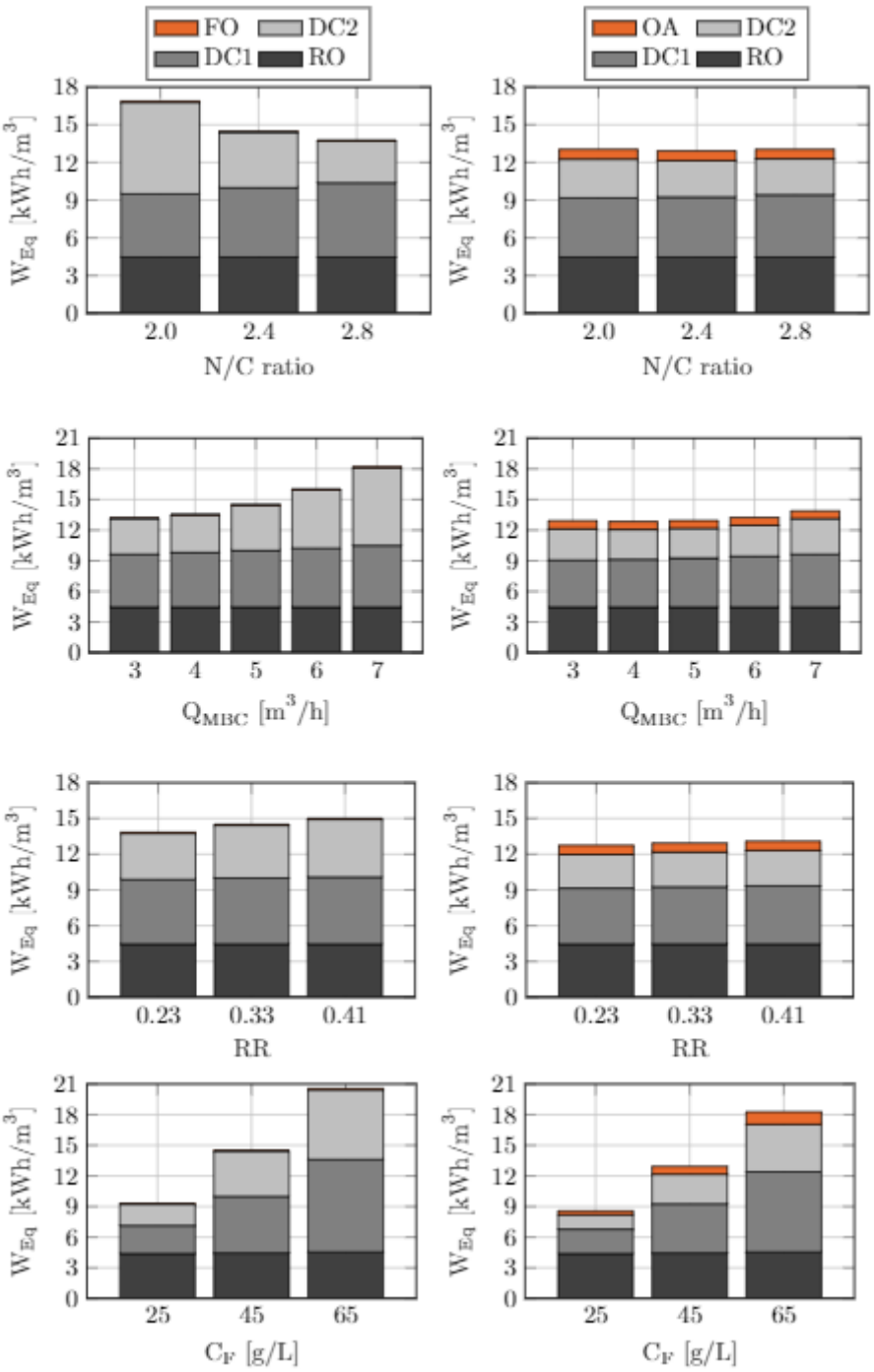


Figure 23: The equivalent work W_{Eq} of the FO (left column) and OARO (right column) integrated ZLD processes with respect to various operational parameters. The standard operational parameters are as follows: N/C is 2.4, Q_{MBC} is 5 m^3/h, RR is 0.33, T_{Cond} is 40°C, feed inlet salinity C_F is 45 g/L and 5 bar saturated steam is used as heat supply to the DSR system. The FO/OARO base case is always given by the central column in each figure.

The required CDS concentration in the OARO base case is approximately 39.3% less than that for its FO counterpart. Because of that, the extent to which the draw solute concentration varies with changes of the N/C ratio is minute, resulting in an insignificant effect on the overall energy consumption of the OARO integrated ZLD process, as seen in the right-hand column of Figure 23.

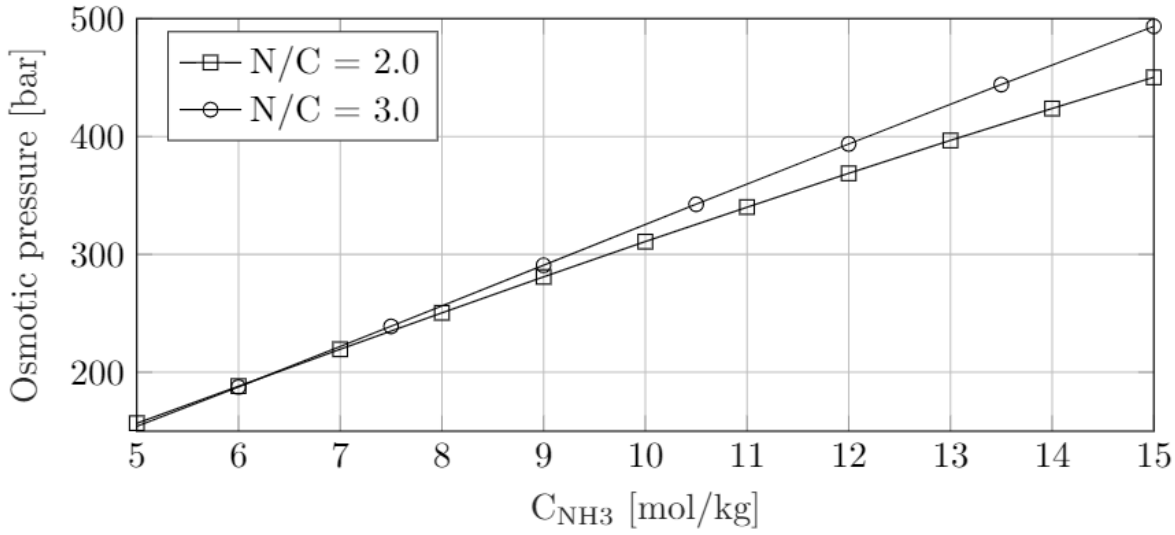


Figure 24: The osmotic pressure of the $NH_3 - CO_2$ thermo-responsive draw solution for two N/C ratios with respect to the ammonia concentration.

4.4.2. Effect of the FO/OARO feed flowrate

For all cases, the recovery of the FO/OARO MBC unit remains approximately constant, as the final target brine concentration is fixed, and the RO brine concentration varies only slightly with operational changes. To achieve the same recovery at higher feed flowrates Q_{MBC} means that the water flux must increase, as less FO/OARO pressure vessels are required in parallel (i.e., the total membrane area decreases) to process the same overall feed rate. To achieve a higher water flux, a stronger driving force is necessary and thus the draw solute concentration has to increase, as the hydraulic feed pressure of each technology remains unchanged. This increase in required draw solute concentration takes its toll on the overall process energy

consumption. The increase in energy consumption is especially evident for DC2. However, high hydraulic pressure in the OARO process tends to limit the required increase in the draw solute concentration with the feed flowrate. Therefore, the energy consumption of the OARO integrated ZLD process is less affected by the change in feed flowrate, while the FO counterpart is significantly affected by it, as seen in the left and right columns of Figure 23.

In terms of fouling, it is difficult to conclude whether a higher feed flowrate is preferred and whether membrane fouling is more likely in OARO or FO operation. Firstly, higher feed flowrates can impede or limit fouling of the membrane surface, as higher cross-flow velocities enhance the shear stress responsible for the detachment of foulants from the membrane surface [172]. Secondly, the water flux is another important indicator of the membrane fouling propensity. According to the critical flux theory, fouling is reversible if the membrane process is operated below the critical flux, but pronounced and irreversible once this flux is exceeded [46,114]. The exact value of the critical flux is unknown for this process, as it depends on several factors including the membrane properties and the feedwater characteristics. Nevertheless, a lower water flux is still preferred to prevent irreversible fouling. Thus, according to the critical flux theory, a lower feed flowrate is beneficial because it leads to lower water fluxes. This then conflicts with the previous statement that higher feed flowrates reduce the fouling rate via turbulence and shear stress enhancement.

The average water flux in the first stage S_1 of the OARO base case is roughly $20.45\ \mathrm{L/(m^2h)}$ and thus greater in comparison to the $17.34\ \mathrm{L/(m^2h)}$ for the FO base case. On the other hand, the average water fluxes in the second (S_2) and third (S_3) stages of the OARO base case (10-5.18 $\mathrm{L/(m^2h)}$) are slightly lower than that for the FO base case (10.44-6 $\mathrm{L/(m^2h)}$). This suggests that irreversible biofouling, organic and/or colloidal fouling, which generally occur in the first membrane modules [132], are more likely for OARO than for FO operation. Nevertheless, irreversible scaling, which is more common in the final membrane modules [132], is more likely

to occur for FO than for OARO operation, due to the higher water fluxes in the last two membrane stages S_2 and S_3.

Figure 25 implies that the brine stream exiting the final stage S_3 of the OARO process is less contaminated by ammonia RSF than that of the FO process. This is because the OARO draw solution is less concentrated than that of the FO process at equivalent recoveries. As stated in Section 4.2.1., ammonia back diffusion can serve as a nutrient source and thus promote increased biofouling on the feed side of the membrane. This suggests that OARO operation with the thermo-responsive draw solution may be less prone to biofouling than FO. Furthermore, the reverse solute flux of the thermo-responsive draw solution lessens with an increase of the feed flowrate, due to the higher water flux against which it must move.

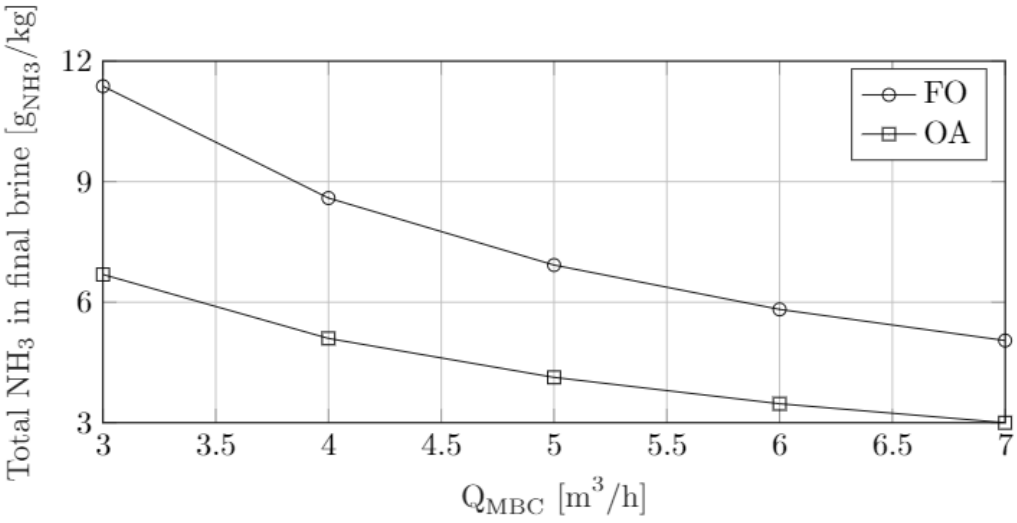


Figure 25: Total ammonia concentration in the brine stream exiting the final FO/OARO stage at various Q_{MBC}.

However, several other studies indicate that FO has a lower fouling propensity than pressure-driven membrane processes, as the fouling layer remains loosely attached to the membrane instead of being compacted onto the membrane surface at high hydraulic pressures [48,173,174]. Nevertheless, opposite to this common claim, the experimental findings presented by Siddiqui et al. [76] show that FO is in fact more prone to alginate fouling than RO and that the hydraulic

operating pressure was not found to play a critical role in foulant layer compaction. Furthermore, Tow et al. [175] state that under the same hydrodynamic conditions, FO has a higher scaling resistance than RO, which is theorised to be due to the difference in the membrane material. But with organic foulants present, both RO and FO experienced a similar flux decline. All of these somewhat contradictory findings make it difficult to conclude which of the two technologies is less prone to fouling. Fouling in OARO processes will be explored further in the next chapter of this thesis.

In terms of the energy consumption, it would be ideal to eliminate the costly brine stripper from the MBC process by minimising the reverse solute flux. This seems more achievable via OARO than FO operation at high Q_{MBC}, as shown in Figure 25. At the maximum feed flowrate, the ammonia concentration in the MBC brine stream will be 40.5% lower for the OARO integrated ZLD process. However, a brine stripper is still required, as 3g/kg of ammonia is still notably higher than the target ammonia concentration of 0.001 g/kg.

The OARO integrated ZLD process at low Q_{MBC} values achieves the desired brine concentration using the lowest draw solute concentration. Operating with a more dilute draw solution also results in a lower saturation pressure of the vapour stream to be condensed. The lower saturation pressure directly translates into lower column operating pressures and hence lower reboiler temperatures. These trends are depicted in Figure 26, and show that OARO is more suited for the integration of low-grade heat sources. At an equivalent feed flowrate, the reboilers in the DSR system of the OARO MBC can be operated at temperatures approximately 12°C lower than their FO counterparts.

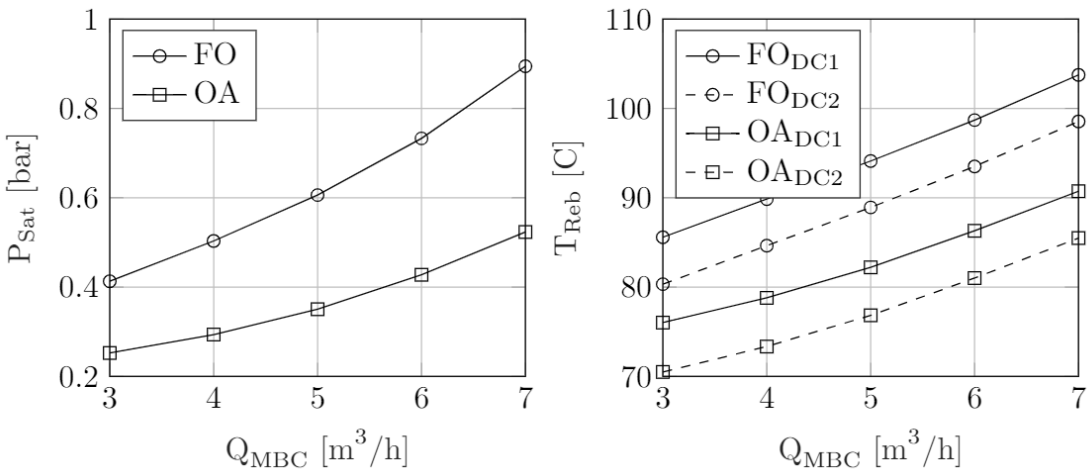


Figure 26: The saturation pressure and the DC1 and DC2 reboiler temperature for the FO and OARO DSR system at various Q_{MBC} and at a constant condenser temperature of 40°C.

4.4.3. Effect of RR

RR is defined as the ratio between the draw and total (feed and draw) flowrate. At lower RR values, the FO/OARO draw stream is less voluminous but more concentrated. In total, the quantity of draw solution to be regenerated is slightly reduced with lower RR values. Hence, DC1 and DC2 consume less energy and can be operated at lower temperatures. However, the energy consumption (see Figure 23) and reboiler temperature of both FO and OARO integrated ZLD processes are relatively insensitive to the RR ratio.

As reasoned in Chapter 3, lower RR values are also more practical. The draw spacer in the OARO draw channel must be denser than the feed spacer to prevent membrane deformation under high feed pressures. That being so, lower draw flowrates reduce the pressure loss in the more constrained draw channel.

4.4.4. Effect of the inlet salinity

All figures in Figure 23 indicate that the energy consumption of the two-pass RO component remains relatively constant, irrespective of any operational changes. This even holds true at

higher inlet salinities, as the recovery of the RO system reduces at higher inlet salinities while the outlet brine concentration remains unchanged. This lower system recovery at higher C_F and the constant inlet flowrate of $100\ m^3/h$ result in higher stream flowrates and salinities in the rest of the ZLD system. Therefore, the total energy contribution of the MBC (DC1, DC2 and FO/OA) increases with C_F.

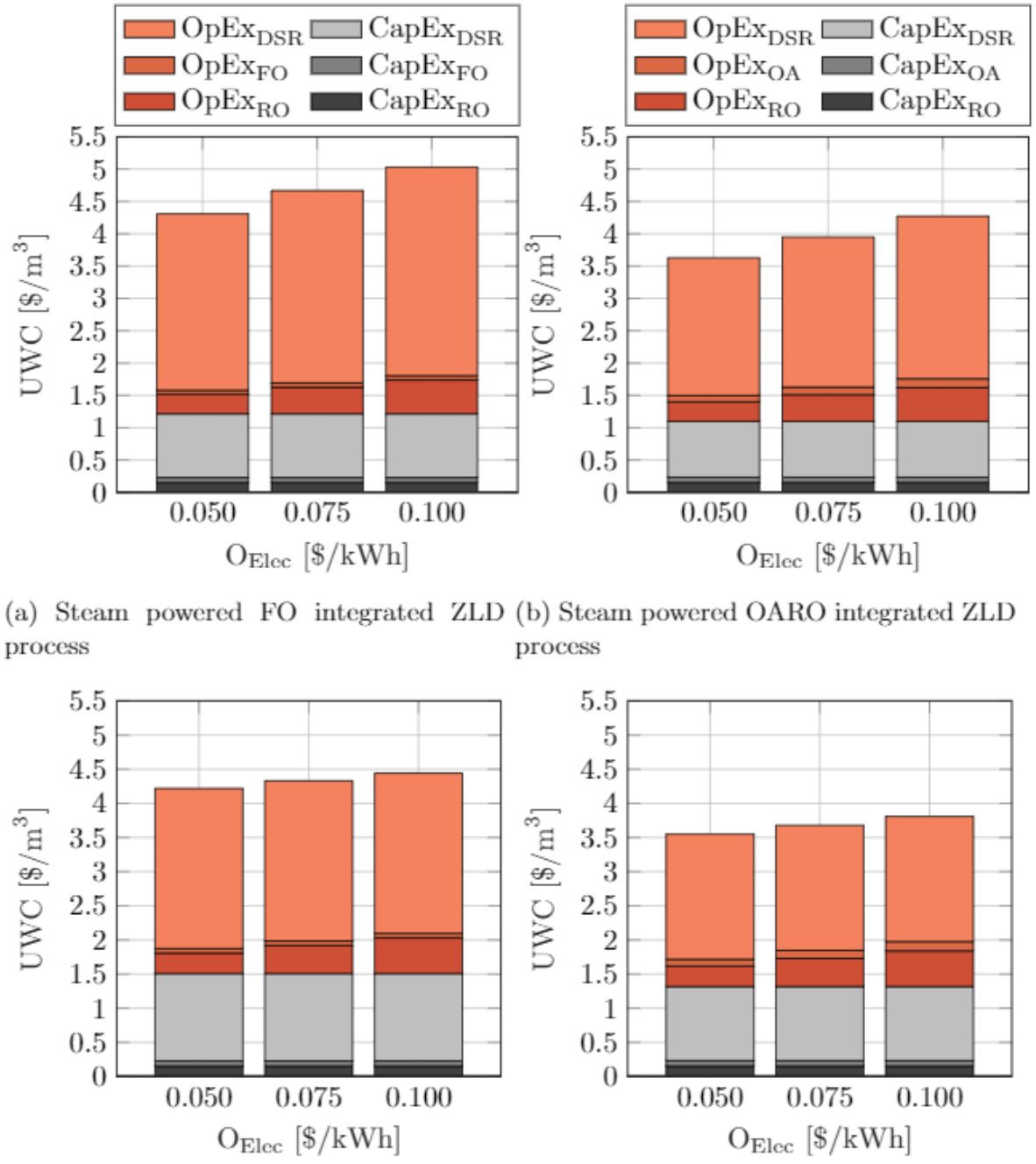
4.5. Techno-economic comparison of the OARO and FO integrated ZLD processes

In this section, a techno-economic comparison of the FO and OARO base cases is performed for a (1) steam and (2) flue gas (i.e., low grade waste heat) powered reboiler. The comparisons are only performed for the base cases, as the operational parameters have already been set to achieve reasonably low reboiler temperatures while simultaneously reducing the energy consumption, the maximum draw solute concentration (to prevent precipitation) and the membrane fouling propensity. The unit water cost is used to determine the economic feasibility of each process.

4.5.1. UWC of the steam-powered FO and OARO base cases

The unit water cost of the steam and flue gas powered FO and OARO base cases is depicted in Figure 27. As shown in the figure, the operational expenses dominate and in total contribute approximately 70-76% towards the overall cost of the steam driven FO and OARO integrated ZLD processes. Thus, the UWC calculation is especially sensitive to fluctuations in the operational financial parameters, which are stated in Table 8 (refer to Appendix C). The UWC is presented for three different electricity costs, as this is in addition to the cooling water cost, the most sensitive variable. If the electricity cost increases from \$0.05 to \$0.1 per kWh, the UWC increases by 16.7% and 17.7% for the steam driven FO and OARO integrated ZLD processes, respectively.

For the steam driven processes, a cost saving of approximately 15.5% can be achieved when operating the MBC in OARO mode instead of FO mode for an equivalent electricity cost. These savings are mainly conferred by reducing the energy consumption of the DSR system, as lower draw solute concentrations are required when operating in OARO mode. Although OARO requires high-pressure pumps and energy recovery devices, the additional cost incurred by this equipment is negligible in comparison to the overall operational and capital cost savings.



(a) Steam powered FO integrated ZLD process

(b) Steam powered OARO integrated ZLD process

(c) LGWH powered FO integrated ZLD process

(d) LGWH powered OARO integrated ZLD process

Figure 27: Sensitivity analysis of the unit water cost for the FO and OARO base cases with respect to the electricity cost.

4.5.2. UWC of the LGWH powered FO and OARO base cases

The findings in Section 4.4. and Section 4.5.1. indicate that the DSR unit is the primary energy consumer, as well as the most expensive process in the analysed ZLD system (excluding pre-treatment and brine crystallisation). Therefore, substituting the valuable steam heat source with a less costly one can significantly lower the overall cost of the ZLD system. A recent study by Gingerich & Mauter [176] estimated that in the U.S. alone, more than 803 million GJ of heat at temperatures greater than 90°C were exhausted to the environment in 2012. Since the analysed ZLD system is located close to a coal-fired power plant, the available boiler hot flue gas comes to mind as a potential source of low-grade heat source. However, depending on the required reboiler temperature, other alternative low-grade heat sources, such as geothermal, nuclear, or solar energy, can also be utilised in the desalination process.

The median flue gas temperature from coal-fired power plants was estimated by Gingerich & Mauter [176] to be 128.4°C. This temperature is more than sufficient to drive the FO and OARO DSR system. As shown in Figure 26, the minimum achievable DC1 and DC2 reboiler temperatures are 76°C and 70.6°C. These low reboiler temperatures are reachable by decreasing Q_{MBC} and operating the MBC in OARO mode rather than in FO mode. For example, the DC1 and DC2 reboiler temperature can be reduced by 12°C at any Q_{MBC} when choosing an OARO configuration of the MBC instead of an FO configuration. Thus, LGWH integration is more feasible via OARO than via FO operation of the MBC.

However, one issue arises when utilising flue gas as a heat source. While the heat transfer coefficient can reach up to $6000\ W/m^2K$ during the condensation of steam, a much lower heat transfer coefficient of $300 - 600\ W/m^2K$ is achieved with flue gas because the gas density is lower and no phase change occurs [169]. Furthermore, the relatively low temperature of the flue gas results in a reduced temperature difference in the reboiler. Both effects result in the

requirement of a larger heat transfer area for the reboiler, which inevitably increases the capital cost of the DSR system.

The energy requirements of seawater RO desalination plants typically lie in the range of $4-8\,\mathrm{kWh/m^3}$ while achieving a brine salinity of approximately 70 g/kg [55]. In the present case, the final brine concentration reaches up to 190 g/kg while the electrical energy consumption can be reduced to $4.54\,\mathrm{kWh/m^3}$ and $5.24\,\mathrm{kWh/m^3}$ with LGWH integration for the FO and OARO base cases, respectively. This significant increase in system recovery for a similar energy consumption is a major advantage of LGWH integration. However, LGWH integration can only reduce the operational expenses of the DSR system to a certain level, as the cost associated with cooling water consumption and maintenance remain unchanged. As shown in Figure 27 (c) and (d), LGWH integration is not worthwhile on economical and technical grounds if the electricity cost is low ($0.05\,\$/\mathrm{kWh}$), as the UWC is only slightly reduced when compared to a steam powered system and the system layout and operation becomes more complex. On the other hand, at high electricity costs ($0.1\,\$/\mathrm{kWh}$), the overall cost savings for both FO and OARO integrated ZLD processes with LGWH integration is approximately 11%.

As stated by Voutchkov [132], the industry average freshwater production cost is $1.1\,\$/\mathrm{m^3}$ for medium to large scale seawater RO desalination systems. With LGWH integration and OARO operation, the UWC of the MBC and the two-pass RO unit alone is still three to four times higher although the achievable electricity consumption falls in the range of a typical RO desalination plant. Another possibility to reduce the freshwater production cost is by increasing the scale of the operation. Increasing the scale of the plant reduces capital expenditures to an extent, as the design, development and construction costs are not directly linked to the plant's freshwater production rate. However, in this case the influence of the capital cost on the UWC is insignificant and thus the cost savings associated with increasing the plant scale are limited.

4.6. Comparing the FO and OARO MBC with the LSRRO and the standard OARO processes

As the parametric and the techno-economic study have proven, utilising an additional hydraulic driving force (OARO) can significantly reduce the cost, energy consumption and the DSR temperature of the purely osmotically driven membrane process (FO) when using a thermolytic DS. However, it is still unclear whether combining OARO with a thermo-responsive DS offers any benefits in comparison to other novel membrane-based BVM techniques. To attempt to answer this question, the FO and OARO MBC are compared to the LSRRO system, which was proposed by Wang et al. [24], and the standard SF-OARO process with a non-responsive DS (i.e., NaCl), which is presented by Bouma & Lienhard [25]. Please refer back to Section 1.2.1. for explanations of the SF-OARO and LSRRO process with non-responsive DS.

The simulation results from all three studies are presented in Table 6. To allow for a fair comparison of the membrane-based ZLD processes, 1) a single-pass RO system is utilised in the FO and OARO MBC instead of a two-pass RO system, and 2) all processes are expected to concentrate the same saline feed from 0.6 M to 4 M. Hence, this test case slightly differs from that in the previous sections, in which a saline feed is concentrated from 0.77 M (5 g/L) to 3.76 M (220 g/L). For this new test case, the equivalent work of the FO and OARO MBC are 11.1 kWh/m^3 and 9.3 kWh/m^3 when using a single-pass RO system and 5 bar saturated steam to power the DC reboilers.

Table 6: Comparison of the LSRRO, the standard OARO and the FO and OARO MBC with a thermo-responsive DS to concentrate a 35 g/kg saline stream to 205 g/kg (0.6 M to 4 M). The FO and OARO MBC are operated using a single RO pass and with the following parameters: N/C = 2.4, $Q_{MBC} = 5\ m^3/h$, RR = 0.33, $P_{RO1} = 80$ bar, $Q_{RO} = 12\ m^3/h$.

		FO [a] (thermo-responsive DS)	OARO [a] (thermo-responsive DS)	LSRRO [b]	OARO [c] (non-responsive DS)
Total stages (+RO)		4	4	4	6
ΔP_{Max}	[bar]	1.0	48.3	70.0	68.0
CDS_{Th}	[mol/L]	7.0	4.3	-	-
$T_{Reb,DC1}$	[C]	97.2	86.1	-	-
$T_{Reb,DC2}$	[C]	91.5	80.3	-	-
SCL	$[MJ/m^3]$	351	242	-	-
W_{Eq}	$[kWh/m^3]$	11.1	9.3	5.14	3.9
SEEC	$[kWh/m^3]$	2.94	3.47	5.14	3.9

[a] This study [b] Wang et al. [24] [c] Bouma & Lienhard [25]

There are two methods to further reduce the overall energy consumption of the FO and OARO MBC system. Firstly, heat pumps (i.e. vapor compression) can be utilised instead of steam to power the reboilers [147], or secondly, LGWH can be utilised to supply the required thermal load. Assuming that LGWH integration is possible, the FO and OARO MBC energy cost can be substantially reduced to $2.94\ kWh/m^3$ and $3.47\ kWh/m^3$, respectively.

In comparison, the calculated energy consumption of the 4-stage LSRRO is $5.14\ kWh/m^3$ when it is required to concentrate the same saline feed to 4 M [24]. However, in contrast to our simulation, the calculation of the specific electrical energy consumption performed by Wang et al. [24] neglects 1) external concentration polarisation effects, 2) the pressure drop across membrane modules and 3) assumes that even the highly concentrated solution behaves ideally and conforms to the van't Hoff approximation. All of these simplifications can substantially increase the numerical error in the value of the simulated water flux, as shown by Bartholomew & Mauter [177], and the actual specific electrical energy consumption (SEEC) of the LSRRO process (with a finite membrane area) is expected to be far higher than $5.14\ kWh/m^3$. Even

under ideal LSRRO conditions, the OARO MBC with LGWH integration can outperform the LSRRO process and operate at a 32.5% lower SEEC.

On the other hand, the calculation performed by Bouma & Lienhard [25] for the standard OARO system with a non-responsive DS includes external and internal concentration polarisation. Their calculation shows that the conventional OARO process only requires $3.9\ \mathrm{kWh/m^3}$ and is the most energy efficient technology to achieve the desired brine concentration. However, one main issue with this OARO process is that the achievable water fluxes in the final three membrane stages are very low (<1 $\mathrm{L/(m^2h)}$). Therefore, a total of 6 stages with large membrane areas are required to achieve the desired brine concentration. Furthermore, the OARO stages have to be operated at a maximum transmembrane pressure ΔP of 68 bar, while the membrane's S-value is assumed to be only $564\ \mu\mathrm{m}$, which is comparable to the membrane's S-value used in this study. These high operating pressures may inevitably lead to the failure of these thin OARO membranes. In contrast, the OARO MBC can be operated at lower hydraulic pressures and at economically feasible water fluxes (>5 $\mathrm{L/(m^2h)}$) when using a strong, thermo-responsive DS.

As shown in Figure 28, the OARO process can achieve brine concentrations of up to 245 g/kg when operated at technically feasible pressures (48.3 bar [131]) and draw solute concentrations ($\approx 6\ \mathrm{mol/kg}$ on a carbon basis [147]). Theoretically, even higher recoveries can be achieved by the OARO system, as the required thermo-responsive DS concentration in the CDS stream $\mathrm{CDS_{Th}}$ could be increased beyond 6 mol/kg (on a carbon basis); the solubility limit of the thermolytic draw solution is approximately 13 M [134]. In any case, such high brine concentrations cannot be achieved by conventional OARO systems utilising non-responsive DS. Similarly, the FO MBC also cannot achieve such high brine concentrations without exceeding the suggested upper limit of $\mathrm{CDS_{Th}}$.

The OARO MBC can achieve brine concentrations of up to 245 g/kg while operating at $W_{Eq} = 10.8\ kWh/m^3$ and a maximum reboiler temperature of 94.1°C, whereas the FO MBC requires $W_{Eq} = 11.1\ kWh/m^3$ and a maximum reboiler temperature of 97.2°C to achieve a lower brine concentration of 205 g/kg. This means that combining OARO with a strong thermo-responsive DS can substantially reduce the overall energy consumption of the entire ZLD process, as the brine volume to be treated by the energy intensive brine crystalliser can be reduced by more than 15 % when increasing the target brine concentration from 205 g/kg to 245 g/kg for the MBC.

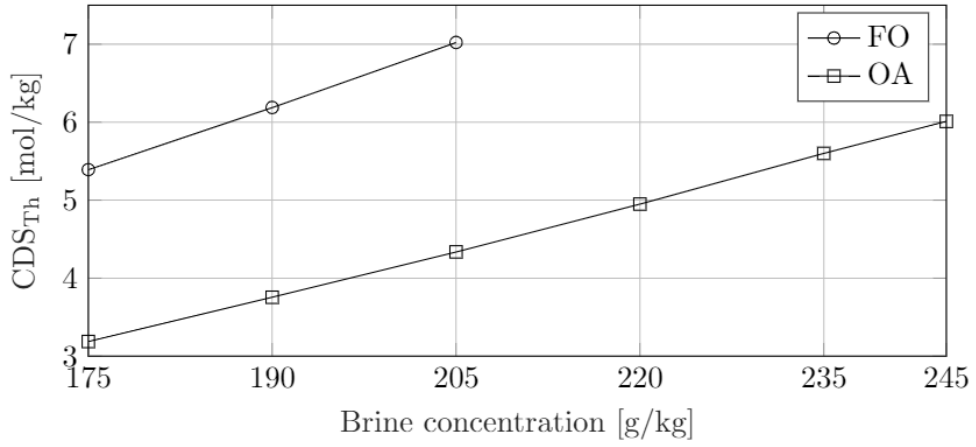


Figure 28: The required concentration of the thermo-responsive DS in the CDS stream CDS_{Th} with respect to the target brine concentration. The initial feed concentration is 3 g/kg NaCl.

One aspect of this comparison which has not been discussed so far is that the LSRRO and the conventional OARO process do not require any cooling water or heat transfer equipment, which conversely can significantly increase the cost of the FO and OARO MBC. Therefore, when operating with a thermo-responsive DS, the OARO MBC outperforms the FO MBC in terms of a 31% lower specific cooling load (SCL) and a DSR temperature which is approximately 11°C lower; both factors can reduce the cost of the heat transfer equipment and reduce the size of the reboilers, when powered by the same thermal source.

Choosing OARO with either a non-responsive or a responsive DS therefore seems not only technically feasible, but also both options offer a significantly lower SEEC than LSRRO (when assuming that LGWH is essentially ‘free energy’).

4.7. Chapter conclusions

In this Chapter, a numerical model is developed to simulate an OARO and an FO integrated ZLD process, whose design is based on the membrane brine concentrator. A direct parametric and techno-economic comparison is performed between both processes to highlight the benefits of combining OARO with a thermo-responsive DS and how OARO can alleviate several of the shortcomings of FO. Furthermore, the OARO and FO MBC are compared to the conventional (non-thermolytic DS) OARO and the LSRRO process in order to identify which of these novel membrane-based ZLD processes is the more energy efficient technology.

The findings from this study can be summarised as follows:

- Extremely high brine concentrations of up to 245 g/kg can be achieved by the OARO MBC at technically feasible operating pressures (48.3 bar) and at reasonable draw solute concentrations (6 mol/kg on a carbon basis). This high brine concentration is not achievable by the FO MBC utilising the same thermo-responsive DS or by the conventional OARO system using a non-responsive DS.
- Utilising a thermo-responsive DS allows for the utilisation of low-grade thermal energy to drive the desalination process. The integration of LGWH can substantially reduce the required electrical energy consumption to levels below those achievable by LSRRO and by the conventional OARO process. However, one main disadvantage of utilising thermo-responsive draw solutes is that additional heat transfer equipment and cooling water are required, which is not the case for LSRRO and the conventional OARO process. These disadvantages can, however, be minimised by the OARO MBC, as the specific cooling load is reduced by 31% in comparison to its FO counterpart.
- In comparison to FO, the high hydraulic pressure operation of OARO reduces the draw solute concentration required to achieve the same water flux and process recovery. This offers benefits, such as a lower susceptibility to ICP and a lower reverse solute flux,

which in turn may confer additional advantages, such as allowing the removal of the energy intensive and costly brine stripper (DC1 in Figure 18) from the process when combined with the development of more selective membranes or of draw solutes with a lower reverse transport rate.

- The UWC of the BVM process can be reduced by approximately 15.5% by operating the MBC in OARO mode. Furthermore, OARO is more suited to LGWH integration than FO, as the reboilers of the OARO MBC can be operated at temperatures up to 12°C lower. LGWH integration is economically more sensible for high prevailing grid electricity costs, as the operational cost savings then begin to outweigh the capital cost increase caused by the use of larger reboilers.
- With regards to membrane fouling, several uncertainties remain as to whether OARO or FO are more prone to membrane fouling, and as to whether high pressure operation of the OARO membrane process is deleterious because of the deformation of the thin membrane. Fouling has not been fully considered so far in this work, and is discussed in greater detail in the subsequent Chapter.

Chapter 5

Exploring the technical limitations of OARO: Membrane fouling and the limiting flux

Numerical estimates of the achievable OARO brine concentration are exemplary, as shown by the results presented in Chapters 3 and 4. In practice, however, the performance of OARO processes is expected to be inevitably affected by membrane fouling, which is an issue that has not been systematically examined to date.

OARO is susceptible to both severe membrane deformation [68] and fouling, as OARO membranes (1) are exposed to high hydraulic pressures, (2) ideally have a thin substrate to minimise ICP, and (3) are used to treat highly concentrated solutions with impurities. In comparison to other membrane desalination processes, OARO can utilise the same feed and draw solution which can contain a range of organic and inorganic fouling species and may vary from wastewater [62], seawater to concentrated brine [5,18,25,35,52]. Hence, fouling on both sides of the OARO membrane is highly likely. Of special concern is internal membrane fouling on the draw side, where pore clogging can occur if foulants enter the membrane's porous substrate [102]. In this case, fouling enhanced ICP would substantially lower the OARO water flux. Depending on the chosen draw solution, internal membrane fouling in FO in AL-FS mode was found to be either significant [109] or not [178] and hence, deserves experimental investigation in OARO. Although the permeate water flow also opposes the accumulation of foulants within the membrane substrate, high pressure operation is expected to significantly change the hydrodynamic conditions within the OARO draw channel, as explained in Section 2.3.

Compaction of the membrane and its spacer support narrow the flow channels, which can lead to enhanced foulant deposition and plugging of the spacer [96,97] and potentially of the membrane.

As mentioned in Section 2.4., significant foulant accumulation on a pristine membrane and the associated flux reduction are predicted to occur, once the water flux exceeds the so-called critical flux [114,120,179]. The critical flux is not fixed and depends on the foulant-membrane interactions, which are related to the feedwater properties, membrane characteristics and operational conditions. However, under extreme fouling conditions, as often faced in OARO processes, the entire membrane surface can be potentially covered by foulants. Once this happens, the fouling development is independent of the pristine membrane properties, as shown by Tang et al. [115]. Similar results were observed in other studies [100,180] and it was shown that the water flux after long-term fouling tended to achieve an identical pseudo-stable value, termed the limiting flux. While the limiting flux was shown to be independent of the membrane properties in RO [115,181] and FO [124] (AL-FS mode), this may not, however, be the case for OARO if internal membrane fouling is a concern. For example, in pressure retarded osmosis (PRO) the limiting flux was shown to be dependent on the membrane's structural parameter *S* when scaling within the membrane substrate was substantial [125,182]. It is necessary to examine how the operating pressure and membrane properties influence the limiting flux in OARO and further to gain an understanding of the technical implications for OARO operation.

As OARO exhibits certain similarities to FO, dilutive ICP at the draw side will significantly reduce the effective driving force and thus result in a lower-than-expected flux [68]. On the other hand, several studies on FO fouling reported that flux remained relatively stable during membrane fouling in AL-FS mode due to the ICP self-compensation effect [76,110,111]. Tang et al. [113] related this observation to the fact that any minute reduction in the membrane's water flux due to fouling will immediately be counterbalanced by a reduction in ICP, and hence, will result in a milder reduction of the membrane's water flux. While the ICP self-compensation

effect is presumably applicable as well in OARO, it is important to investigate how it affects the OARO flux behaviour during fouling.

As laid out in Section 2.3. and this Chapter, several complex and interdependent mechanisms of membrane fouling may occur during OARO operation. The objective of this Chapter is then to explore these mechanisms and to gain a better understanding of the technical limitations of OARO as a result of membrane fouling. This Chapter covers a detailed investigation into the effects on the OARO process performance of the feed and draw compositions, the membrane properties and the hydraulic pressure. Additionally, possible membrane cleaning methods, such as osmotic backwashing and surface flushing, are evaluated for their efficacy in alleviating fouling and restoring the membrane's initial water flux.

5.1. Materials and methods

5.1.1. Experimental setup, membranes and spacer backing

The experimental setup used in this study was adopted from the one reported in a previous PRO study with two minor modifications [97]. Firstly, no dosing pumps were utilized during the experiments to control the concentrations of the feed and draw solutions. Hence, the salinity of the feed and draw solution had to be continuously monitored to determine their concentration changes with operational time. Secondly, the feed solution was pressurised in this study instead of the draw solution. The weight of the draw solution was continuously measured to determine the water flux. A schematic of the experimental setup is shown in Figure 29.

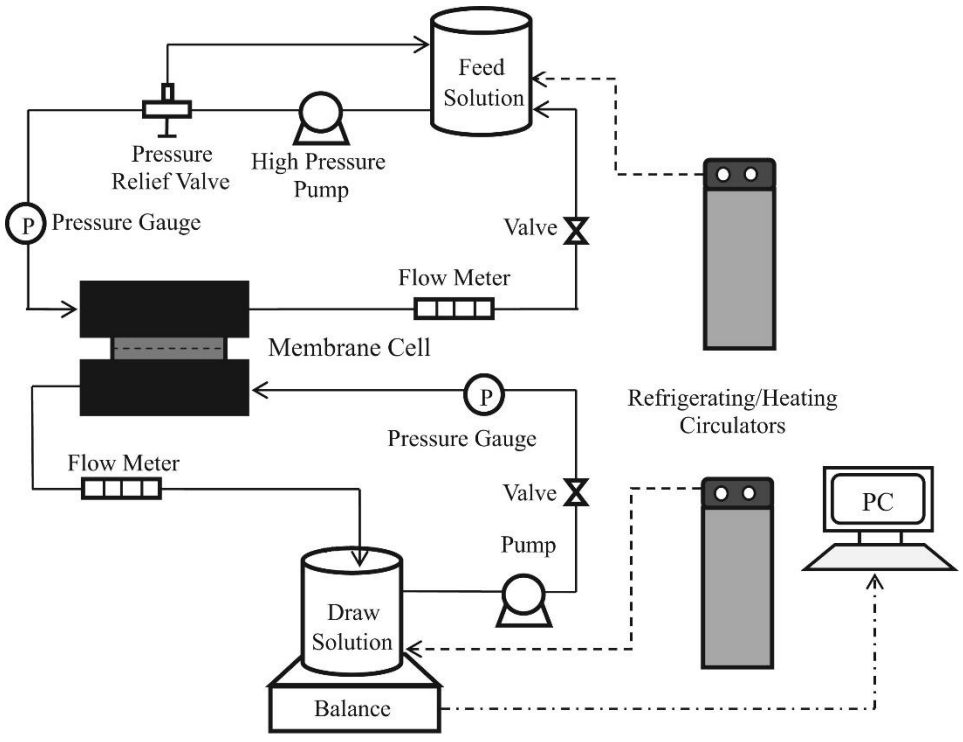


Figure 29: Schematic of the experimental setup (modified from She et al.[97]).

The feed solution was recirculated by a high-pressure Hydra-Cell pump (D/G-03, Minneapolis, MN), while the draw solution was recirculated by a gear pump (Cole-Palmer, Vernon Hills, Illinois). The pressure in the feed solution was set by a back pressure regulator

located down-stream to the membrane cell, and the pressure reading was monitored by a digital pressure transmitter. The draw pressure was monitored with a mechanical pressure gauge. The temperature of both feed and draw solutions were maintained constant using water chillers/heaters (PolyScience, Niles, IL).

To adequately support the membrane under the high pressure in the feed solution and to minimize membrane deformation, a 3D printed spacer (Figure 30) and a tricot-type RO permeate carrier, which was obtained from a commercial RO spiral wound module [90], were placed in the permeate (draw) channel of the membrane test cell. This spacer combination in the permeate (draw) channel could fully support the membranes at operating pressures of up to 60 bar when operated in RO/OARO mode. The 3D printed spacer was produced from polylactic acid (PLA). PLA prints have a good dimensional accuracy, which allows for an intricate spacer design to enhance mixing and mass transfer in the draw channel while ensuring that the membrane is well supported. PLA is widely used for 3D printing because of its relatively low melting temperature and good mechanical strength and stiffness. To reduce the spacer openings, the RO permeate carrier was placed on top of the 3D printed spacer to further improve the membrane's support structure. No feed spacer was used in the membrane experiments to prevent its interference with the membrane's active layer.

Two commercially available membranes, namely an aquaporin (AQP) based TFC membrane from Aquaporin A/S (Copenhagen, Denmark) and a FilmTec flat-sheet brackish water RO membrane (BW30LE), were used in this study to investigate OARO fouling. Both membranes were considered to be suitable OARO membranes and were already fully characterised at operating pressures of up to 60 bar [68]. The membranes were stored at 4°C and extensively rinsed and soaked in Milli-Q water for over 24 hours before use. All tested membrane coupons had an active membrane area of approximately 42 cm^2.

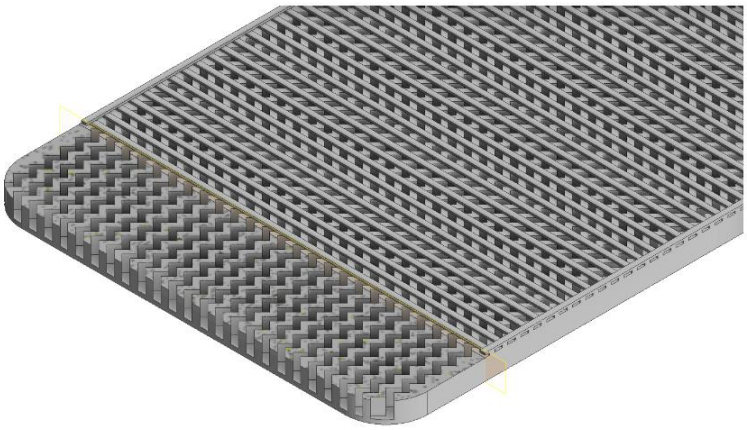


Figure 30: 3D printed spacer designed to support the RO permeate carrier and the membrane when used in the permeate channel within the membrane test-cell. The underlying pattern is revealed in the figure to exhibit the three-dimensional spacer shape designed to improve the flow turbulence while offering a rigid support for the membrane.

5.1.2. Chemicals and solutions

OARO membrane fouling was investigated using five different combinations of feed and draw solutions. Unless otherwise stated, all solutions were prepared with ACS grade chemicals/reagents and prepared using ultra-pure water. All draw and feed solutions were calculated to have a comparable osmotic pressure of approximately 35 bar using OLI Studio 10.0 software (OLI Systems Inc., Morris Plains, NJ). The compositions of the synthetic solutions are stated in Table 7.

As dosing the feed and draw solutions was deemed unnecessary and impractical, a reference case (RC), with pure NaCl feed and draw solutions, was used to record the water flux reduction that was solely caused by the changes of the concentrations of feed and draw solutions during OARO operation (i.e., due to feed concentration and draw dilution).

Firstly, the effects of membrane scaling on the OARO process performance were investigated using test case F1. Inorganic fouling can be a serious concern for seawater and brackish water desalination. Typically, the most common scaling constituents in seawater are calcite ($CaCO_3$) and gypsum ($CaSO_4 \cdot 2H_2O$) [183]. Therefore, calcite [184–186] and gypsum [187–189] scaling have been

widely studied for a variety of membrane processes. As OARO is generally utilised to concentrate RO brines [35], the concentrations of gypsum and calcite precursor ions were chosen to be representative of those present in seawater RO brines (at 50% recovery) [97,190]. The saturation index (SI) of gypsum and calcite in F1 were calculated using OLI Studio 10.0 software and are -0.14 and 0.73, respectively. For supersaturated solutions (SI>0), scale formation is a likely phenomenon [191,192] which may inevitably cause a flux reduction in OARO.

For test case F2, gypsum and calcite precipitates were directly added to the feed and draw solutions to investigate whether the presence of already formed precipitates in the bulk solutions would enhance membrane fouling. Test cases F3 to F5 investigate organic fouling in the presence of calcium ions. Sodium alginate is chosen in this study as a model foulant due to its ubiquity in surface waters and its known strong interaction with calcium ions [97].

In F3, sodium alginate is only added to the draw side to determine whether organic fouling on the OARO membrane's draw side is significant or not. On the other hand, in test cases F4 and F5 sodium alginate is also added to the feed solution. The inorganic precipitates (calcite and gypsum crystals) are also added to both feed and draw in test case F4 to simulate the OARO process under the most extreme fouling conditions.

Table 7: Composition of the synthetic feed and draw solutions used for the OARO fouling experiments.

Test Case [a]	RC	F1	F2	F3	F4	F5
Feed composition (mmol/L)						
NaCl	750	600	600	600	600	600
$CaCO_3$(s)	0	0	0.25	0	0.25	0
$CaSO_4$ (s)	0	0	11	0	11	0
$CaCl_2$ [b]	0	21.62	21.62	21.62	21.62	21.62
Na_2SO_4 [b]	0	57.75	57.75	57.75	57.75	57.75
$NaHCO_3$ [b]	0	4.76	4.76	4.76	4.76	4.76
Alginate [c]	0	0	0	0	0.46	0.46
Draw composition (mmol/L)						
NaCl	750	600	600	600	600	600
$CaCO_3$ (s)	0	0	0.25	0.25	0.25	0
$CaSO_4$ (s)	0	0	11	11	11	0
$CaCl_2$ [b]	0	21.62	21.62	21.62	21.62	21.62
Na_2SO_4 [b]	0	57.75	57.75	57.75	57.75	57.75
$NaHCO_3$ [b]	0	4.76	4.76	4.76	4.76	4.76
Alginate [c]	0	0	0	0.46	0.46	0.46

[a] RC: Reference case, only NaCl present in the solutions; F1: Scaling precursors dissolved in both feed solution (FS) and draw solution (DS), neither crystals nor alginate present in bulk solutions; F2: Crystals present in bulk solutions and scaling precursors dissolved in both FS and DS; F3: scaling precursors dissolved in both FS and DS, alginate dissolved in DS only and crystals present in DS only; F4: Crystals present in bulk solutions and scaling precursors and alginate dissolved in both FS and DS; F5: Scaling precursors and alginate dissolved in both FS and DS and no crystal present in bulk solutions.
[b] Concentrations calculated based on a 50% recovery of a seawater RO plant [97,190].
[c] Alginate concentration is 100 mg/L (MW: 216 g/mol).

5.1.3. OARO fouling experiments

All fouling experiments were carried out in a Sterlitech membrane test cell that can withstand operating pressures of up to 69 bar. The digital pressure gauges were only calibrated for operating pressures of up to 60 bar, which was therefore set as maximum pressure for all tests performed. The test-rig utilised in this study is described in detail in She et al. [97]. As previously mentioned, no dosing pumps were utilised during the fouling experiments. The temperature of the pressurised feed solution was kept constant at 25±1 °C using a cooling coil.

Prior to the addition of alginate in test cases F3-F5, the membrane was firstly compacted at the required operating pressure for 30 min to ensure that any sudden flux reduction was solely caused by membrane fouling and not by membrane deformation. The duration of each fouling experiment was approximately 4 hours with the water flux J_W, operating pressure ΔP and the feed and draw conductivities recorded in 10-second intervals. For all experiments, the cross-flow velocity (CFV) was set as 10 cm/s in both feed and draw channels [68].

5.1.4. OARO cleaning experiments

Three different cleaning strategies were investigated in this study. Flushing the fouled membrane using deionised (DI) water constituted the first. The other two cleaning strategies for OARO focussed on osmotic backwashing (OB) using different feed and draw solutions. The ideal OB strategy would use a deionised draw solution, whereas the real OB utilised a synthetic seawater solution as draw. The three cleaning strategies modelled the use of either product water or less expensive feedwater (i.e., seawater) as possible cleaning solutions to determine their efficacy. A more detailed description of the cleaning strategies is given in Appendix D.

5.2. Effect of feed and draw solution composition on OARO fouling

Figure 31 shows the water flux results obtained for the reference case and the five fouling scenarios with different FS and DS compositions. All experiments were performed with the AQP membrane at a constant operating pressure of 50 bar. This resulted in an initial flux of approximately 22-24 L/(m^{2}h) for all tests. The water flux of the RC reduced from an initial water flux J_0 of 23 L/(m^{2}h) down to 18 L/(m^{2}h) after a 4-hour OARO operation. This flux reduction is caused by the increasing transmembrane osmotic pressure difference, as the feed solution was concentrated, and the draw solution was diluted.

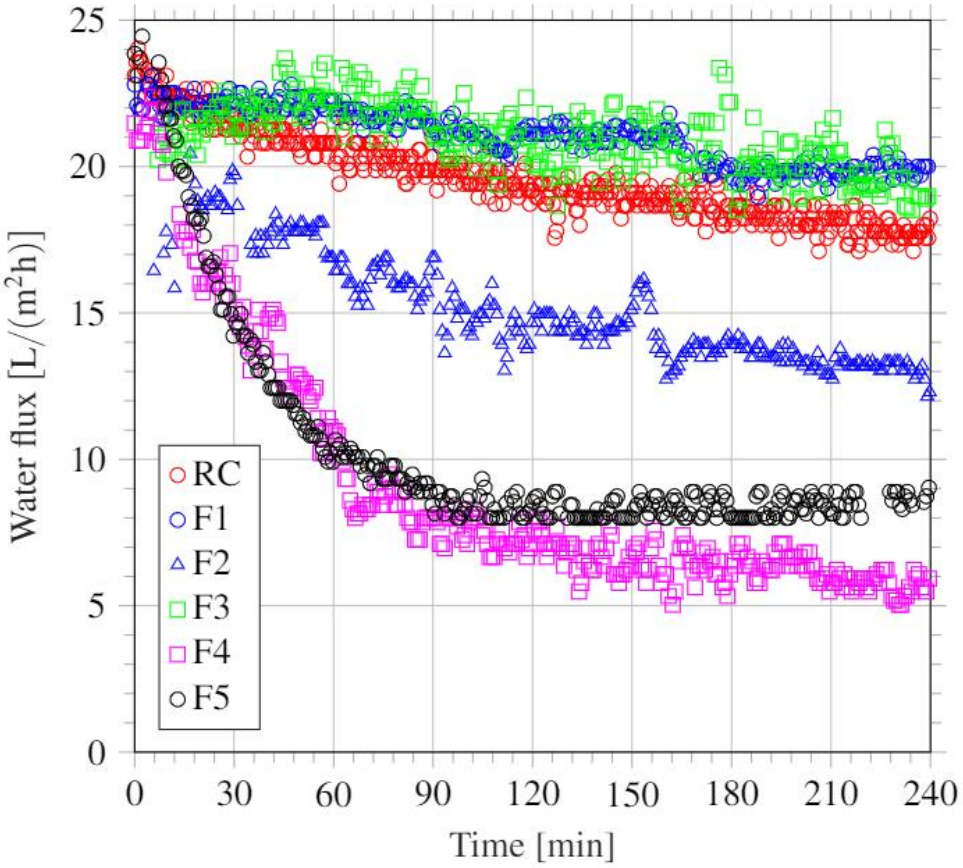


Figure 31: Effect of feed and draw solution composition on OARO permeate flux evolution. All fouling experiments were carried out using the AQP membrane at 50 bar with cross-flow velocity of 10 cm/s. RC: Reference case, and solution compositions for F1-F5 are listed in Table 7.

It was observed that the flux for test scenario F1 is similar to that of RC. The inclusion of scale precursor ions in both the feed and draw solutions (test case F1) did not lead to a more severe

flux reduction within the 4-hour operational window. Hence, it can be concluded that membrane scaling was not significant under the given operational conditions. Solute precipitation is mainly expected on the membrane's feed side, as the feed solution is continuously concentrated while the draw is diluted. In addition, concentrative ECP causes higher solute concentrations near the membrane surface and hence, may lead to surface crystallization if the saturation limit is exceeded [193]. In scenario F1, the main scaling precipitates are gypsum (calcium sulphate), which has a relatively high solubility. It is expected that the small amount of gypsum precipitates formed on the membrane surface would be removed at the high crossflow velocity on the feed side. Furthermore, no feed spacer was employed in this study to prevent any stagnant regions between the feed spacer filaments and the membrane surface, where potential precipitates would form [194].

Besides the scale precursor ions, inorganic precipitates were added to the feed and draw solutions in test case F2, which simulates a scenario for which bulk crystallization has already occurred. While the water flux of F1 did not deviate from that of the reference case, the water flux of F2 was substantially lower than that of the reference case after 4 hours. The F2 water flux dropped to 13 $\mathrm{L/(m^2 h)}$. The difference in the J_W trends between F1 and F2 suggests that the additional flux reduction in F2 must be caused by the deposition and agglomeration of the inorganic precipitates on the membrane surface. In general, there are two distinct precipitation pathways in membrane modules, namely surface crystallisation, and bulk crystallisation. Both pathways of crystallisation can occur simultaneously and initiate/aggravate each other [195]. For example, homogeneous crystal formation in the bulk can lead to scale deposition and cake layer formation on the membrane, due to the continuous transport of crystals towards the membrane surface, which is the dominant scaling mechanism for F2 scenario. Moreover, this cake layer may offer a secondary nucleation site for further scale formation under supersaturated conditions, which further increases the resistance to water transport through the membrane.

As shown in Figure 31, test case F3 also shows no deviation from the reference case. The objective of test case F3 was to investigate whether organic fouling, scaling and/or inorganic precipitates on the membrane's draw side cause any significant flux decline. Obviously, as no deviation from the reference case was observed, it can be concluded that fouling on the membrane's draw side was negligible and caused no significant loss in OARO performance. A similar finding was made by Boo et al. [178], who found that internal fouling on the draw side is negligible for forward osmosis processes operated in the AL-FS mode. This is due to the fact that the permeate water flow opposes the accumulation of foulants within the membrane substrate in the AL-FS mode. This is also an important finding for OARO operation, as it suggests that membrane fouling is only likely to be a concern on the membrane's feed side (particularly in view of the additional hydraulic pressure gradient). This might suggest that untreated solutions can potentially be used directly as OARO draw solution without any concern for membrane fouling. It should be noted that although no OARO internal fouling was observed in AL-FS mode, even when using a draw solution which was highly concentrated with organic and inorganic foulants, this might not be the case when using other draw solutions (e.g., surfactants [109]) or when operating at lower water fluxes. Zohrabian et al. [109] found that when the foulant's adsorptive and diffusive forces exceeded the counteracting convective forces (i.e., the permeate water flux), internal membrane fouling in FO in AL-FS mode was possible and hence, internal membrane fouling may also be possible in OARO. In addition, while no flux reduction was observed during F3, some organic matter was still observed to be trapped within the tight and compacted draw spacer. Pictures of the plugged draw spacers are shown in the supporting information (refer to Appendix D). She et al. [97,125] made a similar finding for PRO, and found that the compacted feed spacer was plugged by organic material during operation. This means that any precipitates should still be filtered from the draw solution to prevent any pressure loss caused by the plugging of the compacted OARO draw spacer.

The most severe flux decline was observed for test cases F4 and F5, in which alginate was added in the feed solution and combined organic fouling and inorganic scaling occurred. While the flux decline was similar for both scenarios in the first 2 hours, the final "steady-state" water flux differed. After 4 hours of operation, F4 and F5 reached a water flux of $6\ \mathrm{L/(m^2h)}$ and $9\ \mathrm{L/(m^2h)}$, respectively. In comparison to test case F3 where only inorganic scaling occurred, the combined organic fouling and inorganic scaling for F4 and F5 led to a more significant flux decline. In F4, inorganic precipitates were also present in both the bulk feed solution and the draw solution. It is expected that the calcium alginate (Ca-Alg) agglomerates in combination with the inorganic precipitates form a denser and thicker fouling layer in F4 than the Ca-Alg agglomerates alone in F5 [196,197]. This would explain why the final water flux was lower for F4 than F5. Both test cases suggested that the formation of Ca-Alg agglomerates and their interaction and deposition on the membrane surface caused a severe flux decline.

As for any membrane process, organic fouling remains a major challenge and has been widely investigated [97,102,196,198]. The severity of organic fouling in OARO is dependent on a multitude of factors and is mainly related to the feed side properties.

5.3. Pressure independent limiting flux in OARO

The effects of the operating pressure (i.e., the initial water flux) on the OARO fouling propensity are shown in Figure 32. All presented results were obtained using the AQP membrane and the solution compositions specified for test case F5 (Table 7).

As shown in Figure 32 (a), the initial water flux J_0 increased from 10 $\mathrm{L/(m^2h)}$ to 30 $\mathrm{L/(m^2h)}$ when the operating pressure was increased from 30 bar to 60 bar. A higher initial water flux is associated with a higher fouling rate [114] and hence, a steeper flux reduction was observed at higher operating pressures. A limiting flux can be observed at approximately 9 $\mathrm{L/(m^2h)}$ for the OARO process, above which the membrane flux cannot be sustained. This limiting flux is reached in both of the 50 bar and 60 bar fouling experiments. For a more detailed introduction and derivation of the limiting flux, please refer back to Section 2.4.

While the initial water flux at 40 bar (15 $\mathrm{L/(m^2h)}$) supersedes the limiting flux, the final water flux (5 $\mathrm{L/(m^2h)}$) is below the limiting flux. This is contrary to the findings of Tang and Leckie [123] who observed a well-defined limiting flux behaviour where (1) almost no flux decline was recorded when the initial flux was less than the limiting flux and (2) the final flux was equivalent to the limiting flux if the initial flux exceeded the limiting flux. In this case, an intermediate state is reached at 40 bar in which the obtained pseudo-stable water flux $J_W^{40\ bar}$ ranges between the critical flux (J_C) and limiting flux (J_L), i.e., $J_C < J_W^{40\ bar} < J_L$. While the critical flux was not directly determined in this study, Bacchin [120] showed that the critical flux is lower than the limiting flux for colloidal systems and hence, the barrier force (repulsive force) between the foulant in the solution and the clean AQP membrane ($\mathrm{F}_{\mathrm{Barrier}}^{f-m}$) is expected to be lower than that between the foulant and the formed foulant layer on the membrane ($\mathrm{F}_{\mathrm{Barrier}}^{f-f}$). This intermediary state is also observed for the 30 bar fouling experiment. The initial water flux at 30 bar (9 $\mathrm{L/(m^2h)}$) is equivalent to the observed limiting flux, but the final pseudo-stable water flux (4 $\mathrm{L/(m^2h)}$) is lower than the limiting flux. For these two scenarios,

the barrier forces at the pseudo-stable flux for 30 bar and 40 bar (i.e., $F_{Barrier}^{30\ bar}$ and $F_{Barrier}^{40\ bar}$, respectively) are expected to be:

$$F_{Barrier}^{f-m} < F_{Barrier}^{40\ bar} < F_{Barrier,L}^{f-f} \quad (34)$$

and:

$$F_{Barrier}^{f-m} < F_{Barrier}^{30\ bar} < F_{Barrier,L}^{f-f} \quad (35)$$

where $F_{Barrier,L}^{f-f}$ is the barrier force offered by the fouled membrane when the limiting flux is reached.

The relationship between the initial water flux J_0 and the final pseudo-stable water flux is shown in Figure 32 (b). The intermediary state at 30 bar ($J_C < J_W^{30\ bar} < J_L$) and 40 bar ($J_C < J_W^{40\ bar} < J_L$) is clearly visible from this figure, as in both scenarios the final pseudo stable water flux is below J_L, although $J_0 \geq J_L$. It is noted that a similar relationship between the initial water flux and the final pseudo-stable flux was observed by She et al. [199] in the study of UF membrane fouling. She et al. [199] reasoned that this non-ideal, intermediary state occurs due to the non-homogeneity of UF membranes, such that localised microscale fluxes can exceed or fall below the apparent macroscale average flux. In regions where local fluxes are higher than the limiting flux, those local fluxes will decline and eventually stabilized at the limiting flux level. Noting that in other regions local fluxes are lower than the limiting flux, the apparent macroscale average flux in all regions will decline to below the limiting flux.

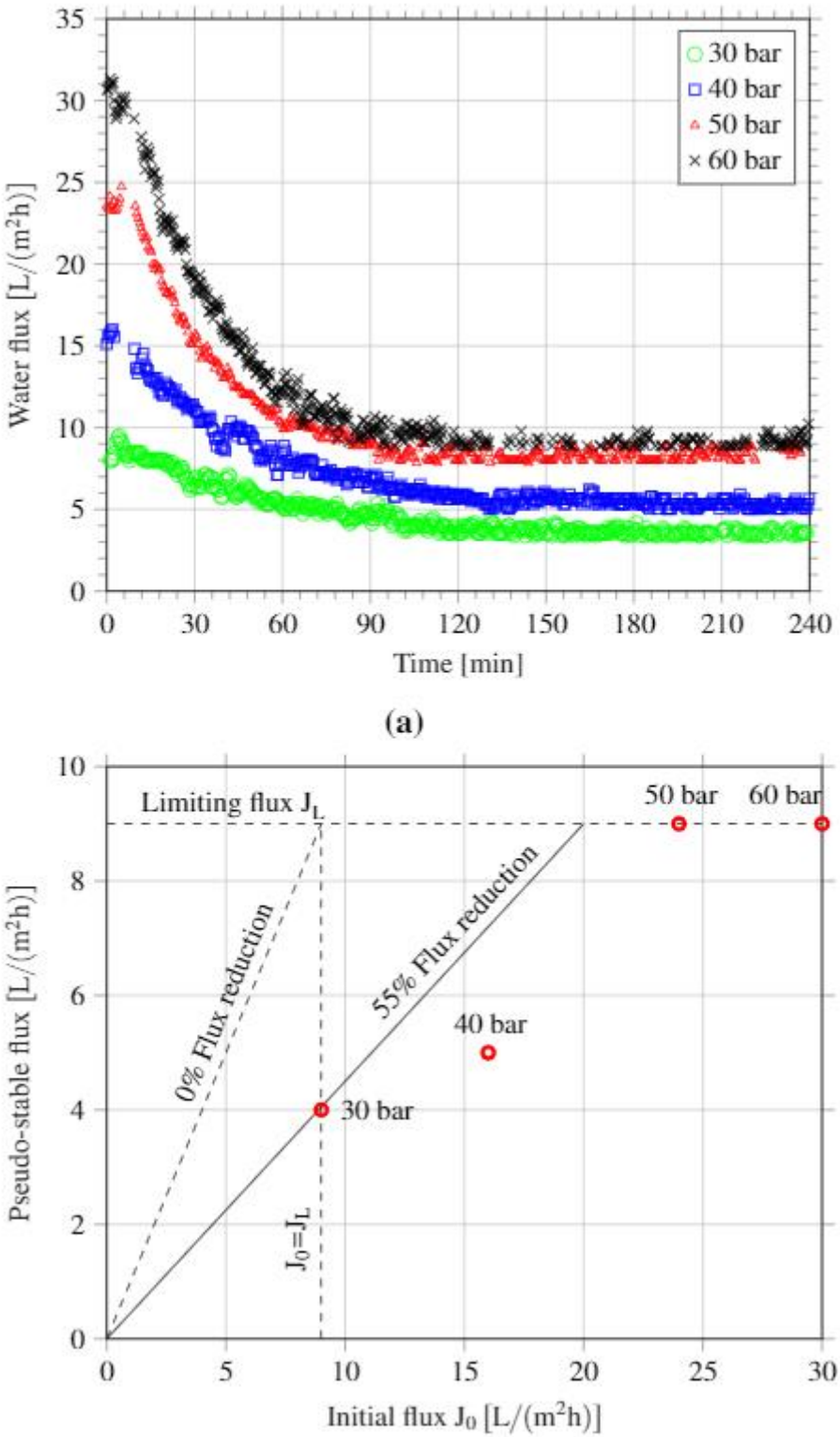


Figure 32: (a) Effect of the applied hydraulic pressure on OARO permeate flux evolution. All fouling experiments were carried out using the AQP membrane using the solutions specified for test case F5 in Table 7. (b) Relationship between the initial and final, pseudo-stable water flux.

Thus, it can be hypothesised that membrane fouling is more severe in regions with high local water fluxes, whereas fouling is less severe in regions with lower local water fluxes, causing the formation of a non-homogenous fouling layer so that $F_{Barrier}^{f-m} < \mathrm{F_{Barrier}} < F_{Barrier,L}^{f-f}$. This also explains the greater than expected flux reductions at 30 bar and 40 bar, as the actual barrier force is less than that induced by a fully, homogeneously fouled membrane.On the other hand, it is expected that the AQP membrane is completely covered by a homogeneous foulant layer at operating pressures exceeding 50 bar with a relatively high initial water flux, as the final pseudo stable water fluxes at 50 bar and 60 bar are equivalent to the limiting flux. This means that for long-term OARO operation, without continuous membrane cleaning, it is not advised to operate the AQP membrane at pressures exceeding 50 bar, as the same limiting flux will be reached under the given feed conditions. In essence, an energy saving of 16.7% can be achieved by operating the OARO process at 50 bar instead of 60 bar while operating at the same long-term water flux.

5.4. Membrane independent limiting flux in OARO

In this subsection, two different membranes were tested to determine whether the limiting flux of OARO (operated in AL-FS mode) is independent of the membrane properties.

In Figure 33, the water flux trends of the AQP and BW30LE membrane are presented for test case F5 (Table 7). The AQP and BW30LE membranes were operated at respective pressures of 50 bar and 40 bar, to ensure that the initial water fluxes were comparable and exceeded $20\ \mathrm{L/(m^2h)}$. Both membranes were operated at the same cross-flow velocity to ensure that no difference in the hydrodynamic conditions affected the limiting flux results. As shown in the figure, the water fluxes of both membranes converged to the same pseudo-stable water flux of approximately $9\ \mathrm{L/(m^2h)}$, which was previously determined to be the limiting flux. Hence, the presented results in Figure 33 suggest that the OARO limiting flux is independent of the membrane properties when operated in AL-FS mode. The membrane-independent limiting flux observed in OARO is consistent with the findings by Tang et al. in conventional RO/NF processes [115,121]. Similarly, Morrow et al. [124] also found that the limiting flux obtained in FO operation was membrane independent in the AL-FS mode.

Although both membranes achieved the same limiting flux, the flux reduction rate differed between the two. While the flux stabilised for the BW30LE membrane after 1 hour of alginate addition to the feed and draw solutions, the flux of the AQP membrane only stabilised after approximately 1.5 hours. Hence, it seems that the BW30LE membrane was more prone to fouling but in fact, the slower flux reduction of the AQP membrane can be attributed to a stronger ICP-self compensation effect – any minute reduction in the membrane's water flux due to fouling would immediately be counterbalanced by a reduction in ICP [113].

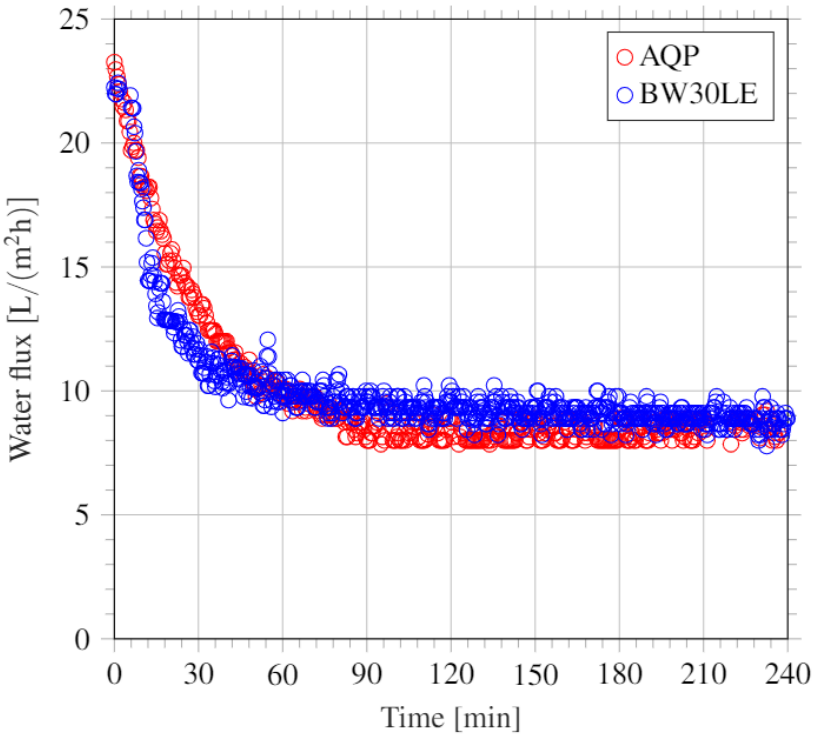


Figure 33: Effect of the membrane properties on OARO permeate flux evolution. All fouling experiments were carried out using the solutions specified for test case F5 in Table 1. The AQP and BW30LE membrane were operated at 50 bar and 40 bar, respectively.

The effective driving force (DF_{Eff}) of OARO can be described using the osmotic resistance filtration model, as was done in Section 2.1. The dilutive concentration polarisation factor f_{DCP} is modelled in Figure 34 (a) and the effective driving force DF_{Eff} is plotted in Figure 34 (b) for the given test case. If f_{DCP} equals 1, the contribution of the draw solution towards the overall driving force is basically nullified and the process is conventional RO. On the other hand, if f_{DCP} equals 0 then the draw solution fully contributes towards the overall driving force, which is ideal for osmotically driven membrane processes. The membrane properties stated in Peters et al. [68] for the AQP membrane at 50 bar ($A = 2.13\ \mathrm{L/(m^2h\ bar)}$, $B = 1.55\ \mathrm{L/(m^2h)}$, $S = 810\mu m$) and for the BW30LE membrane at 40 bar ($A = 6.41\ \mathrm{L/(m^2h\ bar)}$, $B = 2.24\ \mathrm{L/(m^2h)}$, $S = 2100\mu m$) were used to calculate the change in f_{DCP} for both membranes under the given fouling conditions. As shown in Figure 34 (a), f_{DCP} of the AQP membrane reduces more significantly than that of the BW30LE membrane with the progress of the fouling

test. Furthermore, Figure 34 (b) shows that the effective driving force of the AQP membrane increases by approximately 15 bar, whereas that of the BW30LE membrane only increases by roughly 9 bar. This showcases the stronger ICP self-compensation effect of the AQP membrane at higher operational water fluxes ($J_W > 4\ \mathrm{L/(m^2h)}$) due to its smaller structural parameter. It should be noted that the AQP membrane may also experience a weaker ICP self-compensation effect in the relatively low flux regime ($J_W \leq 4\ \mathrm{L/(m^2h)}$), but this is not the case in this study (refer to Appendix D).

This difference in the f_{DCP} trends shows that the membrane properties play a vital role during the transient flux decline period (Approximately the first 1.5 hours of operation). In addition, differences in the AQP membrane morphology (surface roughness: 96 nm [200], surface charge: -45 mV (pH=7) [200], -41 mV (pH=5.3)[201], contact angle: 53° [200], 58.6° [201], 68.2° [202]) and that of the BW30LE membrane (surface roughness: 53 nm, surface charge: -30 mV (pH=6.5), contact angle: 42°)[203] may be another cause for different fouling propensities. To identify which of the two membranes is more prone to fouling, the foulant resistance R_F can be calculated [76], as discussed in Section 2.1. Using the membrane properties given in Peters et al. [68] and the given operating conditions in this Chapter, the change in the foulant resistance during the experiment can be calculated.

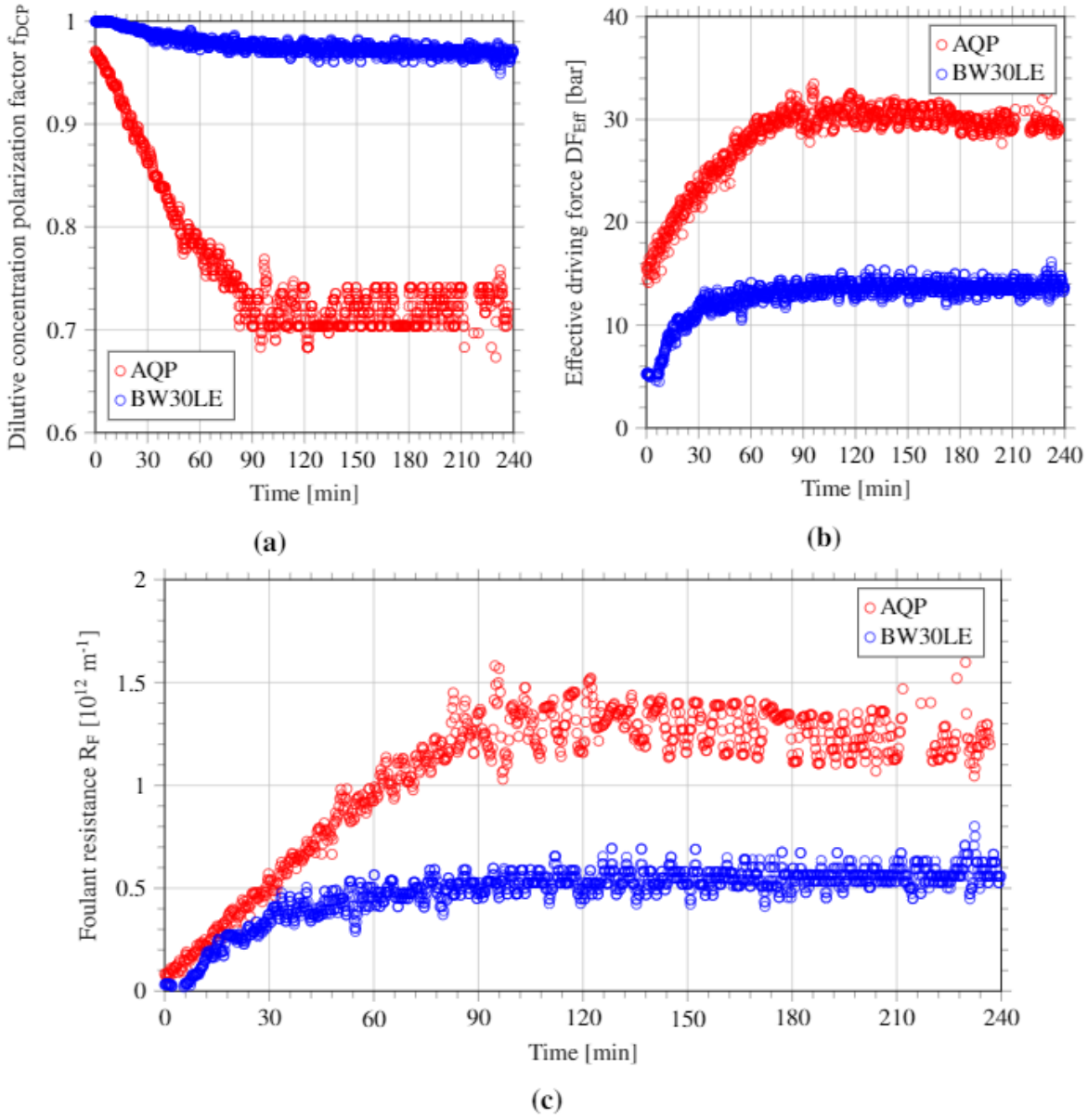


Figure 34: (a) Visualisation of the ICP self-compensation effect for the AQP and BW30LE membrane using the change of f_{DCP} as indicator, (b) the change of the effective driving force with fouling progression, and (c) the calculated foulant resistance of both membranes during the F5 fouling scenario.

As shown in Figure 34 (c), the foulant resistance of the AQP membrane increased more drastically during the initial stage of the flux decline period than for the BW30LE membrane. The higher fouling resistance of the AQP membrane can be attributed to its higher DF_{Eff} during the experiment [76]. Once the limiting flux is reached for either membrane, R_F remains constant, which shows that a pseudo-stable state is reached in which its foulant resistance

remains relatively constant, suggesting additional foulant accumulation on the membrane would not occur.

As observed above, the membrane properties are not important when operating at the limiting flux, but they are still important during the initial stages of the fouling period or when the final pseudo-stable flux is lower than the limiting flux [114,124]. Therefore, the OARO membrane properties are an important consideration when (1) continuous membrane cleaning is considered, or when (2) operating at pressures and feed conditions where the final pseudo-stable flux is below the limiting flux. Depending on the membrane properties, the operating conditions and the feed composition, the critical flux and hence the onset of membrane fouling will differ between the AQP and BW30LE membrane. Thus, the conceptual flux behaviour will differ between the two membranes. Under the given feed and operating conditions, the AQP membrane has a higher fouling propensity than the BW30LE membrane, as shown in Figure 34 (b). Hence, it is likely that the critical flux of the AQP membrane is lower than that of the BW30LE membrane. This issue has, however, not been investigated further in this work.

5.5. OARO membrane fouling reversibility

Three cleaning scenarios (i.e., surface flushing, osmotic backwashing using DI water (ideal OB), and osmotic backwashing using non-pure solution (real OB)) were tested on the AQP membrane to investigate the fouling reversibility. The results presented in Figure 35 show that the ideal OB is the best cleaning strategy, which is capable of fully restoring the initial water flux in OARO. Similarly, the ideal OB approach also exhibited high cleaning efficiency for the BW30LE membrane (Refer to Appendix D), despite its lower back washing flux and different membrane properties from that of the AQP membrane.

A high flux recovery can be related to the relatively weak interaction between alginate and the membrane surface, as alginate is of a hydrophilic nature. In addition, larger aggregates were formed when calcium ions bound the carboxylic functional groups of adjacent alginate macromolecules. Hence, the larger alginate aggregates were easily loosened from the membrane surface due to the lifting force created by the backwash permeation. The loosened cake/gel layer was then fully removed from the membrane surface by the shear-induced erosion caused by the cross-flow velocity on the membrane's feed side [204]. This finding is consistent with those made in prior studies on the reversibility of alginate fouling in FO [204,205]. In another study, Blandin et al. [206] found that although osmotic backwashing effectively removed alginate and humic acid aggregates from the membrane surface, the dislodged foulants would not be effectively removed from the feed channel at low CFV (10 cm/s). Instead Blandin et al. [206] found they had to use a higher CFV of 0.35 m/s to fully remove the foulants from the feed channel. This issue was not observed during our OB experiments, which were carried out at a CFV of 10 cm/s, as no feed spacer was employed.

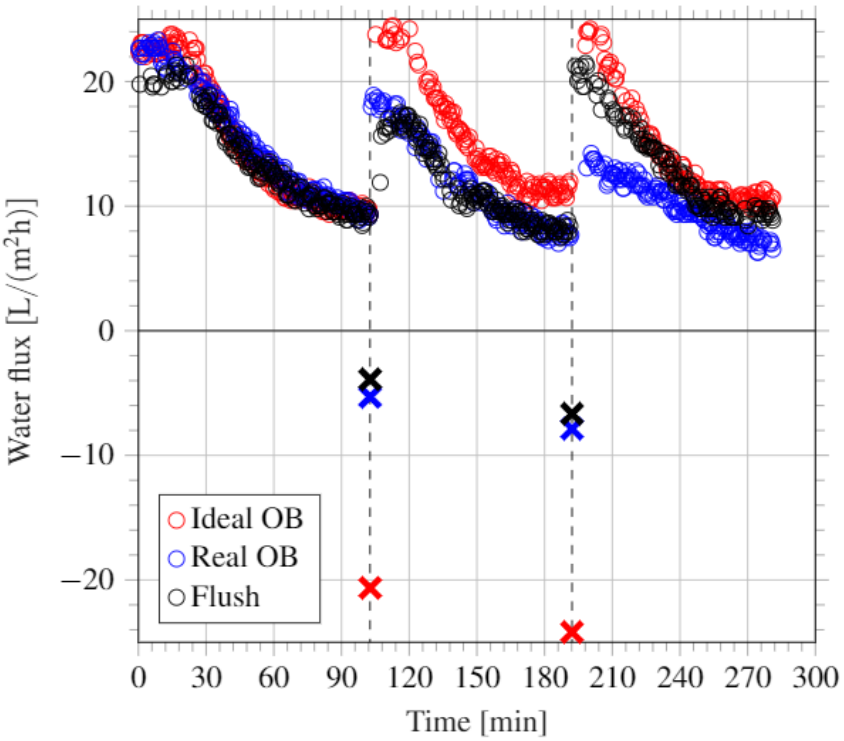


Figure 35: The effectiveness of the three cleaning scenarios. Ideal OB: Osmotic backwash using 2.4M NaCl feed and DI water as draw. Real OB: Osmotic backwash using OARO brine as feed and draw according to test case F5 (Table 7). Flush: surface flushing using DI water as feed and draw solution. The different cleaning conditions are specified in Section 5.1.4. and Appendix D. All fouling experiments were carried out using the solutions specified for test case F5 in Table 1. The AQP membrane was operated at 50 bar with a CFV of 10 cm/s during the fouling cycles. Each of the three fouling cycles lasted 80 min, to give a total fouling duration of 4 hours whereas each cleaning cycle lasted 10 minutes. The negative flux in the figure indicates that the flux is reversed during cleaning.

In comparison to the ideal OB, the initial water flux could not be fully restored using the real OB. The initial water flux decreased for each subsequent fouling cycle, indicating that the foulant resistance R_F increased cumulatively after each fouling and cleaning cycle. As would be expected, using saline draw solutions lowered the reverse water flux, as shown in Figure 35. This in turn meant that the hydrodynamic drag force used to detach the foulants from the membrane surface was lowered. Moreover, as the permeating flux was momentarily reversed during OB, foulants from the draw solution could have been drawn into the membrane substrate, which could cause pore blockage. In this case, removing the deposited foulants within the membrane substrate could be difficult even after the direction of the operational OARO water flux was restored after cleaning. Pore blockage was observed by several

researchers, and is generally regarded as irreversible [204,205,207,208]. Therefore, cleaning of the OARO membrane is also not advised using impure draw solutions. On-line osmotic backwashing of the OARO membrane is therefore not recommended if impure draw solutions are to be utilised.

While the efficiency between the different flushing cycles seems to differ, membrane flushing is still deemed more effective than real OB. As previously mentioned, the calcium alginate aggregates caused a severe flux decline during OARO operation, but these were easily removed from the membrane surface due to their large size. It is also important to mention that although the membrane was flushed with deionised feed and draw solutions, a reverse water flux was still generated (as shown in Figure 35), which may have improved the flushing efficiency. Similarly, Kim et al. also observed a reverse water flux during surface flushing [205]. This backwashing water flux can be attributed to the CECP phenomenon (Refer to Section 2.3.). Generally, ions are trapped between the membrane's active layer and the adjacent foulant layer due to CECP. Once the draw and feed solutions are swapped from the fouling solutions to the deionised solutions, these ions are still trapped in the foulant layer and cause a transmembrane osmotic pressure difference from feed to draw side. Hence, reverse water permeation is induced during membrane flushing. This is beneficial in the sense that simple membrane flushing induces a reverse water flux that helps to dislodge the cake/gel layer from the membrane surface. However, the magnitude of the backwash water flux is not constant between cleaning cycles, and its duration is relatively short. This may explain the varying efficiency of membrane flushing.

5.6. Chapter conclusions

In this Chapter, fouling in the OARO membrane process has been systematically investigated. The presented findings offer insights into (1) the fouling mechanisms occurring during OARO operation, and (2) the impacts of membrane fouling on the process performance. Furthermore, the presented results offer guidance for OARO operation under extreme operating conditions with harsh feed and draw solutions. The following conclusions highlight the findings of the study:

- The presented results suggest that the limiting flux was independent of the OARO membrane properties. However, the membrane properties played a vital role (1) when operating at pseudo-stable fluxes below the limiting flux, (2) during the initial stages of fouling when the limiting flux has not yet been reached, and (3) during membrane cleaning.
    - The AQP membrane with a thinner substrate experienced a higher fouling resistance due to its stronger ICP self-compensation effect at the high operating flux.
    - Membranes with a thinner substrate are preferred for osmotic backwashing or flushing, as a higher backwash flux could be achieved during membrane cleaning.
- Long-term OARO operation at 50 bar was more energy efficient than at 60 bar for the given feed composition, as the same pseudo-stable flux (limiting flux) was achieved at both pressures.
- For an AL-FS orientation, fouling on the membrane's draw side was negligible during OARO operation. Fouling mainly occurred due to the formation of a cake/gel layer on the membrane's active layer on the feed side.

    - Hence, impure draw solutions could potentially be used for OARO operation with a low risk of membrane fouling. However, fouling and plugging of the draw channel can increase the draw side pressure loss.
    - Conversely, using impure draw solutions prohibits the use of on-line osmotic backwashing, as foulants may enter the membrane's substrate during cleaning and cause irreversible membrane fouling. In addition, using saline draw solutions during backwashing lowers the reverse water flux and hence, lowers the OB cleaning efficacy.
- Fouling by alginate in the presence of calcium ions was severe during OARO operation. This fouling layer was, however, easily detachable from the membrane.
- To prevent severe membrane fouling in OARO, continuous membrane cleaning is required, or the feed solution must be softened and/or alginate removed.

The experimental work presented in this Chapter showcases the detrimental effects of membrane fouling on OARO operation. While it is difficult to compare the fouling propensity of different membrane processes under equivalent operating conditions, it is highly likely that other membrane processes would also suffer from membrane fouling when operated under these extreme fouling conditions and at the tested water fluxes. Hence, OARO remains a promising BVM/ZLD technology, especially when membrane fouling can be minimised via sufficient feed pre-treatment or via cyclic membrane cleaning.

Chapter 6

Conclusions and future work

In order to advance desalination as a globally accessible and sustainable source of potable water, this thesis aims to numerically and experimentally investigate the potential technical and economic feasibility of OARO. OARO was chosen as the sole focus of this study because of its potential as a low-cost, energy efficient, and sustainable BVM technology. To minimise the environmental footprint of desalination and make it more sustainable, attention was given to three main considerations, which were:

(1) Reducing the process specific energy consumption of desalination to facilitate a potentially lower carbon footprint. This was done by modelling the efficiency of different OARO process flowsheets in Chapter 3 to determine the most energy efficient and least expensive flowsheet. In addition, the incorporation of cheaper and alternative energy sources into OARO processes was investigated in Chapter 4 in the hope that the use of 'waste' heat could lower the overall process cost, and to reduce the consumption of electricity and other high-grade forms of energy.

(2) Lowering the chemical additive (e.g., anti-fouling and anti-scaling agents) and consumable materials demand, such as when fouled membrane modules need to be replaced for the latter. This was done by experimentally investigating the fouling behaviour of OARO processes in Chapter 5. Different fouling mitigation techniques were investigated to improve process performance and to prolong membrane life without the use of chemical cleaning agents.

(3) Increasing process recovery to lower the amount of feedwater required and the brine discharged. BVM and ZLD technologies are preferred solutions in areas in which brine disposal is difficult and/or where regulations are strict due to environmental concerns. The development of high recovery OARO processes was a main focus in Chapters 3 and 4, whereas Chapter 5 focussed on the technical viability of OARO operation under extreme, non-ideal feed conditions.

In addition to improving the sustainability of desalination, another main objective was to lower the overall capital and operating cost of the developed BVM and ZLD processes to improve their applicability. This was done by:

(1) Enhancing the energy efficiency of the desalination process to lower the unit water cost. Energy efficiency and economics of the proposed desalination processes were a main focus in Chapters 3 and 4.

(2) Improving the reliability and process performance of the desalination process to lower the unit water cost. To ensure that the OARO process can run continuously and at a high water flux, a thorough investigation was made in Chapter 5 to understand OARO membrane fouling and the ways in which it can be mitigated.

6.1. Chapter summaries

The numerical work presented in Chapter 3 showcases that OARO integrated processes are economically viable alternatives to current brine dewatering techniques, as they offer the possibility to achieve high system recoveries at comparatively lower energy costs and operating pressures. Pressure driven membrane processes have proven to be significantly more energy efficient than their thermal, non-membrane counterparts. Furthermore, the lower specific energy consumption of OARO in comparison to other osmotically driven membrane processes, such as FO/PAO, make it an economically viable process addition for brine volume minimisation. In comparison to MSRO, OARO is technically feasible as a means to achieve the desired brine concentration. High pressure RO, MSRO, FO/PAO and OARO are not mutually exclusive processes. and can be combined to eventually achieve brine concentrations of up to 250 g/L in a more cost efficient and sustainable manner to compete with, or replace thermal processes.

Of the six OARO integrated flow processes, SF-1 shows the best performance at lower feed concentrations. Recoveries of up to 72% from a 35 g/L saline feed are possible when operating at the membrane burst pressure of 48.3 bar. It is the only technically feasible process to achieve the desired process recovery with a maximum of three OARO stages. SF-1 also has the second lowest energy consumption and capital expenditure after C-1, which is however, the least feasible OARO integrated flow process due to its high capital expenditure. The energy consumption of SF-1 is approximately 4.00 kWh/m3, which is significantly lower than that in currently employed high recovery thermal processes, such as mechanical vapour compression ($7-25\ \mathrm{kWh/m^3}$). Furthermore, the permeate salinity for SF-1 is of acceptable quality according to the WHO drinking water guidelines.

At the higher inlet salinity (70 g/L), C-2 shows the greatest promise, as it achieves a reasonable permeate quality while achieving the desired recovery at feasible OARO feed pressures. The maximum recovery of 44% is achieved at an average energy consumption of 6.37 kWh/m3.

In Chapter 4, an additional draw solute is used in the OARO process to enhance the recovery. This draw solute is thermo-responsive and can be regenerated using low-grade heat. A direct parametric and techno-economic comparison is performed between this OARO process and its FO equivalent to highlight the benefits of combining OARO with a thermo-responsive draw solute and how OARO can alleviate several of the shortcomings of FO. Furthermore, the OARO and FO MBC are compared to the conventional OARO and the LSRRO process to identify which of these novel membrane-based ZLD processes is the superior technology.

Extremely high brine concentrations of up to 245 g/kg can be achieved by the OARO MBC at technically feasible operating pressures (48.3 bar) and at reasonable draw solute concentrations (6 mol/kg on a carbon basis). This high brine concentration is not achievable by the FO MBC utilising the same thermo-responsive DS or by the conventional OARO system using a non-responsive DS. Utilising a thermo-responsive DS allows for the utilisation of low-cost thermal energy to drive the desalination process. The integration of LGWH can substantially reduce the required electrical energy consumption to levels below those achievable by LSRRO and by the conventional OARO process. However, one main disadvantage of utilising thermo-responsive draw solutes is that additional heat transfer equipment and cooling water are required, which is not the case for LSRRO and the conventional OARO process. These disadvantages can, however, be minimised by the OARO MBC, as the specific cooling load is reduced by 31% in comparison to its FO counterpart.

The SEC and UWC of the BVM process can be reduced by approximately 10.8% and 15.5% by operating the MBC in OARO mode, respectively. Furthermore, OARO is more suited to

LGWH integration than is FO, as the reboilers of the OARO MBC can be operated at temperatures up to 12°C lower. LGWH integration is economically more sensible for high prevailing grid electricity costs, as the operational cost savings then more greatly outweigh the capital cost increases caused by the use of larger reboilers.

In comparison to other hydraulic pressure-driven ZLD technologies, such as low-salt-rejection RO (LSRRO), the electrical energy consumption of OARO can be significantly offset when powered by LGWH and using a thermo-responsive draw solute. The specific electrical energy consumption can be as low as 3.47 kWh/m3 when concentrating a saline stream from 0.6 M to 4 M using 4 membrane stages. At the same time, a 4-stage LSRRO system would consume approximately 48% more electricity to achieve the same concentration factor. Furthermore, OARO processes operating with a thermo-responsive draw solution can outperform those using non-responsive draw solutes. Brine concentrations of up to 245 g/kg can be achieved using technically feasible operating pressures and draw solute concentrations, while the number of required membrane stages is almost halved from 6 to 4.

In Chapter 5, fouling in the OARO membrane process has been systematically investigated. The presented findings offer insights into (1) the fouling mechanisms occurring during OARO operation, and (2) the impacts of membrane fouling on the process performance. Furthermore, the presented results offer guidance for OARO operation under extreme operating conditions with harsh feed and draw solutions.

The limiting flux is independent of the OARO membrane properties. However, the membrane properties play a vital role (1) when operating at pseudo-stable fluxes below the limiting flux, (2) during the initial stages of fouling when the limiting flux has not yet been reached, and (3) during membrane cleaning.

Long-term OARO operation at 50 bar was more energy efficient than at 60 bar for the given feed composition, as the same pseudo-stable flux (limiting flux) was achieved at both pressures. For an AL-FS orientation, fouling on the membrane's draw side was negligible during OARO operation. Fouling mainly occurred due to the formation of a cake/gel layer on the membrane's active layer on the feed side. Hence, impure draw solutions could be potentially used for OARO operation at low risk of membrane fouling. However, fouling and plugging of the draw channel can increase the draw side pressure loss. Conversely, using impure draw solutions prohibits the use of on-line osmotic backwashing, as foulants may enter the membrane's substrate during cleaning and cause irreversible membrane fouling. In addition, using saline draw solutions during backwashing lowers the reverse water flux and hence, lowers the OB cleaning efficacy.

Fouling by alginate in the presence of calcium ions was severe during OARO operation. This fouling layer was, however, easily detachable from the membrane. To prevent severe membrane fouling in OARO, continuous membrane cleaning is required, or the feed solution must be softened and/or alginate removed.

6.2. Future work

The work presented in this thesis highlights the potential of OARO as a BVM/ZLD technology as well as its technical limitations due to membrane fouling. Although in Chapter 3 some OARO integrated flow processes have been investigated, these are still relatively simple when compared to the endless possibilities offered by integrating various high-recovery membrane processes. For example, as LSRRO, OARO and MSRO are not mutually exclusive processes, these can be combined into a single process to achieve the desired recovery at possibly lower cost and higher energy efficiencies but at higher operational complexity. The combination of these processes can lead to new process designs that benefit from the various advantages offered by each technology and should be further investigated.

Similarly, only a single thermo-responsive draw solute was investigated as model draw solute in Chapter 4. Various different draw solutions have been investigated for FO [28] that may also be beneficial to OARO. The investigation of the inclusion of various draw solutes, especially those that can be regenerated using low-grade heat or any other form of cheap energy, into OARO processes may lead to the further development of low-cost, high recovery desalination processes.

In addition to modelling new process layouts and new draw solutes, it is also important to enhance the process reliability at the lowest cost possible by potentially incorporating additional processes that combat membrane fouling. For example, extensive pre-treatment that minimises organic and biological content downstream may be worthwhile if the reliability and process performance of the high recovery membrane processes can be increased. In the presented numerical work, fouling was excluded. Expanding numerical models of OARO processes to include fouling tendencies will be helpful in choosing additional processes to be incorporated, or to determine operational conditions and cleaning regimes that minimise plant downtime and optimise process performance.

In terms of experimental work, it would be useful to test the fouling mitigation techniques presented in Chapter 5 on entire membrane modules to further optimise the OARO module design. In addition, the development of cheap hollow-fibre or spiral wound membrane modules with membranes that (1) have a low structural parameter to minimise ICP, (2) can withstand high transmembrane pressures, and (3) have the ideal permeability and selectivity to optimise the process performance would significantly advance this technology.

Appendix A

A.1. Practical SEC and P_{Max} of the single-stage SF-OARO process

The single stage SF-OARO process is displayed in Figure 36. The SEC of the entire system is given by:

$$SEC_{SF-OARO} = SEC_{RO} + SEC_{OARO1}$$

$$SEC_{SF-OARO} = \frac{k\pi_2(Y_S V_F)}{Y_S V_F} + \frac{k(\pi_B - \pi_2)[(1 - RR)V_2 - (1 - Y_S)V_F]}{Y_S V_F} \quad (36)$$

where k, Y_S and RR are the over-pressurization factor ($k = 1.15$ [18]), the system recovery and the flowrate ratio, which is defined as:

$$RR = \frac{V_3}{V_2} \quad (37)$$

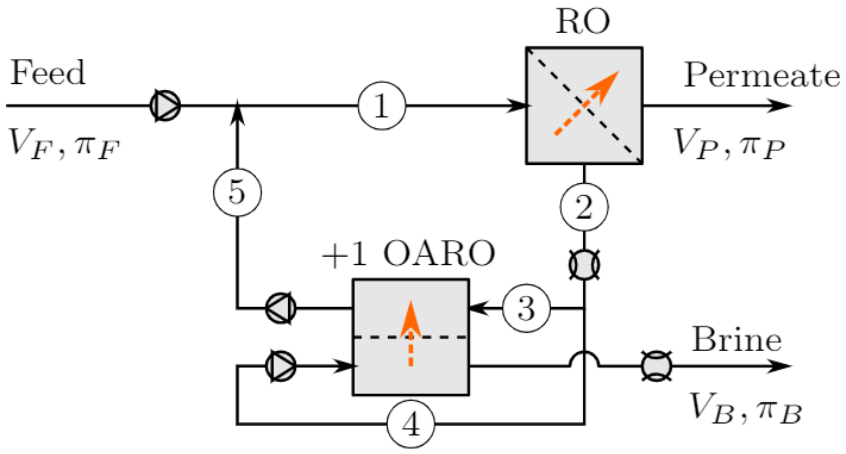


Figure 36: Single stage SF-OARO process layout

Under ideal operating conditions, the concentration of the recirculated stream V_5 is the same as that of the feed solution V_F ($\pi_5 = \pi_F,\ \pi_1 = \pi_F$) to prevent entropy losses incurred by mixing

of streams with different salinities. Furthermore, it is assumed that all pumps and energy recovery devices (ERDs) have a 100% efficiency and that all membranes have a 100% solute rejection. Hence, the solute mass balance across the RO membrane stage is given by:

$$V_2\pi_2 = V_1\pi_F$$

$$(V_1 - Y_S V_F)\pi_2 = V_1\pi_F$$

$$\pi_2 = \frac{V_1}{(V_1 - Y_S V_F)}\pi_F \tag{38}$$

Similarly, the solute mass balance on the pressurised side of the OARO stage is given as:

$$V_4\pi_4 = V_B\pi_B$$

$$(1 - RR)(V_1 - Y_S V_F)\pi_2 = (1 - Y_S)V_F\frac{\pi_F}{1 - Y_S} \tag{39}$$

Substituting π_2 into Equation (39) gives:

$$V_1 = \frac{V_F}{1 - RR} \tag{40}$$

and hence:

$$V_2 = (V_1 - Y_S V_F) = V_F\left(\frac{1 - Y_S(1 - RR)}{1 - RR}\right) \tag{41}$$

$$\pi_2 = \frac{1}{1 - Y_S(1 - RR)}\pi_F \tag{42}$$

Substituting π_2 and V_2 into Equation (36) then gives $SEC_{SF-OARO}$ in terms of the flowrate ratio:

$$SEC_{SF-OARO} = k\pi_F\left[\frac{1 - RR}{1 - (1 - RR)Y_S} + \frac{RR}{1 - Y_S}\right] \tag{43}$$

The maximum operating pressure required is given by:

$$P_{Max} = \max\left(\frac{k\pi_F}{1 - Y_S(1 - RR)}, \left[\frac{k\pi_F}{1 - Y_S} - \frac{k\pi_F}{1 - Y_S(1 - RR)}\right]\right) \tag{44}$$

A.2. Practical SEC and P_{Max} of the two-stage SF-OARO process

The two-stage SF-OARO process is depicted in Figure 37. It is assumed that the flowrate ratio RR is equivalent for both OARO processes. Therefore, the SEC of the entire process is given by:

$$SEC_{SF-OARO} = SEC_{RO} + SEC_{OARO1} + SEC_{OARO2}$$

$$SEC_{SF-OARO} = \frac{k\pi_2(Y_S V_F)}{Y_S V_F} + \frac{k(\pi_6 - \pi_2)[(1-RR)V_2 - V_6]}{Y_S V_F} + \frac{k(\pi_B - \pi_6)[(1-RR)V_6 - (1-Y_S)V_F]}{Y_S V_F} \quad (45)$$

The solute mass conservation across the first OARO module gives:

$$(V_1 - V_F)\pi_F = RR(V_2 + V_9)\pi_2 \quad (46)$$

$$V_6\pi_6 = (1-RR)\,(V_2 + V_9)\pi_2 \quad (47)$$

Equating equations (46) and (47) gives:

$$\frac{V_6\pi_6}{1-RR} = \frac{(V_1 - V_F)\pi_F}{RR} \quad (48)$$

The solute mass balances across the second OARO process are given by:

$$V_8\pi_6 = V_B\pi_B$$

$$(1-RR)V_6\pi_6 = (1-Y_S)V_F\frac{\pi_F}{1-Y_S} \quad (49)$$

And:

$$V_7\pi_6 = V_9\pi_2$$

$$RR\,V_6\pi_6 = V_9\pi_2 \quad (50)$$

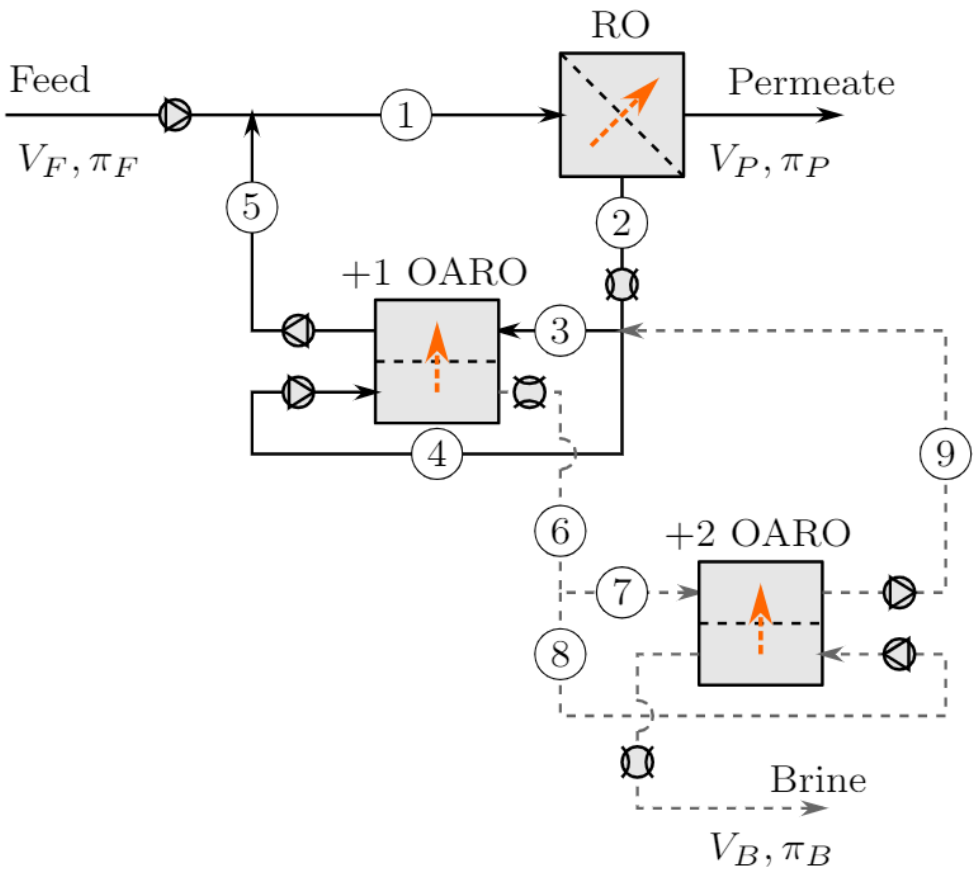


Figure 37: Two stage SF-OARO process layout

Substituting equation (50) into (49) gives:

$$\frac{V_F \pi_F}{(1 - RR)^2} = \frac{(V_1 - V_F)\pi_F}{RR}$$

$$V_1 = V_F \left(\frac{RR}{(1 - RR)^2} + 1 \right) \tag{51}$$

V_1 can then be used to find the remaining unknowns in equation (45):

$$V_2 = V_1 - Y_S V_F = V_F \left(\frac{RR}{(1 - RR)^2} + 1 - Y_S \right) \tag{52}$$

$$\pi_2 = \frac{V_1}{(V_1 - Y_S V_F)}\pi_F = \pi_F \frac{\left(\frac{RR}{(1-RR)^2} + 1\right)}{\left(\frac{RR}{(1-RR)^2} + 1 - Y_S\right)} \quad (53)$$

$$\frac{V_F \pi_F}{1 - RR} = \frac{V_9 \pi_2}{RR}$$

$$V_9 = \frac{RR}{1 - RR} \times \frac{V_F\, \pi_F}{\pi_2} \quad (54)$$

$$V_6 = V_B + V_9 = (1 - Y_S)V_F + \frac{RR}{1 - RR} \times \frac{\pi_F}{\pi_2} \quad (55)$$

$$\pi_6 = \frac{V_F \pi_F}{(1 - RR)V_6} \quad (56)$$

The maximum operating pressure for each RR value is given by:

$$P_{Max} = \max\left(k\pi_2, k(\pi_6 - \pi_2), k(\pi_B - \pi_6)\right) \quad (57)$$

The variation of $SEC_{SF-OARO}$ and P_{Max} with respect to the flowrate ratio for both SF-OARO systems are displayed in Figure 38. The results displayed in Figure 4 for the SF-OARO are given for the RR value at which the lowest SEC point.

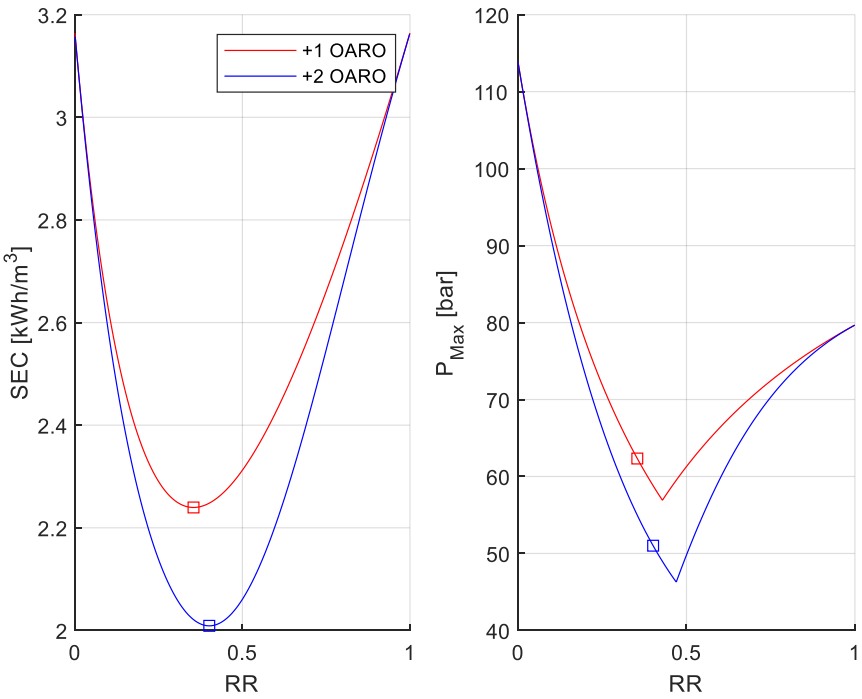


Figure 38: The SEC and the maximum operating pressure for the SF-OARO system as a function of the flowrate ratio RR

f

Appendix B

B.1. Model validation using ROSA

The self-developed model based on the advanced solution-diffusion model is utilised to simulate both RO/NF processes and the OARO process. An NF (NF90-400) and SWRO (SW30HR LE-400) membrane are modelled for different operating parameters using ROSA, which is a RO system analysis (ROSA) software developed by the membrane manufacturer DOW, and the self-developed model. The simulation set-up in both the ROSA and the self-developed model is equivalent.

B.1.1. Validation of RO modelling capability

Figure 39 and Figure 40 compare the obtained water flux and permeate salinity at different RO feed pressures and two inlet flowrates. The feed salinity and temperature are constant at 35 g/L and 25°C respectively. 8 membrane modules are packed in each pressure vessel. The RO inlet flowrate is set at $12\ m^3/h$ (solid line) and $8\ m^3/h$ (dashed line).

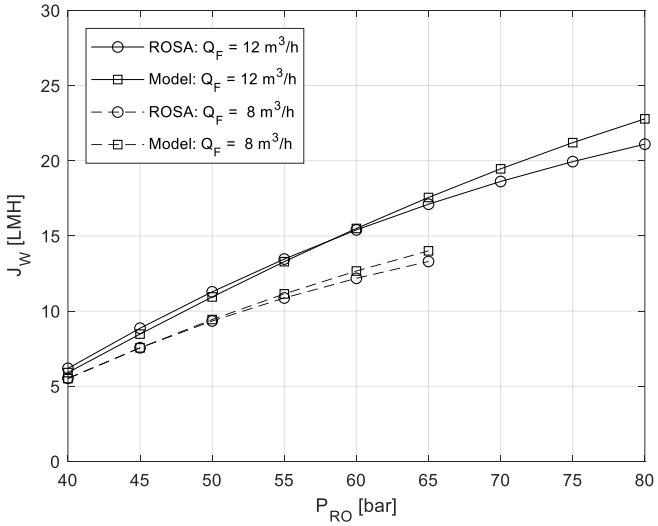


Figure 39: Water flux with respect to the RO feed pressure for two different inlet flowrates.

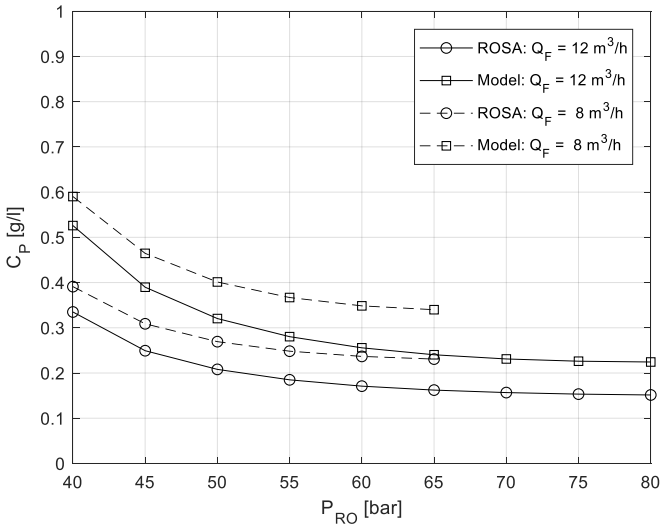


Figure 40: Permeate salinity with respect to the RO feed pressure for two different inlet flowrates.

The obtained water flux of both simulations is almost equivalent, whereas the permeate salinity is approximately 0.2 g/L higher for the self-developed model. This means that the salt diffusion is over-predicted for the self-developed model and that the simulated permeate quality is lower than if modelled by ROSA.

Both models were also compared at various inlet salinities as shown in Figure 41 and Figure 42. Two different RO feed pressures were simulated at a constant feed flowrate of 12 m^3/h. As shown, the water flux is again comparable between the two simulations. Furthermore, the permeate salinity is predicted accurately even when the water flux is very low at an inlet salinity of 60 g/L and a 50 bar feed pressure.

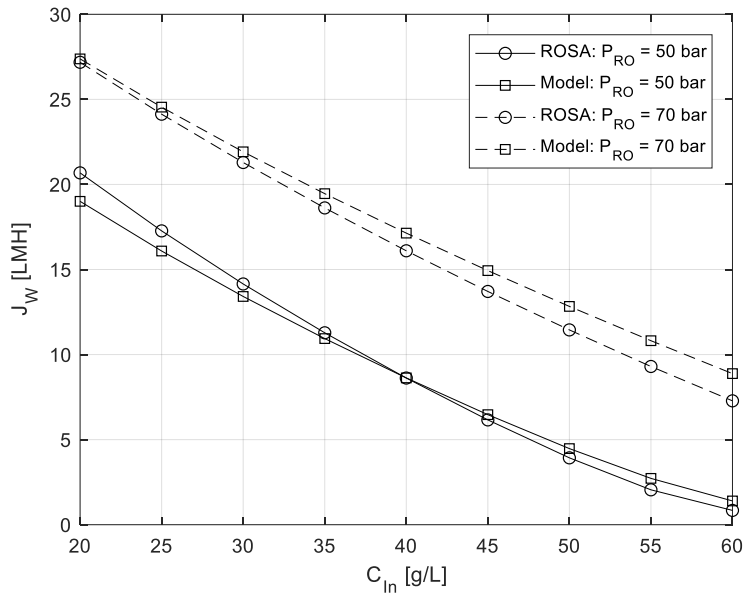


Figure 41: Water flux with respect to the feed inlet salinity for two different RO operating pressures.

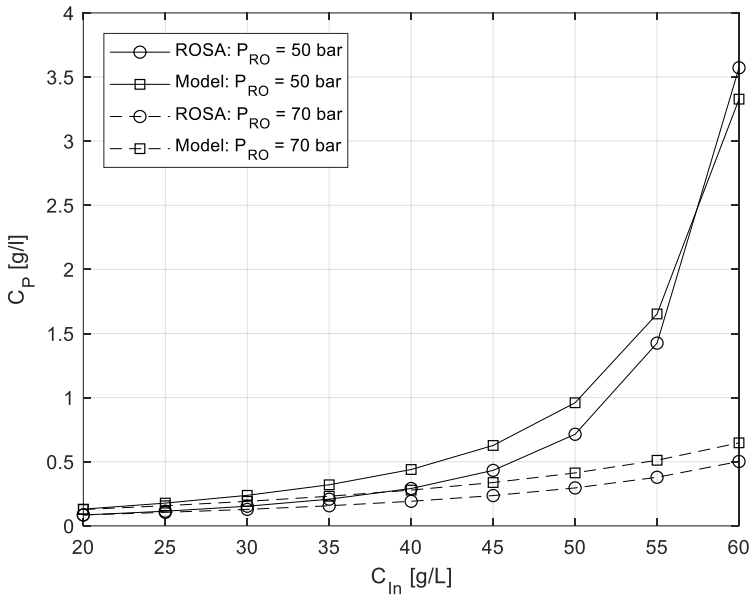


Figure 42: Permeate salinity with respect to the feed inlet salinity for two different RO operating pressures.

B.1.2. Validation of NF modelling capability

As mentioned by Blandin et al. [73], the solution-diffusion model presents a reasonable fit with experimental values for the NF90 membrane. For looser NF membranes this might not be the case, as ion transport in looser membranes does not occur only via solution diffusion mechanisms, but also via convection and electro-migration. Therefore, ion transport in looser

NF membranes, such as the NF270, should be simulated by models based on the extended Nernst-Planck equation, as done by Bowen & Welfoot [209].

In this case, NF90 is modelled in both ROSA and the self-developed model with the help of the solution-diffusion model. Figure 43 and Figure 44 present the predicted water flux and permeate salinity of both models. Each NF pressure vessel consists of 6 membrane modules and the inlet salinity and temperature are 35 g/L and 25°C, respectively. As done before, the NF feed pressure is varied for feed flowrates of $12\ m^3/h$ (solid line) and $8\ m^3/h$ (dashed line).

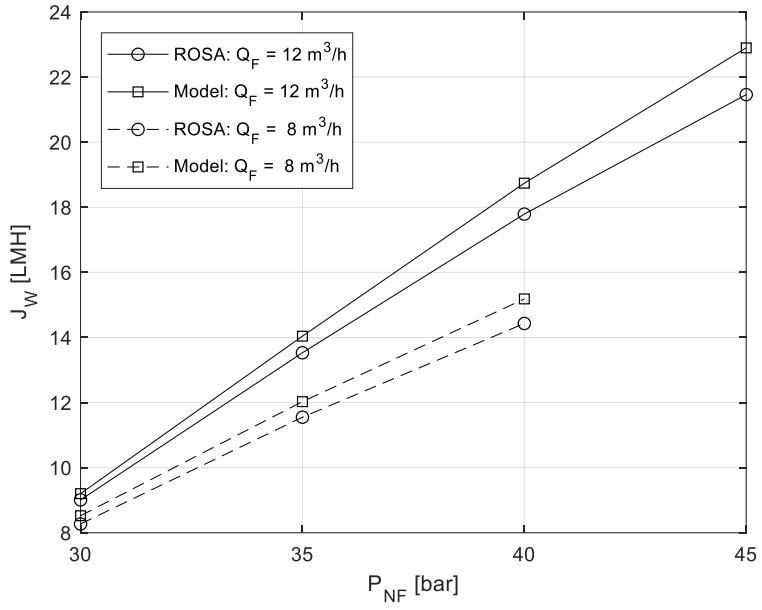


Figure 43: Water flux with respect to the NF feed pressure for two different inlet flowrates.

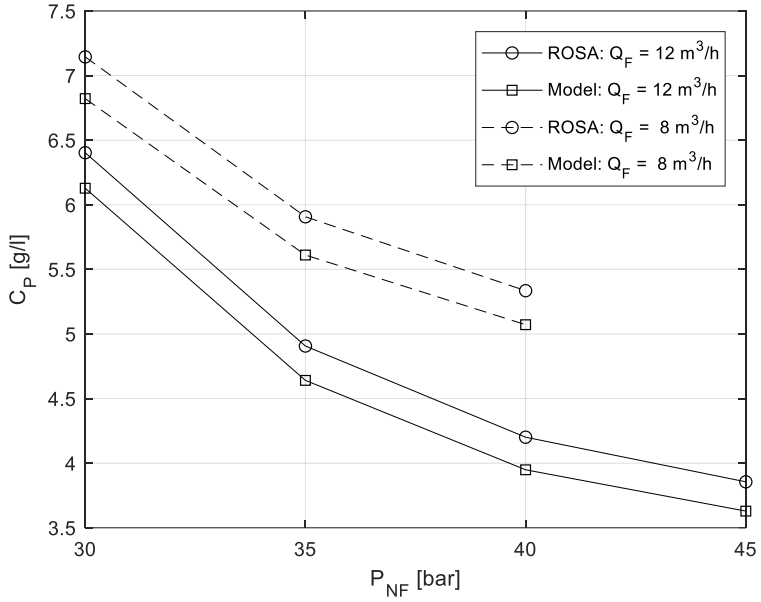


Figure 44: Permeate salinity with respect to the NF feed pressure for two different inlet flowrates.

Furthermore, the applicability of the self-developed model to simulate tight NF membranes was further tested by simultaneously increasing the feed salinity and NF feed pressure. The simulation results of the water flux and permeate salinity are depicted in Figure 45 and Figure 46, respectively.

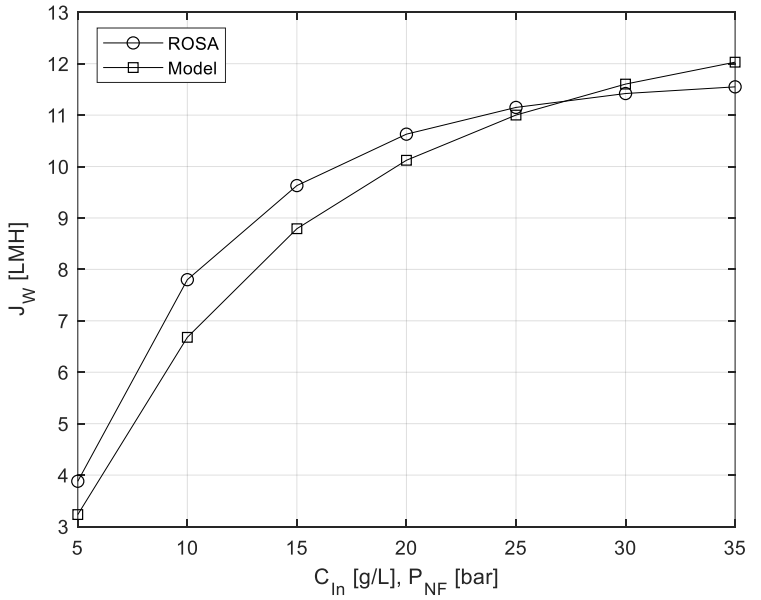


Figure 45: Water flux with respect to the NF feed pressure and inlet salinity.

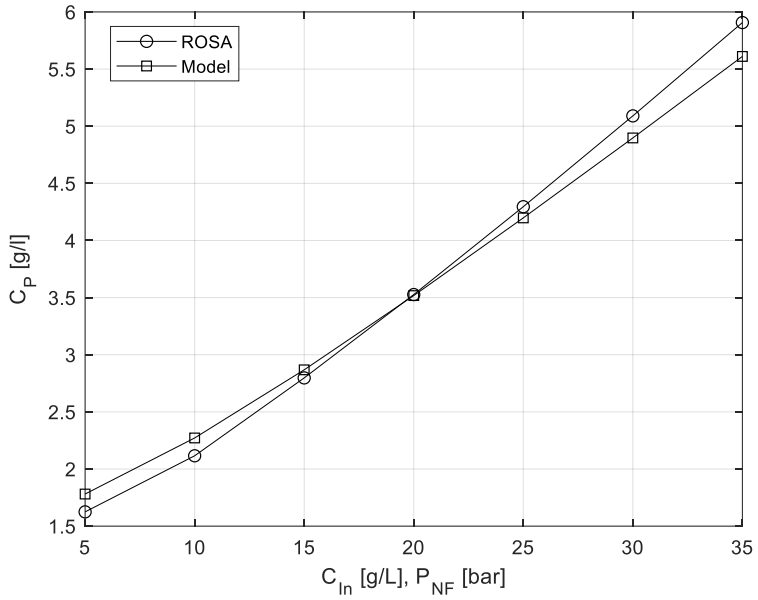


Figure 46: Permeate salinity with respect to the NF feed pressure and inlet salinity.

All four figures show a relatively good fit between the ROSA and the self-developed model results. Thus, it is assumed that the self-developed model can accurately simulate the NF90 membrane process.

B.2. Model validation using experimental data for PAFO module testing

The self-developed model has been validated for NF and RO operations, but it is still important to validate the model under FO and PAFO operation to ensure the model's accuracy at lower feed pressures and higher permeate concentrations.

Jeon et al. [136] presented experimental data for an FO spiral wound module. Five of these experiments were simulated using the self-developed model under the same operating conditions and membrane properties. Figure 47 displays the experimental and modelled water flux with respect to the difference in NaCl concentration of the draw and feed solution. All five experiments were either performed at different feed flowrates, RR values or slightly different hydraulic pressure differences. As shown, the model tends to generally underestimate the experimental water flux at both high and low concentration differences.

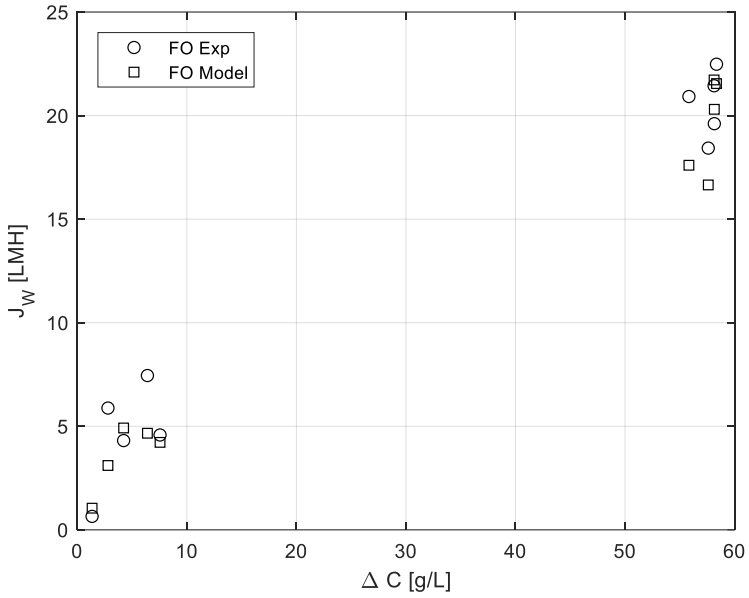


Figure 47: Water flux with respect to the concentration difference between the feed and draw stream. Experimental data is obtained from Jeon et al. [136].

The self-developed model was further validated under slightly higher feed pressures of up to 2.5 bar for a CTA and TFC FO membrane module. The experimental findings are stated by Kim et al. [145]. All operational conditions are clearly stated, but the membrane's solute diffusion coefficient and structural parameter are not mentioned. Therefore, the structural parameter for the CTA and TFC membrane were assumed to be 1.028 mm and 0.471 mm, respectively [81]. B was however assumed to be approximately 1.2 $\mathrm{L}/(\mathrm{m}^2\mathrm{h})$ for both membranes.

As shown in Figure 48 and Figure 49, the self-developed model can also accurately predict the water and salt flux under these operating conditions. To conclude, the advanced solution-diffusion model is applicable to simulate RO/NF and FO/PAFO operations.

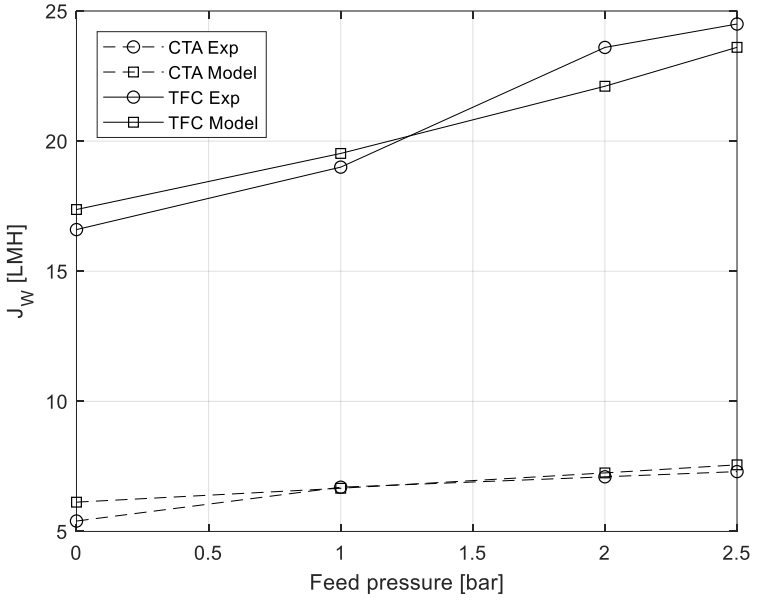


Figure 48: The experimental and modelled water flux for two different FO membrane modules under PAFO operation. Experimental data is obtained from (Kim, Blandin, & Phuntsho, 2017)

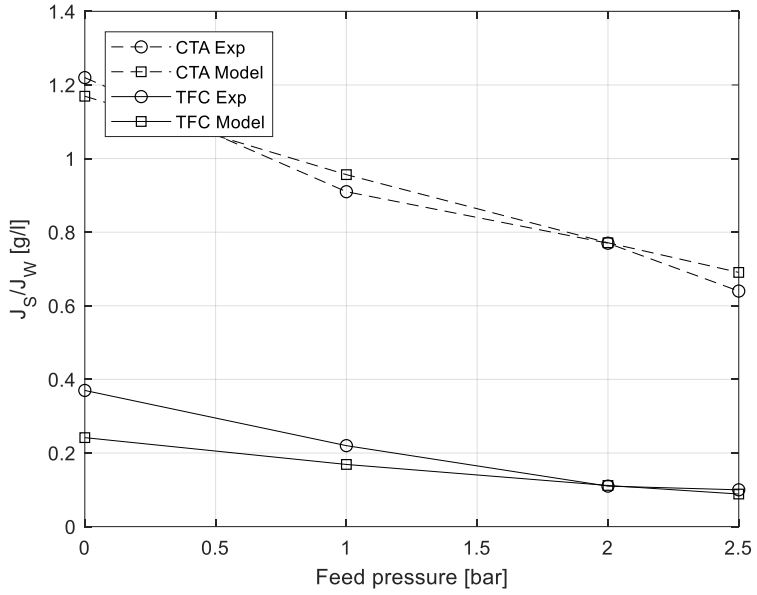


Figure 49: The ratio of the salt to water flux with respect to the PAFO feed pressure. Experimental data is obtained from (Kim, Blandin, & Phuntsho, 2017)

Appendix C

C.1. The equivalent work principle and the unit water cost calculation

C.1.1. Equivalent work principle

As the reboilers in the DSR system are thermally powered, the principal of equivalent work W_{Eq} is used to estimate the overall electrical energy consumption of the MBC and the two-pass RO system. The steam used to supply the required thermal energy to the reboilers of the DSR system is extracted from a steam turbine and is thus no longer available for electricity generation. Using the W_{Eq} method, thermal energy is assigned an electrical energy value, based on the capacity of that thermal energy to generate electricity in a steam turbine, which allows for a theoretical comparison of thermal process efficiencies. The equivalent work (kWh/m^3) of the desalination process is calculated as follows [157]:

$$W_{Eq} = \frac{\eta_{Tur}(h_{g,Steam} - h_{g,Cond})}{3.6\ GOR} + \sum SEEC \quad (58)$$

where $h_{g,Steam}$ and $h_{g,Cond}$ are the enthalpy (kJ/kg) of the extracted steam and the steam at the point where it would normally enter the turbine condenser, respectively. As previously mentioned, the condenser temperature is assumed to be 40°C and is equivalent to the condenser temperature T_{Cond} of the DSR system. The turbine efficiency η_{Tur} is assumed to be 85%, which is a typical value for the isentropic efficiency of a steam turbine [210]. The gained output ratio (GOR) is calculated as follows:

$$GOR = \frac{h_{fg,Steam}}{\sum STEC} \quad (59)$$

where $h_{fg,Steam}$ is the vaporisation enthalpy (kJ/kg) of the utilised steam (which is saturated at 5 bar). The total specific thermal energy consumption (STEC) of DC1 and DC2 is given in kJ/kg. Furthermore, the specific electrical energy consumption (SEEC) of all the electrically driven equipment in the MBC and two-pass RO system is given in kWh/m^3.

C.1.2. Unit water cost calculation

The unit water cost is calculated as follows:

$$\mathrm{UWC} = \frac{\mathrm{TAC}\ [\frac{\$}{\mathrm{year}}]}{\mathrm{Annual\ water\ production}\ [\mathrm{m^3/year}} \tag{60}$$

where the total annual cost (TAC) is given by:

$$\mathrm{TAC} = \mathrm{CF} \times\ \mathrm{CapEx}\ +\ \mathrm{OpEx} \tag{61}$$

The capitalisation factor (CF) is assumed to be 10%, as used by Bartholomew et al. [52] for small-scale applications. The capital expenditures for the membrane systems are calculated by:

$$\mathrm{CapEx_{Mem}} = \mathrm{F_{Mem}} \sum (\mathrm{C_{Mem}} + \mathrm{C_{HPP}} + \mathrm{C_{BP}} + \mathrm{C_{ERD}} + \mathrm{C_{DS}} + \mathrm{C_{PV}}) \tag{62}$$

and the capital expenditure for the DSR system is given by:

$$\mathrm{CapEx_{DSR}} = \mathrm{F_{DSR}} \sum (\mathrm{C_{DC}} + \mathrm{C_{HEX}} + \mathrm{C_{Cond}} + \mathrm{C_{Reb}}) \tag{63}$$

The operational membrane and DSR expenditure are given by:

$$\mathrm{OpEx_{Mem}} = \sum (\mathrm{O_{Elec}} + \mathrm{O_{DS}} + \mathrm{O_{Mem}} + \mathrm{O_{ML}} + \mathrm{O_{Chem}}) \tag{64}$$

and:

$$\mathrm{OpEx_{DSR}} = \sum (\mathrm{O_{Elec}} + \mathrm{O_{CW}} + \mathrm{O_{ML}}) \tag{65}$$

Each factor in Equation (62) to (65) is defined and given in Table 8.

Table 8: Financial parameters for the calculation of the unit water cost

Capital financial parameters		Value
Practical investment factor	$F_{FO,OA}$ [a]	1.6
(Lang factor)	F_{RO} [a]	1.4
	F_{DSR} [b]	3.68
Membrane unit cost [a]	$C_{Mem,FO/OA}$	$50\,\$/m^2$
	$C_{Mem,RO}$	$30\,\$/m^2$
High-pressure and booster	C_{HPP}	$53\,\$/(m^3/h\,bar)$
pump costs [a]	C_{BP}	$53\,\$/(m^3/h\,bar)$
Energy recovery device cost [a]	C_{ERD}	$3134.7\,(Q_{ERD}\,[m^3/h])^{0.58}\,\$$
(Only employed if $P_F > 10\,bar$)		
Draw solute purchasing cost [c]	C_{DS}	$8.75\,\$/kg$
Pressure vessel unit cost [d]	C_{PV}	$1000\,\$/vessel$
Distillation column cost [e]	C_{DC}	$17640 * \varnothing^{1.066} * L^{0.802}\,\$$
Heat exchanger cost [e]	C_{HEX}	$7296\,(A_{HEX}\,[m^2])^{0.65}\,\$$
	C_{Cond}	$7296\,(A_{Cond}\,[m^2])^{0.65}\,\$$
	C_{Reb}	$7296\,(A_{Reb}\,[m^2])^{0.65}\,\$$
Operational financial parameters		**Value**
Electricity cost [a]	O_{Elec}	$0.075\,\$/kWh$
Draw solute replenishment cost [f]	O_{DS}	$0.01\,C_{DS}\,\$/year$
Membrane replacement cost [a]	O_{Mem}	$0.15\,C_{Mem}\,\$/year$
Maintenance and labour cost	$O_{ML,Mem}$ [a]	$0.02\,CapEx_{Mem}\,\$/year$
	$O_{ML,DSR}$ [b]	$0.04\,CapEx_{DSR}\,\$/year$
Chemical consumption cost [a]	O_{Chem}	$0.01\,CapEx_{Mem}\,\$/year$
Cooling water consumption cost [e]	O_{CW}	$0.016\,\$/kWh$

[a] Bartholomew et al. [52]

[b] Lara et al. [211]

[c] Johnson et al. [47]

[d] Lu et al. [212]

[e] Luyben [170]

[f] Assumed value to model the DS loss through the product and brine stream

Appendix D

D.1. OARO cleaning strategies

As shown in Figure 50, three different cleaning strategies including surface flushing, osmotic backwashing (OB) and real OB are investigated in this study. The organic fouling experiments (F5) were repeated three times, each lasting approximately 80 minutes to give a total fouling duration of 4 hours. In between the fouling cycles, cleaning cycles were carried out and lasted for approximately 10 minutes.

Flushing the fouled membrane using deionised (DI) water constitutes the first strategy. A cross-flow velocity (CFV) of 20 cm/s was chosen in our flushing experiments, which is similar to the CFV used by Mi and Elimelech [213] and Vu et al. [214]. The flow direction was not altered during membrane cleaning. The other two cleaning strategies for OARO focus on osmotic backwashing using different feed and draw solutions. In comparison to flushing, a reverse water flux is induced during OB that can theoretically enhance the dissociation and dislodging of the fouling layer from the membrane's active layer [206]. To enhance the reverse water flux, the operating pressure is reduced in both OB cleaning scenarios to approximately zero. In practice, however, osmotic backwashing can be used on-line, without stopping the high-pressure pumps [215,216]. In addition, OB is a rapid cleaning method that is also membrane and environmentally friendly, as no additional cleaning chemicals are used.

In the ideal OB scenario, deionised water is used as draw solution, whereas a pure 2.4 M NaCl solution is used as feed solution. This case is deemed ideal, as no foulants are present in either draw or feed solution, and the transmembrane hydraulic pressure is at a minimum, meaning that the maximum reverse water flux can be achieved. The 2.4 M NaCl solution reflects the salinity achievable by OARO membrane processes [25,35]. Hence, the OARO brine could be

ideally used for the OB procedure without incurring any additional cost. However, using deionised water during the OB or flushing process is costly, as the OARO/RO product water must be utilised for this. To circumvent using DI water for the OB process, a more realistic OB scenario is also investigated in this study. Instead of using DI water, the original draw solution from test case F5 is utilised in the real OB scenario to simulate on-line OB. Furthermore, the feed solution is chosen to resemble OARO brine with organics (100 mg/L alginate) and ion concentrations 3.2 times higher than the concentrations specified for the F5 feed solution.

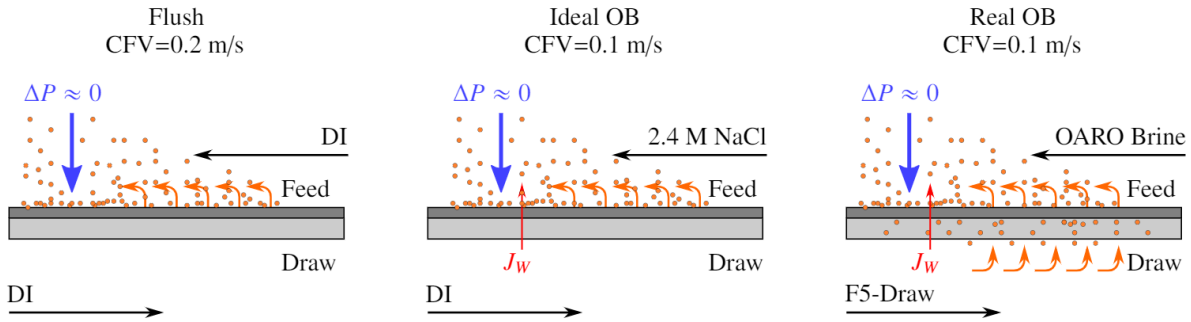


Figure 50: The three different cleaning scenarios investigated.

D.2. Plugged OARO draw spacer

As shown in Figure 51, Ca-Alg aggregates are entrapped within the 3D printed and the tricot-type RO permeate carrier after the completion of the F3 fouling experiment.

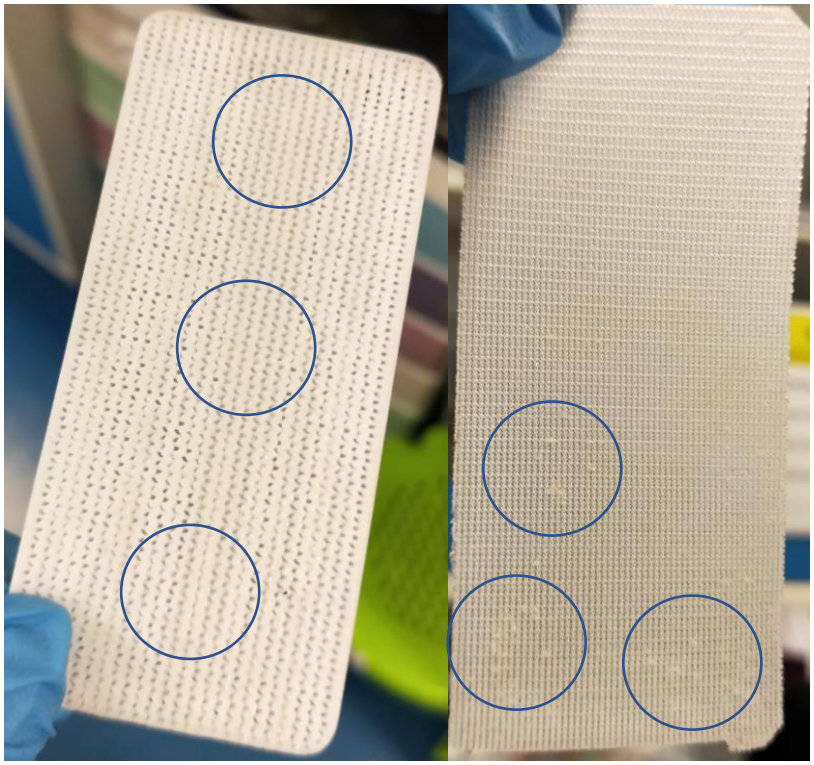


Figure 51: Plugged OARO draw spacer.

D.3. The ICP self-compensation effect at different water fluxes

ICP is modelled in the osmotic resistance model using the dilutive concentration polarisation factor $\mathrm{f_{DCP}}$ for OARO membranes operated in AL-FS mode:

$$\mathrm{f_{DCP}} = (1 - \exp(-J_W S/D)) \tag{66}$$

Hence, the ICP self-compensation effect is strongly dependent on the water flux J_W and the membrane's structural parameter S. Therefore, a change in f_{DCP} due to a change in J_W is given by:

$$\frac{\mathrm{df_{DCP}}}{dJ_W} = \frac{S}{D}\exp(-J_W S/D) \tag{67}$$

A larger change in the gradient of f_{DCP} (represented by Equation (67)) represents a stronger ICP self-compensation effect, as a small change in J_W causes a larger response of the apparent driving force.

As shown in Figure 52 (a), the f_{DCP} factor rapidly approaches 1 for the BW30LE membrane due to its larger S-value. On the other hand, the increase of f_{DCP} for the AQP membrane is more gradual with J_W. The more rapid increase of f_{DCP} for the BW30LE membrane at lower operational water fluxes ($J_W \leq 4\ \mathrm{L/(m^2h)}$) means that in this range it has a stronger ICP self-compensation effect than the AQP membrane. This is verified by Figure 52 (b) where the gradient of f_{DCP} for the BW30LE membrane exceeds that of the AQP membrane. However, at higher operational water fluxes ($J_W > 4\ \mathrm{L/(m^2h)}$) the AQP membrane has a stronger ICP self-compensation effect, as the change in f_{DCP} with the water flux is greater (Figure 52 (b)).

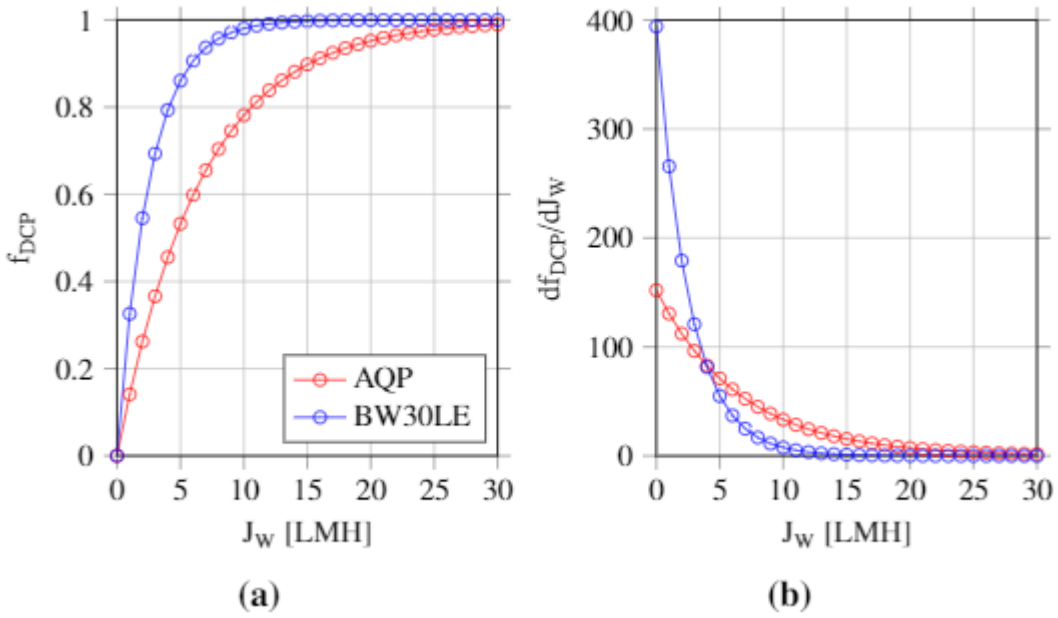


Figure 52: (a) The dilutive concentration polarisation factor f_{DCP} and (b) it's derivative with respect to the water flux. The S-value of the AQP and BW30LE membrane are 810 μm and 2100 μm, respectively.

D.4. Ideal OB of the AQP and BW30LE membrane

Figure 53 compares the efficacy of the ideal OB strategy for both the AQP and BW30LE membrane. As shown in the figure, the magnitude of the backwash water flux is significantly lower for the BW30LE membrane than for the AQP membrane, due to the larger *S* value (and thus more severe ICP) of the BW30LE membrane. Farooque et al. [217] and Blandin et al. [206] state that the feed solutes diffuse into the membrane's substrate during osmotic backwashing and hence, concentrative ICP in the membrane's thick substrate causes a severe flux decline during backwashing. This explains why the BW30LE membrane with the thicker substrate has the lower backwash flux. However, as shown in the figure, the initial water flux is fully recovered after each cleaning cycle for both membranes. While the water flux can be fully recovered for the alginate fouled BW30LE membrane, the flux recovery is uncertain for other organic foulants that may be present in other OARO feed solutions. During the fouling experiments, the BW30LE and AQP membrane do not reach the same final water flux after each fouling cycle. Therefore, it can be assumed that the fouling duration is not sufficiently long for both membranes to reach the limiting flux of approximately $9\ \mathrm{L/(m^2h)}$.

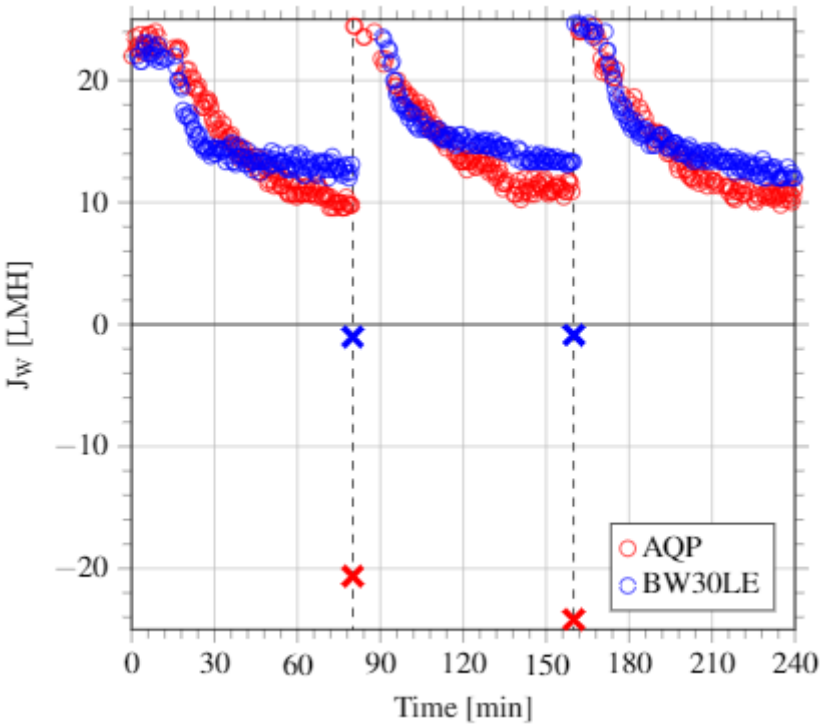


Figure 53: Comparing the effectiveness of the ideal OB cleaning strategy on the AQP and BW30LE membrane. The AQP membrane and BW30LE membrane are operated at 50 bar and 40 bar with a CFV of 10 cm/s during the fouling cycles. Each of the three fouling cycles lasted 80 min, to give a total fouling duration of 4 hours whereas each cleaning cycle lasted 10 minutes.

Appendix E

E.1. Chapter 3 Matlab source code

E.1.1. Main Function

```
% Code used for parameter optimisation for all flow diagrams

% Created by C.D. Peters
% 1 July 2018

clc
clear all

% Assumptions:
% Constant T
% Only NaCl
% Spiral wound SWRO and NF90 modules

%% Choice of Flow Diagram
FD          = 41;
% Flow Diagram 0  (UF-RO)
% Flow Diagram 1  (C-OARO 1)
% Flow Diagram 2  (C-OARO 2)
% Flow Diagram 3  (C-OARO 3)
% Flow Diagram 41 (MP-OARO 1)
% Flow Diagram 42 (MP-OARO 2)
% Flow Diagram 5  (SF-OARO)

%% Choice of Scenario
Scenario    = 1;

if Scenario == 1
    S_0     = 35;                               % Choice of Inlet Salinity [g/L]
else
    S_0     = 70;
end


%% Input parameters
FD_Err  = 0.005;

m_0     = 100;                                  % Inlet mass flowrate
T_0     = 25+273.15;    P_0     = 1;            % Standard piping pressure [Bar]
Q_PFin  = 1000/3600;                            % Total required permeate flow rate per year

Y_UF    = 1;            A_UF    = 60;           % UF recovery and membrane area (REF: PentAir
AquaFlex)
LMH_UF  = 100/1000/3600;                        % UF 100 LMH (REF: DOW UF Manual)
eff_P   = 0.8;          eff_PEX = 0.96;         % Pump and PEX efficiency (REF: 0 Energy use
for membrane)

P_Intake= 2.815;        P_UF    = 4.44;         % Intake and UF feed pressure [Bar] (Max TMP =
3 Bar REF: PentAir AquaFlex)
P_Dis   = 4;            P_Post  = 5.32;         % Brine discharge pressure loss  and post with
product water delivery pressure [Bar]
P_Ry    = 1;

P_F_RO  = 80;                                   % RO feed pressure [bar]
FF_RO   = 1.0;                                  % Flow factor RO (If <1 then fouling
considered)

% Feedwater related parameters
i       = 2;            MW      = 58.4;         % [NaCl], later include: CaCO3, CaSO4, MgCO3,
MGSO4 [g/mol]
R       = 0.0831446;                            % L bar/ K mol
```

```
% Shooting method related
It_P    = 2;            SM      = 100;          % Initial iteration point count and iteration
limit
It_FD   = 100;

%% Reverse Osmosis settings
Type_RO = 1;            Flow_RO = 0;            % Type (Membrane), Flow = 0 (Co-Current) or 1
(Counter current)
n_RO    = 7;
P_D_RO  = 1;
Q_F_RO  = 12/3600;      AL_RO   = 0;            % 0 = AL-FS (RO operation), 1 = AL-DS (PRO
operation)
St_RO   = 2;

%% OARO settings
Type_OA = 3;        Flow_OA = 1;                % Type (Membrane), Flow = 0 (Co-Current) or 1
(Counter current)
FF_OA   = FF_RO;    n_OA    = n_RO;
P_D_OA  = 1;
Q_F_OA  = 6/3600;   AL_OA   = 0;                % 0 = AL-FS (RO operation), 1 = AL-DS (PRO
operation)
RR      = 1;        St_OA   = 0;                % St_OA is always 0.5 mm
X       = 1;

%% Recovery settings
Y_Err           = 10^(-3);
if S_0 == 35
    Y_Aim       = Y_UF*0.72;
elseif S_0 == 70
    Y_Aim       = Y_UF*0.44;
elseif S_0 == 140
    Y_Aim       = Y_UF*0.3;
end

%% FDs
if FD == 0
    %% Flow Diagram 0 (UF-RO)
    % Each stage has same recovery!!
    N_RO    = 4;
    P_F_RO  = 69.4;
    P_F_RO2 = 78.9;
    P_F_RO3 = 89.85;
    P_F_RO4 = 102.5;

    if S_0 == 35
        if N_RO == 1
            Y_1     = 0.72;
        elseif N_RO == 2
            Y_1     = 0.4708;
        elseif N_RO == 3
            Y_1     = 0.3458;
        elseif N_RO == 4
            Y_1     = 0.2726;
        end
    elseif S_0 == 70
        if N_RO == 1
            Y_1     = 0.44;
        elseif N_RO == 2
            Y_1     = 0.2517;
        elseif N_RO == 3
            Y_1     = 0.1757;
        elseif N_RO == 4
            Y_1     = 0.1349;
        end
    end

aa  = 0;
fprintf('\nOuter loop:\n')
aa  = aa+1;
fprintf('\nPressure loop: P_F = %.1f Bar\n',P_F_RO)
    a   = 1;

    % Basic Parameter Input vector
    Input_Bas(1,:)      = [FD       FD_Err  m_0     S_0     T_0     P_0         Q_PFin];
    Input_Bas(2,:)      = [Y_UF     A_UF    LMH_UF  eff_P   eff_PEX P_Intake    P_UF];
    Input_Bas(3,:)      = [P_Dis    P_Post  i       MW      R       It_P        SM];
    % RO Input vector
```

```
    Input_Vec           = [Type_RO  Flow_RO FF_RO   n_RO    P_F_RO  P_D_RO      Q_F_RO  AL_RO
St_RO N_RO P_F_RO2 P_F_RO3 P_F_RO4];


    % Call FD function
    [Err_Vec, En_Vec, Mod_Vec, QQ]      = V4_FD(Input_Bas, Input_Vec);

    % Results
    Y_Sys(aa,a)     = QQ(11,1)/QQ(1,1);
    C_P_Sys(aa,a)   = QQ(11,2);
    En_Sys(aa,a)    = En_Vec(end);

    Mod_RO1(aa,a)   = Mod_Vec(1);
    Mod_RO2(aa,a)   = Mod_Vec(2);
    Mod_RO3(aa,a)   = Mod_Vec(3);
    Mod_RO4(aa,a)   = Mod_Vec(4);
    Mod_UF(aa,a)    = Mod_Vec(5);

    Err_Mat(aa,:)   = Err_Vec;
    QQ_Mat(:,:,aa)  = QQ;

Excel   = [ P_F_RO; P_F_RO2; P_F_RO3; P_F_RO4;
                Y_Sys(aa,a)*100; Y_1*100;
                En_Sys(aa,a);
                C_P_Sys(aa,a);
                Mod_UF(aa,a)/4;
                (Mod_RO2(aa,a)+Mod_RO3(aa,a)+Mod_RO4(aa,a))/n_RO;
                Mod_RO1(aa,a)/n_RO]
Err_Mat(end,:)



elseif FD == 1
    %% Flow Diagram 1 (C-OARO 1)
    N_OA    = 1;

    P_F_OA_It   = [64 70 zeros(1,48)];

    for aa = 1:size(P_F_OA_It')
        P_F_OA = P_F_OA_It(aa);

        fprintf('\nOARO Pressure: %.1f Bar\n',P_F_OA)
         fprintf('\nRO Pressure: %.1f Bar\n',P_F_RO)
            a   = 1;

            % Basic Parameter Input vector
            Input_Bas(1,:)      = [FD       FD_Err  m_0     S_0     T_0     P_0
Q_PFin];
            Input_Bas(2,:)      = [Y_UF     A_UF    LMH_UF  eff_P   eff_PEX P_Intake    P_UF];
            Input_Bas(3,:)      = [P_Dis    P_Post  i       MW      R       It_P        SM];

            Input_Vec(1,:)      = [Type_RO  Flow_RO FF_RO   n_RO    P_F_RO  P_D_RO      Q_F_RO
AL_RO   St_RO   0];
            Input_Vec(2,:)      = [It_FD    X       RR      0       0       0           0
0       0       0];
            Input_Vec(3,:)      = [Type_OA  Flow_OA FF_OA   n_OA    P_F_OA  P_D_OA      Q_F_OA
AL_OA   St_OA   N_OA];

            % Call FD function
            [Err_Vec, En_Vec, Mod_Vec, QQ]      = V4_FD(Input_Bas, Input_Vec);

            Y_Sys(aa,a)     = QQ(13,1)/QQ(1,1);
            C_P_Sys(aa,a)   = QQ(13,2);
            En_Sys(aa,a)    = En_Vec(end);

            Mod_RO(aa,a)    = Mod_Vec(1);
            Mod_OA1(aa,a)   = Mod_Vec(2);
            Mod_OA2(aa,a)   = Mod_Vec(3);
            Mod_OA3(aa,a)   = Mod_Vec(4);
            Mod_UF(aa,a)    = Mod_Vec(5);

            Err_Mat(aa,:)   = Err_Vec;
            QQ_Mat(:,:,aa)  = QQ;

        if aa > 1
```

```
            P_F_OA_It(aa+1)    = (Y_Aim-Y_Sys(aa-1,a))/(Y_Sys(aa,a)-Y_Sys(aa-
1,a))*(P_F_OA_It(aa)-P_F_OA_It(aa-1))+P_F_OA_It(aa-1);
        end
        if abs(Y_Sys(aa,a)/Y_Aim-1)<Y_Err
            Excel   = [ P_F_OA;
                        Y_Sys(aa,a)*100;
                        En_Sys(aa,a);
                        C_P_Sys(aa,a);
                        Mod_UF(aa,a)/4;
                        (Mod_OA1(aa,a)+Mod_OA2(aa,a)+Mod_OA3(aa,a))/n_OA;
                        Mod_RO(aa,a)/n_RO]
            Err_Mat(end,:)
            break
        end
    end



elseif FD == 2
    %% Flow Diagram 2 (C-OARO 2)
    N_OA1   = 1;
    N_OA2   = 2;

    P_F_OA_It   = [55 50 zeros(1,48)];

    for aa = 1:size(P_F_OA_It')
        P_F_OA  = P_F_OA_It(aa);

        fprintf('\nOARO Pressure: %.1f Bar\n',P_F_OA)
        fprintf('\nRO Pressure: %.1f Bar\n',P_F_RO)
            a   = 1;

            % Basic Parameter Input vector
            Input_Bas(1,:)      = [FD       FD_Err  m_0     S_0     T_0     P_0
Q_PFin];
            Input_Bas(2,:)      = [Y_UF     A_UF    LMH_UF  eff_P   eff_PEX P_Intake    P_UF];
            Input_Bas(3,:)      = [P_Dis    P_Post  i       MW      R       It_P        SM];

            Input_Vec(1,:)  = [Type_RO  Flow_RO     FF_RO   n_RO    P_F_RO  P_D_RO  Q_F_RO
AL_RO   St_RO   0       0];
            Input_Vec(2,:)  = [It_FD    X           RR      0       0       0         0
0     0       0       0];
            Input_Vec(3,:)  = [Type_OA  Flow_OA     FF_OA   n_OA    P_F_OA P_D_OA  Q_F_OA
AL_OA   St_OA    N_OA1   N_OA2];

            % Call FD function
            [Err_Vec, En_Vec, Mod_Vec, QQ]      = V4_FD(Input_Bas, Input_Vec);

            Y_Sys(aa,a)     = QQ(18,1)/QQ(1,1);
            C_P_Sys(aa,a)   = QQ(18,2);
            En_Sys(aa,a)    = En_Vec(end);

            Mod_RO(aa,a)    = Mod_Vec(1);
            Mod_OA1(aa,a)   = Mod_Vec(2);
            Mod_OA2(aa,a)   = Mod_Vec(3);
            Mod_OA3(aa,a)   = Mod_Vec(4);
            Mod_UF(aa,a)    = Mod_Vec(5);

            Err_Mat(aa,:)   = Err_Vec;
            QQ_Mat(:,:,aa)  = QQ;

        if aa > 1
            P_F_OA_It(aa+1)    = (Y_Aim-Y_Sys(aa-1,a))/(Y_Sys(aa,a)-Y_Sys(aa-
1,a))*(P_F_OA_It(aa)-P_F_OA_It(aa-1))+P_F_OA_It(aa-1);
        end
        if abs(Y_Sys(aa,a)/Y_Aim-1)<Y_Err
            Excel   = [ P_F_OA;
                        Y_Sys(aa,a)*100;
                        En_Sys(aa,a);
                        C_P_Sys(aa,a);
                        Mod_UF(aa,a)/4;
                        (Mod_OA1(aa,a)+Mod_OA2(aa,a)+Mod_OA3(aa,a))/n_OA;
                        Mod_RO(aa,a)/n_RO]
            Err_Mat(end,:)
            break
        end
    end
```

```
elseif FD == 3
    %% Flow Diagram 3 (C-OARO 3)
    P_F_OA_It   = [57.01 55 zeros(1,48)];

    for aa = 1:size(P_F_OA_It')
        P_F_OA = P_F_OA_It(aa);

        fprintf('\nOARO Pressure: %.1f Bar\n',P_F_OA)
        fprintf('\nRO Pressure: %.1f Bar\n',P_F_RO)
            a   = 1;

            % Basic Parameter Input vector
            Input_Bas(1,:)      = [FD       FD_Err  m_0     S_0     T_0     P_0
Q_PFin];
            Input_Bas(2,:)      = [Y_UF     A_UF    LMH_UF  eff_P   eff_PEX P_Intake    P_UF];
            Input_Bas(3,:)      = [P_Dis    P_Post  i       MW      R       It_P        SM];

            Input_Vec(1,:)      = [Type_RO  Flow_RO     FF_RO   n_RO    P_F_RO  P_D_RO  Q_F_RO
AL_RO   St_RO];
            Input_Vec(2,:)      = [It_FD    X           RR      0       0       0       0
0       0    ];
            Input_Vec(3,:)      = [Type_OA  Flow_OA     FF_OA  n_OA     P_F_OA  P_D_OA  Q_F_OA
AL_OA   St_OA];

            % Call FD function
            [Err_Vec, En_Vec, Mod_Vec, QQ]      = V4_FD(Input_Bas, Input_Vec);

            Y_Sys(aa,a)     = QQ(19,1)/QQ(1,1);
            C_P_Sys(aa,a)   = QQ(19,2);
            En_Sys(aa,a)    = En_Vec(end);

            Mod_RO(aa,a)    = Mod_Vec(1);
            Mod_OA1(aa,a)   = Mod_Vec(2);
            Mod_OA2(aa,a)   = Mod_Vec(3);
            Mod_OA3(aa,a)   = Mod_Vec(4);
            Mod_UF(aa,a)    = Mod_Vec(5);

            Err_Mat(aa,:)   = Err_Vec;
            QQ_Mat(:,:,aa)  = QQ;

        if aa > 1
            P_F_OA_It(aa+1)    = (Y_Aim-Y_Sys(aa-1,a))/(Y_Sys(aa,a)-Y_Sys(aa-
1,a))*(P_F_OA_It(aa)-P_F_OA_It(aa-1))+P_F_OA_It(aa-1);
        end
        if abs(Y_Sys(aa,a)/Y_Aim-1)<Y_Err
            Excel   = [ P_F_OA;
                        Y_Sys(aa,a)*100;
                        En_Sys(aa,a);
                        C_P_Sys(aa,a);
                        Mod_UF(aa,a)/4;
                        (Mod_OA1(aa,a)+Mod_OA2(aa,a)+Mod_OA3(aa,a))/n_OA;
                        Mod_RO(aa,a)/n_RO]
            Err_Mat(end,:)
            break
        end
    end




elseif FD == 41 || FD == 42
    %% Flow Diagram 4 (MP-OARO 1 & MP-OARO 2)
    X           = 1;
    N_OA1       = 3;
    N_OA2       = 1;
    RR          = 1;

    P_F_OA_It   = [57.8 58 zeros(1,48)];

    for aa = 1:size(P_F_OA_It')
        P_F_OA = P_F_OA_It(aa);
```

dd

```
        fprintf('\nOARO Pressure: %.1f Bar\n',P_F_OA)
        fprintf('\nRO Pressure: %.1f Bar\n',P_F_RO)
            a   = 1;

            % Basic Parameter Input vector
            Input_Bas(1,:)      = [FD       FD_Err  m_0     S_0     T_0     P_0
Q_PFin];
            Input_Bas(2,:)      = [Y_UF     A_UF    LMH_UF  eff_P   eff_PEX P_Intake    P_UF];
            Input_Bas(3,:)      = [P_Dis    P_Post  i       MW      R       It_P        SM];

            Input_Vec(1,:)  = [Type_RO  Flow_RO     FF_RO   n_RO    P_F_RO  P_D_RO  Q_F_RO
AL_RO   St_RO   0       0       0];
            Input_Vec(2,:)  = [It_FD    X           RR      0       0       0         0
0     0       0       0       0];
            Input_Vec(3,:)  = [Type_OA  Flow_OA     FF_OA   n_OA    P_F_OA P_D_OA   Q_F_OA
AL_OA   St_OA   P_Ry    N_OA1   N_OA2];

            % Call FD function
            [Err_Vec, En_Vec, Mod_Vec, QQ]      = V4_FD(Input_Bas, Input_Vec);

            if FD == 41
                Y_Sys(aa,a)     = QQ(12,1)/QQ(1,1);
                C_P_Sys(aa,a)   = QQ(12,2);
            else
                Y_Sys(aa,a)     = QQ(16,1)/QQ(1,1);
                C_P_Sys(aa,a)   = QQ(16,2);
            end


            En_Sys(aa,a)    = En_Vec(end);

            Mod_RO(aa,a)    = Mod_Vec(1);
            Mod_OA1(aa,a)   = Mod_Vec(2);
            Mod_OA2(aa,a)   = Mod_Vec(3);
            Mod_OA3(aa,a)   = Mod_Vec(4);
            Mod_UF(aa,a)    = Mod_Vec(5);

            Err_Mat(aa,:)   = Err_Vec;
            QQ_Mat(:,:,aa)  = QQ;

        if aa > 1
            P_F_OA_It(aa+1)    = (Y_Aim-Y_Sys(aa-1,a))/(Y_Sys(aa,a)-Y_Sys(aa-
1,a))*(P_F_OA_It(aa)-P_F_OA_It(aa-1))+P_F_OA_It(aa-1);
        end
        if abs(Y_Sys(aa,a)/Y_Aim-1)<Y_Err
            Excel   = [ P_F_OA;
                        Y_Sys(aa,a)*100;
                        En_Sys(aa,a);
                        C_P_Sys(aa,a);
                        Mod_UF(aa,a)/4;
                        (Mod_OA1(aa,a)+Mod_OA2(aa,a)+Mod_OA3(aa,a))/n_OA;
                        Mod_RO(aa,a)/n_RO]
            Err_Mat(end,:)
            break
        end
    end




elseif FD == 5
    %% Flow Diagram 5 (SF-OARO)
    X       = 0.5;
    RR      = 1;
    N_OA    = 3;

    P_F_OA_It   = [50 60   zeros(1,48)];
    for aa = 1:size(P_F_OA_It')
        P_F_OA = P_F_OA_It(aa);
        aa=1;
        fprintf('\nOARO Pressure: %.1f Bar\n',P_F_OA)
        fprintf('\nRO Pressure: %.1f Bar\n',P_F_RO)
            a   = 1;

            % Basic Parameter Input vector
```

```
            Input_Bas(1,:)      = [FD       FD_Err  m_0     S_0     T_0     P_0
Q_PFin];
            Input_Bas(2,:)      = [Y_UF     A_UF    LMH_UF  eff_P   eff_PEX P_Intake    P_UF];
            Input_Bas(3,:)      = [P_Dis    P_Post  i       MW      R       It_P        SM];

            Input_Vec(1,:)  = [Type_RO  Flow_RO     FF_RO   n_RO    P_F_RO  P_D_RO  Q_F_RO
AL_RO   St_RO   0];
            Input_Vec(2,:)  = [It_FD    X           RR      0       0       0         0
0     0       0];
            Input_Vec(3,:)  = [Type_OA  Flow_OA     FF_OA   n_OA    P_F_OA P_D_OA   Q_F_OA
AL_OA   St_OA   N_OA];
            Input_Vec(4,:)  = [P_Ry     0           0       0       0       0       0       0
0       0];

            % Call FD function
            [Err_Vec, En_Vec, Mod_Vec, QQ]      = V4_FD(Input_Bas, Input_Vec);

            Y_Sys(aa,a)     = QQ(13,1)/QQ(1,1);
            C_P_Sys(aa,a)   = QQ(13,2);
            En_Sys(aa,a)    = En_Vec(end);

            Mod_RO(aa,a)    = Mod_Vec(1);
            Mod_OA1(aa,a)   = Mod_Vec(2);
            Mod_OA2(aa,a)   = Mod_Vec(3);
            Mod_OA3(aa,a)   = Mod_Vec(4);
            Mod_UF(aa,a)    = Mod_Vec(5);

            Err_Mat(aa,:)   = Err_Vec;
            QQ_Mat(:,:,aa)  = QQ;

        if aa > 1
            P_F_OA_It(aa+1)    = (Y_Aim-Y_Sys(aa-1,a))/(Y_Sys(aa,a)-Y_Sys(aa-
1,a))*(P_F_OA_It(aa)-P_F_OA_It(aa-1))+P_F_OA_It(aa-1);
        end
        if abs(Y_Sys(aa,a)/Y_Aim-1)<Y_Err
            Excel   = [ P_F_OA;
                        Y_Sys(aa,a)*100;
                        En_Sys(aa,a);
                        C_P_Sys(aa,a);
                        Mod_UF(aa,a)/4;
                        (Mod_OA1(aa,a)+Mod_OA2(aa,a)+Mod_OA3(aa,a))/n_OA;
                        Mod_RO(aa,a)/n_RO]
            Err_Mat(end,:)
            break
        end
    end


end
```

E.1.2. FD (Flow-diagram) function

```
%% Flow Diagram function
% This function is used to calculate the different OARO flow diagrams

function [Err_Vec, En_Vec, Mod_Vec, QQ]     = V4_FD(Input_Bas, Input_Vec)

FD      = Input_Bas(1,1);   FD_Err      = Input_Bas(1,2);
Q_0     = Input_Bas(1,3);   S_0         = Input_Bas(1,4);
T_0     = Input_Bas(1,5);   P_0         = Input_Bas(1,6);
Q_PFin  = Input_Bas(1,7);

Y_UF    = Input_Bas(2,1);   A_UF        = Input_Bas(2,2);
LMH_UF  = Input_Bas(2,3);   eff_P       = Input_Bas(2,4);
eff_PEX = Input_Bas(2,5);   P_Intake    = Input_Bas(2,6);
P_UF    = Input_Bas(2,7);

P_Dis   = Input_Bas(3,1);   P_Post      = Input_Bas(3,2);
i       = Input_Bas(3,3);   MW          = Input_Bas(3,4);
R       = Input_Bas(3,5);   It_P        = Input_Bas(3,6);
SM      = Input_Bas(3,7);

Type_RO = Input_Vec(1,1);   Flow_RO     = Input_Vec(1,2);
```

```
FF_RO   = Input_Vec(1,3);   n_RO        = Input_Vec(1,4);
P_F_RO  = Input_Vec(1,5);   P_D_RO      = Input_Vec(1,6);
Q_F_RO  = Input_Vec(1,7);   AL_RO       = Input_Vec(1,8);
St_RO   = Input_Vec(1,9);

rho     = Rho(S_0, T_0);                % Seawater density
phi     = Phi(S_0,T_0);                 % Osmotic coefficient
k_RO    = 100*n_RO+1;                   % Number of iteration points


if FD == 0
    %% Flow diagram 0
    N_RO    = Input_Vec(1,10);
    P_F_RO2 = Input_Vec(1,11);
    P_F_RO3 = Input_Vec(1,12);
    P_F_RO4 = Input_Vec(1,13);

    % Mass calculations & stream specifications
    % Inlet stream
    QQ(1,:)     = [Q_0          S_0       T_0       P_0];
    % UF permeate stream
    QQ(2,:)     = [Y_UF*QQ(1,1) QQ(1,2)   QQ(1,3)   QQ(1,4)];

    fprintf('RO1:\t\t')
    [m_D, C_D, m_F, C_F, m_M, RSF, CP_F, CP_D, P_F, P_D]    = V4_Q_M_It(n_RO, k_RO, FF_RO,
rho, phi, i, MW, R, T_0, 0, 0, Q_F_RO, QQ(2,2), P_F_RO, P_D_RO, Type_RO, Flow_RO, AL_RO,
St_RO);
    Y_RO1       = (m_F(1)-m_F(end))/m_F(1);

    % RO brine stream
    QQ(3,:)     = [(1-Y_RO1)*QQ(2,1)    C_F(end)    QQ(2,3) P_F(end)];
    % RO permeate stream
    QQ(7,:)     = [Y_RO1*QQ(2,1)        C_D(end)    QQ(2,3) P_0];

    Y_RO2       = 0;
    Y_RO3       = 0;
    Y_RO4       = 0;

    %% Number of RO stages
    if N_RO     == 1
        QQ(4,:) = QQ(3,:);
        QQ(5,:) = QQ(3,:);
        QQ(6,:) = QQ(3,:);

        QQ(8,:) = zeros(1,4);
        QQ(9,:) = zeros(1,4);
        QQ(10,:)= zeros(1,4);

    elseif N_RO == 2
        fprintf('RO2:\t\t')
        [m_D, C_D, m_F, C_F, m_M, RSF, CP_F, CP_D, P_F, P_D]    = V4_Q_M_It(n_RO, k_RO, FF_RO,
rho, phi, i, MW, R, T_0, 0, 0, Q_F_RO, QQ(3,2), P_F_RO2, P_D_RO, Type_RO, Flow_RO, AL_RO,
St_RO);
        Y_RO2       = (m_F(1)-m_F(end))/m_F(1);

        QQ(4,:)     = [(1-Y_RO2)*QQ(3,1)    C_F(end)    QQ(3,3) P_F(end)];
        QQ(8,:)     = [Y_RO2*QQ(3,1)        C_D(end)    QQ(3,3) P_0];

        QQ(5,:) = QQ(4,:);
        QQ(6,:) = QQ(4,:);

        QQ(9,:) = zeros(1,4);
        QQ(10,:)= zeros(1,4);

    elseif N_RO == 3
        fprintf('RO2:\t\t')
        [m_D, C_D, m_F, C_F, m_M, RSF, CP_F, CP_D, P_F, P_D]    = V4_Q_M_It(n_RO, k_RO, FF_RO,
rho, phi, i, MW, R, T_0, 0, 0, Q_F_RO, QQ(3,2), P_F_RO2, P_D_RO, Type_RO, Flow_RO, AL_RO,
St_RO);
        Y_RO2       = (m_F(1)-m_F(end))/m_F(1);

        QQ(4,:)     = [(1-Y_RO2)*QQ(3,1)    C_F(end)    QQ(3,3) P_F(end)];
        QQ(8,:)     = [Y_RO2*QQ(3,1)        C_D(end)    QQ(3,3) P_0];

        fprintf('RO3:\t\t')
```

```
        [m_D, C_D, m_F, C_F, m_M, RSF, CP_F, CP_D, P_F, P_D]    = V4_Q_M_It(n_RO, k_RO, FF_RO,
rho, phi, i, MW, R, T_0, 0, 0, Q_F_RO, QQ(4,2), P_F_RO3, P_D_RO, Type_RO, Flow_RO, AL_RO,
St_RO);
        Y_RO3       = (m_F(1)-m_F(end))/m_F(1);

        QQ(5,:)     = [(1-Y_RO3)*QQ(4,1)    C_F(end)    QQ(4,3) P_F(end)];
        QQ(9,:)     = [Y_RO3*QQ(4,1)        C_D(end)    QQ(4,3) P_0];

        QQ(6,:) = QQ(5,:);
        QQ(10,:)= zeros(1,4);
    elseif N_RO == 4
        fprintf('RO2:\t\t')
        [m_D, C_D, m_F, C_F, m_M, RSF, CP_F, CP_D, P_F, P_D]    = V4_Q_M_It(n_RO, k_RO, FF_RO,
rho, phi, i, MW, R, T_0, 0, 0, Q_F_RO, QQ(3,2), P_F_RO2, P_D_RO, Type_RO, Flow_RO, AL_RO,
St_RO);
        Y_RO2       = (m_F(1)-m_F(end))/m_F(1);

        QQ(4,:)     = [(1-Y_RO2)*QQ(3,1)    C_F(end)    QQ(3,3) P_F(end)];
        QQ(8,:)     = [Y_RO2*QQ(3,1)        C_D(end)    QQ(3,3) P_0];

        fprintf('RO3:\t\t')
        [m_D, C_D, m_F, C_F, m_M, RSF, CP_F, CP_D, P_F, P_D]    = V4_Q_M_It(n_RO, k_RO, FF_RO,
rho, phi, i, MW, R, T_0, 0, 0, Q_F_RO, QQ(4,2), P_F_RO3, P_D_RO, Type_RO, Flow_RO, AL_RO,
St_RO);
        Y_RO3       = (m_F(1)-m_F(end))/m_F(1);

        QQ(5,:)     = [(1-Y_RO3)*QQ(4,1)    C_F(end)    QQ(4,3) P_F(end)];
        QQ(9,:)     = [Y_RO3*QQ(4,1)        C_D(end)    QQ(4,3) P_0];

        fprintf('RO4:\t\t')
        [m_D, C_D, m_F, C_F, m_M, RSF, CP_F, CP_D, P_F, P_D]    = V4_Q_M_It(n_RO, k_RO, FF_RO,
rho, phi, i, MW, R, T_0, 0, 0, Q_F_RO, QQ(5,2), P_F_RO4, P_D_RO, Type_RO, Flow_RO, AL_RO,
St_RO);
        Y_RO4       = (m_F(1)-m_F(end))/m_F(1);

        QQ(6,:)     = [(1-Y_RO4)*QQ(5,1)    C_F(end)    QQ(5,3) P_F(end)];
        QQ(10,:)    = [Y_RO4*QQ(5,1)        C_D(end)    QQ(5,3) P_0];
    end

    % Permeate streams mixed
    QQ(11,1)     = QQ(7,1)+QQ(8,1)+QQ(9,1)+QQ(10,1);
    QQ(11,2)     =
(QQ(7,1)*QQ(7,2)+QQ(8,1)*QQ(8,2)+QQ(9,1)*QQ(9,2)+QQ(10,1)*QQ(10,2))/QQ(11,1);
    QQ(11,3)     =
(QQ(7,1)*QQ(7,3)+QQ(8,1)*QQ(8,3)+QQ(9,1)*QQ(9,3)+QQ(10,1)*QQ(10,3))/QQ(11,1);
    QQ(11,4)     = QQ(7,4);

    % Mass error
    Water_Err   = QQ(1,1)-(1-Y_UF)*QQ(1,1)-QQ(6,1)-QQ(11,1);
    Salt_Err    = QQ(1,1)*QQ(1,2)-(1-Y_UF)*QQ(1,1)*QQ(1,2)-QQ(6,1)*QQ(6,2)-QQ(11,1)*QQ(11,2);

    RO1_Err_W   = QQ(2,1)-QQ(3,1)-QQ(7,1);
    RO1_Err_S   = QQ(2,1)*QQ(2,2)-QQ(3,1)*QQ(3,2)-QQ(7,1)*QQ(7,2);

    RO2_Err_W   = QQ(3,1)-QQ(4,1)-QQ(8,1);
    RO2_Err_S   = QQ(3,1)*QQ(3,2)-QQ(4,1)*QQ(4,2)-QQ(8,1)*QQ(8,2);

    RO3_Err_W   = QQ(4,1)-QQ(5,1)-QQ(9,1);
    RO3_Err_S   = QQ(4,1)*QQ(4,2)-QQ(5,1)*QQ(5,2)-QQ(9,1)*QQ(9,2);

    RO4_Err_W   = QQ(5,1)-QQ(6,1)-QQ(10,1);
    RO4_Err_S   = QQ(5,1)*QQ(5,2)-QQ(6,1)*QQ(6,2)-QQ(10,1)*QQ(10,2);

    Err_Vec     = [Water_Err RO1_Err_W RO2_Err_W RO3_Err_W RO4_Err_W Salt_Err RO1_Err_S
RO2_Err_S RO3_Err_S RO4_Err_S];

    %% Energy calculations
    P_Input(1)      = P_Intake;
    P_Input(2)      = P_UF;
    P_Input(3)      = P_Dis;
    P_Input(4)      = P_Post;
    P_Input(5)      = P_F_RO2;
    P_Input(6)      = P_F_RO3;
    P_Input(7)      = P_F_RO4;
    P_Input(8)      = P_F_RO;

    [En_Vec]    = V4_Energy0(N_RO, QQ ,P_Input , eff_P, eff_PEX);
```

```
    %% Capital calculations
    [Mod_Vec]   = V4_Capital0(QQ, [Q_F_RO Q_F_RO Q_F_RO Q_F_RO], Q_PFin, n_RO, Y_RO1, Y_RO2,
Y_RO3, Y_RO4, A_UF, LMH_UF);

    if N_RO == 1
            [Y_RO1]
        elseif N_RO == 2
            [Y_RO1 Y_RO2]
        elseif N_RO == 3
            [Y_RO1 Y_RO2 Y_RO3 ]
        elseif N_RO == 4
            [Y_RO1 Y_RO2 Y_RO3 Y_RO4]
    end



elseif FD == 1
    %% Flow diagram 1: OARO
    % Input data
    It_FD   = Input_Vec(2,1);   X           = Input_Vec(2,2);
    RR      = Input_Vec(2,3);

    Type_OA = Input_Vec(3,1);   Flow_OA     = Input_Vec(3,2);
    FF_OA   = Input_Vec(3,3);   n_OA        = Input_Vec(3,4);
    P_F_OA  = Input_Vec(3,5);   P_D_OA      = Input_Vec(3,6);
    Q_F_OA  = Input_Vec(3,7);   AL_OA       = Input_Vec(3,8);
    St_OA   = Input_Vec(3,9);   N_OA        = Input_Vec(3,10);

    % Mass calculations
    QQ(1,:) = [Q_0          S_0     T_0     P_0];
    QQ(2,:) = [Y_UF*QQ(1,1) QQ(1,2) QQ(1,3) QQ(1,4)];
    QQ(12,:)= [X*QQ(1,1)    QQ(1,2) QQ(1,3) P_F_OA];    % Initial guess
    QQ(11,:)= [X*QQ(1,1)    QQ(1,2) QQ(1,3) P_F_OA];    % Initial guess
    QQ(7,:) = [X*QQ(1,1)    QQ(1,2) QQ(1,3) P_F_OA];    % Initial guess

    for aa = 1:It_FD
        fprintf('\n\nIteration: %d\n\n',aa)

        QQ(3,:)= [RR*QQ(7,1)        QQ(2,2) QQ(2,3) QQ(2,4)];
        QQ(4,:)= [QQ(2,1)-QQ(3,1)   QQ(2,2) QQ(2,3) QQ(2,4)];

        for aaa = 1:N_OA
            Q_FI(aaa)   = Q_F_OA;
            if aaa == 1
                Q_DI(aaa)   = QQ(3,1)/QQ(12,1)*Q_F_OA;

                C_DI(aaa)   = QQ(3,2);
                C_FI(aaa)   = QQ(12,2);
            elseif aaa == 2
                Q_DI(aaa)   = QQ(9,1)/QQ(11,1)*Q_F_OA;

                C_DI(aaa)   = QQ(9,2);
                C_FI(aaa)   = QQ(11,2);
            elseif aaa == 3
                Q_DI(aaa)   = QQ(10,1)/QQ(7,1)*Q_F_OA;

                C_DI(aaa)   = QQ(10,2);
                C_FI(aaa)   = QQ(7,2);
            end

            fprintf('OARO %d:\t',aaa)   % V4_SM(n,  , FF,     i, MW, R, T,   P,      P_D1,
Q_FS,      Q_DS,      C_DS,      C_FS,      SM, It_P, Type,    Flow,    AL   , St)
            [Res_OA, E_Vec]             = V4_SM(n_OA, FF_OA,  i, MW, R, T_0, P_F_OA, P_D_OA,
Q_FI(aaa), Q_DI(aaa), C_DI(aaa), C_FI(aaa), SM, It_P, Type_OA, Flow_OA, AL_OA, St_OA);
            Y_OA                        = (Res_OA(3,1)-Res_OA(3,end))/Res_OA(3,1);

            C_DO(aaa)   = Res_OA(2,1);
            C_FO(aaa)   = Res_OA(4,end);
            P_FO(aaa)   = Res_OA(9,end);
            P_DO(aaa)   = Res_OA(10,1);
            P_DI(aaa)   = Res_OA(10,end);

            if aaa == 1
                QQ(8,:)     = [(1-Y_OA)*QQ(12,1)        C_FO(1) T_0 P_FO(1)];
                QQ(9,:)     = [QQ(3,1)+QQ(12,1)-QQ(8,1) C_DO(1) T_0 P_DO(1)];
```

```
            QQ(3,4)     = P_DI(1);

        elseif aaa == 2
            QQ(12,:)    = [(1-Y_OA)*QQ(11,1)            C_FO(2) T_0 P_FO(2)];
            QQ(10,:)    = [QQ(9,1)+QQ(11,1)-QQ(12,1)    C_DO(2) T_0 P_DO(2)];
            QQ(9,4)     = P_DI(2);

        elseif aaa == 3
            QQ(11,:)    = [(1-Y_OA)*QQ(7,1)             C_FO(3) T_0 P_FO(3)];
            QQ(5,:)     = [QQ(10,1)+QQ(7,1)-QQ(11,1)    C_DO(3) T_0 P_DO(3)];
            QQ(10,4)    = P_DI(3);

        end
    end

    if N_OA == 1
        QQ(12,:)    = QQ(7,:);
        QQ(11,:)    = QQ(7,:);
        QQ(10,:)    = QQ(9,:);
        QQ(5,:)     = QQ(9,:);
    elseif N_OA == 2
        QQ(11,:)    = QQ(7,:);
        QQ(5,:)     = QQ(10,:);
    end

    QQ(6,1)    = (QQ(4,1)+QQ(5,1));
    QQ(6,2)    = (QQ(4,1)*QQ(4,2)+QQ(5,1)*QQ(5,2))/QQ(6,1);
    QQ(6,3)     = (QQ(4,1)*QQ(4,3)+QQ(5,1)*QQ(5,3))/QQ(6,1);
    if QQ(4,4) ~= QQ(5,4)
        fprintf('Pressure P_2 = %.2f and P_5 = %.2f do not match!\n',QQ(4,4),QQ(5,4))
    else
        QQ(6,4) = QQ(4,4);
    end

    fprintf('RO:\t\t')                                      % V4_Q_M_It(n,          FF,
i, MW, R, T, Q_D1, C_D1,   Q_F1,   C_F1,       P_F1,   P_D1,   Type,       Flow,        AL)
    [m_D, C_D, m_F, C_F, m_M, RSF, CP_F, CP_D, P_F, P_D]    = V4_Q_M_It(n_RO, k_RO, FF_RO,
rho, phi, i, MW, R, T_0, 0,  0,      Q_F_RO, QQ(6,2),    P_F_RO, P_D_RO, Type_RO,    Flow_RO,
AL_RO, St_OA);
    Y_RO        = (m_F(1)-m_F(end))/m_F(1);

    QQ(7,:)     = [(1-Y_RO)*QQ(6,1)         C_F(end)    QQ(6,3)     P_F(end)];
    QQ(13,:)    = [Y_RO*QQ(6,1)             C_D(end)    QQ(6,3)     P_0];

    % Mass error
    Water_Err(aa)   = QQ(1,1)-(1-Y_UF)*QQ(1,1)-QQ(8,1)-QQ(13,1);
    Salt_Err(aa)    = QQ(1,1)*QQ(1,2)-(1-Y_UF)*QQ(1,1)*QQ(1,2)-QQ(8,1)*QQ(8,2)-
QQ(13,1)*QQ(13,2);

    OARO_Err_W1 = QQ(3,1)+QQ(12,1)-QQ(8,1)-QQ(9,1);
    OARO_Err_S1 = QQ(3,1)*QQ(3,2)+QQ(12,1)*QQ(12,2)-QQ(8,1)*QQ(8,2)-QQ(9,1)*QQ(9,2);

    OARO_Err_W2 = QQ(9,1)+QQ(11,1)-QQ(10,1)-QQ(12,1);
    OARO_Err_S2 = QQ(9,1)*QQ(9,2)+QQ(11,1)*QQ(11,2)-QQ(10,1)*QQ(10,2)-QQ(12,1)*QQ(12,2);

    OARO_Err_W3 = QQ(10,1)+QQ(7,1)-QQ(5,1)-QQ(11,1);
    OARO_Err_S3 = QQ(10,1)*QQ(10,2)+QQ(7,1)*QQ(7,2)-QQ(5,1)*QQ(5,2)-QQ(11,1)*QQ(11,2);

    RO_Err_W    = QQ(6,1)-QQ(7,1)-QQ(13,1);
    RO_Err_S    = QQ(6,1)*QQ(6,2)-QQ(7,1)*QQ(7,2)-QQ(13,1)*QQ(13,2);

    Err_Vec     = [Water_Err(aa) OARO_Err_W1 OARO_Err_W2 OARO_Err_W3 RO_Err_W Salt_Err(aa)
OARO_Err_S1 OARO_Err_S2 OARO_Err_S3 RO_Err_S]

    if aa >= 5 && abs(Salt_Err(aa)/(QQ(1,1)*QQ(1,2))) < FD_Err &&
abs(Water_Err(aa)/QQ(1,1)) < FD_Err
        fprintf('\nFlow diagram converged!\n')
        break
    elseif aa == It_FD
        fprintf('\nFlow diagram did not converge!\n')
    end
end


% Energy calculations
Q_Input(1,:)    = QQ(1,:);              P_Input(1)      = P_Intake;
                                        P_Input(2)      = P_UF;
```

```
    Q_Input(2,:)     = QQ(8,:);              P_Input(3)      = P_Dis;
    Q_Input(3,:)     = QQ(13,:);             P_Input(4)      = P_Post;
    Q_Input(4:5,:)   = [QQ(12,:);QQ(8,:)];   P_Input(5)      = P_F_OA;
    Q_Input(6:7,:)   = [QQ(11,:);QQ(12,:)];  P_Input(6)      = P_F_OA;
    Q_Input(8:9,:)   = [QQ(7,:);QQ(11,:)];   P_Input(7)      = P_F_OA;
    Q_Input(10:11,:)= [QQ(6,:);QQ(7,:)];     P_Input(8)      = P_F_RO;

    Q_Input(12,:)    = zeros(1,4);           P_Input(9)      = 0;

    Q_Input(13,:)    = QQ(3,:);              P_Input(10)     = QQ(3,4)-P_D_OA;
    Q_Input(14,:)    = QQ(9,:);              P_Input(11)     = QQ(9,4)-P_D_OA;
    Q_Input(15,:)    = QQ(10,:);             P_Input(12)     = QQ(10,4)-P_D_OA;

    if N_OA == 1
        P_Input(6)       = 0;                P_Input(11)     = 0;
        P_Input(7)       = 0;                P_Input(12)     = 0;
    elseif N_OA == 2
        P_Input(7)       = 0;                P_Input(12)     = 0;
    end

   [En_Vec] = V4_Energy(Q_Input ,P_Input , eff_P, eff_PEX);

    % Capital calculations
    Q_Input(1)       = Q_PFin;               m_Rat_Input(1)  = QQ(12,1)/QQ(6,1);
    Q_Input(2)       = Q_F_RO;               m_Rat_Input(2)  = QQ(11,1)/QQ(6,1);
    Q_Input(3)       = Q_F_OA;               m_Rat_Input(3)  = QQ(7,1)/QQ(6,1);
    Q_Input(4)       = Q_F_OA;               m_Rat_Input(4)  = QQ(1,1)/QQ(13,1);
    Q_Input(5)       = Q_F_OA;

    n_Input(1)       = n_RO;

    if N_OA == 1
        n_Input(2)       = n_OA;
        n_Input(3)       = 0;
        n_Input(4)       = 0;
    elseif N_OA == 2
        n_Input(2)       = n_OA;
        n_Input(3)       = n_OA;
        n_Input(4)       = 0;
    elseif N_OA == 3
        n_Input(2)       = n_OA;
        n_Input(3)       = n_OA;
        n_Input(4)       = n_OA;
    end

    [Mod_Vec]    = V4_Capital(Q_Input, m_Rat_Input, n_Input, Y_RO, A_UF, LMH_UF);


elseif FD == 2
    %% Flow Diagram 2
    % Input data
    It_FD    = Input_Vec(2,1);   X           = Input_Vec(2,2);
    RR       = Input_Vec(2,3);

    Type_OA = Input_Vec(3,1);    Flow_OA     = Input_Vec(3,2);
    FF_OA    = Input_Vec(3,3);   n_OA        = Input_Vec(3,4);
    P_F_OA   = Input_Vec(3,5);   P_D_OA      = Input_Vec(3,6);
    Q_F_OA   = Input_Vec(3,7);   AL_OA       = Input_Vec(3,8);
    St_OA    = Input_Vec(3,9);

    N_OA1    = Input_Vec(3,10);
    N_OA2    = Input_Vec(3,11);

    % Mass calculations
    QQ(1,:)      = [Q_0              S_0     T_0       P_0];
    QQ(2,:)      = [Y_UF*QQ(1,1)     QQ(1,2) QQ(1,3) QQ(1,4)];
    QQ(11,:)     = [X*QQ(1,1)        QQ(1,2) QQ(1,3) P_F_OA];    % Initial guess
    QQ(15,:)     = [X*QQ(1,1)        QQ(1,2) QQ(1,3) P_F_OA];    % Initial guess
    QQ(12,:)     = [X*QQ(1,1)        QQ(1,2) QQ(1,3) P_F_OA];    % Initial guess
    QQ(17,:)     = [X*QQ(1,1)        QQ(1,2) QQ(1,3) P_F_OA];    % Initial guess

    for aa = 1:It_FD
        fprintf('\n\nIteration: %d\n\n',aa)

        QQ(3,:) = [RR*QQ(11,1)       QQ(2,2) QQ(2,3) QQ(2,4)];
        QQ(4,:) = [QQ(2,1)-QQ(3,1)   QQ(2,2) QQ(2,3) QQ(2,4)];
```

```
        for aaa = 1:N_OA1
            Q_FI(aaa)   = Q_F_OA;
            if aaa == 1
                Q_DI(aaa)   = QQ(3,1)/QQ(15,1)*Q_F_OA;

                C_DI(aaa)   = QQ(3,2);
                C_FI(aaa)   = QQ(15,2);
            elseif aaa == 2
                Q_DI(aaa)   = QQ(14,1)/QQ(11,1)*Q_F_OA;

                C_DI(aaa)   = QQ(14,2);
                C_FI(aaa)   = QQ(11,2);
            end

            fprintf('1-OARO %d:\t',aaa) % V4_SM(n,   , FF,     i, MW, R, T,   P,      P_D1,
Q_FS,      Q_DS,      C_DS,      C_FS,      SM, It_P, Type,    Flow,    AL   , St)
            [Res_OA, E_Vec]             = V4_SM(n_OA, FF_OA,  i, MW, R, T_0, P_F_OA, P_D_OA,
Q_FI(aaa), Q_DI(aaa), C_DI(aaa), C_FI(aaa), SM, It_P, Type_OA, Flow_OA, AL_OA, St_OA);
            Y_OA                        = (Res_OA(3,1)-Res_OA(3,end))/Res_OA(3,1);

            C_DO(aaa)   = Res_OA(2,1);
            C_FO(aaa)   = Res_OA(4,end);
            P_FO(aaa)   = Res_OA(9,end);
            P_DO(aaa)   = Res_OA(10,1);
            P_DI(aaa)   = Res_OA(10,end);

            if aaa == 1
                QQ(12,:)    = [(1-Y_OA)*QQ(15,1)            C_FO(1) T_0 P_FO(1)];
                QQ(14,:)    = [QQ(3,1)+QQ(15,1)-QQ(12,1)    C_DO(1) T_0 P_DO(1)];
                QQ(3,4)     = P_DI(1);

            elseif aaa == 2
                QQ(15,:)    = [(1-Y_OA)*QQ(11,1)            C_FO(2) T_0 P_FO(2)];
                QQ(5,:)     = [QQ(14,1)+QQ(11,1)-QQ(15,1)   C_DO(2) T_0 P_DO(2)];
                QQ(14,4)    = P_DI(2);

            end
        end

        if N_OA1 == 1
            QQ(15,:)    = QQ(11,:);
            QQ(5,:)     = QQ(14,:);
        end

        QQ(6,1) = (QQ(4,1)+QQ(5,1));
        QQ(6,2) = (QQ(4,1)*QQ(4,2)+QQ(5,1)*QQ(5,2))/QQ(6,1);
        QQ(6,3) = (QQ(4,1)*QQ(4,3)+QQ(5,1)*QQ(5,3))/QQ(6,1);
        if QQ(4,4) ~= QQ(5,4)
            fprintf('Pressure P_4 = %.2f and P_5 = %.2f do not match!\n',QQ(4,4),QQ(5,4))
        else
            QQ(6,4) = QQ(4,4);
        end

        fprintf('RO:\t\t')                                      % V4_Q_M_It(n,     FF,
i, MW, R, T, Q_D1,  C_D1,      Q_F1,   C_F1,       P_F1,   P_D1,   Type,       Flow,   AL)
        [m_D, C_D, m_F, C_F, m_M, RSF, CP_F, CP_D, P_F, P_D]    = V4_Q_M_It(n_RO, k_RO, FF_RO,
rho, phi, i, MW, R, T_0, 0,     0,      Q_F_RO, QQ(6,2),    P_F_RO, P_D_RO, Type_RO,
Flow_RO, AL_RO, St_RO);
        Y_RO        = (m_F(1)-m_F(end))/m_F(1);

        QQ(7,:) = [(1-Y_RO)*QQ(6,1)         C_F(end)        QQ(6,3)     P_F(end)];
        QQ(8,:) = [RR*QQ(12,1)              QQ(7,2)         QQ(7,3)     P_0];
        QQ(9,:) = [QQ(7,1)-QQ(8,1)          QQ(7,2)         QQ(7,3)     P_0];
        QQ(18,:)= [Y_RO*QQ(6,1)             C_D(end)        QQ(6,3)     P_0];

        for aaa = 1:N_OA2
            Q_FI(aaa)   = Q_F_OA;
            if aaa == 1
                Q_DI(aaa)   = QQ(8,1)/QQ(17,1)*Q_F_OA;

                C_DI(aaa)   = QQ(8,2);
                C_FI(aaa)   = QQ(17,2);
            elseif aaa == 2
                Q_DI(aaa)   = QQ(16,1)/QQ(12,1)*Q_F_OA;

                C_DI(aaa)   = QQ(16,2);
                C_FI(aaa)   = QQ(12,2);
```

```
            end

            fprintf('2-OARO %d:\t',aaa) % V4_SM(n,   , FF,     i, MW, R, T,    P,       P_D1,
Q_FS,      Q_DS,      C_DS,      C_FS,       SM, It_P, Type,     Flow,     AL    , St)
            [Res_OA, E_Vec]             = V4_SM(n_OA, FF_OA,  i, MW, R, T_0, P_F_OA, P_D_OA,
Q_FI(aaa), Q_DI(aaa), C_DI(aaa), C_FI(aaa), SM, It_P, Type_OA, Flow_OA, AL_OA, St_OA);
            Y_OA                        = (Res_OA(3,1)-Res_OA(3,end))/Res_OA(3,1);

            C_DO(aaa)    = Res_OA(2,1);
            C_FO(aaa)    = Res_OA(4,end);
            P_FO(aaa)    = Res_OA(9,end);
            P_DO(aaa)    = Res_OA(10,1);
            P_DI(aaa)    = Res_OA(10,end);

            if aaa == 1
                QQ(13,:)     = [(1-Y_OA)*QQ(17,1)             C_FO(1) T_0 P_FO(1)];
                QQ(16,:)     = [QQ(8,1)+QQ(17,1)-QQ(13,1)     C_DO(1) T_0 P_DO(1)];
                QQ(8,4)      = P_DI(1);

            elseif aaa == 2
                QQ(17,:)     = [(1-Y_OA)*QQ(12,1)             C_FO(2) T_0 P_FO(2)];
                QQ(10,:)     = [QQ(16,1)+QQ(12,1)-QQ(17,1)    C_DO(2) T_0 P_DO(2)];
                QQ(16,4)     = P_DI(2);

            end
        end

        if N_OA2 == 1
            QQ(17,:)     = QQ(12,:);
            QQ(10,:)     = QQ(16,:);
        end

        QQ(11,1)     = (QQ(9,1)+QQ(10,1));
        QQ(11,2)     = (QQ(9,1)*QQ(9,2)+QQ(10,1)*QQ(10,2))/QQ(11,1);
        QQ(11,3)     = (QQ(9,1)*QQ(9,3)+QQ(10,1)*QQ(10,3))/QQ(11,1);
        if QQ(9,4) ~= QQ(10,4)
            fprintf('Pressure P_9 = %.2f and P_10 = %.2f do not match!\n',QQ(9,4),QQ(10,4))
        else
            QQ(11,4) = QQ(10,4);
        end

        % Mass error
        Water_Err(aa)    = QQ(1,1)-(1-Y_UF)*QQ(1,1)-QQ(13,1)-QQ(18,1);
        Salt_Err(aa)     = QQ(1,1)*QQ(1,2)-(1-Y_UF)*QQ(1,1)*QQ(1,2)-QQ(13,1)*QQ(13,2)-
QQ(18,1)*QQ(18,2);

        OARO1_Err_W = QQ(3,1)+QQ(15,1)-QQ(12,1)-QQ(14,1);
        OARO1_Err_S = QQ(3,1)*QQ(3,2)+QQ(15,1)*QQ(15,2)-QQ(12,1)*QQ(12,2)-QQ(14,1)*QQ(14,2);

        OARO2_Err_W = QQ(11,1)+QQ(14,1)-QQ(5,1)-QQ(15,1);
        OARO2_Err_S = QQ(11,1)*QQ(11,2)+QQ(14,1)*QQ(14,2)-QQ(5,1)*QQ(5,2)-QQ(15,1)*QQ(15,2);

        OARO4_Err_W = QQ(12,1)+QQ(16,1)-QQ(10,1)-QQ(17,1);
        OARO4_Err_S = QQ(12,1)*QQ(12,2)+QQ(16,1)*QQ(16,2)-QQ(10,1)*QQ(10,2)-QQ(17,1)*QQ(17,2);

        OARO3_Err_W = QQ(8,1)+QQ(17,1)-QQ(13,1)-QQ(16,1);
        OARO3_Err_S = QQ(8,1)*QQ(8,2)+QQ(17,1)*QQ(17,2)-QQ(13,1)*QQ(13,2)-QQ(16,1)*QQ(16,2);

        RO_Err_W     = QQ(6,1)-QQ(7,1)-QQ(18,1);
        RO_Err_S     = QQ(6,1)*QQ(6,2)-QQ(7,1)*QQ(7,2)-QQ(18,1)*QQ(18,2);

        Err_Vec      = [Water_Err(aa) OARO1_Err_W OARO2_Err_W OARO3_Err_W OARO4_Err_W RO_Err_W
Salt_Err(aa) OARO1_Err_S OARO2_Err_S OARO3_Err_S OARO4_Err_S RO_Err_S]

        if aa >= 5 && abs(Salt_Err(aa)/(QQ(1,1)*QQ(1,2))) < FD_Err &&
abs(Water_Err(aa)/QQ(1,1)) < FD_Err
            fprintf('\nFlow diagram converged!\n')
            break
        elseif aa == It_FD
            fprintf('\nFlow diagram did not converge!\n')
        end
    end

    % Energy calculations
    Q_Input(1,:)     = QQ(1,:);              P_Input(1)       = P_Intake;
                                             P_Input(2)       = P_UF;
    Q_Input(2,:)     = QQ(13,:);             P_Input(3)       = P_Dis;
```

```
    Q_Input(3,:)     = QQ(18,:);              P_Input(4)      = P_Post;
    Q_Input(4:5,:)   = [QQ(15,:);QQ(12,:)];   P_Input(5)      = P_F_OA;
    Q_Input(6:7,:)   = [QQ(17,:);QQ(13,:)];   P_Input(6)      = P_F_OA;
                                              P_Input(7)      = P_F_OA;
    Q_Input(10:11,:)= [QQ(6,:);QQ(7,:)];      P_Input(8)      = P_F_RO;

    Q_Input(12,:)    = zeros(1,4);            P_Input(9)      = 0;

    Q_Input(13,:)    = QQ(3,:);               P_Input(10)     = QQ(3,4)-P_D_OA;
    Q_Input(14,:)    = QQ(8,:);               P_Input(11)     = QQ(8,4)-P_D_OA;

    if N_OA1 == 2
        Q_Input(8:9,:)  = [QQ(11,:);QQ(15,:)];
        Q_Input(15,:)   = QQ(14,:);
        P_Input(12)     = QQ(14,4)-P_D_OA;
    elseif N_OA2 == 2
        Q_Input(8:9,:)  = [QQ(12,:);QQ(17,:)];
        Q_Input(15,:)   = QQ(16,:);
        P_Input(12)     = QQ(16,4)-P_D_OA;
    else
        Q_Input(8:9,:)  = zeros(2,4);
        Q_Input(15,:)   = 0;
        P_Input(12)     = 0;
    end



   [En_Vec] = V4_Energy(Q_Input ,P_Input , eff_P, eff_PEX);

    % Capital calculations
    Q_Input(1)      = Q_PFin;                m_Rat_Input(1)  = QQ(15,1)/QQ(6,1);
    Q_Input(2)      = Q_F_RO;                m_Rat_Input(2)  = QQ(17,1)/QQ(6,1);
    Q_Input(3)      = Q_F_OA;
    Q_Input(4)      = Q_F_OA;                m_Rat_Input(4)  = QQ(1,1)/QQ(18,1);
    Q_Input(5)      = Q_F_OA;

    n_Input(1)      = n_RO;

    if N_OA1 == 2
        m_Rat_Input(3)  = QQ(11,1)/QQ(6,1);
    elseif N_OA2 == 2
        m_Rat_Input(3)  = QQ(12,1)/QQ(6,1);
    else
        m_Rat_Input(3)  = 0;
    end


    if N_OA1 == 1 && N_OA2 == 1
        n_Input(2)      = n_OA;
        n_Input(3)      = n_OA;
        n_Input(4)      = 0;
    elseif N_OA1 == 2 || N_OA2 == 2
        n_Input(2)      = n_OA;
        n_Input(3)      = n_OA;
        n_Input(4)      = n_OA;
    end

    [Mod_Vec]   = V4_Capital(Q_Input, m_Rat_Input, n_Input, Y_RO, A_UF, LMH_UF);



elseif FD == 3
    %% Flow Diagram 3
    % Input data
    It_FD   = Input_Vec(2,1);   X           = Input_Vec(2,2);
    RR      = Input_Vec(2,3);

    Type_OA= Input_Vec(3,1);    Flow_OA     = Input_Vec(3,2);
    FF_OA   = Input_Vec(3,3);   n_OA        = Input_Vec(3,4);
    P_F_OA  = Input_Vec(3,5);   P_D_OA      = Input_Vec(3,6);
    Q_F_OA = Input_Vec(3,7);    AL_OA       = Input_Vec(3,8);
    St_OA  = Input_Vec(3,9);

    % Mass calculations
    QQ(1,:)     = [Q_0              S_0     T_0       P_0];
    QQ(2,:)     = [Y_UF*QQ(1,1)     QQ(1,2) QQ(1,3) QQ(1,4)];
```

```
    QQ(11,:)    = [X*QQ(1,1)        QQ(1,2) QQ(1,3) P_F_OA];    % Initial guess
    QQ(16,:)    = [0.5*X*QQ(1,1)    QQ(1,2) QQ(1,3) P_F_OA];    % Initial guess

    for aa = 1:It_FD
        fprintf('\n\nIteration: %d\n\n',aa)

        QQ(3,:) = [RR*QQ(11,1)      QQ(2,2) QQ(2,3) QQ(2,4)];
        QQ(4,:) = [QQ(2,1)-QQ(3,1)  QQ(2,2) QQ(2,3) QQ(2,4)];

        fprintf('OARO1:\t')     % V4_SM(n,    FF,     i, MW, R, T,    P,          P_D1,
Q,       Q_DS,           C_DS,       S,        SM, It_P, Type,    Flow,    AL)
        [Res_OA, E_Vec]         = V4_SM(n_OA, FF_OA,  i, MW, R, T_0, P_F_OA,   P_D_OA,
Q_F_OA, RR*Q_F_OA,        QQ(3,2),    QQ(11,2),   SM, It_P, Type_OA, Flow_OA, AL_OA, St_OA);
        Y_OA1                   = (Res_OA(3,1)-Res_OA(3,end))/Res_OA(3,1);

        QQ(12,:)= [(1-Y_OA1)*QQ(11,1)           Res_OA(4,end)   QQ(11,3)    Res_OA(9,end)];
        QQ(5,:) = [QQ(3,1)+QQ(11,1)-QQ(12,1)    Res_OA(2,1)     QQ(3,3)     Res_OA(10,1)];
        QQ(3,4) = Res_OA(10,end);

        QQ(6,1) = (QQ(4,1)+QQ(5,1));
        QQ(6,2) = (QQ(4,1)*QQ(4,2)+QQ(5,1)*QQ(5,2))/QQ(6,1);
        QQ(6,3) = (QQ(4,1)*QQ(4,3)+QQ(5,1)*QQ(5,3))/QQ(6,1);
        if QQ(4,4) ~= QQ(5,4)
            fprintf('Pressure P_4 = %.2f and P_5 = %.2f do not match!\n',QQ(4,4),QQ(5,4))
        else
            QQ(6,4) = QQ(4,4);
        end

        fprintf('RO:\t\t')                                      % V4_Q_M_It(n,
FF,      i, MW, R, T, Q_D1,  C_D1,   Q_F1,   C_F1,       P_F1,   P_D1,   Type,       Flow,
AL)
        [m_D, C_D, m_F, C_F, m_M, RSF, CP_F, CP_D, P_F, P_D]    = V4_Q_M_It(n_RO, k_RO, FF_RO,
rho, phi, i, MW, R, T_0, 0,     0,      Q_F_RO, QQ(6,2),    P_F_RO, P_D_RO, Type_RO,
Flow_RO, AL_RO, St_RO);
        Y_RO        = (m_F(1)-m_F(end))/m_F(1);

        QQ(7,:) = [(1-Y_RO)*QQ(6,1)         C_F(end)        QQ(6,3)     P_F(end)];
        QQ(8,:) = [RR*QQ(16,1)              QQ(7,2)         QQ(7,3)     P_0];
        QQ(9,:) = [QQ(7,1)-QQ(8,1)          QQ(7,2)         QQ(7,3)     P_0];
        QQ(19,:)= [Y_RO*QQ(6,1)             C_D(end)        QQ(6,3)     P_0];

        fprintf('OARO2:\t')     % V4_SM(n,    FF,     i, MW, R, T,    P,          P_D1,       Q,
Q_DS,       C_DS,       S,          SM, It_P, Type,    Flow,    AL)
        [Res_OA, E_Vec]         = V4_SM(n_OA, FF_OA,  i, MW, R, T_0, P_F_OA,    P_D_OA,
Q_F_OA, RR*Q_F_OA,   QQ(8,2),    QQ(16,2),    SM, It_P, Type_OA, Flow_OA, AL_OA, St_OA);
        Y_OA2                   = (Res_OA(3,1)-Res_OA(3,end))/Res_OA(3,1);

        QQ(17,:)= [(1-Y_OA2)*QQ(16,1)           Res_OA(4,end)   QQ(16,3)    Res_OA(9,end)];
        QQ(10,:)= [QQ(8,1)+QQ(16,1)-QQ(17,1)    Res_OA(2,1)     QQ(8,3)     Res_OA(10,1)];
        QQ(8,4) = Res_OA(10,end);

        QQ(11,1)    = (QQ(9,1)+QQ(10,1));
        QQ(11,2)    = (QQ(9,1)*QQ(9,2)+QQ(10,1)*QQ(10,2))/QQ(11,1);
        QQ(11,3)    = (QQ(9,1)*QQ(9,3)+QQ(10,1)*QQ(10,3))/QQ(11,1);
        QQ(11,4)    = P_F_OA;

        QQ(13,:)    = [RR*QQ(17,1)          QQ(12,2)        QQ(12,3)        P_0];
        QQ(14,:)    = [QQ(12,1)-QQ(13,1)    QQ(12,2)        QQ(12,3)        P_0];

        fprintf('OARO3:\t')     % V4_SM(n,    FF,     i, MW, R, T,    P,          P_D1,       Q,
Q_DS,       C_DS,       S,          SM, It_P, Type,    Flow,    AL)
        [Res_OA, E_Vec]         = V4_SM(n_OA, FF_OA,  i, MW, R, T_0, P_F_OA,    P_D_OA,
Q_F_OA, RR*Q_F_OA,   QQ(13,2),    QQ(17,2),   SM, It_P, Type_OA, Flow_OA, AL_OA, St_OA);
        Y_OA3                   = (Res_OA(3,1)-Res_OA(3,end))/Res_OA(3,1);

        QQ(18,:)= [(1-Y_OA3)*QQ(17,1)           Res_OA(4,end)   QQ(17,3)    Res_OA(9,end)];
        QQ(15,:)= [QQ(13,1)+QQ(17,1)-QQ(18,1)   Res_OA(2,1)     QQ(13,3)    Res_OA(10,1)];
        QQ(3,4) = Res_OA(10,end);

        QQ(16,1)    = (QQ(15,1)+QQ(14,1));
        QQ(16,2)    = (QQ(15,1)*QQ(15,2)+QQ(14,1)*QQ(14,2))/QQ(16,1);
        QQ(16,3)    = (QQ(15,1)*QQ(15,3)+QQ(14,1)*QQ(14,3))/QQ(16,1);
        QQ(16,4)    = P_F_OA;

        % Mass error
        Water_Err(aa)   = QQ(1,1)-(1-Y_UF)*QQ(1,1)-QQ(18,1)-QQ(19,1);
```

```
        Salt_Err(aa)    = QQ(1,1)*QQ(1,2)-(1-Y_UF)*QQ(1,1)*QQ(1,2)-QQ(18,1)*QQ(18,2)-
QQ(19,1)*QQ(19,2);

        OARO1_Err_W = QQ(3,1)+QQ(11,1)-QQ(5,1)-QQ(12,1);
        OARO1_Err_S = QQ(3,1)*QQ(3,2)+QQ(11,1)*QQ(11,2)-QQ(5,1)*QQ(5,2)-QQ(12,1)*QQ(12,2);

        RO_Err_W    = QQ(6,1)-QQ(7,1)-QQ(19,1);
        RO_Err_S    = QQ(6,1)*QQ(6,2)-QQ(7,1)*QQ(7,2)-QQ(19,1)*QQ(19,2);

        OARO2_Err_W = QQ(8,1)+QQ(16,1)-QQ(10,1)-QQ(17,1);
        OARO2_Err_S = QQ(8,1)*QQ(8,2)+QQ(16,1)*QQ(16,2)-QQ(10,1)*QQ(10,2)-QQ(17,1)*QQ(17,2);

        OARO3_Err_W = QQ(13,1)+QQ(17,1)-QQ(15,1)-QQ(18,1);
        OARO3_Err_S = QQ(13,1)*QQ(13,2)+QQ(17,1)*QQ(17,2)-QQ(15,1)*QQ(15,2)-QQ(18,1)*QQ(18,2);

        Err_Vec     = [Water_Err(aa) OARO1_Err_W RO_Err_W OARO2_Err_W OARO3_Err_W Salt_Err(aa)
OARO1_Err_S RO_Err_S OARO2_Err_S OARO3_Err_S]

        if aa >= 5 && abs(Salt_Err(aa)/(QQ(1,1)*QQ(1,2))) < FD_Err &&
abs(Water_Err(aa)/QQ(1,1)) < FD_Err
            fprintf('\nFlow diagram converged!\n')
            break
        elseif aa == It_FD
            fprintf('\nFlow diagram did not converge!\n')
        end
    end

    % Energy calculations
    Q_Input(1,:)    = QQ(1,:);              P_Input(1)      = P_Intake;
                                            P_Input(2)      = P_UF;
    Q_Input(2,:)    = QQ(18,:);             P_Input(3)      = P_Dis;
    Q_Input(3,:)    = QQ(19,:);             P_Input(4)      = P_Post;
    Q_Input(4:5,:)  = [QQ(11,:);QQ(12,:)];  P_Input(5)      = P_F_OA;
    Q_Input(6:7,:)  = [QQ(16,:);QQ(17,:)];  P_Input(6)      = P_F_OA;
    Q_Input(8:9,:)  = [QQ(17,:);QQ(18,:)];  P_Input(7)      = P_F_OA;
    Q_Input(10:11,:)= [QQ(6,:);QQ(7,:)];    P_Input(8)      = P_F_RO;
    Q_Input(12,:)   = zeros(1,4);           P_Input(9)      = 0;

    Q_Input(13,:)   = QQ(3,:);              P_Input(10)     = QQ(3,4)-P_D_OA;
    Q_Input(14,:)   = QQ(8,:);              P_Input(11)     = QQ(8,4)-P_D_OA;
    Q_Input(15,:)   = QQ(13,:);             P_Input(12)     = QQ(13,4)-P_D_OA;

    [En_Vec]    = V4_Energy(Q_Input ,P_Input , eff_P, eff_PEX);

    % Capital calculations
    Q_Input(1)      = Q_PFin;               m_Rat_Input(1)  = QQ(11,1)/QQ(6,1);
    Q_Input(2)      = Q_F_RO;               m_Rat_Input(2)  = QQ(16,1)/QQ(6,1);
    Q_Input(3)      = Q_F_OA;               m_Rat_Input(3)  = QQ(17,1)/QQ(6,1);
    Q_Input(4)      = Q_F_OA;               m_Rat_Input(4)  = QQ(1,1)/QQ(19,1);
    Q_Input(5)      = Q_F_OA;

    n_Input(1)      = n_RO;
    n_Input(2)      = n_OA;
    n_Input(3)      = n_OA;
    n_Input(4)      = n_OA;

    [Mod_Vec]   = V4_Capital(Q_Input, m_Rat_Input, n_Input, Y_RO, A_UF, LMH_UF);




elseif FD == 41
%% Flow Diagram 4_1
    % Input data
    It_FD   = Input_Vec(2,1);   X           = Input_Vec(2,2);
    RR      = Input_Vec(2,3);

    Type_OA= Input_Vec(3,1);    Flow_OA     = Input_Vec(3,2);
    FF_OA   = Input_Vec(3,3);   n_OA        = Input_Vec(3,4);
    P_F_OA  = Input_Vec(3,5);   P_D_OA      = Input_Vec(3,6);
    Q_F_OA = Input_Vec(3,7);    AL_OA       = Input_Vec(3,8);
    St_OA  = Input_Vec(3,9);

    P_Ry    = Input_Vec(3,10);
    N_OA    = Input_Vec(3,11);
    N_OA2   = Input_Vec(3,12);
```

```
    % Mass calculations
    QQ(1,:)     = [Q_0              S_0         T_0         P_0];
    QQ(2,:)     = [Y_UF*QQ(1,1)     QQ(1,2)     QQ(1,3)     QQ(1,4)];
    QQ(9,:)     = [RR*QQ(2,1)       85          QQ(1,3)     QQ(1,4)];
    QQ(11,:)    = [RR*QQ(2,1)       85          QQ(1,3)     QQ(1,4)];
    QQ(6,:)     = [RR*QQ(2,1)       85          QQ(1,3)     QQ(1,4)];

    for aa = 1:It_FD
        fprintf('\n\nIteration: %d\n\n',aa)

        for aaa = 1:N_OA
            Q_FI(aaa)   = Q_F_OA;
            if aaa == 1
                Q_DI(aaa)   = QQ(9,1)/QQ(2,1)*Q_F_OA;

                C_DI(aaa)   = QQ(9,2);
                C_FI(aaa)   = QQ(2,2);
            elseif aaa == 2
                Q_DI(aaa)   = QQ(11,1)/QQ(8,1)*Q_F_OA;

                C_DI(aaa)   = QQ(11,2);
                C_FI(aaa)   = QQ(8,2);
            elseif aaa == 3
                Q_DI(aaa)   = QQ(6,1)/QQ(10,1)*Q_F_OA;

                C_DI(aaa)   = QQ(6,2);
                C_FI(aaa)   = QQ(10,2);
            end

            fprintf('OARO %d:\t',aaa)   % V4_SM(n,  , FF,     i, MW, R, T,   P,      P_D1,
Q_FS,      Q_DS,      C_DS,      C_FS,      SM, It_P, Type,    Flow,    AL   , St)
            [Res_OA, E_Vec]             = V4_SM(n_OA, FF_OA,  i, MW, R, T_0, P_F_OA, P_D_OA,
Q_FI(aaa), Q_DI(aaa), C_DI(aaa), C_FI(aaa), SM, It_P, Type_OA, Flow_OA, AL_OA, St_OA);
            Y_OA                        = (Res_OA(3,1)-Res_OA(3,end))/Res_OA(3,1);

            C_DO(aaa)   = Res_OA(2,1);
            C_FO(aaa)   = Res_OA(4,end);
            P_FO(aaa)   = Res_OA(9,end);
            P_DO(aaa)   = Res_OA(10,1);
            P_DI(aaa)   = Res_OA(10,end);

            if aaa == 1
                QQ(8,:)     = [(1-Y_OA)*QQ(2,1)             C_FO(1) T_0 P_FO(1)];
                QQ(4,:)     = [QQ(2,1)+QQ(9,1)-QQ(8,1)      C_DO(1) T_0 P_DO(1)];
                QQ(9,4)     = P_DI(1);

            elseif aaa == 2
                QQ(10,:)    = [(1-Y_OA)*QQ(8,1)             C_FO(2) T_0 P_FO(2)];
                QQ(9,:)     = [QQ(8,1)+QQ(11,1)-QQ(10,1)    C_DO(2) T_0 P_DO(2)];
                QQ(11,4)     = P_DI(2);

            elseif aaa == 3
                QQ(3,:)     = [(1-Y_OA)*QQ(10,1)            C_FO(3) T_0 P_FO(3)];
                QQ(11,:)    = [QQ(10,1)+QQ(6,1)-QQ(3,1)     C_DO(3) T_0 P_DO(3)];
                QQ(6,4)     = P_DI(3);
            end
        end

        fprintf('RO:\t\t')                                          % V4_Q_M_It(n,     FF,
i, MW, R, T, Q_D1,  C_D1,  Q_F1,   C_F1,       P_F1,   P_D1,   Type,       Flow,        AL)
        [m_D, C_D, m_F, C_F, m_M, RSF, CP_F, CP_D, P_F, P_D]    = V4_Q_M_It(n_RO, k_RO, FF_RO,
rho, phi, i, MW, R, T_0, 0,      0,  Q_F_RO, QQ(4,2),    P_F_RO, P_D_RO, Type_RO,    Flow_RO,
AL_RO, St_RO);
        Y_RO        = (m_F(1)-m_F(end))/m_F(1);

        QQ(5,:) = [(1-Y_RO)*QQ(4,1)         C_F(end)        QQ(4,3)     P_F(end)];
        QQ(12,:)= [Y_RO*QQ(4,1)             C_D(end)        QQ(4,3)     P_0];

        if QQ(5,1)>RR*QQ(2,1)
            QQ(7,:) = [QQ(5,1)-RR*QQ(2,1)   QQ(5,2)         QQ(5,3)     P_0];
            QQ(6,:) = [RR*QQ(2,1)           QQ(5,2)         QQ(5,3)     P_0];
        else
            QQ(6,:) = [QQ(5,1)              QQ(5,2)         QQ(5,3)     P_0];
            QQ(7,:) = [0                    QQ(5,2)         QQ(5,3)     P_0];
        end
```

```
        if N_OA == 1
            QQ(9,:)     = QQ(6,:);
            QQ(10,:)    = QQ(8,:);
            QQ(11,:)    = QQ(6,:);
            QQ(3,:)     = QQ(8,:);
        elseif N_OA == 2
            QQ(11,:)    = QQ(6,:);
            QQ(3,:)     = QQ(10,:);
        end

        alpha=0.5;
        QQ(2,1) = alpha*(QQ(2,1))+(1-alpha)*(Y_UF*QQ(1,1)+X*QQ(7,1));
        QQ(2,2) = (Y_UF*QQ(1,1)*QQ(1,2)+X*QQ(7,1)*QQ(7,2))/QQ(2,1);
        QQ(2,3) = (Y_UF*QQ(1,1)*QQ(1,3)+X*QQ(7,1)*QQ(7,3))/QQ(2,1);
        QQ(2,4) = QQ(1,4);

        % Mass error
        Water_Err(aa)   = QQ(1,1)-(1-Y_UF)*QQ(1,1)-QQ(3,1)-QQ(12,1)-(1-X)*QQ(7,1);
        Salt_Err(aa)    = QQ(1,1)*QQ(1,2)-(1-Y_UF)*QQ(1,1)*QQ(1,2)-QQ(3,1)*QQ(3,2)-
QQ(12,1)*QQ(12,2)-(1-X)*QQ(7,1)*QQ(7,2);

        OARO1_Err_W = QQ(2,1)+QQ(9,1)-QQ(8,1)-QQ(4,1);
        OARO1_Err_S = QQ(2,1)*QQ(2,2)+QQ(9,1)*QQ(9,2)-QQ(8,1)*QQ(8,2)-QQ(4,1)*QQ(4,2);

        OARO2_Err_W = QQ(8,1)+QQ(11,1)-QQ(9,1)-QQ(10,1);
        OARO2_Err_S = QQ(8,1)*QQ(8,2)+QQ(11,1)*QQ(11,2)-QQ(9,1)*QQ(9,2)-QQ(10,1)*QQ(10,2);

        OARO3_Err_W = QQ(10,1)+QQ(6,1)-QQ(3,1)-QQ(11,1);
        OARO3_Err_S = QQ(10,1)*QQ(10,2)+QQ(6,1)*QQ(6,2)-QQ(3,1)*QQ(3,2)-QQ(11,1)*QQ(11,2);

        RO_Err_W    = QQ(4,1)-QQ(5,1)-QQ(12,1);
        RO_Err_S    = QQ(4,1)*QQ(4,2)-QQ(5,1)*QQ(5,2)-QQ(12,1)*QQ(12,2);

        Err_Vec     = [Water_Err(aa) OARO1_Err_W OARO2_Err_W OARO3_Err_W RO_Err_W Salt_Err(aa)
OARO1_Err_S OARO2_Err_S OARO3_Err_S RO_Err_S]

        if aa >= 5 && abs(Salt_Err(aa)/(QQ(1,1)*QQ(1,2))) < FD_Err &&
abs(Water_Err(aa)/QQ(1,1)) < FD_Err
            fprintf('\nFlow diagram converged!\n')
            break
        elseif aa == It_FD
            fprintf('\nFlow diagram did not converge!\n')
        end

    end

    % Energy calculations
    Q_Input(1,:)    = QQ(1,:);              P_Input(1)      = P_Intake;
                                            P_Input(2)      = P_UF;
    Q_Input(2,:)    = QQ(3,:);              P_Input(3)      = P_Dis;
    Q_Input(3,:)    = QQ(12,:);             P_Input(4)      = P_Post;
    Q_Input(4:5,:)  = [QQ(2,:);QQ(8,:)];    P_Input(5)      = P_F_OA;
    Q_Input(6:7,:)  = [QQ(8,:);QQ(10,:)];   P_Input(6)      = P_F_OA;
    Q_Input(8:9,:)  = [QQ(10,:);QQ(3,:)];   P_Input(7)      = P_F_OA;
    Q_Input(10:11,:)= [QQ(4,:);QQ(5,:)];    P_Input(8)      = P_F_RO;

    Q_Input(12,:)   = QQ(4,:);              P_Input(9)      = P_Ry;

    Q_Input(13,:)   = QQ(9,:);              P_Input(10)     = QQ(9,4)-P_D_OA;
    Q_Input(14,:)   = QQ(11,:);             P_Input(11)     = QQ(11,4)-P_D_OA;
    Q_Input(15,:)   = QQ(6,:);              P_Input(12)     = QQ(6,4)-P_D_OA;

    if N_OA == 1
        P_Input(6)      = 0;                P_Input(11)     = 0;
        P_Input(7)      = 0;                P_Input(12)     = 0;
    elseif N_OA == 2
        P_Input(7)      = 0;                P_Input(12)     = 0;
    end

   [En_Vec] = V4_Energy(Q_Input ,P_Input , eff_P, eff_PEX);

    % Capital calculations
    Q_Input(1)      = Q_PFin;               m_Rat_Input(1)  = QQ(2,1)/QQ(4,1);
    Q_Input(2)      = Q_F_RO;               m_Rat_Input(2)  = QQ(8,1)/QQ(4,1);
    Q_Input(3)      = Q_F_OA;               m_Rat_Input(3)  = QQ(10,1)/QQ(4,1);
    Q_Input(4)      = Q_F_OA;               m_Rat_Input(4)  = QQ(1,1)/QQ(12,1);
    Q_Input(5)      = Q_F_OA;
```

```
    n_Input(1)      = n_RO;

    if N_OA == 1
        n_Input(2)      = n_OA;
        n_Input(3)      = 0;
        n_Input(4)      = 0;
    elseif N_OA == 2
        n_Input(2)      = n_OA;
        n_Input(3)      = n_OA;
        n_Input(4)      = 0;
    elseif N_OA == 3
        n_Input(2)      = n_OA;
        n_Input(3)      = n_OA;
        n_Input(4)      = n_OA;
    end

    [Mod_Vec]   = V4_Capital(Q_Input, m_Rat_Input, n_Input, Y_RO, A_UF, LMH_UF);




elseif FD == 42
%% Flow Diagram 4_2
    % Input data
    It_FD   = Input_Vec(2,1);   X           = Input_Vec(2,2);
    RR      = Input_Vec(2,3);

    Type_OA= Input_Vec(3,1);    Flow_OA     = Input_Vec(3,2);
    FF_OA   = Input_Vec(3,3);   n_OA        = Input_Vec(3,4);
    P_F_OA  = Input_Vec(3,5);   P_D_OA      = Input_Vec(3,6);
    Q_F_OA = Input_Vec(3,7);    AL_OA       = Input_Vec(3,8);
    St_OA  = Input_Vec(3,9);

    P_Ry    = Input_Vec(3,10);
    N_OA1   = Input_Vec(3,11);
    N_OA2   = Input_Vec(3,12);

    % Mass calculations
    QQ(1,:)     = [Q_0          S_0         T_0         P_0];
    QQ(2,:)     = [Y_UF*QQ(1,1) QQ(1,2)     QQ(1,3)     QQ(1,4)];
    QQ(4,:)     = [RR*QQ(2,1)   85          QQ(1,3)     QQ(1,4)];
    QQ(6,:)     = [RR*QQ(2,1)   85          QQ(1,3)     QQ(1,4)];
    QQ(8,:)     = [RR*QQ(2,1)   70          QQ(1,3)     QQ(1,4)];
    QQ(13,:)    = [RR*QQ(2,1)   85          QQ(1,3)     QQ(1,4)];
    QQ(15,:)    = [RR*QQ(2,1)   110         QQ(1,3)     QQ(1,4)];

    for aa = 1:It_FD
        fprintf('\n\nIteration: %d\n\n',aa)

        fprintf('RO:\t\t')                                      % V4_Q_M_It(n,          FF,
i, MW, R, T, Q_D1,  C_D1,      Q_F1,   C_F1,        P_F1,   P_D1,   Type,       Flow,
AL)
        [m_D, C_D, m_F, C_F, m_M, RSF, CP_F, CP_D, P_F, P_D]    = V4_Q_M_It(n_RO, k_RO, FF_RO,
rho, phi, i, MW, R, T_0, 0,      0,      Q_F_RO, QQ(8,2),    P_F_RO, P_D_RO, Type_RO,
Flow_RO, AL_RO, St_RO);
        Y_RO        = (m_F(1)-m_F(end))/m_F(1);

        QQ(9,:) = [(1-Y_RO)*QQ(8,1)         C_F(end)        QQ(8,3)     P_F(end)];
        QQ(16,:)= [Y_RO*QQ(8,1)             C_D(end)        QQ(8,3)     P_0];

        if QQ(9,1)>RR*QQ(4,1)
            QQ(11,:) = [QQ(9,1)-RR*QQ(4,1)  QQ(9,2)         QQ(9,3)     P_0];
            QQ(10,:) = [RR*QQ(4,1)          QQ(9,2)         QQ(9,3)     P_0];
        else
            QQ(11,:) = [0                   QQ(9,2)         QQ(9,3)     P_0];
            QQ(10,:) = [QQ(9,1)             QQ(9,2)         QQ(9,3)     P_0];
        end

        if N_OA2 == 1
            QQ(15,:)    = QQ(10,:);
            Loop        = 2;
        else
            Loop        = 3;
        end
```

```
        for ii = 1:Loop
        for aaa = 1:N_OA2
            Q_FI(aaa)   = Q_F_OA;
            if aaa == 1
                Q_DI(aaa)   = QQ(15,1)/QQ(4,1)*Q_F_OA;

                C_DI(aaa)   = QQ(15,2);
                C_FI(aaa)   = QQ(4,2);
            elseif aaa == 2
                Q_DI(aaa)   = QQ(10,1)/QQ(14,1)*Q_F_OA;

                C_DI(aaa)   = QQ(10,2);
                C_FI(aaa)   = QQ(14,2);
            end

            fprintf('2-OARO %d:\t',aaa) % V4_SM(n,  , FF,     i, MW, R, T,   P,      P_D1,
Q_FS,      Q_DS,      C_DS,      C_FS,      SM, It_P, Type,    Flow,    AL   , St)
            [Res_OA, E_Vec]            = V4_SM(n_OA, FF_OA,  i, MW, R, T_0, P_F_OA, P_D_OA,
Q_FI(aaa), Q_DI(aaa), C_DI(aaa), C_FI(aaa), SM, It_P, Type_OA, Flow_OA, AL_OA, St_OA);
            Y_OA                       = (Res_OA(3,1)-Res_OA(3,end))/Res_OA(3,1);

            C_DO(aaa)   = Res_OA(2,1);
            C_FO(aaa)   = Res_OA(4,end);
            P_FO(aaa)   = Res_OA(9,end);
            P_DO(aaa)   = Res_OA(10,1);
            P_DI(aaa)   = Res_OA(10,end);

            if aaa == 1
                QQ(14,:)    = [(1-Y_OA)*QQ(4,1)             C_FO(1) T_0 P_FO(1)];
                QQ(8,:)     = [QQ(4,1)+QQ(15,1)-QQ(14,1)    C_DO(1) T_0 P_DO(1)];
                QQ(15,4)    = P_DI(1);

            elseif aaa == 2
                QQ(5,:)     = [(1-Y_OA)*QQ(14,1)            C_FO(2) T_0 P_FO(2)];
                QQ(15,:)    = [QQ(10,1)+QQ(14,1)-QQ(5,1)    C_DO(2) T_0 P_DO(2)];
                QQ(10,4)    = P_DI(2);

            end
        end
        if N_OA2 == 1
            QQ(5,:)     = QQ(14,:);
        end
        end

        if QQ(5,1)>RR*QQ(2,1)
            QQ(7,:) = [QQ(5,1)-RR*QQ(2,1)   QQ(5,2)         QQ(5,3)     P_0];
            QQ(6,:) = [RR*QQ(2,1)           QQ(5,2)         QQ(5,3)     P_0];
        else
            QQ(6,:) = [QQ(5,1)              QQ(5,2)         QQ(5,3)     P_0];
            QQ(7,:) = [0                    QQ(5,2)         QQ(5,3)     P_0];
        end

        if N_OA1 == 1
            QQ(13,:)    = QQ(6,:);
            Loop        = 2;
        else
            Loop        = 3;
        end

        for ii = 1:Loop
        for aaa = 1:N_OA1
            Q_FI(aaa)   = Q_F_OA;
            if aaa == 1
                Q_DI(aaa)   = QQ(13,1)/QQ(2,1)*Q_F_OA;

                C_DI(aaa)   = QQ(13,2);
                C_FI(aaa)   = QQ(2,2);
            elseif aaa == 2
                Q_DI(aaa)   = QQ(6,1)/QQ(12,1)*Q_F_OA;

                C_DI(aaa)   = QQ(6,2);
                C_FI(aaa)   = QQ(12,2);
            end

            fprintf('1-OARO %d:\t',aaa) % V4_SM(n,  , FF,     i, MW, R, T,   P,      P_D1,
Q_FS,      Q_DS,      C_DS,      C_FS,      SM, It_P, Type,    Flow,    AL   , St)
```

```
            [Res_OA, E_Vec]             = V4_SM(n_OA, FF_OA,  i, MW, R, T_0, P_F_OA, P_D_OA,
Q_FI(aaa), Q_DI(aaa), C_DI(aaa), C_FI(aaa), SM, It_P, Type_OA, Flow_OA, AL_OA, St_OA);
            Y_OA                        = (Res_OA(3,1)-Res_OA(3,end))/Res_OA(3,1);

            C_DO(aaa)    = Res_OA(2,1);
            C_FO(aaa)    = Res_OA(4,end);
            P_FO(aaa)    = Res_OA(9,end);
            P_DO(aaa)    = Res_OA(10,1);
            P_DI(aaa)    = Res_OA(10,end);

            if aaa == 1
                QQ(12,:)     = [(1-Y_OA)*QQ(2,1)             C_FO(1) T_0 P_FO(1)];
                QQ(4,:)      = [QQ(2,1)+QQ(13,1)-QQ(12,1)    C_DO(1) T_0 P_DO(1)];
                QQ(13,4)     = P_DI(1);

            elseif aaa == 2
                QQ(3,:)      = [(1-Y_OA)*QQ(12,1)            C_FO(2) T_0 P_FO(2)];
                QQ(13,:)     = [QQ(6,1)+QQ(12,1)-QQ(3,1)     C_DO(2) T_0 P_DO(2)];
                QQ(6,4)      = P_DI(2);

            end
        end

        if N_OA1 == 1
            QQ(3,:)      = QQ(12,:);
        end
        end

        alpha   = 0.5;
        QQ(2,1) = alpha*(QQ(2,1))+(1-alpha)*(Y_UF*QQ(1,1)+X*(QQ(7,1)+X*QQ(11,1)));
        QQ(2,2) = (Y_UF*QQ(1,1)*QQ(1,2)+X*QQ(7,1)*QQ(7,2)+X*QQ(11,1)*QQ(11,2))/QQ(2,1);
        QQ(2,3) = (Y_UF*QQ(1,1)*QQ(1,3)+X*QQ(7,1)*QQ(7,3)+X*QQ(11,1)*QQ(11,3))/QQ(2,1);
        QQ(2,4) = QQ(1,4);


        % Mass error
        Water_Err(aa)    = QQ(1,1)-(1-Y_UF)*QQ(1,1)-QQ(3,1)-QQ(16,1)-(1-X)*(QQ(7,1)+QQ(11,1));
        Salt_Err(aa)     = QQ(1,1)*QQ(1,2)-(1-Y_UF)*QQ(1,1)*QQ(1,2)-QQ(3,1)*QQ(3,2)-
QQ(16,1)*QQ(16,2)-(1-X)*(QQ(7,1)*QQ(7,2)+QQ(11,1)*QQ(11,2));

        OARO1_Err_W = QQ(2,1)+QQ(13,1)-QQ(12,1)-QQ(4,1);
        OARO1_Err_S = QQ(2,1)*QQ(2,2)+QQ(13,1)*QQ(13,2)-QQ(12,1)*QQ(12,2)-QQ(4,1)*QQ(4,2);

        OARO2_Err_W = QQ(12,1)+QQ(6,1)-QQ(13,1)-QQ(3,1);
        OARO2_Err_S = QQ(12,1)*QQ(12,2)+QQ(6,1)*QQ(6,2)-QQ(13,1)*QQ(13,2)-QQ(3,1)*QQ(3,2);

        OARO3_Err_W = QQ(4,1)+QQ(15,1)-QQ(14,1)-QQ(8,1);
        OARO3_Err_S = QQ(4,1)*QQ(4,2)+QQ(15,1)*QQ(15,2)-QQ(14,1)*QQ(14,2)-QQ(8,1)*QQ(8,2);

        OARO4_Err_W = QQ(14,1)+QQ(10,1)-QQ(5,1)-QQ(15,1);
        OARO4_Err_S = QQ(14,1)*QQ(14,2)+QQ(10,1)*QQ(10,2)-QQ(5,1)*QQ(5,2)-QQ(15,1)*QQ(15,2);

        RO_Err_W    = QQ(8,1)-QQ(9,1)-QQ(16,1);
        RO_Err_S    = QQ(8,1)*QQ(8,2)-QQ(9,1)*QQ(9,2)-QQ(16,1)*QQ(16,2);

        Err_Vec     = [Water_Err(aa) OARO1_Err_W OARO2_Err_W OARO3_Err_W OARO4_Err_W RO_Err_W
Salt_Err(aa) OARO1_Err_S OARO2_Err_S OARO3_Err_S OARO4_Err_S RO_Err_S]

        if aa >= 5 && abs(Salt_Err(aa)/(QQ(1,1)*QQ(1,2))) < FD_Err &&
abs(Water_Err(aa)/QQ(1,1)) < FD_Err
            fprintf('\nFlow diagram converged!\n')
            break
        elseif aa == It_FD
            fprintf('\nFlow diagram did not converge!\n')
        end

    end

    % Energy calculations
    Q_Input(1,:)    = QQ(1,:);              P_Input(1)      = P_Intake;
                                            P_Input(2)      = P_UF;
    Q_Input(2,:)    = QQ(3,:);              P_Input(3)      = P_Dis;
    Q_Input(3,:)    = QQ(16,:);             P_Input(4)      = P_Post;
    Q_Input(4:5,:)  = [QQ(2,:);QQ(12,:)];   P_Input(5)      = P_F_OA;
    Q_Input(6:7,:)  = [QQ(4,:);QQ(14,:)];   P_Input(6)      = P_F_OA;
                                            P_Input(7)      = P_F_OA;
    Q_Input(10:11,:)= [QQ(8,:);QQ(9,:)];    P_Input(8)      = P_F_RO;
```

```
    Q_Input(12,:)    = QQ(4,1)+QQ(8,1);       P_Input(9)       = P_Ry;

    Q_Input(13,:)    = QQ(13,:);              P_Input(10)      = QQ(13,4)-P_D_OA;
    Q_Input(14,:)    = QQ(15,:);              P_Input(11)      = QQ(15,4)-P_D_OA;

    if N_OA1 == 2
        Q_Input(8:9,:)  = [QQ(12,:);QQ(3,:)];
        Q_Input(15,:)   = QQ(6,:);
        P_Input(12)     = QQ(6,4)-P_D_OA;
    elseif N_OA2 == 2
        Q_Input(8:9,:)  = [QQ(14,:);QQ(5,:)];
        Q_Input(15,:)   = QQ(10,:);
        P_Input(12)     = QQ(10,4)-P_D_OA;
    else
        Q_Input(8:9,:)  = zeros(2,4);
        Q_Input(15,:)   = 0;
        P_Input(12)     = 0;
    end

   [En_Vec] = V4_Energy(Q_Input ,P_Input , eff_P, eff_PEX);

    % Capital calculations
    Q_Input(1)       = Q_PFin;               m_Rat_Input(1)  = QQ(2,1)/QQ(8,1);
    Q_Input(2)       = Q_F_RO;               m_Rat_Input(2)  = QQ(4,1)/QQ(8,1);
    Q_Input(3)       = Q_F_OA;
    Q_Input(4)       = Q_F_OA;               m_Rat_Input(4)  = QQ(1,1)/QQ(16,1);
    Q_Input(5)       = Q_F_OA;

    n_Input(1)       = n_RO;

    if N_OA1 == 2
        m_Rat_Input(3)  = QQ(12,1)/QQ(8,1);
    elseif N_OA2 == 2
        m_Rat_Input(3)  = QQ(14,1)/QQ(8,1);
    else
        m_Rat_Input(3)  = 0;
    end


    if N_OA1 == 1 && N_OA2 == 1
        n_Input(2)       = n_OA;
        n_Input(3)       = n_OA;
        n_Input(4)       = 0;
    elseif N_OA1 == 2 || N_OA2 == 2
        n_Input(2)       = n_OA;
        n_Input(3)       = n_OA;
        n_Input(4)       = n_OA;
    end

    [Mod_Vec]   = V4_Capital(Q_Input, m_Rat_Input, n_Input, Y_RO, A_UF, LMH_UF);




elseif FD == 5
    %% Flow Diagram 5
    % Input data
    It_FD   = Input_Vec(2,1);   X           = Input_Vec(2,2);
    RR      = Input_Vec(2,3);

    Type_OA = Input_Vec(3,1);   Flow_OA     = Input_Vec(3,2);
    FF_OA   = Input_Vec(3,3);   n_OA        = Input_Vec(3,4);
    P_F_OA  = Input_Vec(3,5);   P_D_OA      = Input_Vec(3,6);
    Q_F_OA  = Input_Vec(3,7);   AL_OA       = Input_Vec(3,8);
    St_OA   = Input_Vec(3,9);    N_OA       = Input_Vec(3,10);

    P_Ry    = Input_Vec(4,1);

    % Mass calculations
    QQ(1,:)      = [Q_0          S_0         T_0     P_0];
    QQ(2,:)      = [Y_UF*QQ(1,1) QQ(1,2)     QQ(1,3) QQ(1,4)];
    QQ(6,:)      = [X*QQ(1,1)    QQ(1,2)     QQ(1,3) P_0];    % Initial guess
    QQ(12,:)     = [X*QQ(1,1)    QQ(1,2)     QQ(1,3) P_0];    % Initial guess
```

```
    QQ(10,:)    = [X*QQ(1,1)    QQ(1,2)     QQ(1,3) P_0];    % Initial guess
    for aa = 1:It_FD
        fprintf('\n\nIteration: %d\n\n',aa)

        QQ(3,1)    = (QQ(2,1)+QQ(6,1));
        QQ(3,2)    = (QQ(2,1)*QQ(2,2)+QQ(6,1)*QQ(6,2))/QQ(3,1);
        QQ(3,3)     = (QQ(2,1)*QQ(2,3)+QQ(6,1)*QQ(6,3))/QQ(3,1);
        if QQ(2,4) ~= QQ(6,4)
            fprintf('Pressure P_2 = %.2f and P_6 = %.2f do not match!\n',QQ(2,4),QQ(6,4))
        else
            QQ(3,4) = QQ(2,4);
        end

        fprintf('RO:\t\t')                                          % V4_Q_M_It(n,     FF,
i, MW, R, T, Q_D1,  C_D1,   Q_F1,   C_F1,       P_F1,   P_D1,   Type,       Flow,       AL)
        [m_D, C_D, m_F, C_F, m_M, RSF, CP_F, CP_D, P_F, P_D]    = V4_Q_M_It(n_RO, k_RO, FF_RO,
rho, phi, i, MW, R, T_0, 0,     0,      Q_F_RO, QQ(3,2),    P_F_RO, P_D_RO, Type_RO,
Flow_RO, AL_RO, St_RO);
        Y_RO        = (m_F(1)-m_F(end))/m_F(1);

        QQ(4,:)     = [(1-Y_RO)*QQ(3,1)         C_F(end)    QQ(3,3)     P_F(end)];
        QQ(13,:)    = [Y_RO*QQ(3,1)             C_D(end)    QQ(3,3)     P_0];

        QQ(5,:)= [X*QQ(4,1)         QQ(4,2) QQ(4,3) P_0];
        QQ(7,:)= [QQ(4,1)-QQ(5,1)   QQ(4,2) QQ(4,3) QQ(4,4)];

        if N_OA == 1
            QQ(12,:)    = QQ(7,:);
            QQ(10,:)    = QQ(7,:);
        elseif N_OA == 2
            QQ(12,:)    = QQ(7,:);
        end

        for aaa = 1:N_OA
            Q_FI(aaa)   = Q_F_OA;
            if aaa == 1
                Q_DI(aaa)   = QQ(5,1)/QQ(10,1)*Q_F_OA;

                C_DI(aaa)   = QQ(5,2);
                C_FI(aaa)   = QQ(10,2);
            elseif aaa == 2
                Q_DI(aaa)   = QQ(9,1)/QQ(12,1)*Q_F_OA;

                C_DI(aaa)   = QQ(9,2);
                C_FI(aaa)   = QQ(12,2);
            elseif aaa == 3
                Q_DI(aaa)   = QQ(11,1)/QQ(7,1)*Q_F_OA;

                C_DI(aaa)   = QQ(11,2);
                C_FI(aaa)   = QQ(7,2);
            end

            fprintf('OARO %d:\t',aaa)   % V4_SM(n,  , FF,     i, MW, R, T,    P,      P_D1,
Q_FS,      Q_DS,      C_DS,      C_FS,       SM, It_P, Type,     Flow,     AL    , St)
            [Res_OA, E_Vec]             = V4_SM(n_OA, FF_OA,  i, MW, R, T_0, P_F_OA, P_D_OA,
Q_FI(aaa), Q_DI(aaa), C_DI(aaa), C_FI(aaa), SM, It_P, Type_OA, Flow_OA, AL_OA, St_OA);
            Y_OA                        = (Res_OA(3,1)-Res_OA(3,end))/Res_OA(3,1);

            C_DO(aaa)   = Res_OA(2,1);
            C_FO(aaa)   = Res_OA(4,end);
            P_FO(aaa)   = Res_OA(9,end);
            P_DO(aaa)   = Res_OA(10,1);
            P_DI(aaa)   = Res_OA(10,end);

            if aaa == 1
                QQ(8,:)     = [(1-Y_OA)*QQ(10,1)            C_FO(1) T_0 P_FO(1)];
                QQ(9,:)     = [QQ(5,1)+QQ(10,1)-QQ(8,1)     C_DO(1) T_0 P_DO(1)];
                QQ(5,4)     = P_DI(1);

            elseif aaa == 2
                QQ(10,:)    = [(1-Y_OA)*QQ(12,1)            C_FO(2) T_0 P_FO(2)];
                QQ(11,:)    = [QQ(9,1)+QQ(12,1)-QQ(10,1)    C_DO(2) T_0 P_DO(2)];
                QQ(9,4)     = P_DI(2);

            elseif aaa == 3
                QQ(12,:)    = [(1-Y_OA)*QQ(7,1)             C_FO(3) T_0 P_FO(3)];
                QQ(6,:)     = [QQ(11,1)+QQ(7,1)-QQ(12,1)    C_DO(3) T_0 P_DO(3)];
```

```
                QQ(11,4)    = P_DI(3);

            end
        end

        if N_OA == 1
            QQ(6,:)     = QQ(9,:);
            QQ(11,:)    = QQ(9,:);
        elseif N_OA == 2
            QQ(6,:)     = QQ(11,:);
        end

        Water_Err(aa)   = QQ(1,1)-(1-Y_UF)*QQ(1,1)-QQ(8,1)-QQ(13,1);
        Salt_Err(aa)    = QQ(1,1)*QQ(1,2)-(1-Y_UF)*QQ(1,1)*QQ(1,2)-QQ(8,1)*QQ(8,2)-
QQ(13,1)*QQ(13,2);

        OARO_Err_W1     = QQ(5,1)+QQ(10,1)-QQ(8,1)-QQ(9,1);
        OARO_Err_S1     = QQ(5,1)*QQ(5,2)+QQ(10,1)*QQ(10,2)-QQ(8,1)*QQ(8,2)-QQ(9,1)*QQ(9,2);

        OARO_Err_W2     = QQ(9,1)+QQ(12,1)-QQ(10,1)-QQ(11,1);
        OARO_Err_S2     = QQ(9,1)*QQ(9,2)+QQ(12,1)*QQ(12,2)-QQ(10,1)*QQ(10,2)-
QQ(11,1)*QQ(11,2);

        OARO_Err_W3     = QQ(11,1)+QQ(7,1)-QQ(12,1)-QQ(6,1);
        OARO_Err_S3     = QQ(11,1)*QQ(11,2)+QQ(7,1)*QQ(7,2)-QQ(12,1)*QQ(12,2)-QQ(6,1)*QQ(6,2);

        RO_Err_W    = QQ(3,1)-QQ(4,1)-QQ(13,1);
        RO_Err_S    = QQ(3,1)*QQ(3,2)-QQ(4,1)*QQ(4,2)-QQ(13,1)*QQ(13,2);

        Err_Vec     = [Water_Err(aa) OARO_Err_W1 OARO_Err_W2 OARO_Err_W3 RO_Err_W Salt_Err(aa)
OARO_Err_S1 OARO_Err_S2 OARO_Err_S3 RO_Err_S]

        if aa >= 5 && abs(Salt_Err(aa)/(QQ(1,1)*QQ(1,2))) < FD_Err &&
abs(Water_Err(aa)/QQ(1,1)) < FD_Err
            fprintf('\nFlow diagram converged!\n')
            break
        elseif aa == It_FD
            fprintf('\nFlow diagram did not converge!\n')
        end
    end

    % Energy calculations
    Q_Input(1,:)    = QQ(1,:);              P_Input(1)      = P_Intake;
                                            P_Input(2)      = P_UF;
    Q_Input(2,:)    = QQ(8,:);              P_Input(3)      = P_Dis;
    Q_Input(3,:)    = QQ(13,:);             P_Input(4)      = P_Post;
    Q_Input(4:5,:)  = [QQ(10,:);QQ(8,:)];   P_Input(5)      = P_F_OA;
    Q_Input(6:7,:)  = [QQ(12,:);QQ(10,:)];  P_Input(6)      = P_F_OA;
    Q_Input(8:9,:)  = [QQ(7,:);QQ(12,:)];   P_Input(7)      = P_F_OA;
    Q_Input(10:11,:)= [QQ(3,:);QQ(4,:)];    P_Input(8)      = P_F_RO;

    Q_Input(12,:)   = QQ(6,:);              P_Input(9)      = P_Ry;

    Q_Input(13,:)   = QQ(5,:);              P_Input(10)     = QQ(5,4)-P_D_OA;
    Q_Input(14,:)   = QQ(9,:);              P_Input(11)     = QQ(9,4)-P_D_OA;
    Q_Input(15,:)   = QQ(11,:);             P_Input(12)     = QQ(11,4)-P_D_OA;

    if N_OA == 1
        P_Input(6)      = 0;                P_Input(11)     = 0;
        P_Input(7)      = 0;                P_Input(12)     = 0;
    elseif N_OA == 2
        P_Input(7)      = 0;                P_Input(12)     = 0;
    end

   [En_Vec] = V4_Energy(Q_Input ,P_Input , eff_P, eff_PEX);

    % Capital calculations
    Q_Input(1)      = Q_PFin;               m_Rat_Input(1)  = QQ(10,1)/QQ(3,1);
    Q_Input(2)      = Q_F_RO;               m_Rat_Input(2)  = QQ(12,1)/QQ(3,1);
    Q_Input(3)      = Q_F_OA;               m_Rat_Input(3)  = QQ(7,1)/QQ(3,1);
    Q_Input(4)      = Q_F_OA;               m_Rat_Input(4)  = QQ(1,1)/QQ(13,1);
    Q_Input(5)      = Q_F_OA;

    n_Input(1)      = n_RO;

    if N_OA == 1
        n_Input(2)      = n_OA;
```

```
        n_Input(3)      = 0;
        n_Input(4)      = 0;
    elseif N_OA == 2
        n_Input(2)      = n_OA;
        n_Input(3)      = n_OA;
        n_Input(4)      = 0;
    elseif N_OA == 3
        n_Input(2)      = n_OA;
        n_Input(3)      = n_OA;
        n_Input(4)      = n_OA;
    end

    [Mod_Vec]   = V4_Capital(Q_Input, m_Rat_Input, n_Input, Y_RO, A_UF, LMH_UF);



end
```

E.2. Chapter 4 source code

E.2.1. Main function

```
clc
clear all
close all

%% Input parameters
FD_Choice       = 1;                                                    % 1 = FO-Thermal
DSR_Choice      = 2;                                                    % 1 = (P_DC1=1.02
bar and P_DC2=1.00 bar), 2 = (P_DC1=0.52 bar and P_DC2=0.50 bar)
Err_Tol         = 0.0001;                                               % Flow process
maximum Salt and water error

P_F_RO1         = 81;
P_F_RO2         = 41;
QF_RO           = 12/3600;

NC              = 2.4;                                                  % NH3/CO2
concentration ratio (= 2, 2.4 or 2.8)
Op_OA           = 2;                                                    % 1 = RO, 2 = TFC-
FO, 3 = CTA-FO
Stages_OA1      = 3;
P_F_OA_Vec      = 49.3;%[49.3 2];
RR_OA1          = 0.5;

QF_OA1          = 5/3600;
% QF_OA1            = [3:7]/3600;

%% Initial guesses
S_OA_Brine      = 130;                                                  % OARO
concentrated brine [g/kg]
TS_Init         = 2.6;                                                  % Initial Guess:
Change MM(9,1) and TS(1,1)
TS_Step         = 0.5;
DC2_VapVol      = 16700;
Stage_Grad      = 0.10;                                                 % Varies gradient
in OA_stages.m function (0.05 to 0.25)
TS_CF           = 1;                                                    % Convergence
factor for TS

%% Constants
It_Brine        = 50;

n_OA            = 7;                k_OA            = 25*n_OA+1;
FF_OA           = 1;                Flow_OA         = 1;                % Flow_OA: 0 = Co-
current, 1 = Counter-current
Mem_Type_OA     = Op_OA;                                                % 1 = RO, 2 = FO
or OA (same for membrane type)

n_RO            = 7;                k_RO            = 100*n_OA+1;
FF_RO           = 1;                Flow_RO         = 0;
```

```
Op_RO           = 1;                Mem_Type_RO     = Op_RO;

MW_Na           = 58.4;             MW_CO2          = 44;
MW_NH3          = 17;
T               = 25+273.15;        P_DO            = 1;

%% Feed conditions
QF_Tot          = 100;                                                  % [m^3/h]
Increased to 100 m^3/h (REF: Going big with FO = 26.4)
S_In            = 45;                                                   % [g/L] REF: Going
big with FO
C_Out           = 190/MW_Na;                                            % Outlet NaCl
concentration (190 g/kg = 220 g/L) converted into mol/kg

%% Open ASPEN DSR simulation
P_HPS           = 5;                                                    % High Pressure
Saturated Steam for Reboiler [bar]

Aspen = actxserver('Apwn.Document.35.0');
if DSR_Choice == 1
    InitFromFile2(Aspen, [cd,'\DC1-DC2-V5-1.0-Chem-Therm.apwz']);       % Open simulation
file (1.02-1.00 bar)
    P_LPS           = 2;                                                % Low Pressure
Saturated Steam for Reboiler [bar]

elseif DSR_Choice == 2
    InitFromFile2(Aspen, [cd,'\DC1-DC2-V5-0.5-Chem-Therm.apwz']);       % Open simulation
file (0.52-0.5 bar)
    P_LPS           = 1;                                                % Low Pressure
Saturated Steam for Reboiler [bar]
end
Aspen.SuppressDialogs = 1;                                              % Suppress dialogs
= true
Aspen.visible = true;

for xx = 1:5
    if xx == 1
        C_In    = S_In/MW_Na;
    else
        C_In    = S_In/MW_Na/rho_F*1000;
    end
    [~,~,rho_F] = Rho_Com(C_In, 0, NC);
end
MF_Tot          = QF_Tot*rho_F;

%% Flow Diagrams
if FD_Choice == 1
    %% FO-Thermal
    for aaaaa = 1:length(P_F_OA_Vec)
        P_F_OA      = P_F_OA_Vec(aaaaa);
            for aaa = 1:length(QF_OA1)
                QF_OA               = QF_OA1(aaa);

                MM                  = zeros(14,5);                                  % [MM]
= [kg/h, mol/kg NaCl, mol/kg CO2, K, bar]
                MM(1,:)             = [MF_Tot, C_In, 0, T, P_DO];
                TS                  = zeros(1,It_Brine);
                Brine_S             = zeros(1,It_Brine);

                TS(1,1)             = TS_Init+TS_Step*aaa;

                MM(3,:)             = [68000    1.23,   0,          T,  P_DO];
                MM(9,1)             = DC2_VapVol;
                MM(5,1)             = RR_OA1*MM(3,1);
                MM(5,2:5)           = [         0.07,   TS(1,1),    T,  P_DO];
                MM(13,:)            = [4500     0.06,   0,          T,  P_DO];

                for aa = 1:It_Brine
                    if aa > 1
                        S_OA_Brine  = MM(10,2)*MW_Na;
                        Stage_Grad  = (OA1(9,1)-OA1(10,1))/OA1(9,1);
                    end

                    fprintf('\nIt: %d\tTS\t= %.2f\nS_Brine\t %.1f\nGradient\t=
%.2f\n\n',aa,TS(1,aa),S_OA_Brine,Stage_Grad)

                    %% OA1
```

```
                    Scalars         = [n_OA, k_OA, FF_OA , Mem_Type_OA, Flow_OA, ...
                                       MW_Na, T, P_DO, P_F_OA, 0, NC];
                    Scalars_OA      = [Stages_OA1, MM(3,1), QF_OA, RR_OA1, S_OA_Brine
Stage_Grad];

                    CF_In           = MM(3,2:3);
                    CD_In           = MM(5,2:3);

                    [OA1]           = V6_OA_Stages(Op_OA, Scalars, Scalars_OA, CF_In, CD_In);

                    MM(3,5)         = P_F_OA;
                    MM(5,5)         = OA1(1,5);
                    MM(6,:)         = OA1(2*Stages_OA1,:);
                    MM(10,:)        = OA1(end,:);

                    %% Separator
                    MM(4,1)         = RR_OA1*MM(3,1)-MM(9,1);
                    MM(4,2:5)       = MM(6,2:5);

                    MM(7,1)         = MM(6,1)-MM(4,1);
                    MM(7,2:5)       = MM(6,2:5);

                    %% DC1 and DC2
                    fprintf('DC1 and DC2\n')

                    [MM(8,:), MM(9,:), MM(11,:), En_T, En_E, WH_Cond, T_DC1, T_DC2, T_Cond_In,
A_HEX1, A_HEX2, DC1_Dia, DC2_Dia, DC1_L, DC2_L, P_Cond, P_DC1, P_DC2]    = ...
                                    V6_DSR_Interface(NC, MW_Na, MW_CO2, MW_NH3, MM(7,:), MM(10,:),
Aspen);

                    %% Mixer 1
                    [MM(2,:)]       = Mixer(MM([1 8 13],:), P_DO);

                    %% RO - 1st Pass
                    Scal_RO1        = [n_RO, k_RO, FF_RO , Mem_Type_RO, Flow_RO, ...
                                       MW_Na, T, P_DO, P_F_RO1, 0, NC];
                    Vect_RO1        = [0 0 0; QF_RO MM(2,2) MM(2,3)];

                    [MM(2,:), MM(3,:), MM(12,:)]    = RO(Op_RO, Scal_RO1, Vect_RO1, MM(2,:));

                    %% RO - 2nd Pass
                    Scal_RO2        = [n_RO, k_RO, FF_RO , Mem_Type_RO, Flow_RO, ...
                                       MW_Na, T, P_DO, P_F_RO2, 0, NC];
                    Vect_RO2        = [0 0 0; QF_RO MM(12,2) MM(12,3)];

                    [MM(12,:), MM(13,:), MM(14,:)]  = RO(Op_RO, Scal_RO2, Vect_RO2, MM(12,:));


                    %% Mixer 2
                    [MM(5,:)]       = Mixer(MM([4 9],:), P_DO);

                    Brine_S(aa)     = MM(11,2);
                    if aa == 1
                        TS(1,aa+1)  = C_Out/MM(11,2)*TS(1,aa);
                    else
                        TS(1,aa+1)  = (C_Out-Brine_S(aa-1))/(Brine_S(aa)-Brine_S(aa-
1))*(TS(1,aa)-TS(1,aa-1))+TS(1,aa-1);
                    end
                    TS(1,aa+1)      = TS_CF*TS(1,aa+1)+(1-TS_CF)*TS(1,aa);

                    MM5_DS_OLd      = MM(5,3);
                    MM(5,3)         = TS(1,aa+1);

                    %% Convergence Test
                    Water_Err       = (MM(1,1)-MM(11,1)-MM(14,1))/MM(1,1);
                    Salt1_Err       = MM(1,1)*MM(1,2)-MM(11,1)*MM(11,2)-MM(14,1)*MM(14,2);
                    Salt2_Err       = MM(1,1)*MM(1,3)-MM(11,1)*MM(11,3)-MM(14,1)*MM(14,3);
                    Err_MM5         = MM5_DS_OLd/TS(1,aa+1)-1;

                    fprintf('\nWater_Err\t= %.4f\nSalt1_Err\t= %.4f\nSalt2_Err\t=
%.4f\nMM5_Err\t\t=  %.4f\nBri_Err\t\t=  %.4f\n\n', Water_Err, Salt1_Err, Salt2_Err, Err_MM5,
MM(11,2)/C_Out-1)

                    if abs(Water_Err)< Err_Tol && abs(MM(11,2)/C_Out-1)< Err_Tol
                        break
                    end
                end
```

```
                [~, A_RO, ~, ~, ~, ~]    = V6_Mem_Type(Op_RO, Mem_Type_RO);
                [~, A_OA, ~, ~, ~, ~]    = V6_Mem_Type(Op_OA, Mem_Type_OA);


                % Write all results into Excel File
                Folder = './1 V6 Sim_Results';
                Filename    = sprintf('V6 DSR=%d, QF=%.1f, S_In=%.1f, NC=%.1f, Op_OA=%d.xlsx',
...
                                DSR_Choice,QF_Tot,S_In,NC,Op_OA);
                fullFileName = fullfile(Folder, Filename);
                if ~exist(Folder, 'dir')
                    mkdir(Folder);
                end

                Headings_RO = ["P_F_RO1 [bar]", "P_F_RO2 [bar]","QF_RO [m^3/h]","n_RO","A_RO
[m^2]"]';
                Headings_OA = ["P_F_OA [bar]","QF_OA [m^3/h]","n_OA","A_OA [m^2]","N/C"]';
                Headings_DC = ["En_E_Sum [kW]","En_T_DC1 [kW]","En_T_DC2 [kW]","WH_Cond
[kW]","P_LPS [bar]","P_HPS [bar]",...
                                "A_HEX1 [m^2]", "A_HEX2 [m^2]","T_DC1_Top [°C]","T_DC1_Bot
[°C]","T_DC2_Top [°C]","T_DC2_Bot [°C]",...
                                "DC1_Dia [m]","DC2_Dia [m]","DC1_L [m]","DC2_L [m]", "P_Cond
[bar]", "P_DC1 [bar]", "P_DC2 [bar]"]';

                Sheet       = ['Q' num2str(QF_OA*3600)...
                               ',P' num2str(P_F_OA-1)...
                               ',RR' num2str(RR_OA1)];

                xlswrite(fullFileName,Headings_RO,Sheet,'A1')
                xlswrite(fullFileName,[P_F_RO1 P_F_RO2 QF_RO*3600 n_RO A_RO]',Sheet,'B1')
                xlswrite(fullFileName,Headings_OA,Sheet,'C1')
                xlswrite(fullFileName,[P_F_OA-1 QF_OA*3600 n_OA A_OA NC]',Sheet,'D1')
                xlswrite(fullFileName,Headings_DC,Sheet,'E1')
                xlswrite(fullFileName,[sum(En_E) En_T WH_Cond P_LPS P_HPS A_HEX1 A_HEX2 T_DC1
T_DC2 DC1_Dia DC2_Dia DC1_L DC2_L P_Cond P_DC1 P_DC2]',Sheet,'F1')

                xlswrite(fullFileName,["kg/h","mol/kg NaCl","mol/kg
CO2","K","bar"],Sheet,'H1')
                xlswrite(fullFileName,MM,Sheet,'H2')
                xlswrite(fullFileName,["kg/h","mol/kg NaCl","mol/kg
CO2","K","bar"],Sheet,'N1')
                xlswrite(fullFileName,OA1,Sheet,'N2')

                fprintf('\n\nSimulation complete\n')
                fprintf('Iterations: %d, %d\n', aaa, aa)
            end
    end
end
load gong
sound(y,Fs)

%% Figures
figure(1)
plot(1:2*Stages_OA1,OA1(2*Stages_OA1:-1:1,1),'rs-
',1:2*Stages_OA1,OA1(2*Stages_OA1+1:end,1),'bs-')
grid on
xlabel('Steps along stages')
ylabel('Flowrate [kg/h]')
legend('Draw','Feed')

figure(2)
plot(1:2*Stages_OA1,OA1(2*Stages_OA1:-1:1,2)*58.4,'rs-
',1:2*Stages_OA1,OA1(2*Stages_OA1+1:end,2)*58.4,'bs-')
grid on
xlabel('Steps along stages')
ylabel('Salinity [g/kg]')
legend('Draw','Feed')

figure(3)
plot(1:2*Stages_OA1,OA1(2*Stages_OA1:-1:1,3),'rs-
',1:2*Stages_OA1,OA1(2*Stages_OA1+1:end,3),'bs-')
grid on
xlabel('Steps along stages')
ylabel('DS Concentration [mol_{CO2}/kg]')
legend('Draw','Feed')
```

```
figure(4)
plot(1:2*Stages_OA1,OA1(2*Stages_OA1:-1:1,5),'rs-
',1:2*Stages_OA1,OA1(2*Stages_OA1+1:end,5),'bs-')
grid on
xlabel('Steps along stages')
ylabel('Pressure [bar]')
legend('Draw','Feed')


%% Extra functions
function [Outlet]   = Mixer(Inlet, P_DO)

    Outlet(1,1)     = sum(Inlet(:,1));
    Outlet(1,2)     = sum(Inlet(:,1).*Inlet(:,2))/Outlet(1,1);
    Outlet(1,3)     = sum(Inlet(:,1).*Inlet(:,3))/Outlet(1,1);
    Outlet(1,4)     = sum(Inlet(:,1).*Inlet(:,4))/Outlet(1,1);
    Outlet(1,5)     = P_DO;

end

function [Feed, Brine, Permeate]        = RO(Op_RO, Scalars_RO, Vectors_RO, Feed)

    [Water_RO, Salt_RO, Pressure_RO]    = V6_Q_M_It(Op_RO, Scalars_RO, Vectors_RO);

    Feed(1,5)       = Pressure_RO(2,1);

    Brine(1,1)      = Water_RO(2,end)/Water_RO(2,1)*Feed(1,1);
    Brine(1,2)      = Salt_RO(3,end);
    Brine(1,3)      = Salt_RO(4,end);
    Brine(1,4)      = Scalars_RO(7);
    Brine(1,5)      = Pressure_RO(2,end);

    Permeate(1,1)   = (1-Water_RO(2,end)/Water_RO(2,1))*Feed(1,1);
    Permeate(1,2)   = Salt_RO(1,end);
    Permeate(1,3)   = Salt_RO(2,end);
    Permeate(1,4)   = Scalars_RO(7);
    Permeate(1,5)   = Pressure_RO(1,end);

end
```

E.2.2. DSR (Aspen) Interface

```
function [MM_DC2_P, MM_DC2_CDS, MM_DC1_B, En_T, En_E, WH_Cond, T_DC1, T_DC2, T_Cond_In,
A_HEX1, A_HEX2, DC1_Dia, DC2_Dia, DC1_L, DC2_L, P_Cond, P_DC1, P_DC2] = ...
                V6_DSR_Interface(Rat_NC, MW_Na, MW_CO2, MW_NH3, MM_DC2_In, MM_DC1_In, Aspen)

%% Input conversions from Matlab to ASPEN
DC2_In(1)   = MM_DC2_In(1);                                                 % kg/hr
DC2_In(2)   = MM_DC2_In(2)*MW_Na/1000;                                      % NaCl mol/kg into
MF (kg/kg)
DC2_In(3)   = MM_DC2_In(3)*MW_CO2/1000;                                     % CO2 mol/kg into
MF (kg/kg)
DC2_In(4)   = DC2_In(3)/MW_CO2*MW_NH3*Rat_NC;                               % NH3 mol/kg into
MF (kg/kg)
DC2_In(5)   = 1-DC2_In(2)-DC2_In(3)-DC2_In(4);                              % H2O mol/kg into
MF (kg/kg)

DC1_In(1)   = MM_DC1_In(1);
DC1_In(2)   = MM_DC1_In(2)*MW_Na/1000;
DC1_In(3)   = MM_DC1_In(3)*MW_CO2/1000;
DC1_In(4)   = DC1_In(3)/MW_CO2*MW_NH3*Rat_NC;
DC1_In(5)   = 1-DC1_In(2)-DC1_In(3)-DC1_In(4);


%% Setting the MF of MM-6 and MM-10
Aspen.Application.Tree.FindNode("\Data\Streams\DC2-IN\Input\TOTFLOW\MIXED").Value       =
DC2_In(1);
Aspen.Application.Tree.FindNode("\Data\Streams\DC2-IN\Input\FLOW\MIXED\NACL").Value     =
DC2_In(2);
Aspen.Application.Tree.FindNode("\Data\Streams\DC2-IN\Input\FLOW\MIXED\CO2").Value      =
DC2_In(3);
Aspen.Application.Tree.FindNode("\Data\Streams\DC2-IN\Input\FLOW\MIXED\NH3").Value      =
DC2_In(4);
```

```
Aspen.Application.Tree.FindNode("\Data\Streams\DC2-IN\Input\FLOW\MIXED\H2O").Value      =
DC2_In(5);

Aspen.Application.Tree.FindNode("\Data\Streams\DC1-IN\Input\TOTFLOW\MIXED").Value       =
DC1_In(1);
Aspen.Application.Tree.FindNode("\Data\Streams\DC1-IN\Input\FLOW\MIXED\NACL").Value     =
DC1_In(2);
Aspen.Application.Tree.FindNode("\Data\Streams\DC1-IN\Input\FLOW\MIXED\CO2").Value      =
DC1_In(3);
Aspen.Application.Tree.FindNode("\Data\Streams\DC1-IN\Input\FLOW\MIXED\NH3").Value      =
DC1_In(4);
Aspen.Application.Tree.FindNode("\Data\Streams\DC1-IN\Input\FLOW\MIXED\H2O").Value      =
DC1_In(5);

%% Running the simulation
% Reinit(Aspen.Engine);
% Reinitialize simulation
for ii = 1:3
    Run2(Aspen.Engine);
% Run simulation

    P_Cond      = Aspen.Application.Tree.FindNode("\Data\Blocks\COND1\Output\B_PRES").Value;
    Aspen.Application.Tree.FindNode("\Data\Blocks\DC1\Input\PRES1").Value    = P_Cond+0.05;
    Aspen.Application.Tree.FindNode("\Data\Blocks\DC2\Input\PRES1").Value    = P_Cond+0.025;
end

%% Reading the results MM-7, MM-8 and MM-11
DC2_P(1)     = Aspen.Application.Tree.FindNode("\Data\Streams\DC2-
P\Output\MASSFLMX_LIQ").Value;
DC2_P(2)     = Aspen.Application.Tree.FindNode("\Data\Streams\DC2-
P\Output\MASSFRAC\MIXED\NACL").Value;
DC2_P(3)     = Aspen.Application.Tree.FindNode("\Data\Streams\DC2-
P\Output\MASSFRAC\MIXED\CO2").Value;
DC2_P(4)     = Aspen.Application.Tree.FindNode("\Data\Streams\DC2-
P\Output\MASSFRAC\MIXED\NH3").Value;
DC2_P(5)     = Aspen.Application.Tree.FindNode("\Data\Streams\DC2-
P\Output\MASSFRAC\MIXED\H2O").Value;

DC2_CDS(1)   = Aspen.Application.Tree.FindNode("\Data\Streams\DC2-
CDS\Output\MASSFLMX_LIQ").Value;
DC2_CDS(2)   = Aspen.Application.Tree.FindNode("\Data\Streams\DC2-
CDS\Output\MASSFRAC\MIXED\NACL").Value;
DC2_CDS(3)   = Aspen.Application.Tree.FindNode("\Data\Streams\DC2-
CDS\Output\MASSFRAC\MIXED\CO2").Value;
DC2_CDS(4)   = Aspen.Application.Tree.FindNode("\Data\Streams\DC2-
CDS\Output\MASSFRAC\MIXED\NH3").Value;
DC2_CDS(5)   = Aspen.Application.Tree.FindNode("\Data\Streams\DC2-
CDS\Output\MASSFRAC\MIXED\H2O").Value;

DC1_B(1)     = Aspen.Application.Tree.FindNode("\Data\Streams\DC1-
B\Output\MASSFLMX_LIQ").Value;
DC1_B(2)     = Aspen.Application.Tree.FindNode("\Data\Streams\DC1-
B\Output\MASSFRAC\MIXED\NACL").Value;
DC1_B(3)     = Aspen.Application.Tree.FindNode("\Data\Streams\DC1-
B\Output\MASSFRAC\MIXED\CO2").Value;
DC1_B(4)     = Aspen.Application.Tree.FindNode("\Data\Streams\DC1-
B\Output\MASSFRAC\MIXED\NH3").Value;
DC1_B(5)     = Aspen.Application.Tree.FindNode("\Data\Streams\DC1-
B\Output\MASSFRAC\MIXED\H2O").Value;
DC1_B(6)     = Aspen.Application.Tree.FindNode("\Data\Streams\DC1-
B\Output\TEMP_OUT\MIXED").Value;

%% Reading thermal energy consumption of DC1, DC2 and Condenser Duty
En_T_DC1     = Aspen.Application.Tree.FindNode("\Data\Blocks\DC1\Output\REB_DUTY").Value*1163;
% Gcal/hr into kW
En_T_DC2     = Aspen.Application.Tree.FindNode("\Data\Blocks\DC2\Output\REB_DUTY").Value*1163;
WH_Cond      = Aspen.Application.Tree.FindNode("\Data\Blocks\COND1\Output\QCALC").Value*1163;
P_Cond       = Aspen.Application.Tree.FindNode("\Data\Blocks\COND1\Output\B_PRES").Value;
P_DC1        = Aspen.Application.Tree.FindNode("\Data\Blocks\DC1\Output\PRES1").Value;
P_DC2        = Aspen.Application.Tree.FindNode("\Data\Blocks\DC2\Output\PRES1").Value;

%% Reading electrical energy consumption of P1, P2 and P3
En_E_P1      = Aspen.Application.Tree.FindNode("\Data\Blocks\P1\Output\ELEC_POWER").Value;
% kW
En_E_P2      = Aspen.Application.Tree.FindNode("\Data\Blocks\P2\Output\ELEC_POWER").Value;
% kW
```

ddd

```
En_E_P3     = Aspen.Application.Tree.FindNode("\Data\Blocks\P3\Output\ELEC_POWER").Value;
% kW

T_DC1(1)    = Aspen.Application.Tree.FindNode("\Data\Blocks\DC1\Output\TOP_TEMP").Value;
T_DC1(2)    = Aspen.Application.Tree.FindNode("\Data\Blocks\DC1\Output\BOTTOM_TEMP").Value;

T_DC2(1)    = Aspen.Application.Tree.FindNode("\Data\Blocks\DC2\Output\TOP_TEMP").Value;
T_DC2(2)    = Aspen.Application.Tree.FindNode("\Data\Blocks\DC2\Output\BOTTOM_TEMP").Value;

T_Cond_In   = Aspen.Application.Tree.FindNode("\Data\Streams\10\Output\TEMP_OUT\MIXED").Value;

En_T        = [En_T_DC1 En_T_DC2];
En_E        = [En_E_P1 En_E_P2 En_E_P3];

%% Read HEX Areas
A_HEX1      = Aspen.Application.Tree.FindNode("\Data\Blocks\HEX1\Output\HX_AREAP").Value;
% m^2
A_HEX2      = Aspen.Application.Tree.FindNode("\Data\Blocks\HEX2\Output\HX_AREAP").Value;
% m^2

%% DC column diameters
DC1_Dia     = Aspen.Application.Tree.FindNode("\Data\Blocks\DC1\Subobjects\Column
Internals\INT-1\Subobjects\Sections\CS-1\Input\CA_DIAM\INT-1\CS-1").Value;
DC2_Dia     = Aspen.Application.Tree.FindNode("\Data\Blocks\DC2\Subobjects\Column
Internals\INT-1\Subobjects\Sections\CS-1\Input\CA_DIAM\INT-1\CS-1").Value;

DC1_L       = 2.53;
DC2_L       = 2.53;

%% Output conversion from ASPEN to Matlab
MM_DC2_P(1)     = DC2_P(1);                                                 % kg/hr
MM_DC2_P(2)     = DC2_P(2)/MW_Na*1000;                                      % NaCl MF (kg/kg)
into mol/kg
MM_DC2_P(3)     = DC2_P(3)/MW_CO2*1000;                                     % CO2 MF (kg/kg)
into mol/kg
MM_DC2_P(4)     = MM_DC2_In(4);                                             % Assume T at
inlet and outlet is almost equivalent
MM_DC2_P(5)     = MM_DC2_In(5);                                             % Assume P at
inlet and outlet is almost equivalent

MM_DC2_CDS(1)   = DC2_CDS(1);
MM_DC2_CDS(2)   = DC2_CDS(2)/MW_Na*1000;
MM_DC2_CDS(3)   = DC2_CDS(3)/MW_CO2*1000;
MM_DC2_CDS(4)   = MM_DC2_In(4);
MM_DC2_CDS(5)   = MM_DC2_In(5);

MM_DC1_B(1)     = DC1_B(1);
MM_DC1_B(2)     = DC1_B(2)/MW_Na*1000;
MM_DC1_B(3)     = DC1_B(3)/MW_CO2*1000;
MM_DC1_B(4)     = DC1_B(6)+273.15;
MM_DC1_B(5)     = MM_DC1_In(5);

% Aspen.Quit (); delete (Aspen);
end
```

E.2.3. MBC stages

```
function [OA]   = V6_OA_Stages(Operation, Scalars, Scalars_OA, CF_In, CD_In)

%% Inputs
SM              = 200;
It_QQ           = 15;
QQ_Err          = 5*10^(-3);

T               = Scalars(7);
P_FI            = Scalars(9);

Stages          = Scalars_OA(1);
MF_T            = Scalars_OA(2);
QF              = Scalars_OA(3);
RR              = Scalars_OA(4);
S_Brine         = Scalars_OA(5);
Stage_Grad      = Scalars_OA(6);
```

```
Q_DO_Guess      = (1-CF_In(1)/S_Brine)*QF+RR*QF;

OA              = zeros(Stages*4,5);

W_Err_OA        = zeros(1,Stages);
S_Err_OA        = zeros(2,Stages);


%% Solver
MM_OA               = zeros(4,5,Stages);
MM_OA(3,:,Stages)   = [MF_T         [CF_In(1)    CF_In(2)]  T   P_FI];
MM_OA(1,:,1)        = [RR*MF_T      [CD_In(1)    CD_In(2)]  T   0];

%% For iteration loop for convergence of QQ's
for zz = 1:It_QQ
    fprintf('zz = %d\n', zz)

    for zzz = 1:Stages
        fprintf('OA-%d\n',zzz)

        if zz == 1
            if zzz < Stages
                MM_OA(3,1,zzz) = (Stage_Grad*(zzz-Stages)+1)*MF_T;
                MM_OA(3,2,zzz) = (-Stage_Grad*(zzz-Stages)+1)*CF_In(1);
                MM_OA(3,3,zzz) = (-Stage_Grad*(zzz-Stages)+1)*CF_In(2);
                MM_OA(3,4,zzz) = T;
                MM_OA(3,5,zzz) = P_FI;
            end
        end

        Inlets  = [QF*MM_OA(1,1,zzz)/MM_OA(3,1,zzz)     MM_OA(1,2,zzz)  MM_OA(1,3,zzz);...
                   QF                                   MM_OA(3,2,zzz)  MM_OA(3,3,zzz)];

        [Water, Salt, Pressure, Error]  = V6_SM(Operation, Scalars, Inlets, SM, Q_DO_Guess);

        MM_OA(1,5,zzz)      = Pressure(1,end);

        MM_OA(2,1,zzz)      = Water(1,1)/Water(1,end)*MM_OA(1,1,zzz);
        MM_OA(2,2,zzz)      = Salt(1,1);
        MM_OA(2,3,zzz)      = Salt(2,1);
        MM_OA(2,4,zzz)      = T;
        MM_OA(2,5,zzz)      = Pressure(1,1);

        MM_OA(4,1,zzz)      = Water(2,end)/Water(2,1)*MM_OA(3,1,zzz);
        MM_OA(4,2,zzz)      = Salt(3,end);
        MM_OA(4,3,zzz)      = Salt(4,end);
        MM_OA(4,4,zzz)      = T;
        MM_OA(4,5,zzz)      = Pressure(2,end);

        if zzz-1 >=1
            MM_OA(3,:,zzz-1)= [MM_OA(4,1:4,zzz) P_FI];
        end

        if zzz+1 <=Stages
            MM_OA(1,:,zzz+1)= [MM_OA(2,1:4,zzz) 0];
        end

        W_Err_OA(zzz)   = MM_OA(1,1,zzz)+MM_OA(3,1,zzz)-MM_OA(2,1,zzz)-MM_OA(4,1,zzz);
        S_Err_OA(1,zzz) = MM_OA(1,1,zzz)*MM_OA(1,2,zzz)+MM_OA(3,1,zzz)*MM_OA(3,2,zzz)...
                          -MM_OA(2,1,zzz)*MM_OA(2,2,zzz)-MM_OA(4,1,zzz)*MM_OA(4,2,zzz);
        S_Err_OA(2,zzz) = MM_OA(1,1,zzz)*MM_OA(1,3,zzz)+MM_OA(3,1,zzz)*MM_OA(3,3,zzz)...
                          -MM_OA(2,1,zzz)*MM_OA(2,3,zzz)-MM_OA(4,1,zzz)*MM_OA(4,3,zzz);

        fprintf('W_Err_OA-%d\t= %.6f\n',zzz,W_Err_OA(zzz))
        fprintf('S_Err_OA-%d\t= %.6f\n',zzz,S_Err_OA(1,zzz))
        fprintf('\t\t\t= %.6f\n\n',S_Err_OA(2,zzz))

        OA(2*(zzz)-1:2*zzz,:)                       = MM_OA(1:2,:,zzz);
        OA(4*Stages-2*zzz+1:4*Stages-2*zzz+2,:)     = MM_OA(3:4,:,zzz);
    end
    W_Tot       = OA(1,1)+OA(Stages*2+1,1)-OA(Stages*2,1)-OA(end,1);
    S_Tot_1     = OA(1,1)*OA(1,2)+OA(Stages*2+1,1)*OA(Stages*2+1,2)...
                  -OA(Stages*2,1)*OA(Stages*2,2)-OA(end,1)*OA(end,2);
    S_Tot_2     = OA(1,1)*OA(1,3)+OA(Stages*2+1,1)*OA(Stages*2+1,3)...
                  -OA(Stages*2,1)*OA(Stages*2,3)-OA(end,1)*OA(end,3);
```

fff

```
    fprintf('W_Err_Tot\t= %.6f\n',W_Tot)
    fprintf('S_Err_Tot\t= %.6f\n',S_Tot_1)
    fprintf('\t\t\t= %.6f\n\n',S_Tot_2)

    if W_Tot < QQ_Err && S_Tot_1 < QQ_Err && S_Tot_2 < QQ_Err
        break
    end
end
```

E.3. General functions

E.3.1. SM (Shooting method) function

```
function [Res_Vec, E_Vec]   = V4_SM(n, FF, i, MW, R, T, P, P_D1, Q, Q_DS, C_DS, S, SM, It_P,
Type, Flow, AL, St_Type)

rho         = Rho(C_DS, T);                 % Seawater density
phi         = Phi(C_DS,T);                  % Osmotic coefficient
k           = 100*n+1;                      % Number of iteration points


%% Diluted Draw Solution Assumptions (Shooting method)
[Mod_Type, A, P_F_Max, T_Max, Q_F_Max, Q_C_Min, Q_P_Max, Y_Max, beta, B]    =
V4_Mem_Type(Type);

Q_W         = n*A*beta*(i*R*T/MW*(C_DS-S)+P-P_D1);

Q_DI        = linspace(0.1*Q_W+Q_DS,        0.2*Q_W+Q_DS,           It_P );
C_DI        = linspace(C_DS*Q_DS/Q_DI(1),   C_DS*Q_DS/Q_DI(It_P),   It_P );

Q_D_SM      = [Q_DI zeros(1,SM-It_P )];
C_D_SM      = [C_DI zeros(1,SM-It_P )];

%% Shooting method
Q_D_It      = zeros(1,SM);
C_D_It      = zeros(1,SM);

E_M         = zeros(1,SM);
E_C         = zeros(1,SM);

for aa = 1:SM
    if aa >= It_P +1
        Q_D_SM(aa)  = (Q_DS-E_M_V(aa-1,2))/(E_M_V(aa-2,2)-E_M_V(aa-1,2))*(E_M_V(aa-2,3)-
E_M_V(aa-1,3))+E_M_V(aa-1,3);
        C_D_SM(aa)  = (C_DS-E_C_V(aa-1,2))/(E_C_V(aa-2,2)-E_C_V(aa-1,2))*(E_C_V(aa-2,3)-
E_C_V(aa-1,3))+E_C_V(aa-1,3);
    end

    [Q_D, C_D, Q_F, C_F, Q_M, RSF, CP_F, CP_D, P_F, P_D]    = V4_Q_M_It(n, k, FF, rho, phi, i,
MW, R, T, Q_D_SM(aa), C_D_SM(aa), Q, S, P, P_D1, Type, Flow, AL, St_Type);

    Q_D_It(aa)  = Q_D(end);
    C_D_It(aa)  = C_D(end);

    E_M(aa)     = (Q_D_It(aa)/Q_DS-1)^2;
    E_C(aa)     = (C_D_It(aa)/C_DS-1)^2;

    E_M_V(aa,:) = [E_M(aa) Q_D_It(aa) Q_D_SM(aa)];
    E_M_S       = sortrows(E_M_V,1);

    E_C_V(aa,:) = [E_C(aa) C_D_It(aa) C_D_SM(aa)];
    E_C_S       = sortrows(E_C_V,1);

    if aa>1 && E_M(aa)<1e-10 && E_C(aa)<1e-10
        fprintf('Converged at %d!!\n',aa)

        for x = 1:size((Q_M'))
            if Q_M(1,x)<0
                fprintf('Q_M converged below zero at %d\nQ_M = %.5f\n',x,Q_M(1,x))
            end
        end
        if P_D(end)>2
```

```
            fprintf('P_D Inlet = %.5f\n',P_D(end))
        end
        break
    elseif aa == SM
        fprintf('SM did not converge!!\n')
        fprintf('Q_DI = %.5f, Q_DDS= %.5f\n',Q_DI(1)*3600, E_M_S(1,3)*3600)
        fprintf('Q_DO = %.5f, Q_DS= %.5f\n',Q_D(end)*3600, Q_DS*3600)
        fprintf('C_DI = %.5f, C_DDS= %.5f\n',C_DI(1), E_C_S(1,3))
        fprintf('C_DO = %.5f, C_DS= %.5f\n',C_D(end), C_DS)
        fprintf('E_M = %.14f, E_C = %.14f\n\n',E_M(aa),E_C(aa))
    end

end

Res_Vec     = [Q_D; C_D; Q_F; C_F; Q_M; RSF; CP_F; CP_D; P_F; P_D];
E_Vec       = [E_M_V(aa,:) E_C_V(aa,:)];
```

E.3.2. Q_M_It (Mass flowrate) function

```
function [Q_D, C_D, Q_F, C_F, Q_M, RSF, CP_F, CP_D, P_F, P_D]   = V4_Q_M_It(n, k, FF, rho,
phi, i, MW, R, T, Q_D1, C_D1, Q_F1, C_F1, P_F1, P_D1, Type, Flow, AL, St_Type)

%% Membrane related parameters
[Mod_Type, A, P_F_Max, T_Max, Q_F_Max, Q_C_Min, Q_P_Max, Y_Max, beta, B]        =
V4_Mem_Type(Type);
% fprintf('\nExplicit Solver\n')
%% Temperature correction factor
if T>= 298
    TCF = exp(2640*(1/298-1/T));
else
    TCF = exp(3020*(1/298-1/T));
end

%% Calculation related parameters
dA                  = n*A/(k-1);                    % Area per discretised element

%% Vector Initialisation
Q_D                 = [Q_D1 zeros(1,k-1)];          % Counterflow, thus shooting method with Q
as initial guess
C_D                 = [C_D1 zeros(1,k-1)];          % Counterflow, thus shooting method with S
as initial guess

Q_F                 = [Q_F1 zeros(1,k-1)];
C_F                 = [C_F1 zeros(1,k-1)];          % For more salts just add rows

Q_M                 = zeros(1,k);
RSF                 = zeros(1,k);

CP_F                = ones(1,k);                    % Concentration polarisation factor (ECP)
CP_D                = ones(1,k);                    % Concentration polarisation factor
(ICP+ECP)

P_F                 = P_F1*ones(1,k);
P_D                 = P_D1*ones(1,k);

dP_F                = zeros(1,k);
dP_D                = zeros(1,k);

X_F                 = [C_F(1)*Q_F(1) zeros(1,k-1)]; % UNITS: [g/L * m^3/s] !!!! Important
X_D                 = [C_D(1)*Q_D(1) zeros(1,k-1)];

k_M                 = V4_ICP(St_Type);

for a = 1:k-1

    k_F     = V4_ECP(Mod_Type, Q_F(a), rho, T, C_F(a));
    if Q_D(a) == 0
        k_D     = 10^16;
    else
        k_D     = V4_ECP(Mod_Type, Q_D(a), rho, T, C_D(a));
    end

    %% Initial m_M estimate
```

```
    Points          = 500;

    if a == 1
        %% Particle Cloud
        Q_M_PC  = beta*dA*TCF*FF*(P_F(a)-P_D(a)+phi*i*R*T/MW*(C_D(a)-C_F(a))).*rand(1,Points);

        for aa = 1:Points
            if AL == 0
                CP_F_It = exp(Q_M_PC(aa)/(k_F*dA));
                CP_D_It = exp(-Q_M_PC(aa)/(dA)*(1/k_M+1/k_D));
            elseif AL == 1
                CP_F_It = exp(Q_M_PC(aa)/(dA)*(1/k_F+1/k_M));
                CP_D_It = exp(-Q_M_PC(aa)/(k_D*dA));
            end

            EE          = (Q_M_PC(aa)-beta*dA*TCF*FF*(P_F(a)-
P_D(a)+phi*i*R*T/MW*(CP_D_It*C_D(a)-CP_F_It*C_F(a))/(1-B*dA/Q_M_PC(aa)*(CP_D_It-CP_F_It))))^2;
            Err(aa,1:2) = [Q_M_PC(aa) EE];

            if EE < 10^-6
               break
            end
        end
        Err_Min         = sortrows(Err,2);
        Q_M_Init        = Err_Min(1,1);
    elseif a == 2
        Q_M_Init        = Q_M(a-1);
    elseif a == 3
        Q_M_Init        = 2*Q_M(a-1)-Q_M(a-2);
    elseif a >= 4
        Q_M_Init        = 2.5*Q_M(a-1)-2*Q_M(a-2)+0.5*Q_M(a-3);
    end

    %% Newton Raphson Method
    AA              = 10000;
    Q_M_It          = zeros(AA,3);
    CP_F_It         = zeros(AA,3);
    CP_D_It         = zeros(AA,3);
    E_It            = zeros(AA,3);

    for aa = 1:AA
        if aa == 1
            Q_M_It(aa,1)     = Q_M_Init;
        else
            Q_M_It(aa,1)     = Q_M_It(aa-1,1)-E_It(aa-1,1)/((E_It(aa-1,3)-E_It(aa-
1,2))/(Q_M_It(aa-1,3)-Q_M_It(aa-1,2)));
        end

        Q_M_It(aa,2)     = 1.025*Q_M_It(aa,1);
        Q_M_It(aa,3)     = 0.975*Q_M_It(aa,1);

        for x = 1:3
            if AL == 0
                CP_F_It(aa,x)    = exp(Q_M_It(aa,x)/(k_F*dA));
                CP_D_It(aa,x)    = exp(-Q_M_It(aa,x)/(dA)*(1/k_F+1/k_M+1/k_D));
            elseif AL == 1
                CP_F_It(aa,x)     = exp(Q_M_It(aa,x)/(dA)*(1/k_F+1/k_M+1/k_D));
                CP_D_It(aa,x)     = exp(-Q_M_It(aa,x)/(k_D*dA));
            end

            E_It(aa,x)       = (Q_M_It(aa,x)-beta*dA*TCF*FF*(P_F(a)-
P_D(a)+phi*i*R*T/MW*(CP_D_It(aa,x)*C_D(a)-CP_F_It(aa,x)*C_F(a))/(1-
B*dA/Q_M_It(aa,x)*(CP_D_It(aa,x)-CP_F_It(aa,x)))))^2;
        end

        if E_It(aa,1)<1e-16
            Q_M(a)       = Q_M_It(aa,1);
            if AL == 0
                CP_F(a)      = exp(Q_M(a)/(k_F*dA));
                CP_D(a)      = exp(-Q_M(a)/(dA)*(1/k_F+1/k_M+1/k_D));
            elseif AL == 1
                CP_F(a)      = exp(Q_M(a)/(dA)*(1/k_F+1/k_M+1/k_D));
                CP_D(a)      = exp(-Q_M(a)/(k_D*dA));
            end

            if Q_M(a)<0 && Flow == 0
                fprintf('m_M converged below zero at %d\nm_M = %.5f\n', a, Q_M_It(aa,1))
```

```
            end
            break
        elseif aa == AA
            fprintf('m_M did not converge at %d\nm_M = %.5f & ERR = %.16f\n', a, Q_M_It(aa,1),
E_It(aa,1))
            return
        end
    end

    if Flow == 0
        X_F(a+1)    = X_F(a)+B*TCF*dA*(CP_D(a)*C_D(a)-CP_F(a)*C_F(a))/(1-B*dA/Q_M(a)*(CP_D(a)-
CP_F(a)));    % UNITS: [g/L * m^3/s] !!!! Important
        X_D(a+1)    = X_D(a)-B*TCF*dA*(CP_D(a)*C_D(a)-CP_F(a)*C_F(a))/(1-B*dA/Q_M(a)*(CP_D(a)-
CP_F(a)));
        Q_F(a+1)    = Q_F(a)-Q_M(a);
        Q_D(a+1)    = Q_D(a)+Q_M(a);
    elseif Flow == 1
        X_F(a+1)    = X_F(a)+B*TCF*dA*(CP_D(a)*C_D(a)-CP_F(a)*C_F(a))/(1-B*dA/Q_M(a)*(CP_D(a)-
CP_F(a)));     % Uncertain whether both are + or -
        X_D(a+1)    = X_D(a)+B*TCF*dA*(CP_D(a)*C_D(a)-CP_F(a)*C_F(a))/(1-B*dA/Q_M(a)*(CP_D(a)-
CP_F(a)));     % X_F is same as for co-current and X_D in opposite direction (Thus: Both +)

        Q_F(a+1)    = Q_F(a)-Q_M(a);
        Q_D(a+1)    = Q_D(a)-Q_M(a);
    end

    C_F(a+1)    = X_F(a+1)/Q_F(a+1);
    C_D(a+1)    = X_D(a+1)/Q_D(a+1);

    RSF(a)      = B*TCF*(CP_D(a)*C_D(a)-CP_F(a)*C_F(a))/(1-B*dA/Q_M(a)*(CP_D(a)-
CP_F(a)))*1000;  % [g/(m^2 s)]

    dP_F(a+1)   = 68.9476*n/k*(Q_F(a+1)*15.85032)^1.7;
    dP_D(a+1)   = 68.9476*n/k*(Q_D(a+1)*15.85032)^1.7;
    P_F(a+1)    = P_F(a)-dP_F(a+1);

    if Flow == 0
        P_D(a+1)    = P_D(a);
    elseif Flow == 1
        P_D(a+1)    = P_D(a)+dP_D(a+1);
    end

end

%% Membrane module operation window
if max(P_F) > P_F_Max
    fprintf('Operating pressure of membrane module is exceeded!!\n')
    fprintf('P_F = %.2f Bar, P_F_Max = %.2f Bar\n',max(P_F), P_F_Max)
end
if T-273.15 > T_Max
    fprintf('Operating temperature is exceeded!!\n')
    fprintf('T = %.2f °C, T_Max = %.2f °C\n',T-273.15 , T_Max)
end
if max(Q_F) > Q_F_Max
    fprintf('Inlet flow rate of membrane module is exceeded!!\n')
    fprintf('Q_F = %.2f m^3/h, Q_F_Max = %.2f m^3/h\n',max(Q_F)*3600, Q_F_Max*3600)
end
if min(Q_F) < Q_C_Min
    fprintf('Concentrate flow rate of membrane module is too low!!\n')
    fprintf('Q_C = %.2f m^3/h, Q_C_Min = %.2f m^3/h\n',min(Q_F)*3600, Q_C_Min*3600)
end

k_M     = (k-1)/n;
Y_1     = sum(Q_M(1:k_M))/Q_F(1);
Q_P     = sum(Q_M(1:k_M));

if Q_P > Q_P_Max
    fprintf('Permeate flow rate of membrane module is exceeded!!\n')
    fprintf('Q_P = %.2f m^3/h, Q_P_Max = %.2f m^3/h\n',Q_P*3600, Q_P_Max*3600)
end
if Y_1 > Y_Max
    fprintf('Recovery of the first membrane module is exceeded!!\n')
    fprintf('Y_1 = %.3f, Y_Max = %.3f\n',Y_1, Y_Max)
end

end
```

References

1. Guppy, L., Anderson, K., Mehta, P. & Nagabhatla, N. Global water crisis: The facts. *Hamilton, UNU-INWEH* (2017).

2. *OECD Environmental Outlook to 2050*. (OECD, 2012). doi:10.1787/9789264122246-en

3. Alkaisi, A., Mossad, R. & Sharifian-Barforoush, A. A Review of the Water Desalination Systems Integrated with Renewable Energy. *Energy Procedia* **110**, 268–274 (2017).

4. Tong, T. & Elimelech, M. The Global Rise of Zero Liquid Discharge for Wastewater Management: Drivers, Technologies, and Future Directions. *Environ. Sci. Technol.* **50**, 6846–6855 (2016).

5. Bartholomew, T. V, Mey, L., Arena, J. T., Siefert, N. S. & Mauter, M. S. Osmotically assisted reverse osmosis for high salinity brine treatment. *Desalination* **421**, 3–11 (2017).

6. Tsai, J.-H. *et al.* Membrane-based zero liquid discharge: Myth or reality? *J. Taiwan Inst. Chem. Eng.* **80**, 192–202 (2017).

7. Jones, E., Qadir, M., van Vliet, M. T. H., Smakhtin, V. & Kang, S. The state of desalination and brine production: A global outlook. *Sci. Total Environ.* **657**, 1343–1356 (2019).

8. Arnal, J. M. *et al.* Concentration of brines from RO desalination plants by natural evaporation. *Desalination* **182**, 435–439 (2005).

9. Alameddine, I. & El-Fadel, M. Brine discharge from desalination plants: a modeling approach to an optimized outfall design. *Desalination* **214**, 241–260 (2007).

10. Ogunbiyi, O. *et al.* Sustainable brine management from the perspectives of water, energy and mineral recovery: A comprehensive review. *Desalination* **513**, 115055 (2021).

11. Missimer, T. M. & Maliva, R. G. Environmental issues in seawater reverse osmosis

desalination: Intakes and outfalls. *Desalination* **434**, 198–215 (2018).

12. Miller, S., Shemer, H. & Semiat, R. Energy and environmental issues in desalination. *Desalination* **366**, 2–8 (2015).

13. Roberts, D. A., Johnston, E. L. & Knott, N. A. Impacts of desalination plant discharges on the marine environment: A critical review of published studies. *Water Res.* **44**, 5117–5128 (2010).

14. Morillo, J. *et al.* Comparative study of brine management technologies for desalination plants. *Desalination* **336**, 32–49 (2014).

15. Loganathan, P., Naidu, G. & Vigneswaran, S. Mining valuable minerals from seawater: a critical review. *Environ. Sci. Water Res. Technol.* **3**, 37–53 (2017).

16. Reig, M. *et al.* Concentration of NaCl from seawater reverse osmosis brines for the chlor-alkali industry by electrodialysis. *Desalination* **342**, 107–117 (2014).

17. Casas, S., Aladjem, C., Cortina, J. L., Larrotcha, E. & Cremades, L. V. Seawater Reverse Osmosis Brines as a New Salt Source for the Chlor-Alkali Industry: Integration of NaCl Concentration by Electrodialysis. *Solvent Extr. Ion Exch.* **30**, 322–332 (2012).

18. Chen, X. & Yip, N. Y. Unlocking High-Salinity Desalination with Cascading Osmotically Mediated Reverse Osmosis: Energy and Operating Pressure Analysis. *Environ. Sci. Technol.* **52**, 2242–2250 (2018).

19. Davenport, D. M., Deshmukh, A., Werber, J. R. & Elimelech, M. High-Pressure Reverse Osmosis for Energy-Efficient Hypersaline Brine Desalination: Current Status, Design Considerations, and Research Needs. *Environ. Sci. Technol. Lett.* (2018). doi:10.1021/acs.estlett.8b00274

20. Subramani, A. & Jacangelo, J. G. Treatment technologies for reverse osmosis concentrate volume minimization: A review. *Sep. Purif. Technol.* **122**, 472–489 (2014).

21. Sanmartino, J. A., Khayet, M., García-Payo, M. C., El-Bakouri, H. & Riaza, A. Treatment of

reverse osmosis brine by direct contact membrane distillation: Chemical pretreatment approach. *Desalination* **420**, 79–90 (2017).

22. Mericq, J.-P., Laborie, S. & Cabassud, C. Vacuum membrane distillation of seawater reverse osmosis brines. *Water Res.* **44**, 5260–5273 (2010).

23. Ruiz Salmón, I. & Luis, P. Membrane crystallization via membrane distillation. *Chem. Eng. Process. - Process Intensif.* **123**, 258–271 (2018).

24. Wang, Z., Deshmukh, A., Du, Y. & Elimelech, M. Minimal and zero liquid discharge with reverse osmosis using low-salt-rejection membranes. *Water Res.* **170**, 115317 (2020).

25. Bouma, A. T. & Lienhard, J. H. Split-feed counterflow reverse osmosis for brine concentration. *Desalination* **445**, 280–291 (2018).

26. Jamil, S., Jeong, S. & Vigneswaran, S. Application of pressure assisted forward osmosis for water purification and reuse of reverse osmosis concentrate from a water reclamation plant. *Sep. Purif. Technol.* **171**, 182–190 (2016).

27. Blandin, G., Verliefde, A. R. D., Tang, C. Y., Childress, A. E. & Le-Clech, P. Validation of assisted forward osmosis (AFO) process: Impact of hydraulic pressure. *J. Memb. Sci.* **447**, 1–11 (2013).

28. Shaffer, D. L., Werber, J. R., Jaramillo, H., Lin, S. & Elimelech, M. Forward osmosis: Where are we now? *Desalination* **356**, 271–284 (2015).

29. Qin, M. *et al.* Comparison of energy consumption in desalination by capacitive deionization and reverse osmosis. *Desalination* **455**, 100–114 (2019).

30. Campione, A. *et al.* Electrodialysis for water desalination: A critical assessment of recent developments on process fundamentals, models and applications. *Desalination* **434**, 121–160 (2018).

31. Gopi, G., Arthanareeswaran, G. & AF, I. Perspective of renewable desalination by using

membrane distillation. *Chem. Eng. Res. Des.* **144**, 520–537 (2019).

32. Mistry, K. H. *et al.* Entropy Generation Analysis of Desalination Technologies. *Entropy* **13**, 1829–1864 (2011).

33. Elimelech, M. & Phillip, W. A. The Future of Seawater Desalination: Energy, Technology, and the Environment. *Science (80-.).* **333**, 712–717 (2011).

34. Tow, E. W., McGovern, R. K. & Lienhard V, J. H. Raising forward osmosis brine concentration efficiency through flow rate optimization. *Desalination* **366**, 71–79 (2015).

35. Peters, C. D. & Hankins, N. P. Osmotically assisted reverse osmosis (OARO): Five approaches to dewatering saline brines using pressure-driven membrane processes. *Desalination* (2019). doi:10.1016/j.desal.2019.01.025

36. Peters, C. D. & Hankins, N. P. The synergy between osmotically assisted reverse osmosis (OARO) and the use of thermo-responsive draw solutions for energy efficient, zero-liquid discharge desalination. *Desalination* **493**, 114630 (2020).

37. McGovern, R. K. & Lienhard V, J. H. On the potential of forward osmosis to energetically outperform reverse osmosis desalination. *Journal of Membrane Science* **469**, 245–250 (2014).

38. Choi, B. G., Zhan, M., Shin, K., Lee, S. & Hong, S. Pilot-scale evaluation of FO-RO osmotic dilution process for treating wastewater from coal-fired power plant integrated with seawater desalination. *J. Memb. Sci.* **540**, 78–87 (2017).

39. Attarde, D., Jain, M., Singh, P. K. & Gupta, S. K. Energy-efficient seawater desalination and wastewater treatment using osmotically driven membrane processes. *Desalination* **413**, 86–100 (2017).

40. Hancock, N. T., Black, N. D. & Cath, T. Y. A comparative life cycle assessment of hybrid osmotic dilution desalination and established seawater desalination and wastewater reclamation processes. *Water Res.* **46**, 1145–1154 (2012).

41. Chang, H. *et al.* On-Site Treatment of Shale Gas Flowback and Produced Water in Sichuan Basin by Fertilizer Drawn Forward Osmosis for Irrigation. *Environ. Sci. Technol.* **54**, 10926–10935 (2020).

42. Majeed, T. *et al.* Fertilizer-drawn forward osmosis for irrigation of tomatoes. *Desalin. Water Treat.* **53**, 2746–2759 (2015).

43. Shaffer, D. L., Yip, N. Y., Gilron, J. & Elimelech, M. Seawater desalination for agriculture by integrated forward and reverse osmosis: Improved product water quality for potentially less energy. *Journal of Membrane Science* **415**–**416**, 1–8 (2012).

44. Ban, S. H., Im, S. J., Cho, J. & Jang, A. Comparative performance of FO-RO hybrid and two-pass SWRO desalination processes: Boron removal. *Desalination* **471**, 114114 (2019).

45. Al-Najar, B., Peters, C. D., Albuflasa, H. & Hankins, N. P. Pressure and osmotically driven membrane processes: A review of the benefits and production of nano-enhanced membranes for desalination. *Desalination* **479**, 114323 (2020).

46. Nguyen, T.-T., Kook, S., Lee, C., Field, R. W. & Kim, I. S. Critical flux-based membrane fouling control of forward osmosis: Behavior, sustainability, and reversibility. *J. Memb. Sci.* **570**–**571**, 380–393 (2019).

47. Johnson, D. J., Suwaileh, W. A., Mohammed, A. W. & Hilal, N. Osmotic's potential: An overview of draw solutes for forward osmosis. *Desalination* **434**, 100–120 (2018).

48. Cai, Y. & Hu, X. 'Matthew'. A critical review on draw solutes development for forward osmosis. *Desalination* **391**, 16–29 (2016).

49. Cai, Y. *et al.* Energy-efficient desalination by forward osmosis using responsive ionic liquid draw solutes. *Environ. Sci. Water Res. Technol.* **1**, 341–347 (2015).

50. Lin, S. & Elimelech, M. Staged reverse osmosis operation: Configurations, energy efficiency, and application potential. *Desalination* **366**, 9–14 (2015).

51. Lienhard V, J. H. Energy Savings in Desalination Technologies: Reducing Entropy Generation by Transport Processes. *J. Heat Transfer* **141**, (2019).

52. Bartholomew, T. V., Siefert, N. S. & Mauter, M. S. Cost Optimization of Osmotically Assisted Reverse Osmosis. *Environ. Sci. Technol.* (2018). doi:10.1021/acs.est.8b02771

53. Onishi, V. C. *et al.* Shale gas flowback water desalination: Single vs multiple-effect evaporation with vapor recompression cycle and thermal integration. *Desalination* **404**, 230–248 (2017).

54. Karagiannis, I. C. & Soldatos, P. G. Water desalination cost literature: review and assessment. *Desalination* **223**, 448–456 (2008).

55. Mezher, T., Fath, H., Abbas, Z. & Khaled, A. Techno-economic assessment and environmental impacts of desalination technologies. *Desalination* **266**, 263–273 (2011).

56. Atia, A. A., Yip, N. Y. & Fthenakis, V. Pathways for minimal and zero liquid discharge with enhanced reverse osmosis technologies: Module-scale modeling and techno-economic assessment. *Desalination* **509**, 115069 (2021).

57. Werber, J. R., Deshmukh, A. & Elimelech, M. Can batch or semi-batch processes save energy in reverse-osmosis desalination? *Desalination* **402**, 109–122 (2017).

58. Das, A. & Warsinger, D. M. Batch counterflow reverse osmosis. *Desalination* **507**, 115008 (2021).

59. Togo, N. *et al.* Osmotically Assisted Reverse Osmosis Utilizing Hollow Fiber Membrane Module for Concentration Process. *Ind. Eng. Chem. Res.* **58**, 6721–6729 (2019).

60. Chang Kim, Y. & Min, T. Influence of osmotic mediation on permeation of water in reverse osmosis: Experimental and numerical analysis. *J. Memb. Sci.* **595**, 117574 (2020).

61. Nakagawa, K. *et al.* Multistage osmotically assisted reverse osmosis process for concentrating solutions using hollow fiber membrane modules. *Chem. Eng. Res. Des.* **162**, 117–124 (2020).

62. Kim, J., Kim, D. I. & Hong, S. Analysis of an osmotically-enhanced dewatering process for the treatment of highly saline (waste)waters. *J. Memb. Sci.* **548**, 685–693 (2018).

63. Kim, J., Kim, J., Kim, J. & Hong, S. Osmotically enhanced dewatering-reverse osmosis (OED-RO) hybrid system: Implications for shale gas produced water treatment. *J. Memb. Sci.* **554**, 282–290 (2018).

64. Wijmans, J. G. & Baker, R. W. The solution-diffusion model: a review. *J. Memb. Sci.* **107**, 1–21 (1995).

65. Karode, S. K., Kulkarni, S. S. & Ghorpade, M. S. Osmotic dehydration coupled reverse osmosis concentration: Steady-state model and assessment. *J. Memb. Sci.* **164**, 277–288 (2000).

66. Lakerveld, R., Kuhn, J., Kramer, H. J. M., Jansens, P. J. & Grievink, J. Membrane assisted crystallization using reverse osmosis: Influence of solubility characteristics on experimental application and energy saving potential. *Chem. Eng. Sci.* **65**, 2689–2699 (2010).

67. Askari, M., Liang, C. Z., Choong, L. T. (Simon) & Chung, T.-S. Optimization of TFC-PES hollow fiber membranes for reverse osmosis (RO) and osmotically assisted reverse osmosis (OARO) applications. *J. Memb. Sci.* **625**, 119156 (2021).

68. Peters, C. D., Ng, D. Y. F., Hankins, N. P. & She, Q. A novel method for the accurate characterization of transport and structural parameters of deformable membranes utilized in pressure- and osmotically driven membrane processes. *J. Memb. Sci.* **638**, 119720 (2021).

69. Chen, X., Boo, C. & Yip, N. Y. Transport and structural properties of osmotic membranes in high-salinity desalination using cascading osmotically mediated reverse osmosis. *Desalination* **479**, 114335 (2020).

70. Oh, Y., Lee, S., Elimelech, M., Lee, S. & Hong, S. Effect of hydraulic pressure and membrane orientation on water flux and reverse solute flux in pressure assisted osmosis. *J. Memb. Sci.* **465**, 159–166 (2014).

71. She, Q., Jin, X. & Tang, C. Y. Osmotic power production from salinity gradient resource by pressure retarded osmosis: Effects of operating conditions and reverse solute diffusion. *J. Memb. Sci.* **401**–**402**, 262–273 (2012).

72. She, Q., Wang, R., Fane, A. G. & Tang, C. Y. Membrane fouling in osmotically driven membrane processes: A review. *Journal of Membrane Science* **499**, 201–233 (2016).

73. Blandin, G., Myat, D. T., Verliefde, A. R. D. & Le-Clech, P. Pressure assisted osmosis using nanofiltration membranes (PAO-NF): Towards higher efficiency osmotic processes. *J. Memb. Sci.* **533**, 250–260 (2017).

74. Xiao, D., Li, W., Chou, S., Wang, R. & Tang, C. Y. A modeling investigation on optimizing the design of forward osmosis hollow fiber modules. *J. Memb. Sci.* **392**–**393**, 76–87 (2012).

75. Duan, J., Litwiller, E. & Pinnau, I. Solution-diffusion with defects model for pressure-assisted forward osmosis. *J. Memb. Sci.* **470**, 323–333 (2014).

76. Siddiqui, F. A., She, Q., Fane, A. G. & Field, R. W. Exploring the differences between forward osmosis and reverse osmosis fouling. *J. Memb. Sci.* **565**, 241–253 (2018).

77. Al-Najar, B., Peters, C. D., Albuflasa, H. & Hankins, N. P. Pressure and osmotically driven membrane processes: A review of the benefits and production of nano-enhanced membranes for desalination. *Desalination* **479**, (2020).

78. Werber, J. R., Deshmukh, A. & Elimelech, M. The Critical Need for Increased Selectivity, Not Increased Water Permeability, for Desalination Membranes. *Environ. Sci. Technol. Lett.* **3**, 112–120 (2016).

79. Cohen-Tanugi, D., McGovern, R. K., Dave, S. H., Lienhard, J. H. & Grossman, J. C. Quantifying the potential of ultra-permeable membranes for water desalination. *Energy Environ. Sci.* **7**, 1134–1141 (2014).

80. Yip, N. Y. & Elimelech, M. Performance Limiting Effects in Power Generation from Salinity Gradients by Pressure Retarded Osmosis. *Environ. Sci. Technol.* **45**, 10273–10282 (2011).

81. Madsen, H. T., Nissen, S. S., Muff, J. & Søgaard, E. G. Pressure retarded osmosis from hypersaline solutions: Investigating commercial FO membranes at high pressures. *Desalination* **420**, 183–190 (2017).

82. Straub, A. P., Osuji, C. O., Cath, T. Y. & Elimelech, M. Selectivity and Mass Transfer Limitations in Pressure-Retarded Osmosis at High Concentrations and Increased Operating Pressures. *Environ. Sci. Technol.* **49**, 12551–12559 (2015).

83. Li, Y., Wang, R., Qi, S. & Tang, C. Structural stability and mass transfer properties of pressure retarded osmosis (PRO) membrane under high operating pressures. *J. Memb. Sci.* **488**, 143–153 (2015).

84. Davenport, D. M. *et al.* Thin film composite membrane compaction in high-pressure reverse osmosis. *J. Memb. Sci.* **610**, 118268 (2020).

85. Kook, S. *et al.* Serially connected forward osmosis membrane elements of pressure-assisted forward osmosis-reverse osmosis hybrid system: Process performance and economic analysis. *Desalination* **448**, 1–12 (2018).

86. Aghajani, M. *et al.* Influence of support-layer deformation on the intrinsic resistance of thin film composite membranes. *J. Memb. Sci.* **567**, 49–57 (2018).

87. de Roever, E., Fazel, M. & Hallsby, A. Permeate Spacer Imprints on SWRO Membranes: Evidence for Intrusion and Compaction. *IDA Wolrd Congr.* (2009).

88. Idarraga-Mora, J. A., O'Neal, A. D., Pfeiler, M. E., Ladner, D. A. & Husson, S. M. Effect of mechanical strain on the transport properties of thin-film composite membranes used in osmotic processes. *J. Memb. Sci.* **615**, 118488 (2020).

89. She, Q. *et al.* Fabrication and characterization of fabric-reinforced pressure retarded osmosis membranes for osmotic power harvesting. *J. Memb. Sci.* **504**, 75–88 (2016).

90. She, Q., Hou, D., Liu, J., Tan, K. H. & Tang, C. Y. Effect of feed spacer induced membrane deformation on the performance of pressure retarded osmosis (PRO): Implications for PRO

process operation. *J. Memb. Sci.* **445**, 170–182 (2013).

91. Callister Jr, William D and Rethwisch, D. G. *Fundamentals of materials science and engineering: an integrated approach*. (John Wiley \& Sons, 2020).

92. Ward, Ian M and Hadley, D. W. *An introduction to the mechanical properties of solid polymers*. (1993).

93. Ng, D. Y. F., Chen, Y., Dong, Z. & Wang, R. Membrane compaction in forward osmosis process. *Desalination* **468**, 114067 (2019).

94. Hussain, Y. A. & Al-Saleh, M. H. A viscoelastic-based model for TFC membranes flux reduction during compaction. *Desalination* **344**, 362–370 (2014).

95. Lee, C. *et al.* Effect of Spacer Configuration on the Characteristics of FO Membranes: Alteration of Permeation Characteristics by Membrane Deformation and Concentration Polarization. *Environ. Sci. Technol.* **54**, 6385–6395 (2020).

96. Kim, Y. C. & Elimelech, M. Adverse Impact of Feed Channel Spacers on the Performance of Pressure Retarded Osmosis. *Environ. Sci. Technol.* **46**, 4673–4681 (2012).

97. She, Q., Wong, Y. K. W., Zhao, S. & Tang, C. Y. Organic fouling in pressure retarded osmosis: Experiments, mechanisms and implications. *J. Memb. Sci.* **428**, 181–189 (2013).

98. Zou, S., Gu, Y., Xiao, D. & Tang, C. Y. The role of physical and chemical parameters on forward osmosis membrane fouling during algae separation. *J. Memb. Sci.* **366**, 356–362 (2011).

99. She, Q., Jin, X., Li, Q. & Tang, C. Y. Relating reverse and forward solute diffusion to membrane fouling in osmotically driven membrane processes. *Water Res.* **46**, 2478–2486 (2012).

100. Zhang, M., Hou, D., She, Q. & Tang, C. Y. Gypsum scaling in pressure retarded osmosis: experiments, mechanisms and implications. *Water Res.* **48**, 387–95 (2014).

101. Phuntsho, S. *et al.* Membrane scaling and flux decline during fertiliser-drawn forward osmosis desalination of brackish groundwater. *Water Res.* **57**, 172–182 (2014).

102. She, Q., Wang, R., Fane, A. G. & Tang, C. Y. Membrane fouling in osmotically driven membrane processes: A review. *J. Memb. Sci.* **499**, 201–233 (2016).

103. Li, Q. & Elimelech, M. Organic Fouling and Chemical Cleaning of Nanofiltration Membranes: Measurements and Mechanisms. *Environ. Sci. Technol.* **38**, 4683–4693 (2004).

104. Hoek, E. M. V & Elimelech, M. Cake-Enhanced Concentration Polarization: A New Fouling Mechanism for Salt-Rejecting Membranes. *Environ. Sci. Technol.* **37**, 5581–5588 (2003).

105. Chong, T. H., Wong, F. S. & Fane, A. G. Implications of critical flux and cake enhanced osmotic pressure (CEOP) on colloidal fouling in reverse osmosis: Experimental observations. *J. Memb. Sci.* **314**, 101–111 (2008).

106. Lee, S., Boo, C., Elimelech, M. & Hong, S. Comparison of fouling behavior in forward osmosis (FO) and reverse osmosis (RO). *J. Memb. Sci.* **365**, 34–39 (2010).

107. Park, M. *et al.* Modeling of colloidal fouling in forward osmosis membrane: Effects of reverse draw solution permeation. *Desalination* **314**, 115–123 (2013).

108. *Osmotically Driven Membrane Processes*. (IntechOpen, 2018). doi:10.5772/intechopen.68607

109. Zohrabian, L., Hankins, N. P. & Field, R. W. Hybrid forward osmosis-membrane distillation system: Demonstration of technical feasibility. *J. Water Process Eng.* **33**, 101042 (2020).

110. Zou, S. *et al.* Direct microscopic observation of forward osmosis membrane fouling by microalgae: Critical flux and the role of operational conditions. *J. Memb. Sci.* **436**, 174–185 (2013).

111. Zhang, J. *et al.* Membrane biofouling and scaling in forward osmosis membrane bioreactor. *J. Memb. Sci.* **403**–**404**, 8–14 (2012).

112. Parida, V. & Ng, H. Y. Forward osmosis organic fouling: Effects of organic loading, calcium

and membrane orientation. *Desalination* **312**, 88–98 (2013).

113. Tang, C. Y., She, Q., Lay, W. C. L., Wang, R. & Fane, A. G. Coupled effects of internal concentration polarization and fouling on flux behavior of forward osmosis membranes during humic acid filtration. *J. Memb. Sci.* **354**, 123–133 (2010).

114. Bacchin, P., Aimar, P. & Field, R. W. Critical and sustainable fluxes: Theory, experiments and applications. *J. Memb. Sci.* **281**, 42–69 (2006).

115. Tang, C. Y. & Leckie, J. O. Membrane independent limiting flux for RO and NF membranes fouled by humic acid. *Environ. Sci. Technol.* **41**, 4767–4773 (2007).

116. Zhu, X. & Elimelech, M. Colloidal Fouling of Reverse Osmosis Membranes: Measurements and Fouling Mechanisms. *Environ. Sci. Technol.* **31**, 3654–3662 (1997).

117. Song, L. & Elimelech, M. Particle deposition onto a permeable surface in laminar flow. *J. Colloid Interface Sci.* **173**, 165–180 (1995).

118. Belfort, G., Davis, R. H. & Zydney, A. L. The behavior of suspensions and macromolecular solutions in crossflow microfiltration. *Journal of Membrane Science* **96**, 1–58 (1994).

119. Lee, S., Kim, S., Cho, J. & Hoek, E. M. V. Natural organic matter fouling due to foulant-membrane physicochemical interactions. *Desalination* **202**, 377–384 (2007).

120. Bacchin, P. A possible link between critical and limiting flux for colloidal systems: Consideration of critical deposit formation along a membrane. *J. Memb. Sci.* **228**, 237–241 (2004).

121. Tang, C. Y., Kwon, Y. N. & Leckie, J. O. The role of foulant-foulant electrostatic interaction on limiting flux for RO and NF membranes during humic acid fouling-Theoretical basis, experimental evidence, and AFM interaction force measurement. *J. Memb. Sci.* **326**, 526–532 (2009).

122. Hong, S. & Elimelech, M. Chemical and physical aspects of natural organic matter (NOM)

fouling of nanofiltration membranes. *J. Memb. Sci.* **132**, 159–181 (1997).

123. Tang, C. Y., Kwon, Y. N. & Leckie, J. O. Fouling of reverse osmosis and nanofiltration membranes by humic acid-Effects of solution composition and hydrodynamic conditions. *J. Memb. Sci.* **290**, 86–94 (2007).

124. Morrow, C. P. & Childress, A. E. Evidence, Determination, and Implications of Membrane-Independent Limiting Flux in Forward Osmosis Systems. *Environ. Sci. Technol.* **53**, 4380–4388 (2019).

125. She, Q., Zhang, L., Wang, R., Krantz, W. B. & Fane, A. G. Pressure-retarded osmosis with wastewater concentrate feed: Fouling process considerations. *J. Memb. Sci.* **542**, 233–244 (2017).

126. Altaee, A. Computational model for estimating reverse osmosis system design and performance: Part-one binary feed solution. *Desalination* **291**, 101–105 (2012).

127. Semiat, R. Present and Future. *Water Int.* **25**, 54–65 (2000).

128. Henthorne, L. & Boysen, B. State-of-the-art of reverse osmosis desalination pretreatment. *Desalination* **356**, 129–139 (2015).

129. Moser, M., Trieb, F., Fichter, T., Kern, J. & Hess, D. A flexible techno-economic model for the assessment of desalination plants driven by renewable energies. *Desalin. Water Treat.* **55**, 3091–3105 (2015).

130. Pohl, R., Kaltschmitt, M. & Holländer, R. Investigation of different operational strategies for the variable operation of a simple reverse osmosis unit. *Desalination* **249**, 1280–1287 (2009).

131. Straub, A. P., Yip, N. Y. & Elimelech, M. Raising the Bar: Increased Hydraulic Pressure Allows Unprecedented High Power Densities in Pressure-Retarded Osmosis. *Environ. Sci. Technol. Lett.* **1**, 55–59 (2014).

132. Voutchkov, N. Energy use for membrane seawater desalination: Current status and trends.

Desalination **431**, 2–14 (2018).

133. DOW Water Solutions. FILMTEC Reverse Osmosis Membranes: Technical Manual. (2017).

134. Zhou, X., Gingerich, D. B. & Mauter, M. S. Water Treatment Capacity of Forward-Osmosis Systems Utilizing Power-Plant Waste Heat. *Ind. Eng. Chem. Res.* **54**, 6378–6389 (2015).

135. DOW Water Solutions. Filmtec Membranes: Product Information Catalog. (2020).

136. Jeon, J., Jung, J., Lee, S., Choi, J. Y. & Kim, S. A simple modeling approach for a forward osmosis system with a spiral wound module. *Desalination* **433**, 120–131 (2018).

137. Fane, A. G. (Tony). A grand challenge for membrane desalination: More water, less carbon. *Desalination* **426**, 155–163 (2018).

138. Pearce, G. K. UF/MF pre-treatment to RO in seawater and wastewater reuse applications: a comparison of energy costs. *Desalination* **222**, 66–73 (2008).

139. Xu, J. *et al.* Ultrafiltration as pretreatment of seawater desalination: Critical flux, rejection and resistance analysis. *Sep. Purif. Technol.* **85**, 45–53 (2012).

140. Suárez, J., Salgado, B., Casañas, A., González, J. C. & Pordomingo, J. One-year operational experience with ultrafiltration as pretreatment of seawater reverse osmosis desalination system (Maspalomas-I Plant). *Desalin. Water Treat.* **55**, 2813–2821 (2015).

141. Ma, W., Zhao, Y. & Wang, L. The pretreatment with enhanced coagulation and a UF membrane for seawater desalination with reverse osmosis. *Desalination* **203**, 256–259 (2007).

142. Jamaly, S., Darwish, N. N., Ahmed, I. & Hasan, S. W. A short review on reverse osmosis pretreatment technologies. *Desalination* **354**, 30–38 (2014).

143. PentAir. X-FLOW: AQUAFLEX. (2018).

144. Sauvet-Goichon, B. Ashkelon desalination plant: A successful challenge. *Desalination* **203**, 75–81 (2007).

145. Kim, J. *et al.* Practical considerations for operability of an 8" spiral wound forward osmosis module: Hydrodynamics, fouling behaviour and cleaning strategy. *Desalination* **404**, 249–258 (2017).

146. The Dow Chemical Co.: Midland, M. I. DOW Specialty Membrane XUS180804 and XUS180802 Reverse Osmosis Elements Product Data Sheet. (2018).

147. Pendergast, M. M., Nowosielski-Slepowron, M. S. & Tracy, J. Going big with forward osmosis. *Desalin. Water Treat.* **57**, 26529–26538 (2016).

148. Coday, B. D. *et al.* The sweet spot of forward osmosis: Treatment of produced water, drilling wastewater, and other complex and difficult liquid streams. *Desalination* **333**, 23–35 (2014).

149. Claumann, C. A. *et al. Modeling and Process Optimization: An Approach using Aspen Plus and Matlab in the Energy Integration Study of Distillation Columns*. (2015).

150. Fontalvo Alzate, J. Using user models in Matlab® within the Aspen Plus® interface with an Excel® link. *Ing. e Investig.* **34**, 39–43 (2014).

151. Luo, H. *et al.* A review on the recovery methods of draw solutes in forward osmosis. *J. Water Process Eng.* **4**, 212–223 (2014).

152. Zeng, L. *et al.* A Thermodynamical Approach for Evaluating Energy Consumption of the Forward Osmosis Process Using Various Draw Solutes. *Water* **9**, 189 (2017).

153. Wang, K. Y., Ong, R. C. & Chung, T.-S. Double-Skinned Forward Osmosis Membranes for Reducing Internal Concentration Polarization within the Porous Sublayer. *Ind. Eng. Chem. Res.* **49**, 4824–4831 (2010).

154. McGinnis, R. L., Hancock, N. T., Nowosielski-Slepowron, M. S. & McGurgan, G. D. Pilot demonstration of the NH3/CO2 forward osmosis desalination process on high salinity brines. *Desalination* **312**, 67–74 (2013).

155. Hancock, N. T. & Cath, T. Y. Solute Coupled Diffusion in Osmotically Driven Membrane

Processes. *Environ. Sci. Technol.* **43**, 6769–6775 (2009).

156. McCutcheon, J. R., McGinnis, R. L. & Elimelech, M. A novel ammonia—carbon dioxide forward (direct) osmosis desalination process. *Desalination* **174**, 1–11 (2005).

157. McGinnis, R. L. & Elimelech, M. Energy requirements of ammonia–carbon dioxide forward osmosis desalination. *Desalination* **207**, 370–382 (2007).

158. Dong, S., Heyda, J., Yuan, J. & Schalley, C. A. Lower critical solution temperature (LCST) phase behaviour of an ionic liquid and its control by supramolecular host–guest interactions. *Chem. Commun.* **52**, 7970–7973 (2016).

159. Shon, H. K., Chekli, L., Phuntsho, S., Kim, J. & Cho, J. Draw Solutes in Forward Osmosis Processes. in *Forward Osmosis* 85–113 (American Society of Civil Engineers, 2015). doi:10.1061/9780784414071.ch05

160. Chekli, L. *et al.* A comprehensive review of hybrid forward osmosis systems: Performance, applications and future prospects. *J. Memb. Sci.* **497**, 430–449 (2016).

161. Wang, P. *Smart Materials for Advanced Environmental Applications*. (The Royal Society of Chemistry, 2016). doi:10.1039/9781782622192

162. Boo, C., Khalil, Y. F. & Elimelech, M. Performance evaluation of trimethylamine–carbon dioxide thermolytic draw solution for engineered osmosis. *J. Memb. Sci.* **473**, 302–309 (2015).

163. Kim, Y. C. & Park, S.-J. Experimental Study of a 4040 Spiral-Wound Forward-Osmosis Membrane Module. *Environ. Sci. Technol.* **45**, 7737–7745 (2011).

164. Orme, C. J. & Wilson, A. D. 1-Cyclohexylpiperidine as a thermolytic draw solute for osmotically driven membrane processes. *Desalination* **371**, 126–133 (2015).

165. Mok, Y. *et al.* Circulatory osmotic desalination driven by a mild temperature gradient based on lower critical solution temperature (LCST) phase transition materials. *Phys. Chem. Chem. Phys.* **15**, 19510–19517 (2013).

166. RL, L. *et al.* Characterization of a Thermoresponsive Chitosan Derivative as a Potential Draw Solute for Forward Osmosis. *Environ. Sci. Technol.* **50**, 11935–11942 (2016).

167. Jilvero, H., Normann, F., Andersson, K. & Johnsson, F. The Rate of CO2 Absorption in Ammonia—Implications on Absorber Design. *Ind. Eng. Chem. Res.* **53**, 6750–6758 (2014).

168. Petchers, N. *Combined heating, cooling and power handbook: Technologies and applications an integrated approach to energy resource optimization*. (The Fairmont Press, 2012).

169. Cengel, Y. A. & Ghajar, A. J. (Afshin J. *Heat and Mass Transfer: Fundamentals and Applications*. (Mc Graw Hill, 2014).

170. *Distillation Design and Control Using Aspen^{TM} Simulation*. (John Wiley & Sons, Inc., 2013). doi:10.1002/9781118510193

171. Darde, V., Maribo-Mogensen, B., van Well, W. J. M., Stenby, E. H. & Thomsen, K. Process simulation of CO 2 capture with aqueous ammonia using the Extended UNIQUAC model. *Int. J. Greenh. Gas Control* (2012). doi:10.1016/j.ijggc.2012.05.017

172. Franken, A. C. M. Prevention and control of membrane fouling: Practical implications and examining recent innovations. *Membraan Appl. Cent. Twente b.v.* (2009).

173. Lotfi, F. *et al.* Understanding the possible underlying mechanisms for low fouling tendency of the forward osmosis and pressure assisted osmosis processes. *Desalination* **421**, 89–98 (2017).

174. Lee, J., Kook, S., Lee, C. & Kim, I. S. Effect of intermittent pressure-assisted forward osmosis (I-PAFO) on organic fouling. *Desalination* **419**, 60–69 (2017).

175. Tow, E. W. *et al.* Comparison of fouling propensity between reverse osmosis, forward osmosis, and membrane distillation. *J. Memb. Sci.* **556**, 352–364 (2018).

176. Gingerich, D. B. & Mauter, M. S. Quantity, Quality, and Availability of Waste Heat from United States Thermal Power Generation. *Environ. Sci. Technol.* (2015). doi:10.1021/es5060989

177. Bartholomew, T. V. & Mauter, M. S. Computational framework for modeling membrane processes without process and solution property simplifications. *J. Memb. Sci.* **573**, 682–693 (2019).

178. Boo, C., Elimelech, M. & Hong, S. Fouling control in a forward osmosis process integrating seawater desalination and wastewater reclamation. *J. Memb. Sci.* **444**, 148–156 (2013).

179. Bacchin, P. A possible link between critical and limiting flux for colloidal systems: Consideration of critical deposit formation along a membrane. in *Journal of Membrane Science* **228**, 237–241 (Elsevier, 2004).

180. Gu, Y., Wang, Y.-N., Wei, J. & Tang, C. Y. Organic fouling of thin-film composite polyamide and cellulose triacetate forward osmosis membranes by oppositely charged macromolecules. *Water Res.* **47**, 1867–1874 (2013).

181. Tang, C. Y., Chong, T. H. & Fane, A. G. Colloidal interactions and fouling of NF and RO membranes: A review. *Advances in Colloid and Interface Science* **164**, 126–143 (2011).

182. Fei, J. *et al.* Membrane structure-dependent limiting flux behavior and membrane selectivity loss during gypsum scaling: Implications for pressure-retarded osmosis operation and membrane design. *Desalination* **492**, 114644 (2020).

183. Song, Y., Gao, X. & Gao, C. Evaluation of scaling potential in a pilot-scale NF–SWRO integrated seawater desalination system. *J. Memb. Sci.* **443**, 201–209 (2013).

184. Wang, S. Y., Chen, Y. F., Zhou, H., Xu, X. H. & Cheng, L. H. Calcium carbonate scaling in forward osmosis for textile reverse osmosis concentrate treatment. *J. Water Process Eng.* **35**, 101181 (2020).

185. Li, Z. *et al.* Calcium carbonate scaling in seawater desalination by ammonia-carbon dioxide forward osmosis: Mechanism and implications. *J. Memb. Sci.* **481**, 36–43 (2015).

186. Lee, S. & Kim, Y. C. Calcium carbonate scaling by reverse draw solute diffusion in a forward osmosis membrane for shale gas wastewater treatment. *J. Memb. Sci.* **522**, 257–266 (2017).

187. Xie, M. & Gray, S. R. Gypsum scaling in forward osmosis: Role of membrane surface chemistry. *J. Memb. Sci.* **513**, 250–259 (2016).

188. Baoxia, M. I. & Elimelech, M. Gypsum scaling and cleaning in forward osmosis: Measurements and mechanisms. *Environ. Sci. Technol.* **44**, 2022–2028 (2010).

189. Rahardianto, A., Mccool, B. C. & Cohen, Y. Reverse osmosis desalting of inland brackish water of high gypsum scaling propensity: Kinetics and mitigation of membrane mineral scaling. *Environ. Sci. Technol.* **42**, 4292–4297 (2008).

190. ASTM D1141 - 98(2008) Standard Practice for the Preparation of Substitute Ocean Water. *ASTM International* (2008).

191. Yu, W., Song, D., Li, A. & Yang, H. Control of gypsum-dominated scaling in reverse osmosis system using carboxymethyl cellulose. *J. Memb. Sci.* **577**, 20–30 (2019).

192. Chauhan, K., Kumar, R., Kumar, M., Sharma, P. & Chauhan, G. S. Modified pectin-based polymers as green antiscalants for calcium sulfate scale inhibition. *Desalination* **305**, 31–37 (2012).

193. Li, W., Su, X., Palazzolo, A. & Ahmed, S. Numerical modeling of concentration polarization and inorganic fouling growth in the pressure-driven membrane filtration process. *J. Memb. Sci.* **569**, 71–82 (2019).

194. Vrouwenvelder, J. S., Picioreanu, C., Kruithof, J. C. & van Loosdrecht, M. C. M. Biofouling in spiral wound membrane systems: Three-dimensional CFD model based evaluation of experimental data. *J. Memb. Sci.* **346**, 71–85 (2010).

195. Antony, A. *et al.* Scale formation and control in high pressure membrane water treatment systems: A review. *J. Memb. Sci.* **383**, 1–16 (2011).

196. Chen, S. C., Wan, C. F. & Chung, T. S. Enhanced fouling by inorganic and organic foulants on pressure retarded osmosis (PRO) hollow fiber membranes under high pressures. *J. Memb. Sci.* **479**, 190–203 (2015).

197. Liu, Y. & Mi, B. Combined fouling of forward osmosis membranes: Synergistic foulant interaction and direct observation of fouling layer formation. *J. Memb. Sci.* **407**–**408**, 136–144 (2012).

198. Mi, B. & Elimelech, M. Chemical and physical aspects of organic fouling of forward osmosis membranes. *J. Memb. Sci.* **320**, 292–302 (2008).

199. She, Q., Tang, C. Y., Wang, Y. N. & Zhang, Z. The role of hydrodynamic conditions and solution chemistry on protein fouling during ultrafiltration. *Desalination* **249**, 1079–1087 (2009).

200. Balkenov, A. *et al.* Complex organic fouling and effect of silver nanoparticles on aquaporin forward osmosis membranes. *J. Water Process Eng.* **34**, 101177 (2020).

201. Nikbakht Fini, M., Madsen, H. T., Sørensen, J. L. & Muff, J. Moving from lab to pilot scale in forward osmosis for pesticides rejection using aquaporin membranes. *Sep. Purif. Technol.* **240**, 116616 (2020).

202. Xie, M. *et al.* Trace organic contaminant rejection by aquaporin forward osmosis membrane: Transport mechanisms and membrane stability. *Water Res.* **132**, 90–98 (2018).

203. Widjaya, A., Hoang, T., Stevens, G. W. & Kentish, S. E. A comparison of commercial reverse osmosis membrane characteristics and performance under alginate fouling conditions. *Sep. Purif. Technol.* **89**, 270–281 (2012).

204. Motsa, M. M., Mamba, B. B., Thwala, J. M. & Verliefde, A. R. D. Osmotic backwash of fouled FO membranes: Cleaning mechanisms and membrane surface properties after cleaning. *Desalination* **402**, 62–71 (2017).

205. Kim, C., Lee, S. & Hong, S. Application of osmotic backwashing in forward osmosis: mechanisms and factors involved. *Desalin. Water Treat.* **43**, 314–322 (2012).

206. Blandin, G., Verliefde, A. R. D. & Le-Clech, P. Pressure enhanced fouling and adapted anti-fouling strategy in pressure assisted osmosis (PAO). *J. Memb. Sci.* **493**, 557–567 (2015).

207. Yip, N. Y. & Elimelech, M. Influence of natural organic matter fouling and osmotic backwash on pressure retarded osmosis energy production from natural salinity gradients. *Environ. Sci. Technol.* **47**, 12607–12616 (2013).

208. Kim, J. E., Phuntsho, S., Lotfi, F. & Shon, H. K. Investigation of pilot-scale 8040 FO membrane module under different operating conditions for brackish water desalination. *Desalin. Water Treat.* **53**, 2782–2791 (2015).

209. Bowen, W. R. & Welfoot, J. S. Predictive modelling of nanofiltration: membrane specification and process optimisation. *Desalination* **147**, 197–203 (2002).

210. Cengel, Y. A. & Boles, M. A. *Thermodynamics : an engineering approach*. (McGraw-Hill, 2011).

211. Lara, J., Osunsan, O. & Holtzapple, M. Advanced Mechanical Vapor-Compression Desalination System. in *Desalination, Trends and Technologies* (ed. Schorr, M.) (IntechOpen, 2012). doi:10.5772/14711

212. Lu, Y. Y., Hu, Y. D., Zhang, X. L., Wu, L. Y. & Liu, Q. Z. Optimum design of reverse osmosis system under different feed concentration and product specification. *J. Memb. Sci.* (2007). doi:10.1016/j.memsci.2006.10.037

213. Mi, B. & Elimelech, M. Organic fouling of forward osmosis membranes: Fouling reversibility and cleaning without chemical reagents. *J. Memb. Sci.* **348**, 337–345 (2010).

214. Vu, M. T., Ansari, A. J., Hai, F. I. & Nghiem, L. D. Performance of a seawater-driven forward osmosis process for pre-concentrating digested sludge centrate: Organic enrichment and membrane fouling. *Environ. Sci. Water Res. Technol.* **4**, 1047–1056 (2018).

215. Liberman, B. Three methods of forward osmosis cleaning for RO membranes. *Desalination* **431**, 22–26 (2018).

216. Qin, J. J., Oo, M. H., Kekre, K. A. & Liberman, B. Development of novel backwash cleaning technique for reverse osmosis in reclamation of secondary effluent. *J. Memb. Sci.* **346**, 8–14

(2010).

217. Farooque, A. M., Al-Jeshi, S., Saeed, M. O. & Alreweli, A. Inefficacy of osmotic backwash induced by sodium chloride salt solution in controlling SWRO membrane fouling. *Appl. Water Sci.* **4**, 407–424 (2014).